SMOKE EMISSIONS FROM EASTERN CHINA'S AGRICULTURAL RESIDUE BURNING ASSESSED USING REMOTELY SENSING AND IN SITU MEASUREMENT

Zhang, Tianran

Awarding institution:
King's College London

SMOKE EMISSIONS FROM EASTERN CHINA'S AGRICULTURAL RESIDUE BURNING ASSESSED USING REMOTELY SENSING AND IN SITU MEASUREMENT

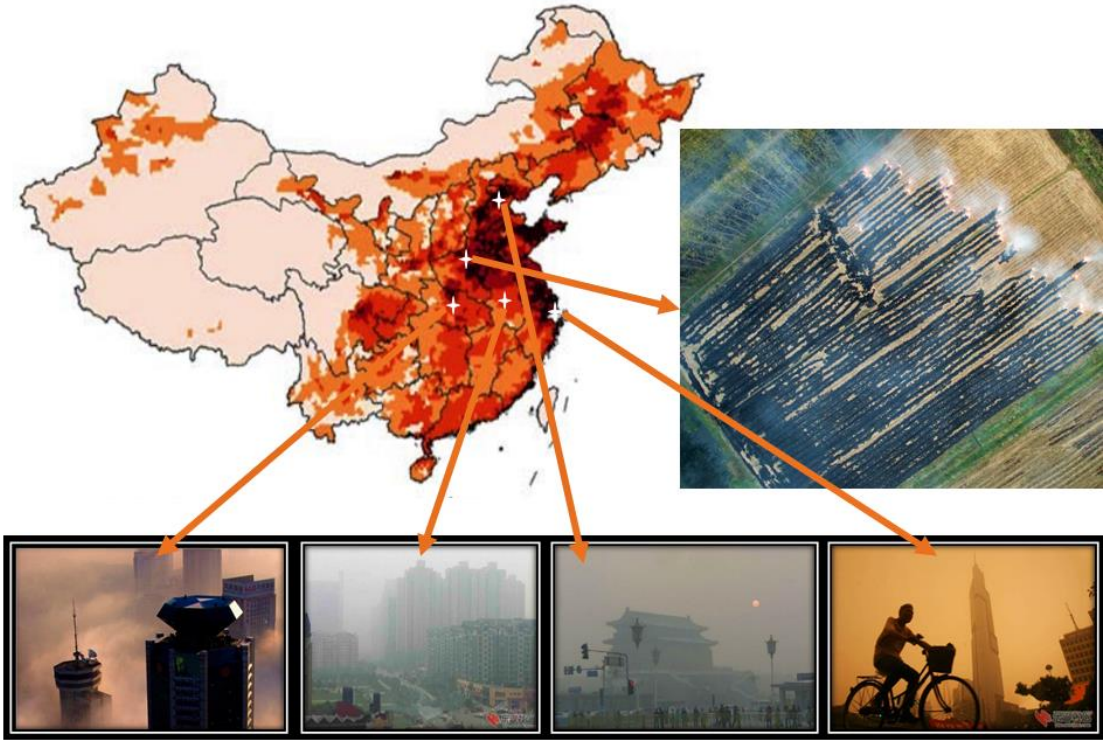

Tianran Zhang

PhD Thesis

Department of Geography, School of Global Affairs

King's College London

2017

ABSTRACT

This thesis exploits satellite remote sensing and *in situ* smoke measurement to estimate emissions from agricultural residue burning in Eastern China, a densely populated region with often poor air quality and which is one of China's main agricultural burning regions. A new active fire (AF) detection and fire radiative power (FRP) retrieval algorithm is developed for use with the Suomi-NPP satellite's VIIRS sensor, whose high spatial resolution band 'I' Bands provide an ability to detect the smaller (low FRP) fires missing from current satellite AF datasets. Daily fire radiative energy (FRE) – and thus fuel consumption - estimates are obtained by a link to diurnal cycle information from the Himawari geostationary spacecraft, and used to estimate emissions (CO_2, CO, $PM_{2.5}$ and BC) via multiplication by emissions factors derived from *in situ* measurements of smoke made by exploiting a new multi-sensor sampling design.

Results show that VIIRS detects AFs with an FRP-minimum below 0.5 MW (cf. 6–8 MW for MODIS), and identifies typically 5 to 10 times more AF pixels across Eastern China. The resulting high spatio-temporal resolution agricultural fire emissions inventory is compared to two state-of-the-art global fire databases (GFAS and GFED), and shows fuel consumption emissions estimates 1 to 4 times higher for the burning seasons, highlighting the significance of the formally undetected low FRP active fires. Mean annual emissions of CO_2, CO, $PM_{2.5}$ and BC range from 16932 to 31107, 562 to 1035, 70 to 130, 6 to 11 Gg respectively (mean of 2012 – 2015), and the interannual variations seen appear potentially linked to changing farming activity and local fire management practices.

This research has improved understanding and quantification of agricultural residue burning in Eastern China, and the new "small fire" detection capability could in future be extended to wider (even global) scales, particularly in agricultural burning regions, in order to reduce the low biases that have been now clearly exposed in current fire emissions estimates of those areas.

THESIS INCORPORATING PUBLICATIONS DECLARATION

Two of the research Chapters of this thesis contain publications:

Publication (1) Zhang, T., Wooster, M.J. and Xu, W., 2017. Approaches for synergistically exploiting VIIRS I-and M-Band data in regional active fire detection and FRP assessment: A demonstration with respect to agricultural residue burning in Eastern China. Remote Sensing of Environment, 198, pp.407-424 (Contained in Chapter 3).

This publication focuses on the development and testing of an active fire detection and FRP measurement method, based on data from NPP VIIRS.

Publication (2) Zhang, T., Wooster, M.J., Green, D.C. and Main, B., 2015. New field-based agricultural biomass burning trace gas, PM 2.5, and black carbon emission ratios and factors measured in situ at crop residue fires in Eastern China. Atmospheric Environment, 121, pp.22-34 (Contained in Chapter 4).

This publication focuses on the derivation of smoke emissions factors based on fieldwork in China.

The author of this PhD thesis is the first author of both publications and did the vast majority (>90 %) of the work for both publications, with the first supervisor of the thesis the second author, and others who assisted in the work also included in the author list.

For Publication (1) The author of this PhD thesis undertook the fieldwork with co-authors (Wooster and Bruce), with co-author Green (2nd supervisor) helping to design the sampling system deployed. The author of the thesis conducted all the data processing, analysis, and drafted the paper.

For Publication (2) The author of this PhD thesis designed the algorithm with advice from co-author Wooster (1st supervisor), and input on atmospheric correction calculation from co-author Xu. The author of this thesis conducted all the data processing, undertook the fieldwork validation, did all the analysis, and drafted the paper.

ACKNOWLEDGEMENTS

First, I would like to express my sincere gratitude to King's China Award and King's Graduate School, who funded most of my PhD study. The PhD project has also been supported by STFC Newton China Agritech Programme, and Chinese Student Awards from the Great Britain-China Educational Trust.

During this 4-year journey, I received lots of inspiring suggestions and encouragement from both of my supervisors Martin and David. I've been learning a lot from both, especially Martin, who is not only a very talented and passionate earth observation scientist always ready to share his knowledge, but also a very warm-hearted tutor who is always happy to help. He works very hard himself as he enjoys his work so much, but he has never put any pressure on me and always shows great appreciation when I spend extra hours trying to get things done. Working with Martin is such a fun thing that it made all the time I spent on my PhD very enjoyable, especially when conducting fieldwork outside. Speaking of which, special thanks should give to Martin's garden which has witnessed (and suffered) lots of Chinese biomass burning.

A very important part of my PhD work is to build and test the sampling box (also known as box of tricks), which wouldn't have been possible without Bruce, a very creative and knowledgeable engineer. He always shows strong interest and concern about students' research project and is happy to go out of his way to help. Carrying a sampling box walking into the smoke at 40^{o}C is definitely a hard job, thank you for never complaining!

During my fieldwork in China, I also got lots of support from Dr Lili Wang and Dr Hefeng Zhang, two Chinese biomass burning experts from local research institutes. They gave me lots of constructive suggestions on fieldwork organisation and preparation. Lots of local farmers, including Mr Wu and Mr Zhang's family, also gave me lots of help during the instrument deployments and fieldwork conducting.

I would also like to acknowledge my colleagues at King's College London, especially Mark and Josh, who provided lots of useful comments and feedback, and Weidong and Jiangping, who have been really helpful on the coding and hardware.

Most of my data processing was accomplished using the STFC-Jasmin system. The helpdesk was extremely helpful every time I emailed them with any stupid question. Thanks for all your patience!

Those four-years of PhD life wouldn't have been fun without many of my dear friends in London, Yishu, Yi, Mark, Anna, Jake and all of the other lovely people that helped and encouraged me. It has been a great life experience here with people from all over the world. Special thanks to Yishu since nothing can be more encouraging to see your best friend also decide to become a PhD student! Another person I would like to show my greatest appreciation to is my boyfriend Pete, who always shows great respect to my research and happy to talk through any problems with me. Your company and introducing me to climbing are most important thing to help me going through the final writing up year of my PhD.

Last but not the least, I want to express my very profound gratitude to my parents for their unfailing and continuous support throughout my life in education. Four years ago, before the first time I departed from China on my journey to the UK, my dad shared with me a dream he had when he was young. In his dream, he went on a big ship, across the ocean. He dreamed that he arrived in the UK and explore the life here. Though he never got the chance to go abroad, he told me he was very excited when he first heard that I received a scholarship from King's and would study in UK. I really enjoy this story because not only this is very Chinese – parents always have high expectation of their children and wish to pass their dreams on, but also very my parents – who never put the pressure on me but are always enthusiastic to celebrate any of my successes no matter how small. My parents are both normal people. My mum was not even able to finish her high school due to lots of reasons that time, but they both value my education as one of the most important thing in the family. I remember during my 4th year in primary school, my parents decide to move the house from a small town to the county so that I could go to the best school there. To do this, they had to purchase a more expensive flat next to the school and spend lots of years working really hard to pay back the mortgage. Looking back now, I can't describe how much I appreciate their efforts, especially my mum, who made this very brave choice and convinced everyone in the family.

Looking back again now, I really appreciate the unique experience of spending four years digging into a research topic to explore all the possibilities there. I would like to end this acknowledgement with my appreciation of science using one of my favourite poem from an ancient Chinese poet Yuan Qu:

The way ahead is long; I see no ending, yet high and low I will search with my will unbending.

To my father - for being the best teacher in my life.

To my mother - for always encouraging me to explore the bigger world.

CONTENTS

LIST OF FIGURES

LIST OF TABLES

LIST OF FREQUENT ABBREVIATIONS

Abbreviation	Meaning	Description
AF	Active Fire	Fires being detected while burning at the time of satellite sensor overpasses.
AHI	Advanced Himawari Imager	A key instrument onboard geostationary satellite Himawari-8.
BC	Black Carbon	A component of fine particulate matter (PM <= 2.5 µm in aerodynamic diameter), which consists of pure carbon in several linked forms.
CYBA	Crop Yield Based Approach	A methodology calculates the amount of crop residue burned in a region from a combination of crop production statistics and related additional parameters.
DMB	Dry Matter Emission	The amount of dry matter emitted during fires burning.
ER	Emission Ratio	Two particular chemical species [x and y] (i.e. [ERx/y] represents their relative abundance in the smoke plume, and is typically expressed in units of mol.mol-1.
EF	Emission Factor	The amount of a particular smoke constituent (either a gas or an aerosol) released per unit of fuel burned; [g.kg-1]
EO	Earth Observation	Gathering of information about planet Earth's physical, chemical and biological systems via remote sensing technologies supplemented by earth surveying techniques, encompassing the collection, analysis and presentation of data.
FRE	Fire Radiative Energy	The temporal integration of FRP (MJ; Wooster *et al.*, 2005)
FRP	Fire Radiative Power	The instantaneous quantification of the rate of radiant thermal emission from a fire over all wavelengths (MW; Wooster *et al.*, 2005)
GFAS	Global Fire Assimilation System	A global fire emission database calculates biomass burning emissions by assimilating FRP observations from the MODIS.
GFED	Global Fire Emissions Database	A global fire emission database calculates biomass burning emissions based on MODIS burned area product.
IR	Infrared	Referring to the infrared wavelengths of the electromagnetic spectrum
LGR	Los Gatos Research	Producer of high performance analysers for measurements of trace gases.
MODIS	Moderate Resolution Imaging Spectroradiometer	A key instrument aboard the Terra and Aqua satellites.
MSI	MultiSpectral Instrument	A key instrument on-board SENTINEL-2 measures the Earth's reflected radiance in 13 spectral bands from VNIR to SWIR.
MWIR	Mid-wave Infrared	Referring to spectral bands within the 3 – 5 µm range
LWIR	Long-wave Infrared	Referring to spectral bands within the 8 – 14 µm range
OC	Organic Carbon	Organic compounds in fine particulate matter.
OLI	Operational Land Imager	Instrument onboard the Landsat 8 satellite
UAV	Unmanned Aerial Vehicle	An aircraft piloted by remote control or onboard computers.
VIIRS	Visible Infrared Imaging Radiometer Suite	A sensor on board the Suomi National Polar-orbiting Partnership (Suomi NPP) weather satellite.

CHAPTER 1: INTRODUCTION

This thesis describes work conducted to improve the understanding and quantification of agricultural residue burning in Eastern China, in particular focusing on the emissions to the atmosphere that result. Agricultural residues represent the 'waste' material left in a field after a crop has been harvested, for example the stubble left after wheat harvest. In still developing economies, such agricultural residues are often removed via *in situ* burning, which in the absence of well-developed large scale agricultural mechanisation is generally the quickest, simplest and cheapest way to get rid of them prior to the next planting (Liu *et al.*, 2008). However, such burning releases smoke into the atmosphere, and this contains many types of gaseous and particulate air pollutants, including CO_2, CO, CH_4, NOx, black carbon and organic carbon. This thesis describes work with new satellite remote sensing data and field measurements of gases and aerosols to investigate and quantify this phenomenon.

In global scale, open biomass burning is one of the major source of aerosols and gases in the atmosphere. For example, research suggests it contributes 6-12% to annual total non-CO_2 emissions, and 40% to global black carbon (Bond et al., 2013; IPCC, 2014; Mieville et al., 2010). Earlier research has shown in Asian, the contribution of biomass burning to CO can be as high as 24% (Streets et al., 2003). Within the same study, Streets et al., (2003) used a crop yield based approach (see Section 2.6) to estimate that approximated 110 million tonnes of crop residue is burned in China ever year (calculated for the year 2000), and this was almost half of that estimated to be burned across the whole of Asia at the time. This total also represented around 60% of the total biomass burned in China, the bulk of the remainder being due to forest fires which, when intense, can consume much more fuel per unit area than can crop residue burns.

Eastern China is the region where the majority of the China's population and agriculture is located, and where the vast majority of agricultural residue burning occurs (Liu *et al.*, 2008). The seasonal burning of agricultural residues here is suspected to contribute significantly to annual air pollution events, including increased tropospheric ozone, particulate matter and public health impacts, visibility problems, and traffic accidents (Fig. 1.1, Chan and Yao, 2008; Li *et al.*, 2010; Wang *et al.*, 2013; Zhang *et al.*, 2011). In terms of forest fires occurring in the main provinces of Eastern China (Anhui, Shandong, Jiangsu and Henan, see Fig. 2.13 in Section 2.7), these represent less than 1% of all forest fires in China according to Street et

al. (2003), which confirms that agricultural fires appear to be by far the main type of open biomass burning found in Eastern China.

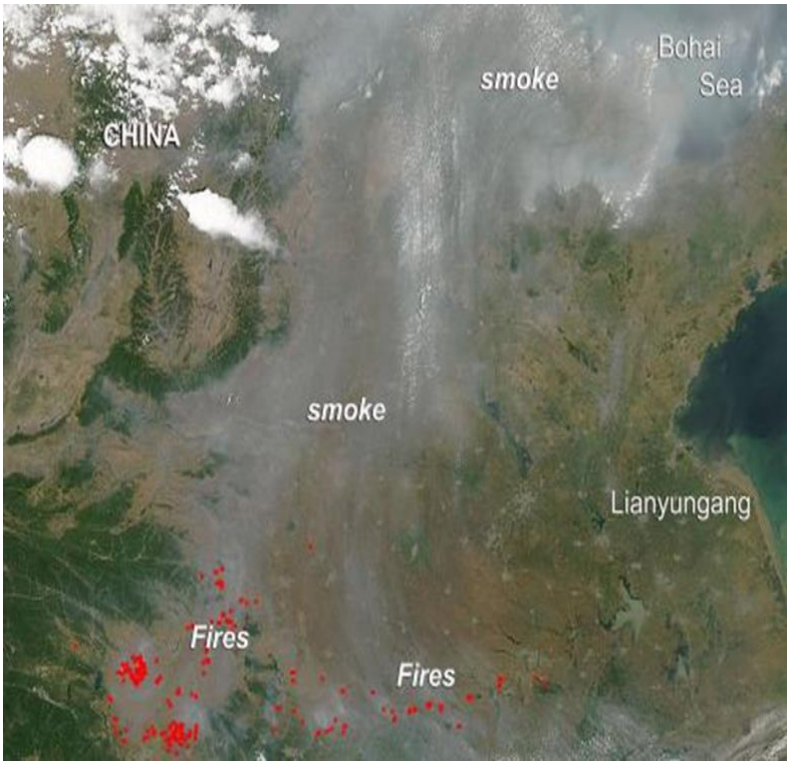

Figure 1.1: NASA's Aqua satellite captured multiple plumes of smoke from agricultural fires and industrial pollution in China (centred at 35ºN, 116ºE, imagery size: 900 x 600 km). The smoke and haze stretches from Inner Mongolia, located north of Beijing, south and west including the provinces of Hebei, Shandong, Henan, Shanxi, Hubei, Hunan, and Chongqing. Image taken from NOAA website (https://www.nasa.gov/mission_pages/fires/main/world/20130604-china-b.html#.WXCFhoQrIdU).

In Eastern China, fields of crops represent over 10% of the total land area, and most are required to support at least two crop rotations per year (Huang *et al.*, 2012; Pan *et al.*, 2013). For example in the southern area of Eastern China, wheat is grown in the winter, harvested in June and the stubble burned, the fields then rapidly flooded via irrigation networks and rice planted, which is then harvested in September/October when the fields are then drained, the rice straw burned and the fields prepared again for wheat (Huang *et al.*, 2012). Sometimes a third crop, particularly in southern China, is planted inbetween, and this cycle continues year on year. Confined to agricultural fields, the individual fires themselves may each be quite small (Fig. 1.2), but they occur in extremely large numbers (Huang *et al.*, 2012) and are generally ignited relatively closely spaced in time (e.g. perhaps within a few weeks) across a huge region (>23,000 km^2) of Eastern China (Yan et al, 2006). This tends to amplify their effect in terms of changing the concentration of various atmospheric pollutants, albeit limiting this to a few periods of the year.

Figure 1.2: Small fires spreading along the Chinese agricultural land, taken by a local resident on airplane (http://blog.sina.com.cn/s/blog_49a143920102v1gi.html).

So great is the scale of the agricultural burning activity, that recent studies have identified this type of widespread "small fire" as a significant contribution to global scale biomass burning totals (Fig. 1.3, Randerson *et al.*, 2012). At present the overall impact is not well quantified due to the problems of detecting smaller fires from satellite remote sensing, even when they are highly numerous in one particular area (Randerson *et al.*, 2012; van der Werf et al., 2017).

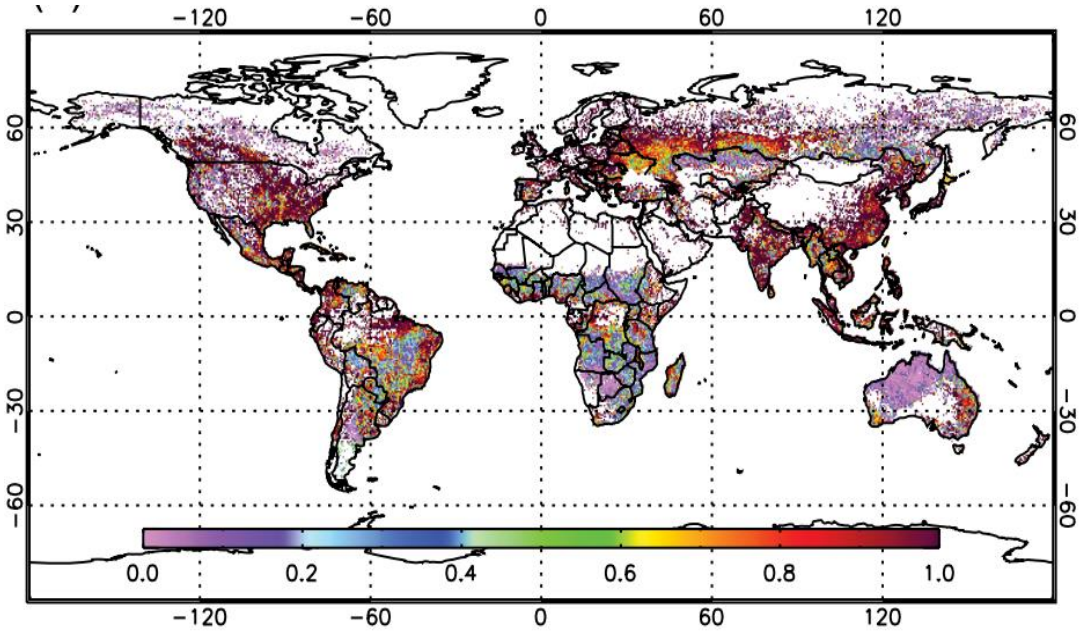

Figure 1.3: Estimate of the ratio of small fire of burned area to total burned area in 0.25º grid cells, calculated during 2001-2010 from a combination of active fire detections, spectral reflectance measures and burned area mapping made by MODIS (Figure 7d from Randerson *et al.*, 2012). In regions of China (e.g. 120° W, 30°N), it is apparent that small fires that are undetected by standard MODIS burned area methods maybe responsible for the vast majority (80% or more) of total area burned, though the methodology used to estimate this is subject to large uncertainties.

The aim of the research described in this thesis is to develop and exploit new satellite earth observation (EO) data and techniques, along with ground-based measurements of fire emissions chemical and particulate makeup, to provide improved quantification of the agricultural residue burning emissions of Eastern China. A number of specific objectives designed to meet this aim are listed at the end of Chapter 2. Ultimately this research may lead to future systems that can be used for monitoring the fire activity impacts on air quality in near real-time, and for the assessment of trends to support new management practices development, since current Chinese Government policies to limit the extent of agricultural burning are apparently of limited success (Liu *et al.,* 2008; Jiang *et al.,* 2012). If such work is successful, then these methods could be extended to wider (even global) scales, in order to reduce the biases in current fire emissions estimates (Randerson *et al.,* 2012).

CHAPTER 2: BACKGROUND, AIMS AND OBJECTIVES

2.1 INTRODUCTION

This chapter provides a more detailed review of the background to this PhD research, and finishes with the list of specific objectives that are designed to meet the overall aim of providing improved quantification of the agricultural residue burning emissions of Eastern China. The background reviews the literature related to the issue of agricultural fires in Eastern China, summarises the primary remote sensing techniques using to date within this field of study, and describes the current state-of-the-art with respect to fire emission databases more generally. Such databases are later compared with results obtained with the methods developed within this study in Chapter 5.

2.2 AGRICULTURAL FIRES IN EASTERN CHINA

China is one of the oldest agricultural countries in the world, with in excess of 300 million farmers who cultivate a very large area of land to support a population of over 1.3 Billion (NBSC, 2007). This PhD research focuses on Eastern China, including the North China Plain and the Middle and Lower Reaches Plain of the Yangtze River (also known as the Yangtze Plain) which are two of the largest agricultural zones in China (Fig.2.1a).

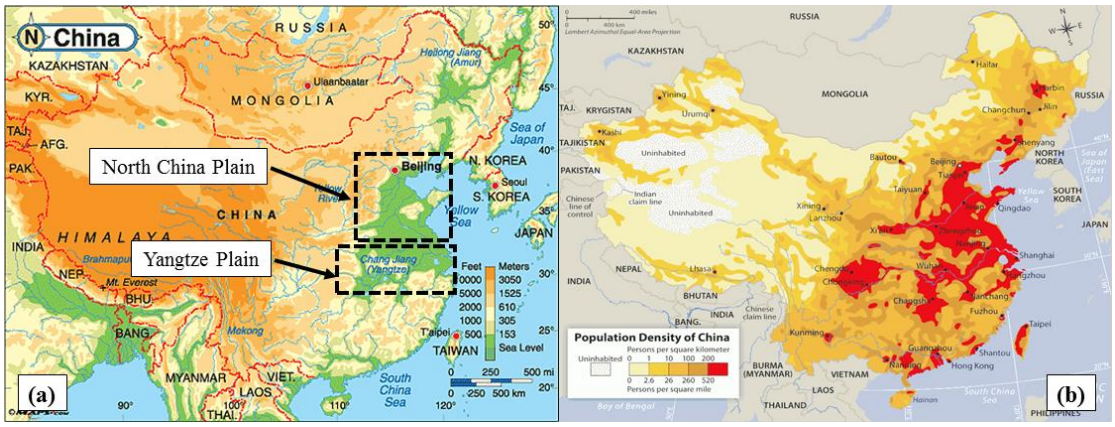

Figure 2.1: Physical and population maps of China. (a) Physical map showing main rivers and two of primary plains in China. (b) population distribution, which is highest in the primary plains along Yellow River and Yangtze River (Berglee, R. 2012).

The North China Plain accounts for approximated 20% of China's farmland, holds 34% of the national rural population, and produces 35% of the countries crop yield, including 75% of national winter wheat and 33% of national summer corn production (NBSC, 2007). The Yangtze Plain only accounts for around 19% of total farmland area, but provides 51% of the national rice yield to support its densely packed population, as well as people elsewhere in the country (Fig. 2.1b). Every year during harvest and pre-planting periods, crop residues from the growth of the prior season's agricultural crops are burned in many locations across Eastern China. Sometimes the residues are burned directly after harvest (e.g. wheat stubble) and sometimes they are collected, piled and burned in 'bonfires' (Fig. 2.2), for example in the case of rice straw after the grains have been removed, or oil seed rape after the oil has been crushed from the plant.

Figure 2.2: Examples of Chinese agricultural fires operated in (a) spreading (http://www.js.xinhuanet.com/2012-10/18/c_113418924.htm), and (b) bonfire way (http://www.southcn.com/news/community/tpxw/200505250232.htm).

Despite Chinese law prohibiting open agricultural burning since 1990, many farmers sill burn crop residues openly in fields, because it seems to be the easiest, quickest and cheapest way to allow subsequent cultivation. When agricultural residues are burned, it releases smoke – and this activity represents a significant source of atmospheric pollution in densely populated Eastern China (Chan and Yao, 2008, Huang *et al.*, 2012). The biomass burning is likely significant contribution to air pollution, which results in reduced visibility, public health problems and traffic accidents. Satellite remote sensing is the main method by which fire activity is assessed worldwide (Giglio *et al.*, 2013, 2016; Ichoku *et al.*, 2008; Kaiser *et al.*, 2012), however there are large uncertainties associated with the magnitudes ascribed to agricultural burning due to the fact that each of the agricultural residue fires are typically rather 'small' in area, limited in intensity, and often burn for a relatively short amount of time (Fig. 2.2), making them currently difficult to identify via satellite Earth Observation (EO). Larger and more intense forest fires are

a much easier to detect target by satellite EO. This issue affects the representation of agricultural residue fires in current emissions inventories, and leads to low-biases in their emissions estimates, as well as possible errors in their timing and spatial distribution. These problems feed into the difficulties when modelling their smoke dispersion and assessing their impact on air quality (Huang *et al.*, 2012; Street *et al.*, 2003; Yan *et al.*, 2006). A clear focus of this PhD research is therefore to improve the characterisation of the types of 'small fire' that dominate agricultural residue burning in order to lower the biases and uncertainties associated with this type of landscape burning in Eastern China.

2.2.1 Spatio-Temporal Patterns of Agricultural Fires in Eastern China

In 2012, Eastern China was estimated to be responsible for 25% of China's total crop production (NBSC, 2012). However, due to geographical variations in crop cultivation, the timing and extent of crop residue burning varies in different areas of Eastern China. In northern areas, corn and wheat are the major crops, while rice dominates in the South, and this resulting different harvest time and post-harvest burning. The main burning period in Eastern China is from late May to early June, after the spring harvest of wheat, with a second intensive burning period in late September/early October after the summer harvest of rice (Huang *et al.*, 2012). Fires may also occur in the southern part of Eastern China related to a third harvest of late rice (Huang *et al.*, 2012). Therefore, most previous studies that have explored the spatial distribution and magnitudes of China's agricultural fires have found that the central provinces of Shandong, Jiangsu, Anhui and Henan (mainly in North China Plain, Fig. 2.13), along with some other provinces in north-eastern and southern China, are the strongest emitting regions (*Huang et al.*, 2012; *Qin and Xie*, 2011; *Streets et al.*, 2003).

One of the key constituents of the smoke emitted by the agricultural fires is Particulate matter (PM2.5), and this is especially important to the human health and visibility impacts, as can be seen in Fig. 2.2. Merged satellite and ground based aerosol optical depth (AOD) data, which quantifies the extinction of the solar beam by atmospheric aerosols, shows that Henan, Jiangsu and Anhui are three main provinces responsible for aerosol emissions during the period of agricultural fires that occurs immediately after the summer harvest (*Xue et al.*, 2014). In this area, which is located within the Eastern China study area of this thesis, crop residue burning frequently occurs in June after the winter wheat harvest (Fig. 2.3a). Based on MODIS active fire detections (Fig. 2.3a), Huang et al. (2012) believe that these June fires represent around 75% of the total number of annual agricultural fires occurring in Eastern China, with the

bulk of the remainder confined to a second fire period on early October (after the summer corn/rice harvest that occurs in September).

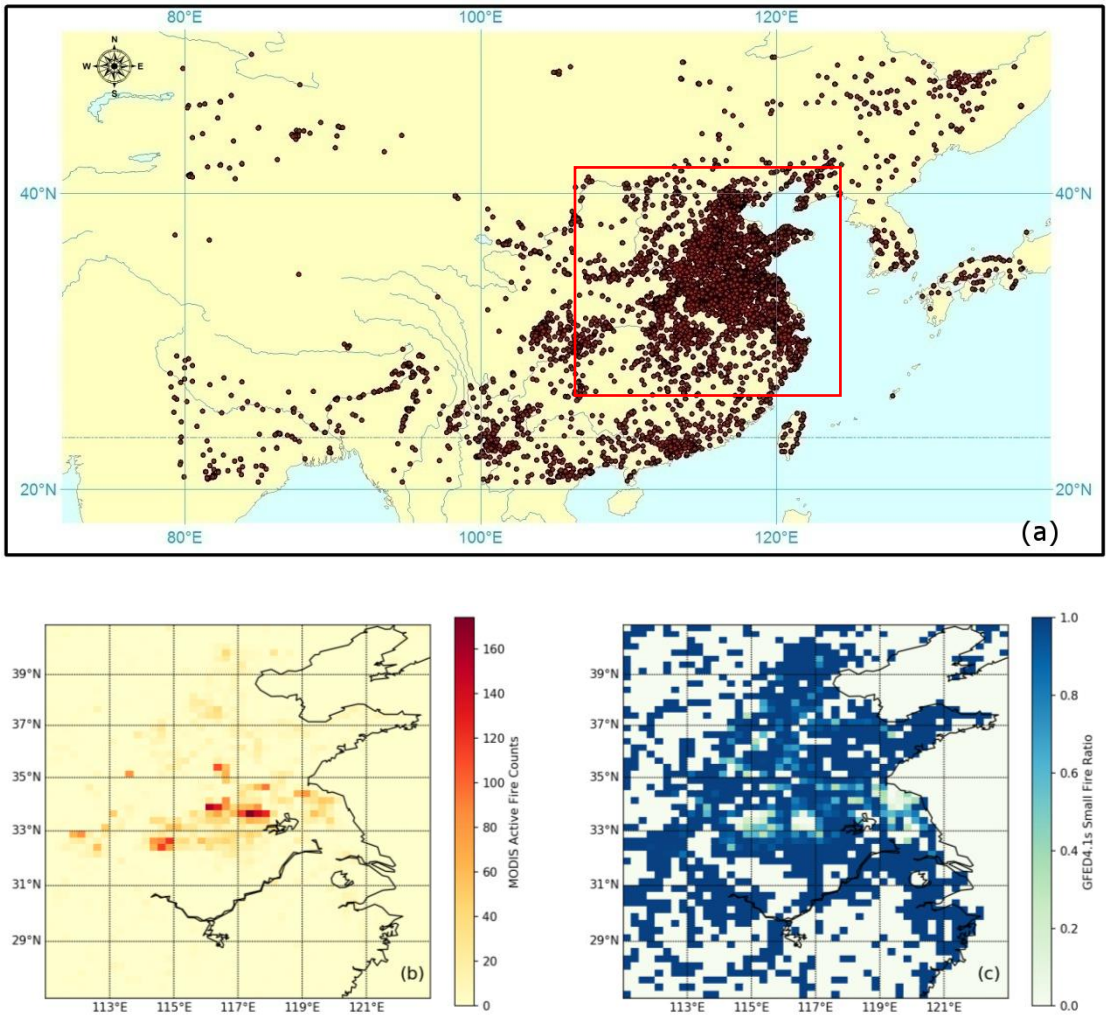

Figure 2.3: (a) Distribution of active fires in China in June 2013, as detected by the MODIS active fire 'hotspot' products (MOD14 and MYD14; Giglio *et al.*, 2003). Each red circle represents a single active fire pixel detection. The main burning region of Eastern China, including the North China Plain and the Yangtze Plain (see Fig. 2.1), is outlined in red. Most fires are located within here, though it is apparent that substantial numbers of fires occurring to the south and further west. (b) 2.5x2.5º gridded MODIS active fire counts in Eastern China only in June 2013. (c) Small fire ratio from GFED4.1s in Eastern China only in June 2013.

As stated in Chapter 1, Randerson et al. (2012) has found that the widespread "small fire" is a significant contribution to global scale biomass burning totals (Fig. 1.3). Fig. 2.3c shows the small fire ratio of Eastern China from GFED4.1s (see Section 2.6.4), which was calculated using the same methodology from Randerson et al. (2012), representing the ratio of small fires in this area. Though many fires can be detected by MODIS AF product (Fig. 2.3b), the high values of small fire ratio in Eastern China (0.8-1.0)

shown in Fig. 2.3c suggested the potential of more small fires existing in this area, which hasn't been well quantified in current fire datasets yet.

Whilst agricultural burning occurs every year in similar locations and at similar times, due to its recurrent nature, some estimates of China's crop residue burning suggest a decrease over the last decades, with for example 40 Tg of biomass being reported as burned in 2006 but 110 Tg in 2000 (*Huang et al.,* 2012; *Streets et al.,* 2003). Such differences may be solely related to differences in methodology and data source, and not fully reflective of reality. The Chinese government enacted a series of regulations to prohibit open-air burning from the 1990's onwards (Liu *et al.,* 2008), so it is possible that burning really is becoming more limited in its application. This has been doubted by some studies, even those based on official Chinese statistical data. Crop yields and cultivated areas appear to have grown quite significantly in parts of China over the past few decades, for example annual statistics issued by the Chinese government (NBSC), show the annual corn yield increased by one third from 2007 to 2012 (see Table 2.1). Estimates of agricultural residue burning based primarily on annual crop yield estimates will be significantly impacted by such reported changes in yield, though there is limited formal reporting of uncertainty bounds so it is unclear whether the reported increases are within the limits of uncertainty. Nevertheless, for example a survey of carbonaceous aerosol emissions based on annual crop yields reported a growth rate of 26% for black carbon between 1990 and 2000 (*Qin and Xie*, 2011). Furthermore, whilst agricultural fires are normally ignited by humans to clear the crop residues after harvest, some researchers have pointed out that climatic variations may have some impact as well (van Wilgen *et al.,* 1997). These issues help to highlight the importance of developing a unified method for developing fire emissions inventories in crop growing regions, able to cover long time periods and large regional scales and take into account even the types of 'small fire' which dominate in agricultural landscapes. Developing and applying such an approach, based on satellite EO methods and data, is the primary target of this PhD.

Table 2.1: Chinese annual major crop yields from 2007 to 2012 ($\times 10^3$ Gg yr^{-1}). Data source: Yearly annual report from 2007-2012 by National Bureau of Statistics of China (NBSC, 2007-2012).

	2007	2008	2009	2010	2011	2012
Rice	186	192	195	196	201	204
Wheat	109	112	115	115	117	121
Corn	152	166	164	177	193	206

2.2.2 CHINESE SOCIO-ECONOMIC AND RURAL MANAGEMENT PRACTICES

There exist a number of socio-economic factors that may have influenced the growth or reduction of crop residue burning in Eastern China over the past few decades, beyond simply the introduction of polices that were aimed at limiting the practice from the early 1990's onwards. China is currently undergoing rapid economic development, and this has increased rural access to commercial energy, leading for example to the decreasing use of crop residues as biofuel (Cao *et al.*, 2006, Zhang *et al.*, 2008). Mechanized harvesting has quickly spread among Chinese farmers, and this fast and convenient harvesting method has helped to offset the loss of much of the young agricultural labour force who have increasingly moved into more urban regions (Heinemann and Shepherd, 2011). However, such mechanized harvesting methods typically leave larger amounts of crop residues on the ground compared to manual harvesting approaches, and this can lead to increasing collection cost and a greater incentive to burn instead. So, even though application of mechanized harvesting in some other countries has apparently successfully limited the burning of residues, for instance the sugarcane in Brazil and South Africa (Arraes *et al.*, 2010; Smith *et al.*, 2008), a similar situation has not occurred in China. In fact, according to a report provided by the Survey Office of the National Bureau of Statistics in China (NBSC, 2008), the immature designs and still-developing techniques used by some new wheat harvesting machines meant that harvested land could not be used directly for the next round of cultivation due to the length of the stubble left behind (too long to decompose quickly in the field and consequently stopping newly sown seed from growing efficiently). This lead to burning becoming even more necessary to remove the crop residue prior to seed planting, making space for the next round of cultivation in order to ensure yield and income is maintained.

Research has pointed out the bioenergy potential of crop residues (Jiang *et al.*, 2012), however with a lack of reliable and effective overall management plan for this alternative use, the undesired scenario of intensive burning across huge areas of farmland in Eastern China still exists (Fig. 2.3). The "top down" prohibition instigated by the Chinese government in the 1990's might, to some extent, have failed to fully consider and deal with all the issues faced by farmers. Liu et al. (2008) report that a maximum of only 30% of crop residues are used for biogas generation (bioenergy), along with forage (animal feed) and other industrial uses, with probably ~ 15% lost during collection. This leaves an estimate of around 20% being directly burnt in the field, and some researchers conclude that, despite many socio-political resources being consumed by efforts aimed at prohibiting open air crop residue burning, such measures cannot reduce the activity by the extent desired (Yang *et al.*, 2008). Thus, despite Government efforts, crop

residue burning remains a significant issue, and one whose importance may be increasing rather than decreasing with time, albeit the current truth of the situation is rather uncertain. Using the new data and approaches developed in this PhD, this thesis will attempt to identify trends in crop residue burning in Eastern China over the last few years (2012-2015).

2.3 GASEOUS/PARTICULATE EMISSIONS FROM RESIDUE BURNING

Smoke emission from agricultural fires contribute to air pollution and to the radiative forcing of the climate in several ways (see Section 2.4). This section will summarize gaseous/particulate emissions from agricultural burning, and will assess the aspects potentially impacting the smoke emission factors (i.e. the amount of a particular smoke constituent (either as gas or aerosol) released per unit of fuel burned; [$g.kg^{-1}$]).

2.3.1 COMBUSTION PROCESSES

The combustion of vegetation releases a plume of gases and aerosols, commonly called 'smoke' (Andreae and Merlet, 2001). In fires where the "combustion completeness" (the proportion of the available fuel that is actually burned) is close to 100%, almost all of the solid fuel is converted into smoke and released into the atmosphere, with only a small amount of 'mineral ash' left behind from the incombustible components of the plants (minerals such as silica, calcite etc; Yusiharni and Gilkes, 2012). Fires with lower combustion completeness by definition leave a higher proportion of unburned and partly burned vegetation/char behind, but can still emit very significant amounts of material into the atmosphere.

The emissions factor of a particular chemical species [x] (expressed as [EFx]) represents the amount [g] of that species that is emitted per kg of dry fuel burned. Carbon dioxide is the dominant species present in smoke, and EF_{CO2} is for example around 1600 – 1900 $g.kg^{-1}$. By contrast, the emission ratio of two particular chemical species [x and y] (i.e. [ERx/y] represents their relative abundance in the smoke plume, and is typically expressed in units of $mol.mol^{-1}$. The emissions factors [$g.kg^{-1}$] vary significantly between different biomes and vegetation types (e.g. Andreae and Merlet, 2001; Akagi *et al.*, 2011), and also between different combustion phases such as flaming and smouldering (Wooster *et al.*, 2011). For non-CO_2 species, the EF variation can be many hundreds of percent between smouldering and flaming for example. Indeed, it is possible that different proportions of smouldering and flaming activity in fires that

occur in different vegetation types maybe responsible for a substantial proportion of the difference in fire emissions makeup seen between biomes (as reported in emissions factor databases such as Andreae and Merlet, 2001). This causes differences between emission factors when derived from measurements conducted *in situ* at fires in the field, or in combustion chamber experiments conducted in the laboratory (Delmas *et al.,* 1995; Wooster *et al.,* 2011). Most often a single "fire averaged" emission factor is calculated to represent the whole fire lifecycle, encompassing both the initial flaming and subsequent smouldering phase (and the initial pyrolysis phase as well; though this typically does not consume much fuel).

Normally, the ratio of excess CO_2 above background (ppmv or mol^{-1}) in the emitted smoke to that of CO plus CO_2 is used to characterise smoke as being produced primarily by smouldering or flaming activity, and this metric is known as the modified combustion efficiency (MCE). A high MCE (> 0.92) is generally classed as predominately flaming, whilst a lower MCE (< 0.75) predominately smouldering (Miyanishi, 2001). In part due to the dominance of finer (e.g. straw) material within their fuel (which is generally more easy to ignite and burn provided it is dry enough), agricultural residue fires are generally believed to show higher MCE values than are typical of most forest fires, with values more similar to those of grassland or savannah burning (Pan *et al.,* 2013; Zhang *et al.,* 2008). If so, this indicates that much of the residue combustion is likely to occur in the flaming phase, which maximises emissions of CO_2 and minimises emissions of CO, CH_4 and particulates compared to the pure smouldering phase. However, before flaming combustion starts, the fuel experiences a drying and distillation process, first releasing vapour and then some volatiles. This phase is termed pyrolysis (*Reid et al.,* 2005), and involves the formation of organic materials such as char, tar and volatiles (visible as white smoke rising from the heated fuel). Typically the temperature of the mixture gradually increases until around 800 K, when the flammable mixture of tar, volatile gases and air can be ignited and flaming combustion starts. During this flaming stage, a variety of soot-like species including some organics like polycyclic aromatic hydrocarbons (PAHs) are released, alongside copious amounts of CO_2 but also some CO and many other gaseous species in lesser quantities. Laboratory studies suggest that the rate of particle production during the flaming stage is empirically related to flame size via a power law (Glassman, 1988), which if confirmed could perhaps be used for the estimation of particulate emission factors. Currently, particulate EFs are mainly derived via the capture of emitted aerosol particles on filters (Cao *et al.*, 2008; Li *et al.*, 2007; Zhang *et al.*, 2008).

After the flaming phase has released most of the volatiles, smouldering combustion typically begins with temperatures reducing to below 850 K (*Chandler et al.,* 1983). The formation of PAHs is less possible at this stage, since such processes are favoured by higher temperatures (*Reid et al.,* 2005). Instead, the organic materials formed during smouldering combustion are largely the result of the condensation of other volatilized organics (*Ward*, 1990). The product emitted in greatest quantity during the smouldering phase is still by far CO_2, just with an emissions factor that is somewhat (perhaps up to around 20%) lower than in the flaming phase. Most other smoke constituents are emitted with much higher EFs in the smouldering phase compared to the flaming phase, and this means that per unit of fuel burned smouldering combustion typically is much more polluting (Hosseini *et al.*, 2013; *Reid et al.*, 2005).

2.3.2 GASEOUS EMISSIONS

Agricultural activity (including crop residue burning) is generally considered to contribute significant amounts of the greenhouse gases CO_2, CH_4 and N_2O to the atmosphere (Smith *et al.*, 2008). In total, agricultural activity is estimated to account for over 10% of total global anthropogenic GHG emissions, of which agricultural fires have been estimated to contribute around 7% (Smith *et al.*, 2007). However, such a figure maybe biased low if current estimates of agricultural burning are significantly underestimated (Randerson *et al.*, 2012). For China, annual total emissions of CO_2, CO, and N_2O based on the burning of crop residues from the three main grain crops were 38677, 3137 and 88 Gg respectively, with corn straw contributing around 50% of these totals, followed by wheat and then rice (Zhang *et al.*, 2008). These estimates are based on national annual crop yield statistics, which will be discussed further in Section 2.6. However, large uncertainties (perhaps over 90%) are considered to exist in the results such methods, making them of limited value (Yan *et al.*, 2006).

The typical modified combustion efficiency (MCE) of agricultural residue burns conducted in laboratory studies is measured to be around 0.90 (Turn *et al.*, 1997; Qie and Xie, 2011), which is consistent with mostly flaming combustion and smoke that has 90% or more of its carbon released as CO_2 (Li *et al.*, 2007; Qie and Xie, 2011). Sugar cane is an exception, with an MCE reported to be generally approximated 0.68 in laboratory burns, though this is not a significant crop type in Chinese cultivation (Qie and Xie, 2011). CO contributes the second most dominant emitted compound, often 5 - 6%, compared to perhaps double this for pure smouldering combustion, and with only 1% or less CH_4 (Li *et al.*, 2007).

During *in situ* (field) burning, it maybe that the MCE is lower than that typically seen during laboratory combustion, due to the possibility of higher fuel moistures than are used for fuels burned in the laboratory. Higher moistures are associated with more smouldering combustion, and this will result in a increase in the proportion of non-CO_2 gaseous compounds such as CO and CH_4 in the smoke (i.e. a higher $ER_{CO/CO2}$ and $ER_{CH4/CO2}$).

With respect to CO_2 emissions in general, assuming the same crops are grown in roughly the same amounts during the next growing season, then the CO_2 released by the burning of the residues left after harvest will in any case effectively be reabsorbed by the new crop growth in the following season (Smith *et al.,* 2008). In this way, the other emitted carbonaceous compounds (e.g. CO), gaseous hydrocarbons and reactive nitrogen compounds are potentially more important to consider than CO_2, particularly as many are considered significant air pollutants. These include active volatile organic compounds (VOCs) and ozone precursors (Mellouki *et al.,* 2015), for example toluene and isoprene, which can be involved in the formation of secondary aerosols.

2.3.3 PARTICULATE EMISSIONS

Vegetation is typically composed of around 50% carbon (Yokelson *et al.,* 1999), and when burned most is oxidized to CO_2 or CO. Typically less than 5% of the carbon is released in the form of particulate matter (Reid *et al.,* 2005), but it is this PM that is one of the key air pollution impactors of biomass burning, and the major health risk (Seinfeld and Pandis, 2012).

When characterising airborne particles, size distribution is a very important parameter. Most particulates released from crop residue fires are fine ($PM_{2.5}$) or submicron (PM_1) particles, with diameters of less than 2.5 µm and 1 µm respectively. For comparison, a human hair is about 100 µm wide, so roughly 40 $PM_{2.5}$ particles could be placed across a hairs breadth. Such fine particles are capable of being inhaled deep into the human respiratory system, whereas much larger particles tend to be trapped in the nose, mouth or throat, and this explains why they pose a significant health risk (Englert, 2004).

$PM_{2.5}$ has been reported to contribute over 93% of the PM mass emitted from wheat straw burning, and 98% of corn stover burning (stover being the stalks, leaves and cobs that remain in fields after the corn harvest; Li *et al.,* 2007). These fine particles can be formed by different processes, and as shown by Fig.2.4, the gas to aerosol conversion process takes place by essentially three processes: condensation, nucleation, and coagulation. Therefore, the mode of the size distribution (i.e. its peak), as well as their

chemical composition, can provide information on how the particles were formed, helping to trace the source (e.g. in areas where PM may come from a variety of other sources as well as biomass combustion).

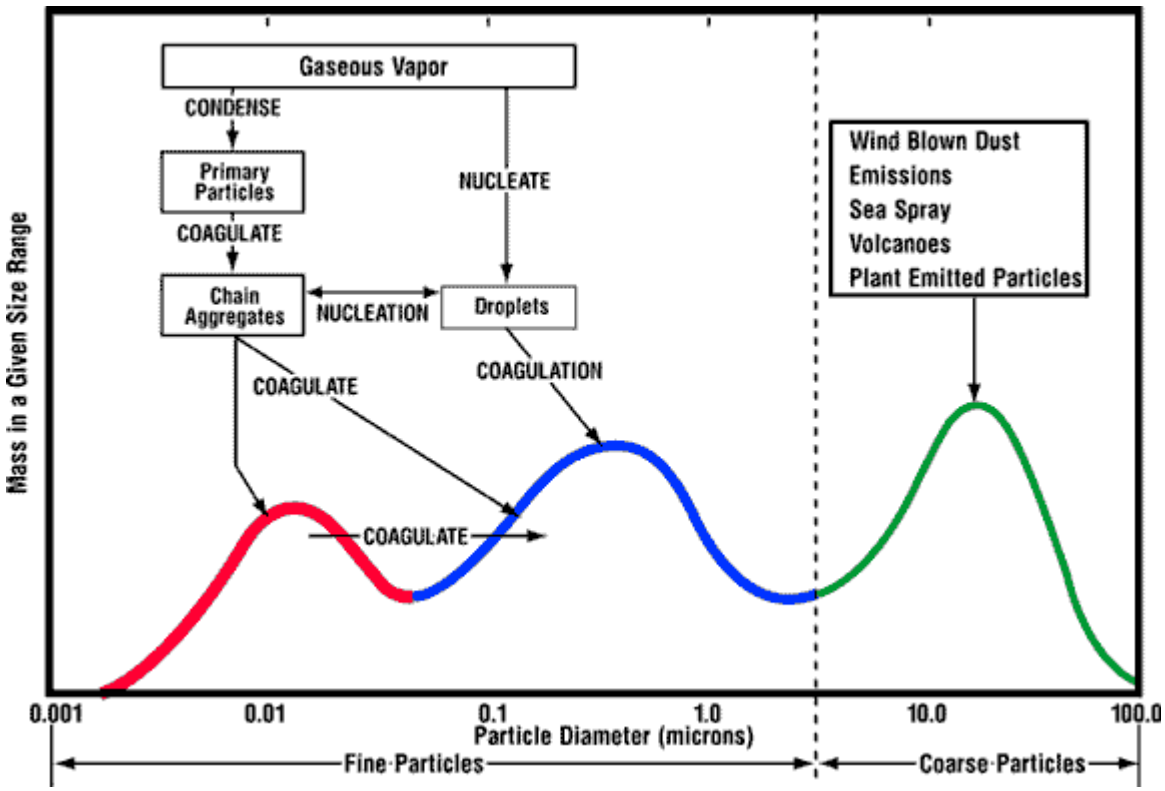

Figure 2.4: A schematic summary of how gases are converted into aerosols of various sizes. Condensation, nucleation, and coagulation are three essentially processes taking place in difference sizes of aerosols as shown (source: http://mtweb.mtsu.edu/nchong/pm-atm3.htm).

Since *in situ* real-time particle size distributions based on mass are very difficult to determine, most studies use the particle size distributions based on particle counts. In a variety of studies on crop residue burning, accumulation mode size distributions (modal peaks in the 0.1 - 1.0 µm range) were reported to predominant in such particle count distributions (da Rocha *et al.*, 2005; Hays *et al.*, 2005; Zhang *et al.*, 2011). This is partly because particle formation, no matter whether from flaming or smouldering combustion, is essentially a condensation process, mostly condensation nuclei limited (Reid *et al.*, 2005). In a Chinese crop residue burning test, Zhang et al. (2011) report that the prominent particle number size distribution accumulation mode peaked at 0.1, 0.15 and 0.15 µm during measurement of fresh smoke from rice, wheat and corn residue fires respectively. Such distributions slightly shifted towards larger particle diameters after 4-hour aerosol aging processes were allowed to occur, with peaks increasing to 0.24, 0.23 and 0.27 µm respectively (Zhang *et al.*, 2011). The highest particle numbers were found to be

just after the peak flaming stage, with a number-modal mean < 0.120 μm (Hays *et al.*, 2005), indicating that decomposition processes during the flaming stage can produce the largest amounts of particles. In terms of particle mass size distribution, single mode values have been reported as 0.26 - 0.38 μm (Li *et al.*, 2007), similar to the particle number size distributions introduced above. Such distributions have also been found at the individual compound level, for example, results from Li et al. (2009) showed that size distribution of both BC (black carbon) and OC (organic carbon) peaked at 0.26-0.38 μm.

In terms of chemical composition, carbonaceous aerosols were found to account for about 46% of the $PM_{2.5}$ mass emitted from wheat straw burning, and 37% of that from corn stover burning (Li *et al.*, 2007). Amongst this particulate carbon, BC is an important component and significant in the global budget (see details in Section 2.4.2). BC is normally formed primarily in flames, and directly emitted into the atmosphere (Bond *et al.*, 2013). Street's et al. (2003) estimated that BC emissions from agricultural fires account for around 10% of all sources in China annually (Cao *et al.*, 2006). However, large (50-160%) underestimates were found in relation to the modelling of BC when compared to remote sensing observations in south and Southeast Asia (Bond *et al.*, 2013). New estimates of agricultural fire emitted BC could potentially improve on such quantifications in the future, and this PhD project will aim to develop these.

Organic carbon aerosols (OC), are emitted alongside BC, and can be efficient cloud condensation nuclei. These aerosols are considered to have an important role in the aerosol indirect effect (IPCC 2011). OC has been assessed is crop residue burning smoke, and accounts for a significant fraction of the total particle mass, ranging from 29 to 55% depending on different size categories (Li *et al.*, 2009). *In situ* aerosol measurements in Beijing also show significant contributions from biomass burning OC, as high as 10 - 32% of the total OC aerosol burden (Duan *et al.*, 2004). Furthermore, during the incomplete combustion of organic matter, some toxic organic compounds were also found in the smoke from agricultural fires, such as PAHs (Polycyclic aromatic hydrocarbons). The emission factor of PAHs is reported as being between 0.12 to 4 $mg.kg^{-1}$ (Jenkins *et al.*, 1996), while an estimate of 1.09 Gg of emissions for the year 2004 was calculated based on Chinese crop residue consumptions estimates (Zhang *et al.*, 2011). Though OC or PAHs estimation is not included in this thesis, it can benefit from the aim of this study to provide better qualifications of FRP and dry matter emissions in Eastern China.

2.4 IMPLICATIONS OF AGRICULTURAL FIRE EMISSIONS FOR AIR QUALITY AND GLOBAL CHANGE

2.4.1 IMPLICATION OF AGRICULTURAL FIRE EMISSIONS ON AIR QUALITY

China is one of the largest agricultural nations in the world, and its crop residue totals are the highest in the world, at 17.3% of global production (Bi *et al.*, 2009). Much of this residue is burned in the fields, as outlined in Section 2.2, and whilst each individual fire might be quite small there can be huge numbers occurring simultaneously or near-simultaneously across agricultural regions. Fig. 2.5 shows a MODIS image collected at a time of severe agricultural burning (11th June 2015). June is typically the most severe month of burning in this region, and significant amounts of smoke can be seen in the image. Their huge number means they contribute significantly to the development of air quality problems – including visibility reductions that can result in serious traffic accidents (Fig. 2.5 inset). The smoke is often termed 'haze' once it spreads away from the source area and potentially mixes with other sources of air pollution, leading to a more regionally spread air pollution event that can extend far away from the casual fires themselves.

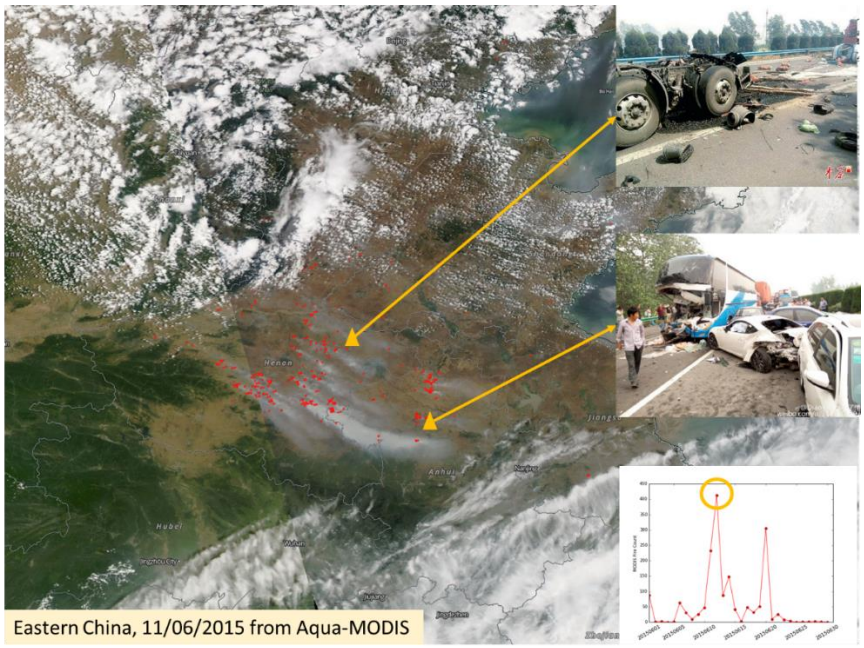

Figure 2.5: MODIS image taken on Jun 11th, 2015 of agricultural fires (red "hotspots") spreading haze in Eastern China, causing serious traffic accidents (locations shown as yellow triangles and same colour line pointing to the pictures taken *in situ*) and public health problem. The number of MODIS active fire pixels reached highest on this day (time-series plot in Jun, 2015 shown right down, highlighted with yellow circle). However, the 1 km MODIS data fails to detect many of the relatively small but likely numerous fires that are clearly producing large amounts of smoke pollution.

It is clear –from Fig, 2.5 - that air pollution impacts from crop residue burning are not limited to the local area immediately surrounding the fires, and in fact the haze can have impacts at the regional scale, for example the Asian Brown Cloud (Bond *et al.,* 2013; Desyaterik *et al.,* 2013; Pan *et al.,* 2013; Zhang *et al.,* 2013). Under the influence of the monsoon system, which in China blows from northwest to southeast during winter, and is reversed in the summer months, smoke from agricultural fires can easily be transported far downwind, into "mega-cities" like Beijing and Shanghai (Cheng *et al.,* 2013; Du *et al.,* 2011; Li *et al.,* 2010). Fig. 2.6 shows data and results from a study by Ding *et al.,* (2013), indicating how the smoke from north of Anhui and Jiangsu Province appears to be transported across approximated 500 km, leading to haze impacts along the whole transport path and affects as far away as Shanghai. A concurrent modelling study (Huang *et al.,* 2012b) suggests that crop residue fires in June 2012, mainly of wheat and rapeseed straw, are likely to have been responsible for this intensive regional air pollution episode. The modelling suggested that PM_{10} concentrations in Xuzhou City were increased by an order of magnitude by the fire-induced haze, to around 158 μg m^{-3}, while for the PM_{10} in Bozhou City (much closer to the crop burning area) the simulated PM_{10} reached in excess of 600 μg m^{-3}.

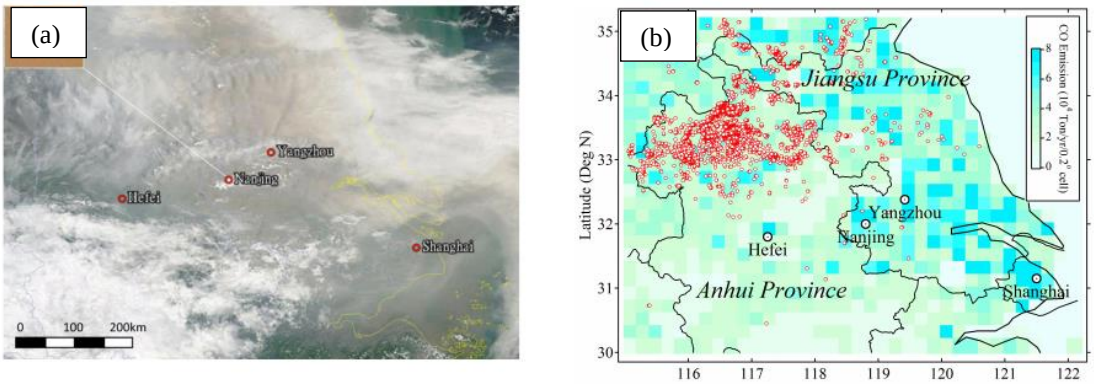

Figure 2.6: A study case from Ding *et al.,* (2013). (a) is a MODIS-Terra true color imagery taken of Eastern China on 10 June, 2012, and (b) shows the emission inventory of carbon monoxide and fire events on 9 June, 2012 at same region. Agricultural fire emissions from Anhui and Jiangsu Province can be transported to Shanghai City, locating over 500 km away from fire source area.

Fig. 2.7 provides a further example of the apparent link between intensive agricultural burning and large scale air quality reductions in Eastern China, where severe instances of air pollution appear spatially and temporally co-located with active fire detections from MODIS. However, the actual contribution of crop residue burning to the air pollution present in large urban regions of China, including its mega-cities, remains quite uncertain. This is partly at least because the remain significant uncertainties in the amounts of particulate matter released into the atmosphere by the fire activity. Based on studies of Asian regional air pollution transport, the large range of values that currently characterises open biomass burning

emissions estimates (> 450% uncertainty) could be the main reason for the noted discrepancy in observed and modelled particle concentrations (Streets *et al.,* 2003).

In situ measurements of air pollutants provide further evidence of the contribution of agricultural burning to urban air pollution. In the northern area of Eastern China, using the potassium content of total suspended particle samples as an indicator of biomass burning (also see in Section 2.3.3), samples collected in Beijing during the burning season was found to be three times higher than during non-burning periods, indicating the regional influence of agricultural fire emissions and the presence of long range transport (Duan *et al.,* 2004). During such periods, OC/K^+ concentration ratio values indicate that overall agricultural fire emissions may contribute around half of the organic carbon PM present in the atmosphere of urban areas (Duan *et al.,* 2004). Based on chemical composition analysis and positive matrix factorization (PMF), the contribution of biomass burning to aerosol samples collected in Beijing was similarly found to be as high as 50% with regard to both OC and BC (Cheng *et al.,* 2013).

Recent studies using the WRF/CMAQ modelling system (Weather Research and Forecasting/ Community Multiscale Air Quality) indicated that in the Yangtze River delta region, around 37% of $PM_{2.5}$ (and 70% of OC and 61% of EC) were attributable to agricultural fire emissions (Cheng *et al.,* 2014), though towards the southern area in the Pearl River Delta Region the contribution decreased to 3.3 - 6.5% of $PM_{2.5}$ (along with 1.8-3.2% of VOCs) (Zhang *et al.,* 2013). Furthermore, during atmospheric inversions, such air pollution tends to stay in the mixing layer and accumulates, resulting in even higher observed particle concentrations close to the ground (Cheng *et al.,* 2014).

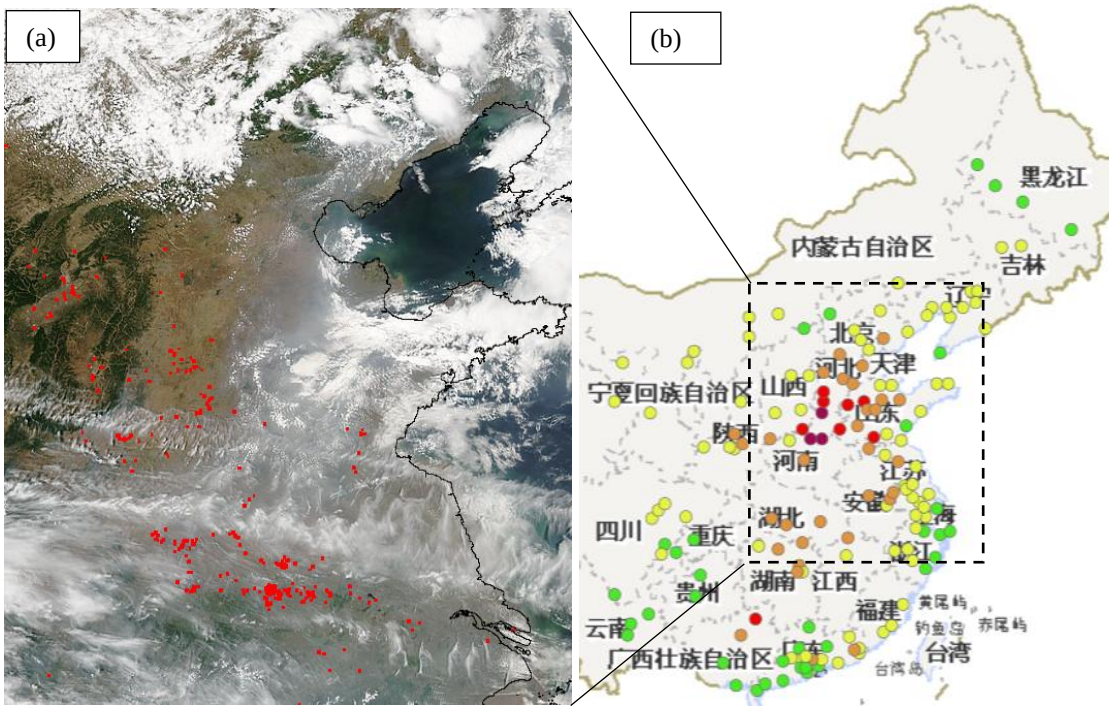

Figure 2.7: Imagery (a) MODIS-Aqua taken on June 9th, 2014 with the next day national air quality index map (b). The red spots in (a) refer to hot spots from MODIS active fire product, which has similar spatial distribution to the orange/red spots area refers to bad air quality in (b). Imagery and data source: http://www.noaa.gov/, http://aqicn.org/map/world/.

The smoke from agricultural fires doesnot generally get injected directly into a totally "clean" atmosphere, but rather mixes with polluted air containing emissions from fossil fuel combustion, local dust etc. This mixing can lead to the formation of haze having a more complex physio-chemical makeup than the original smoke (Li *et al.*, 2010), including further secondary organic and inorganic aerosols (Chen *et al.*, 2016; Cheng *et al.*, 2014; Yamaji *et al.*, 2010; Zhang *et al.*, 2016). Via a comparison of different types of haze generation in Beijing, Li et al. (2010) suggest that agricultural fire emissions approximately double the aerosol optical depth (AOD) on particularly haze days, and a similar situation was also found in Shanghai, where the haze can be attributed to either biomass burning plumes alone or to significant mixing with urban anthropogenic pollution (Du *et al.*, 2011). In the latter case, precursor gases such as SO_2 and NO_2 could convert into sulphate and nitrate on the surface of pre-existing KCl particles emitted from agricultural residue fires (Du *et al.*, 2011).

2.4.2 Implication of Agricultural Fire Emissions for Global Change

The contribution of agricultural fire gas emission to global change is discussed by, for example, Chen et al. (2016), Reid et al. (2005), and Smith et al. (2008). Whilst the equivalent of the emitted CO_2 is

generally re-absorbed during the next growing season (see Section 2.3.2), the CO, CH_4 and VOCs (volatile organic compounds) for example can react with OH radicals in the troposphere, affecting the oxidation capacity of the layer where the vast majority of non-aquatic life on Earth resides (Koppmann *et al.,* 2005). Besides, the emitted nitric oxide and VOCs may also lead to the formation of ozone and other photo oxidants which are known air pollutants and toxic to both humans and plants (Koppmann *et al.,* 2005). Furthermore, the emitted organic matter and some soluble species such as potassium increase their size during atmospheric transport, resulting in more hygroscopic aerosol particles downwind and the possibility of more cloud condensation nuclei (CCN, Li *et al.,* 2010). Formation of increased amounts of CCN was already observed during one field burning experiment (Dusek *et al.,* 2006).

The global open burning of biomass contributes about 40% of black carbon (Bond *et al.,* 2013), which is likely to be the second most important individual climate-forcing agent after carbon dioxide, though with a high uncertainty of about a factor of two (Bond *et al.,* 2013; Streets et al., 2003). For example, "brown" carbon, known as certain fractions of organic aerosols also absorb solar radiation effectively, has been found in such biomass burning. "Asian Brown Cloud" is created by brown carbon like this, which has potentially big impact on regional weather by changing the rainfall patterns and amount (Nakajima *et al.,* 2007). Generally, BC aerosol strongly absorbs solar radiation (IPCC, 2013), though exact particle composition, concentration, lifetime, and size distribution will all impact on the of aerosol to climate change (Bond *et al.,* 2013). What's more, the mixing of open burning emissions with local pollutants is not well understood thus far and may alter the impacts. Some mixing cases have reportedly resulted in dramatic temperature drops by 10 K and changes in rainfall (Ding *et al.,* 2013), though this kind of indirect effect is not well qualified in global scale yet. Research also suggested, as a result of BC emissions from open biomass burning, and the changing optical depths and thus incoming solar irradiance reaching Earth's surface, crop yields themselves maybe affected (Chameides *et al.,* 1999).

2.5 REMOTE SENSING OF AGRICULTURAL FIRES

Satellite remote sensing can be used to map the burned area left by a fire, and can also be used to detect the thermal emissions from the fire whilst it is still burning (Giglio *et al.,* 2006, 2013; Roy *et al.,* 2005,

2008; Wooster *et al.,* 2005). Generally with burned area products, a substantial part of the entire pixel would need to be burned to perform a confident detection (perhaps 20% or more), whereas active fires potentially filling only 0.01-0.1% of the pixel can be detected by thermal remote sensing methods (Giglio *et al.,* 2006, 2008; Schroeder *et al.,* 2014). However, despite their benefit in terms of 'small fire detectability', a key disadvantage of active fire remote sensing approaches is that the satellite must be collecting data whilst the fire is burning, and the short-lived nature of many agricultural fires means that many may burn outside of the time when the appropriate satellite instrument is overhead and collecting imagery and data. Most quantification of biomass burning activity is therefore still performed using so-called 'burned area' products, though active fire products are increasingly being used (e.g. Kaiser *et al.,* 2012).

On average, nearly 3.4% of Earth's terrestrially vegetated area is estimated to burn annually according to analysis of the MODIS burned area product (Giglio *et al.,* 2010). However, many small fires often occur in agricultural settings, as well as other environments such as tropical forests, and many of these are likely to be well below the minimum detection limit of the 500 m spatial resolution MODIS burned area product (Giglio *et al.,* 2006; Roy *et al.,* 2008). Recently this type of "normally undetected" fire was estimated by Randerson et al. (2012) to account for at least 35% of total global burned area, with a sharp increase of 143% in central Asia (Fig. 2.3, including most areas of China according to the classification used in the study). However, the procedure used by Randerson et al. (2012) to estimate the size of the 'undetected burned area' is indirect, and based on an empirical relationship between burned area, spectral reflectance change, and the locations of the thermally detected hotspots representing the presence of an active fire (data which is at a different spatial resolution to the burned area itself). The accuracy of the resulting estimates of 'undetected burned area' is therefore highly uncertain, and the method is currently without any formally published validation. Nevertheless, whilst the absolute magnitudes reported by Randerson et al. (2012) for 'undetected burned area' and the resulting upward adjustments of fuel consumption are of uncertain reliability, the work does indicate that substantial fire activity is missed by the most commonly used burned area product that underlies the most widely used global fire emissions database (GFED; Randerson *et al.,* 2012).

Prior to this work by Randerson et al. (2012), an earlier study using a prior version of the MODIS burned area product concluded that fires in croplands constituted approximately 8-11% of all global active fire detections mapped during 2001-2003 (Korontzi *et al.,* 2006). This number increases to 30 - 40% when considering just mainland China. All these figures should be treated with caution however, since many

(perhaps most) agricultural fires are small fires, smaller than the minimum burned area detectable via MODIS and possibly also smaller than the minimum thermal hotspot detectable by MODIS. For this reason, the proportion of total fire activity that agricultural burning represents is likely to be currently underestimated.

2.6 CURRENT FIRE EMISSIONS DATABASES COVERING CHINA

The large uncertainties that characterise assessments of agricultural burning in China, and which limit our understanding of its impact on air quality and global change, have been described in Section 2.4. Despite these limitations, reasonably high spatial and temporal resolution emission inventories are available, and their methods and characteristics are summarised in this Section.

2.6.1 CROP YIELD BASED APPROACHES

Approaches based on yield statistics are a long-standing, relatively traditional way to estimate fire emissions from agricultural residue burning, and can be traced back to times before satellite remote sensing was applied (e.g. Cao *et al.*, 2006; Huang *et al.*, 2012). The crop yield based approaches (CYBA) calculate the amount of crop residue burned in a region from a combination of crop production statistics and related additional parameters:

$$M = \sum_{i=0}^{n} P_i \; R_i \; F_i \; C \qquad (2.1)$$

Where i stands for each of n different crops; M_i is regional mass of residue from crop i burned in the field (kg); P_i is the regional production of crop i (kg), and is usually derived from annual agricultural statics reports; R_i is the proportion of dry matter residue-to-crop production (unitless proportion between 0 and 1), which depends on the crop type i; F_i is the proportion of residue burned in the field for crop type i in the region under study (unitless proportion between 0 and 1); and C is crop combustion completeness (unitless proportion between 0 and 1, *Huang et al.*, 2012).

Certain of the parameters of Eqn. 2.1 are not so easily determined. For example, in the region under study, the proportion of the crop residue burned in the field for crop type i (F_i) is normally estimated via a limited investigation of the uses of crop residues, which varies between different regions/provinces (Huang *et al.*, 2012). Because of strong variations in socio-economic development across the huge expanse of mainland China, large differences in the estimates of F_i exist, indicating large uncertainties

(Jiang *et al.,* 2012; Liu *et al.,* 2008; Wang *et al.,* 2013; Yamaji *et al.,* 2010). The proportion of residue burned in the field (F_i) used in above study was based on few questionnaires or investigations on the use of crop residues conducted over 10 years ago with a limited number of farmers (Gao *et al.,* 2002; Wang and Zhang, 2008). F_i may however change years since it is hugely impacted by the level of local economic development, the availability of alternative uses for crop residues in the region, and the regional governance of fire prohibition (Chen *et al.,* 2016). Moreover, considering the official prohibition of open air burning, it is possible to question the reliability of data based on surveys that are asking farmer how much residue they burn. Despite this, most studies that include agricultural fire emissions estimation in Eastern China have relied on the Crop Yield Based Approaches (Cao *et al.,* 2006; He *et al.,* 2011; Huang *et al.,* 2011, 2012; Li *et al.,* 2007, 2009; Qin and Xie, 2011; Wang *et al.,* 2008; Yan *et al.,* 2006; Zhao *et al.,* 2011).

2.6.2. SATELLITE-DERIVED BURNED AREA METHODS

Since croplands in China are mostly run by individual households, satellite-based estimates of area burned have often been considered inappropriate for use in agricultural regions of China, due to the small burned areas being outside of the satellite products detection limits. For example, Yan *et al.,* (2006) used the Global Burned Area 2000 (GBA2000) data set that was derived from 1 km satellite EO data to calculate a total of only 4.7 Tg of crop residues had been burned in that year, accounting for less than 1% of the total crop residue production. This is unlikely to be correct, and is the result of most burned area in croplands remaining undetected in the GBA2000 dataset. However, with the development and increasing sophistication of satellite remote sensing tools and techniques, direct observation of burned areas is becoming a much more common and relied up approach in fire emission studies (e.g.: Giglo *et al.,* 2006, 2010, 2013; van der Werf *et al.,* 2010). Based primarily on satellite-derived estimates of the area burned in fires, the mass of fuel burned (M) is derived by combining information on fuel load and the proportion of this fuel that actually burns (i.e. the combustion completeness):

$$M = A\,B\,C \qquad (2.2)$$

Where A is the burned area (m^2); B is the available biomass per unit area, also termed fuel load (kg km^{-2}); and C is the crop combustion completeness the same as in Eqn. 2.1 (unitless proportion between 0 and 1). The original Eqn. 2.2 appeared in Seiler and Crutzen (1980), and is widely used in studies of biomass

burning emissions, for example within the Global Fire Emissions Database (GFED) of van der Werf et al. (2010, see details in Section 2.6.4).

Burned areas for use in Eqn. 2.2 are now routinely estimated from the MODIS spaceborne sensors. For example, the MODIS burned area product (MCD45, Figure 2.8) provides global 500 m spatial resolution burned area information dated to the best estimated day of burn, and works by locating the occurrence of rapid changes in daily surface reflectance in MODIS time series (Roy *et al.,* 2005, 2008). An alternative 'direct broadcast' MODIS burned area product (MCD65) uses a somewhat similar approach, but with a lower requirement for the length of the time-series but a dependence on active fire data in addition to surface reflectance information (Giglio *et al.,* 2009). More spatially detailed burned area information than can be obtained with MODIS is able to be derived from higher spatial resolution sensors, such as Landsat Thematic Mapper and Landsat OLI (e.g. Smith *et al.,* 2007; Stroppiana *et al.,* 2012), and more recently Sentinel-2 MSI (MultiSpectral Instrument), albeit not yet routinely at global scales. Many burned area algorithms, including the MODIS approaches introduced above, are based on differences seen during the observation of the before and after the apparently fire.

One issue with the MODIS burned area products is that they are known to miss smaller burns, as outlined in Section 2.5 and detailed in Randerson et al. (2012). Roy et al (2008) also show that there are many "small fire" situations where active fire methods may detect a fires presence that cannot be easily identified using the MODIS burned area product, in that case MCD45. Therefore, the MODIS burned area product may not be a very reliable nor appropriate tool for use in agricultural residue burning regions. Randerson et al. (2012) estimated the amount of burned area missing from the MODIS burned area datasets, i.e. that due to small fires, to be as high as 35% as detailed in Section 2.5. Amounts were even higher in some cropland areas, including in China (> 80%). Beyond this potential bias, when using Eqn. 2.2, the fuel load and combustion completeness terms can be quite difficult to assess, and must generally be measured during field studies, be taken from prior literature estimates, or can come from the output of vegetation growth models (van der Werf *et al.,* 2010). The fuel load and combustion completeness terms vary widely between and across different biomes, and between different times of year, and are considered to be the key uncertainties in the burned area method of fire emissions calculation (Reid *et al.,* 2005).

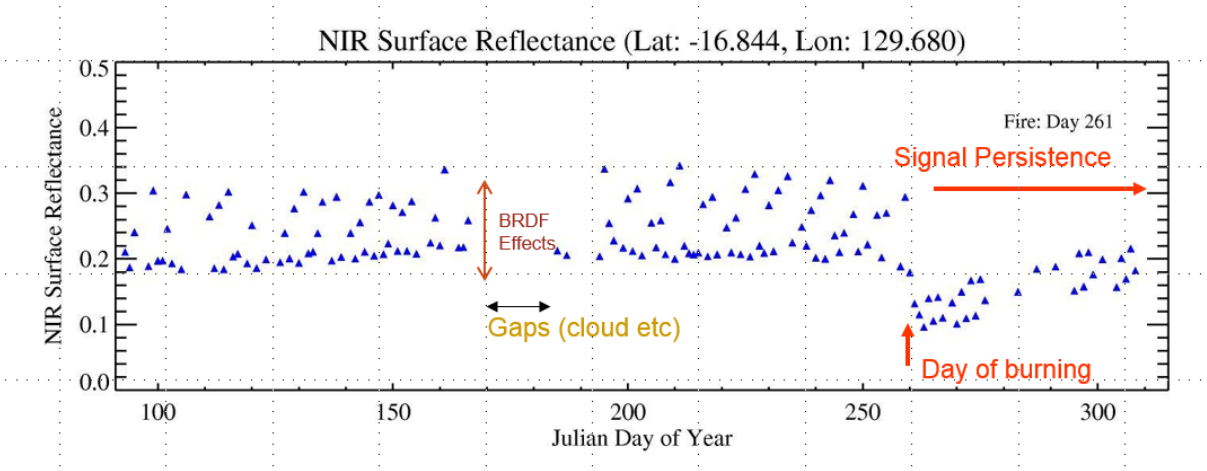

Figure 2.8: Time series of NIR (near-infrared) surface reflectance from MODIS 500m data (Roy *et al.*, 2002). Data fluctuation before day 260 is due to Bidirectional Reflectance Distribution Function (BRDF). The pixel burned around day 261, showing a distinct fall in NIR surface reflectance.

2.6.3 Active Fire Detections and Radiative Power (FRP) Methods

Flaming fires emit significantly in the shortwave infrared (SWIR) atmospheric window (1.6 - 2.5 µm). However, strong daytime solar reflections at these wavelengths has steered the development of active fire detection towards use of the middle infrared (MIR) atmospheric window (3 - 5 µm). Here, levels of solar reflected radiation are lower than in the SWIR (Fig. 2.9), while thermal energy emission rates from fires are very much higher than from the ambient temperature background. By detecting these emitted IR energy signatures, actively burning fires can be detected using satellite remote sensing (Wooster *et al.*, 2003, 2005). Since at MIR wavelengths the spectral radiance (W m^{-2} sr^{-1} μm^{-1}) emitted from flaming vegetation can be up to four orders of magnitude higher than from the surrounding ambient background (Fig. 2.9), areas of combustion occupying even a very small fraction of the pixel area (e.g. 0.1 to 1.0%) can result in significant increases in the pixel-integrated signal (Wooster *et al.*, 2013; Schroeder *et al.*, 2014).

However, the detections of active fires cannot be used to estimate burned area directly for use in Eqn. 2.2, since an identified active fire pixel is not necessarily all ultimately burned. There are, however, a number of demonstrated cases where the number of active fire pixels has been shown to be well correlated to the burned area produced over the same time period, and indeed this method has been employed to estimate burned area in the widely-used GFED database prior to the availability of the MODIS burned area product (e.g. Giglio *et al.*, 2013).

Another approach to directly quantify biomass burning from active fire detections uses the amount of radiant energy released by a fire. This is known as the Fire Radiative Power [FRP] approach (Wooster *et al.*, 2005), and compared to burned area method may in theory work well for smaller fires, since active fire detection methods can detect fires far smaller than can burned area based methods (Kaiser *et al.*, 2012; Wooster *et al.*, 2003, 2005).

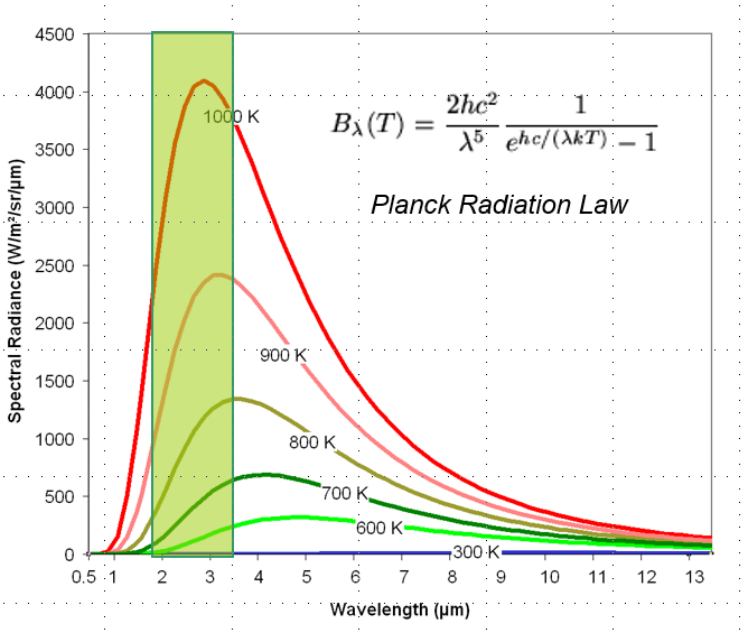

Figure 2.9: Emitted spectral radiant energy distribution across different wavelengths (Fuller, 2000), for objects with different temperatures (300 K = Ambient Earth; 1000 K = vegetation fire). The huge difference of spectral radiance from hot (fire) and cool (Earth) is most apparent in the SWIR to MWIR spectral region (highlighted by the green rectangle) and this region is key for active fire detection from satellite EO data, even when fires are filling far less than the entire pixel.

Nevertheless, since agricultural fires are small and are known to be better detected by active fire methods from MODIS than by the MODIS burned area products (Randerson *et al.*, 2012), it is appropriate to try them here, and in particular to determine whether the FRP approach to emissions estimation can be properly exploited in this "small fire" agricultural environment. The VIIRS sensor is potentially able to detect fires around 10× smaller than those of MODIS due to its much finer pixel area (Schroeder *et al.*, 2014), potentially offering a very useful attribute in agricultural burning regions where small field sizes and limited fire intensities are likely to lead to relatively small active fire signals. One limitation is, however, that VIIRS only images an area twice per day – and this limited sampling alone is unlikely to be able to capture the full picture of an areas fire activity in order to estimate it's FRE.

Multiple FRP observations made at different times during a fire can be integrated to provide an estimate of Fire Radiative Energy (FRE, Wooster *et al.,* 2005), either using a model of the fires diurnal cycle, multiple FRP observations, or some other assumption related to the changing nature of fire activity over the day (Ellicott *et al.,* 2009; Freeborn *et al.,* 2008; Kaiser *et al.,* 2012). Then, a direct estimate of total fuel consumption can be obtained using the FRE estimate and a "radiative energy combustion factor", i.e. an empirical ratio between FRE and fuel consumption (such as the one developed from experiments by Wooster *et al.,* 2005). One thing that should be noted is that not all the radiative energy from the active fire pixel is necessarily recorded by the remote sensing device. Some may be absorbed or obscured by overlying vegetation or by smoke, vapour or cloud existing between the fire and the sensor, and ideally this change should be corrected for in the estimate of FRE (Wooster *et al.,* 2005). Also, the adjustments and corrections needed when integrating FRP to FRE, including accounting for gaps created by clouds and orbital geometry, estimating the diurnal cycle of FRP during periods in between satellite overpasses, and adjusting for any "bow-tie" type viewing geometry effects all ideally need to be taken into account (Freeborn *et al.,* 2009, 2011; Randerson *et al.,* 2012).

2.6.4 Introduction of Two State-of-the-art Global Fire Emissions Databases

The Global Fire Emissions Database (GFED) is one of the most widely used global fire databases available (van der Werf *et al.,* 2010). It was built to combine remotely sensed data on burned area with the CASA (Carnegie Ames Stanford Approach) biogeochemical model of vegetation growth, producing global, spatially explicit, burned area and pyrogenic carbon emissions estimates. Monthly emissions estimates are delivered at a 0.25º grid cell resolution globally, though active fire data is available to improve the temporal resolution by distributing the emissions according to active fire count. Monthly burned area data currently extends back to July 1995, though for the first 5 or 6 years this is derived from ERS-ATSR and TRMM-VIRS active fire detections rather than directly from burned area mapping with the 500-m MODIS MCD64A1 product as is the case for subsequent years. Fig. 2.10 provides an example of GFED4.0 dry matter burned (shown as an areal density map) for 12 months in Eastern China (year 2013).

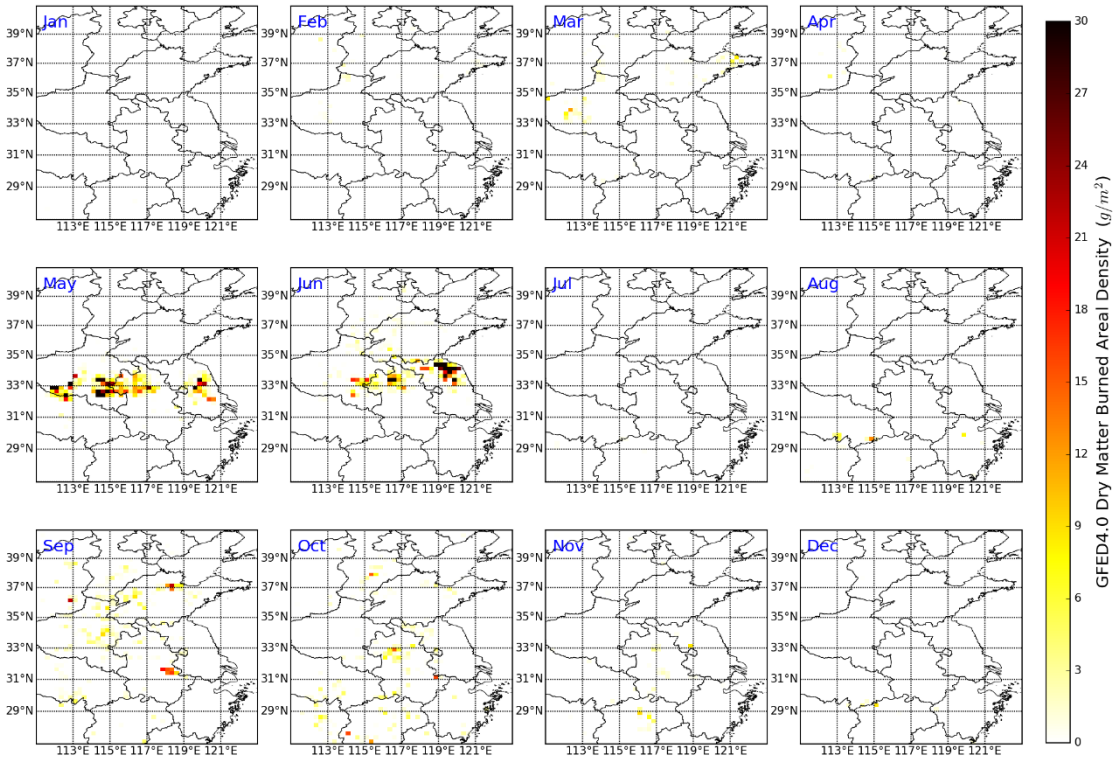

Figure 2.10: Spatial distribution (0.25 × 0.25º grid) of monthly total grid-cell dry matter burned areal density of agricultural fires occurring in Eastern China in 2013 retrieved from GFED4.0.

The most recent version of the Global Fire Emissions Database, GFED4.1s, is used in this study, and has an adaptation for the underestimation of small fires in the MODIS burned area product. This bias correction is based on the work of Randerson et al. (2012) and is calculated using:

$$BA_{total}(i,t,v) = BA_{MCD64A1}(i,t,v) + FC_{out}(i,t,v) \times \alpha_{r,s,v,y} \times \gamma_{r,s,v,y} \quad (2.3)$$

Where the total burned area (BA_{total}) in each grid cell (i), month (t) and vegetation class (v) is the sum of original MCD64A1 burned area ($BA_{MCD64A1}$), as used in the prior GFED4.0 system, and a 'small fire component' calculated from three factors (Eqn. 2.3). These are the total number of MOD14A1 active fire pixels found outside of burned areas in each 0.25º grid cell (α), the ratio of $BA_{MCD64A1}$ to active fire counts, and a scalar (γ). Fig. 2.11 gives the example of the dry matter burned areal density as contained in the GFED4.1s database for 12 months during 2013 in Eastern China. Compare to Fig. 2.10, GFED4.1s holds higher values of dry matter burned areal density in most grid cells, and shows a wider fire distribution across Eastern China. The GFED4.1s database is stored as HDF5 format files and can be downloaded from http://www.falw.vu/~gwerf/GFED/GFED4/.

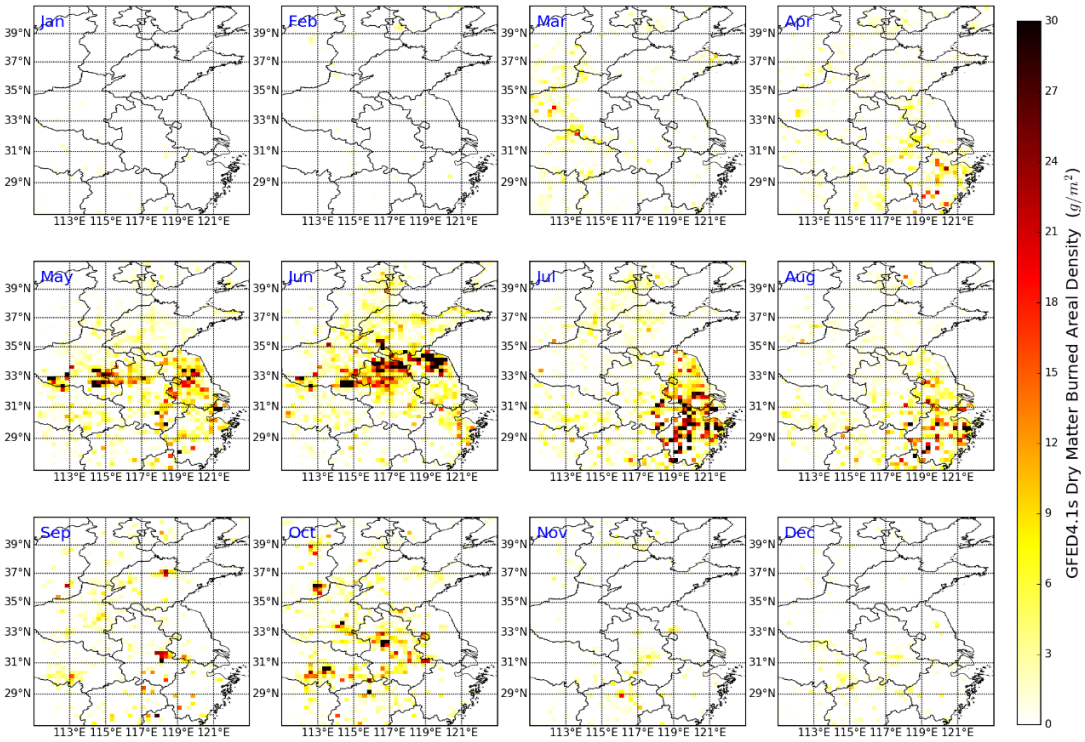

Figure 2.11: Spatial distribution (0.25 × 0.25º grid) of monthly total grid-cell dry matter burned areal density of agricultural fires occurring in Eastern China in 2013 retrieved from GFED4.1s. This version contains small fire boost based on Randerson *et al.*, (2012), which therefore holds higher value of dry matter burned areal density with wider fire distribution compare to GFED4.0 from Fig. 2.10.

The main global alternative to GFED is the Global Fire Assimilation System (GFAS), developed by Kaiser et al. (2012) and based on the FRP method (see Section 2.6.3). MODIS supplies the FRP data, up to 4 times per day at most latitudes, and the emissions of 40 species are calculated every 24 hours at a 0.1º spatial resolution from daily averaged FRP areal density values and a conversion coefficient relating this to the fuel consumption. This coefficient is biome-dependent and was derived from comparisons between GFAS-calculated FRP totals and GFED specified fuel consumptions for the same biomes. Hence GFED and GFAS are forced to agree somewhat, though an apparent underestimation of smoke aerosol emissions by a factor of 2-4 is one of the as yet unexplained characteristics of GFED (Kaiser *et al.*, 2012). Within the GFAS calculation, the diurnal cycle is currently being introduced via a Gaussian function that peaks in early afternoon, the exact characteristics of the function being based on geo-stationary satellite observations (Andela *et al.*, 2015). Fig. 2.12 shows the monthly total grid-cell dry matter burned areal density retrievals provided by GFAS1.2 at a grid cell resolution of 0.1°, including in near real time (which is not the case with GFED; that lags around a year behind real-time). The newest GFAS1.2 data can be retrieved from the ECMWF-hosted Copernicus Atmosphere Monitoring Service (CAMS) website (http://www.gmes-atmosphere.eu/d/services/gac/nrt/fire_radiative_power/).

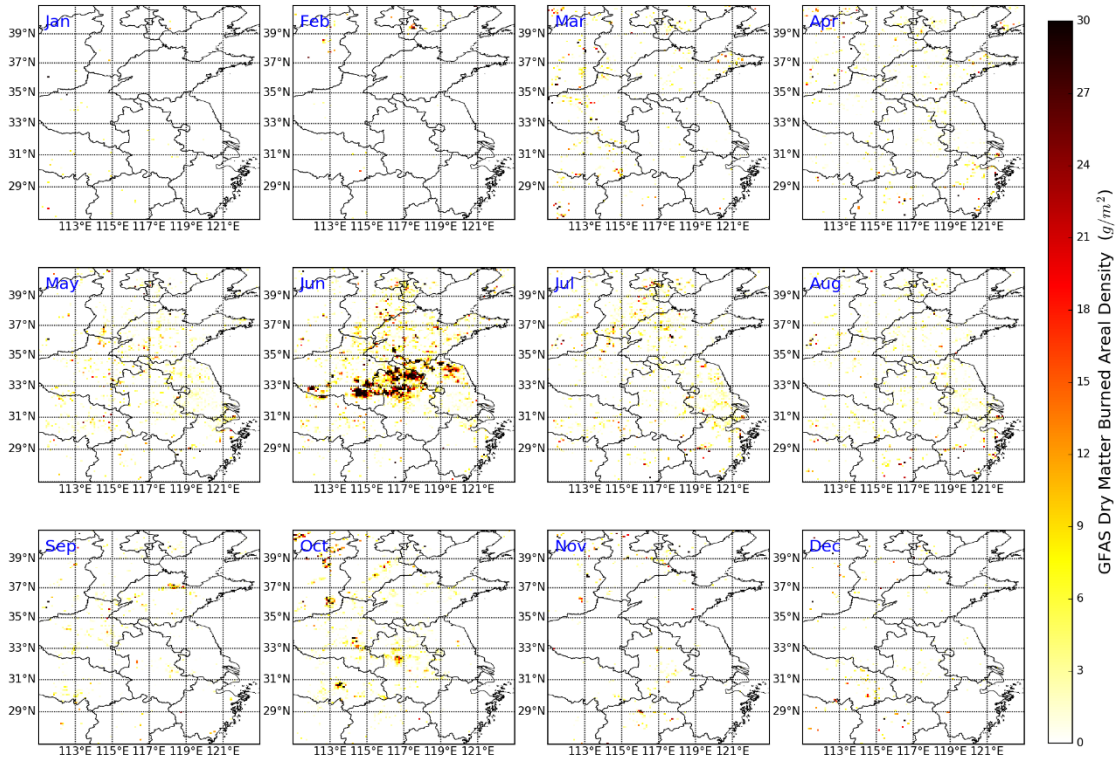

Figure 2.12: Spatial distribution (0.1 × 0.1º grid) of monthly total grid-cell dry matter burned areal density of agricultural fires occurring in Eastern China in 2013 retrieved from GFAS.

2.7 OBJECTIVES

This PhD research focuses on agricultural residue burning in Eastern China (see Fig.2.13), a densely populated area of China which is also one the countries primary agricultural regions and which includes both the North China Plain and the Yangzi Plain. Agricultural fires are known to be widespread in this area, as Fig. 2.13 indicates using fire radiative power (FRP) data introduced in Section 2.6. Intensive double cropping cultivation dominates in Eastern China, with open-air residue burning widely used to prepare the ground before one or both planting periods (late-May to mid-June and late-September to early-October; Huang *et al.*, 2012). Other parts of China show different patterns, with triple cropped areas in the south and later harvesting times in the northeast, but these will not be studied here. Within the Eastern China region, in addition to the rural population and those in urban areas, two mega-cities (Beijing and Shanghai, shown in Fig. 2.13, containing a population of 11.5 and 14.3 million citizens each) are potentially impacted by the transported agricultural fire emissions.

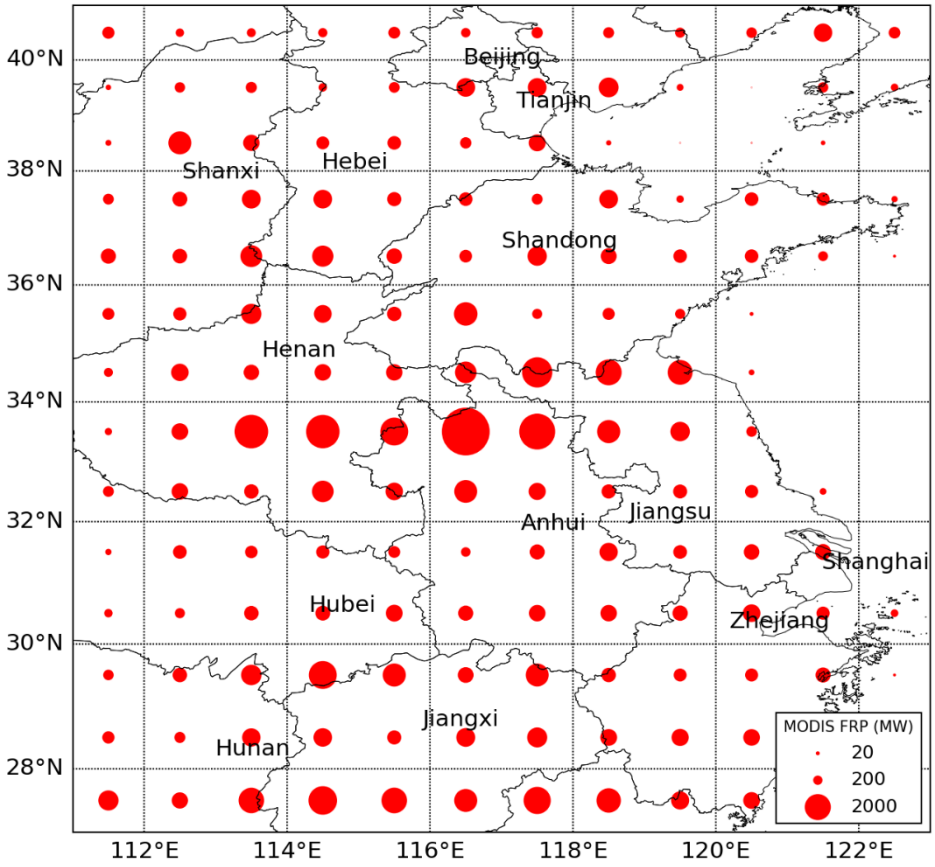

Figure 2.13: Map of research domain in this PhD study, including main provinces and mega-cities in Eastern China (111-123° E, 27-40° N). The red circles depict total FRP observed by MODIS between 2002 and 2015 per 1° grid cell (see legend lower right).

Based on the literature reviewed in Sections 2.2 to 2.4, it is clear that currently there exists some uncertainty about (i) the magnitude of agricultural fire activity in the Eastern China region (Cao *et al.*, 2006; Huang *et al.*, 2012; Li *et al.*, 2007; Zhang *et al.*, 2008), where small fires dominate and many of them might not be included in current satellite fire products yet (Randerson *et al.*, 2012). (ii) whether there exists a significant interannually variability or not, and if so whether this has any relation to e.g. Chinese Government policy initiatives (Pan *et al.*, 2013; Wang et al, 2013) or climatic variations, and (iii) the actual chemical and particulate totals that are released to the atmosphere as a result of the residue burning activity (Cao *et al.*, 2006; Huang *et al.*, 2012; Li *et al.*, 2007). This PhD study aims to address each of these issues using a combination of satellite remote sensing (see review of Section 2.5-2.6) and ground-based field measurements of *in situ* burning. A series of key objectives targeted at meeting the overall aims are listed below:

Obj (i): Quantify the spatio-temporal distribution of agricultural residue burning using active fire satellite Earth Observation approaches that take into account "small fires" more effectively than currently done.

Here the primary task will be to exploit observations from the relatively new VIIRS sensor onboard the Suomi NPP satellite, along with those from the long-standing MODIS sensor onboard the TERRA and AQUA satellites. Whilst actively burning fires that cover only 10^{-4} of the satellite pixel area are potentially detectable with these systems, the very small size of the (highly numerous) agricultural fires means many (perhaps the majority) are missed by MODIS. It is expected that the 375 m spatial resolution "I-band" imagery provided by VIIRS will allow active fires to be detected that are ~ 10× smaller than those that can be detected by MODIS, due to the 10× smaller pixel area of the VIIRS I-Band (Schroeder *et al.*, 2014). This "small fire" detectability is very attractive in Eastern China, where field sizes less than 1/6 ha (1670 m^2) are commonplace (NBSC, 2012). Using VIIRS, the theoretical minimum detectable active fire size at night is ~ 5 m^2 (Schroeder *et al.*, 2014), and by day perhaps twice this, which should easily be small enough for the detection of a very significant fraction of the agricultural fires that are burning when the Suomi NPP satellite passes overhead. To undertake the work related to this objective, a new active fire detection algorithm will be developed for application to VIIRS, and the result will be validated using higher spatial resolution satellite data and/or data collected by UAVs and on the ground. Schroeder et al. (2014) have already demonstrated an early "small fire" active fire detection algorithm based on VIIRS I-band imagery, but reported very large proportion (>40%) low confidence fires in Eastern China – suggesting that many of the detections may actually be false alarms. One task under this objective will be to understand the causes of these apparent "false fire detections", and attempt to significantly reduce them in the newly developed algorithm output, whilst still maintaining a "small fire" detection sensitivity ideally beyond that obtained by Schroeder et al. (2014). Once a validated active fire detection methodology is developed and validated, it will be used to examine the location, timing, interannual and seasonal variability and trends in agricultural residue burning occurrence across the Eastern China study area.

Obj (ii): Estimation of biomass consumption in agricultural residue burning.

Here the task will be to build on the work done under Obj (i) and use VIIRS to assess the FRP (fire radiative power) of the actively burning fires, based on the approach of Wooster et al. (2003). This has

not yet been done using VIIRS, and very rarely has Chinese agricultural burning been specifically targeted for FRP estimation even with MODIS (Huang *et al.,* 2012). A key task will be to combine the I-Band active fire detection results with data from the VIIRS M-Band, which unlike the I-Band, is low risk to saturate over agricultural fires. The combination of I-Band and M-Band can thus be used for FRP retrieval over both small and large agricultural fire events. However, since VIIRS can only measure FRP twice per day, and thus fuel consumption rate at the same temporal interval, further information is most likely required to properly estimate the FRE (fire radiative energy) and total biomass consumed (Freeborn *et al.,* 2011; Roberts *et al.,* 2009). Himawari-8, a Japanese geostationary meteorological satellite launched in 2014 will provide this additional information. The Himawari series of geostationary satellites carries a new instrument called the Advanced Himawari Imager (AHI), offering far improved capabilities in terms of spatial resolution, spectral bands and temporal resolution than the previous MTSAT (Multifunctional Transport Satellites) system. AHI data should allow full diurnal characterisation of the rapidly changing, extremely numerous but typically rather relatively small and short-lived fires that are common in agricultural landscapes, albeit in areas with a lower density of fires there may not be enough of a thermal anomaly signal for AHI to detect. The information derived from VIIRS and Himawari-8 will be combined to estimate FRE and thus daily agricultural burning fuel consumption.

Obj (iii): Confirmation of the emissions factors of Chinese crop residue fires.

Biomass burning emission factors for Chinese crop residues have been most commonly derived from laboratory tests (as outlined in Section 2.3). These values need to be confirmed via *in situ* fieldwork on real fire events, to ensure the derivation of EFs that are representative of real-world conditions, and this will be done during this component of the research programme.

Obj (ix): Estimate daily agricultural residue burning emissions for Eastern China fire seasons throughout 2013-2015.

Here the fuel consumption and EF measures described above will be combined to estimate the mass of key gaseous and particulate species released into the atmosphere. The spatio-temporal distribution of these emission will be analysed and compared to those present in state-of-the-art databases (see Section 2.6.4), focusing on the potential changes that have been introduced via the new ability to include "small fires" within the active fire detection process.

CHAPTER 3: AGRICULTURAL FIRE DETECTION AND FRP ASSESSMENT USING VIIRS

3.1 INTRODUCTION

This Chapter focuses on work conducted to meet Obj. (i) of this research (Section 2.7), that is to '***Quantify the spatio-temporal distribution of agricultural residue burning using active fire satellite Earth observation approaches that take into account "small fires" more effectively than currently done'.***

The chapter primarily describes the development of a 'small active fire' detection algorithm for application to 375 m spatial resolution VIIRS I-Band data. This algorithm has been developed to improve the detection of small, low-intensity agricultural fires occurring in Eastern China. This chapter also covers part of Obj. (ii) by building the methodology for assessing the FRP of the actively burning fires, again using data from VIIRS but this time both from the I- and M-Bands.

Section 3.2 of this Chapter presents a published paper (Zhang *et al.*, 2017: *Remote Sensing of Environment*) that describes the development, application, and evaluation of the 'small active fire' detection algorithm, as well as the FRP retrieval method. The author of this PhD thesis is the first author of this paper, and designed the algorithm with advice from M. Wooster, conducted all the data processing, analysis and field verification. She also drafted the paper. Wooster also provided advice with respect to data analysis and editing, whilst Xu calculated the terms of the atmospheric correction procedure.

3.2 APPROACHES FOR SYNERGISTICALLY EXPLOITING VIIRS I- AND M-BAND DATA IN REGIONAL ACTIVE FIRE DETECTION AND FRP ASSESSMENT: A DEMONSTRATION WITH RESPECT TO AGRICULTURAL RESIDUE BURNING IN EASTERN CHINA

Remote Sensing of Environment 198 (2017) 407–424

Contents lists available at ScienceDirect

Remote Sensing of Environment

journal homepage: www.elsevier.com/locate/rse

Approaches for synergistically exploiting VIIRS I- and M-Band data in regional active fire detection and FRP assessment: A demonstration with respect to agricultural residue burning in Eastern China

Tianran Zhang [a,b,*], Martin J. Wooster [a,b], Weidong Xu [a,b]

[a] King's College London, Department of Geography, Strand, London WC2R 2LS, United Kingdom
[b] NERC National Centre for Earth Observation (NCEO), United Kingdom

ARTICLE INFO

Article history:
Received 29 October 2016
Received in revised form 9 June 2017
Accepted 25 June 2017
Available online xxxx

Keywords:
FRP
VIIRS
Biomass burning
Agricultural fire
MODIS

ABSTRACT

We demonstrate a new active fire (AF) detection and characterisation approach for use with the VIIRS spaceborne sensor. This includes for the first-time joint exploitation of both 375 m I-Band and 750 m M-Band data to provide both AF detections and FRP (fire radiative power) retrievals over the full range of fire and FRP magnitudes. We demonstrate the value of our VIIRS-IM 'synergy' product in an area of eastern China dominated by numerous small agricultural residue burns, which contribute significantly to regional air quality problems but which are often difficult to identify via standard (e.g. MODIS 500 m resolution) burned area mapping. We show that the highly 'fire sensitive' VIIRS I-Band data enables detection of the 'small' active fires (FRP ≤ 1 MW), but this sensitivity can lead to false alarms, often associated with manmade structures. We help avoid these via use of 30 m resolution global land cover data and an OpenStreetMap mask. Comparisons to near-simultaneous Aqua-MODIS AF detections, and the existing VIIRS I-Band AF global product, highlight our VIIRS algorithm's ability to more reliably detect the lowest FRP pixels, associated with the type of agricultural burning dominating eastern China. Our algorithm delivers typically 5 to 10× more AF pixels than does simultaneous-collected MODIS AF data (notwithstanding differences in spatial resolution), and importantly with a AF detection sensitivity that remains much more constant across the swath due to VIIRS' unique pixel aggregation scheme. The VIIRS I4-Band saturates over higher FRP fires, but by combining use of I- and M-Band data our algorithm generates reliable FRP records for all fires regardless of FRP magnitude. Using the VIIRS-IM methodology we find regionally summed FRP's up to 4× higher than are recorded by MODIS over the same fire season, highlighting the significance of the formally undetected low FRP active fires and indicating that current MODIS FRP-based emissions inventories for areas dominated by agricultural burning may be underestimating in a similar way to burned-area based approaches. FRP generation from VIIRS that takes into account both low- and high-FRP fires via use of both the I- and M-Band data should therefore enable significant improvements in global fire emissions estimation, particularly for regions where smaller types of fire are especially dominant.

1. Introduction

Satellite remote sensing is widely used for mapping burned area (Giglio et al., 2010; Roy et al., 2008) and for detecting and characterising actively burning fires (Giglio et al., 2006, 2008; Roy et al., 2005, 2008; Wooster et al., 2005). Burned area (BA) products generally require a substantial fraction of the pixel to be fire-affected for a confident detection to be made, whereas active fires only need cover 0.01–0.1% of the pixel area (Giglio et al., 2006, 2008; Robinson, 1991; Roberts et al., 2005; Schroeder et al., 2014). Randerson et al. (2012) compared 500 m spatial resolution (MCD64A1) MODIS BA data to 1000 m spatial resolution (MOD14/MYD14) MODIS AF (active fire) data to highlight the fact that a large proportion of the typical 'small' fires found in agricultural and tropical deforestation landscapes appear to remain undetected in the BA data, but do appear in the AF products. Burned area is therefore significantly underestimated in such areas, with the most severe impacts (>50% underestimation) apparently located in parts of central Asia where agricultural residue burning across huge numbers of individually small fires dominates. This estimate of the degree of underestimation is itself very uncertain, and maybe a minimum estimate because the MODIS AF product itself often fails to detect active fires whose FRP is significantly below ~8 MW (Zhukov et al., 2006). This minimum detection threshold becomes even higher away from the MODIS swath centre (Freeborn et al., 2011). In most biomes and for most times of year, such low FRP fires seem likely to dominate (e.g. Wooster and

* Corresponding author.
E-mail address: tianran.zhang@kcl.ac.uk (T. Zhang).

http://dx.doi.org/10.1016/j.rse.2017.06.028

Zhang, 2004; Ichoku et al., 2008), so in addition to their potential use in improving the estimation of burned area, low FRP AF detection may also be very significant for regional fire regime characterisation (Freeborn et al., 2014) and for FRP-based smoke emissions assessments (e.g. Kaiser et al., 2012).

Here we present a new AF detection approach, based on data from the Visible Infrared Imaging Radiometer Suite (VIIRS) carried on the Suomi-NPP satellite. The approach is aimed specifically at including detection and characterisation of low FRP fires as well as the much easier-to-detect high FRP fires. Via this approach, we aim to much more fully record regional FRP characteristics at the time of the satellite overpass than hitherto possible.

VIIRS has two middle-wave infrared (MWIR) bands offering (at nadir) 375 m (I-Band) and 750 m (M-Band) spatial resolutions, representing significantly smaller pixel areas and thus an improved active fire detection capability than offered by MODIS (with its 1000 m spatial resolution nadir pixels). Whilst the experimental Hotspot Recognition Sensor (HSRS) on-board the BIRD satellite has previously been used to demonstrate a low-FRP detection capability based on sub-400 m spatial resolution data (Zhukov and Oertel, 2001; Zhukov et al., 2006), unlike BIRD-HSRS, VIIRS offers global twice daily observations. This includes an overpass in the early afternoon, at around the peak of the usual fire diurnal cycle (Freeborn et al., 2011). We apply our analysis of VIIRS data to detect and quantify active fires burning in the agricultural region of eastern China, which Randerson et al. (2012) demonstrate is an area where omission of 'small' crop residue fires by the MODIS (MCD64A1) BA product appears among the most significant worldwide.

Schroeder et al. (2014) have already demonstrated an improved ability to detect 'small fires' using the VIIRS I-Band. Fires down to an FRP around an order of magnitude lower than the minimum detection limit of MODIS can in theory be detected, due to the I-bands 10× smaller (nadir) pixel area. The resulting VIIRS AF product from Schroeder et al. (2014) (VNP14IMGTDL_NRT) indeed shows a generally much more sensitive 'small fire' active fire detection performance compared to the MODIS MOD14/MYD14 product, though the implementation described in Schroeder et al. (2014) did not include FRP retrieval itself. The generally strong performance of the Schroeder et al. (2014) global-I-Band algorithm has inspired our regional algorithm, in which we combine VIIRS I- and M-Band data to generate AF detections and FRP retrievals for both low- ("small") and high-FRP ("large") fires. We optimise our algorithm for eastern China, an area of agricultural burning where the Schroeder et al. (2014) global implementation still has some difficultly, showing a high rate of low confidence AF detections. We compare outputs from our VIIRS I-M synergy product scheme to those from the global algorithm of Schroeder et al. (2014), and to MODIS, illustrating the impact of our enhancements related to both AF detection and FRP characterisation.

2. The VIIRS sensor, scan and data characteristics

2.1. VIIRS sensor

VIIRS currently operates onboard Suomi-NPP (launched October 2011), and is the first of a set of 22-band scanning radiometers designed to fly on the Joint Polar Satellite System (JPSS) over the coming decades (Wolfe et al., 2013). VIIRS offers one set of multi-spectral channels (five "I-Bands") providing 375 m spatial resolution data (at nadir), and a further set (sixteen "M-Bands") recorded simultaneously at 750 m spatial resolution (at nadir). One M-Band pixel thus contains four I-Band pixels.

Table 1 shows the VIIRS bands used herein, and the two I-Bands bands centred on middle and longwave infrared wavelengths (3.74 and 11.45 μm respectively) make it possible to quite easily adapt existing AF detection algorithms (e.g. Giglio et al., 2003) for use with VIIRS I-Band data. In theory, because the I-Band's pixel areas are 10× smaller than MODIS (at nadir), active fires around 10× smaller in area (or with ~10× lower fire intensity FRP), are detectable with VIIRS compared to MODIS.

2.2. VIIRS scan and data characteristics

In addition to its higher spatial resolution, a key difference between VIIRS and MODIS is the former's 'pixel aggregation' scheme which limits pixel area increase with scan angle to a maximum of ×4 compared to MODIS' × 10 (Wolfe et al., 2013). Via this scheme, the standard ungeocoded VIIRS SDR (Sensor Data Record, equivalent to MODIS Level 1b) data (Fig. 1a) is separated into different aggregation zones, with each pixel in 'Aggregation Zone 3' being the signal average of three along-scan sub-pixels, those in 'Aggregation Zone 2' being the average of two sub-pixels, and those in the 'No Aggregation Zone' being the original observations (Wolfe et al., 2013). This greatly lessens VIIRS pixel area increase across the swath, but the data still suffer a MODIS-like "bow tie effect" towards the swath edge due to overlap between consecutive scans (Wolfe et al., 2013). To counteract this, the VIIRS SDR has the four outermost sampling rows of an individual scan line filled with zeros across Aggregation Zone 2, and eight across the outermost "No Aggregation Zone" (Fig. 1). This removes the "bow-tie" effect seen in ungeocoded MODIS level 1b data, where near swath-edge pixels appear replicated along-track due to their dimensions being far larger than the satellites along-track movement during a single scan (Wolfe et al., 2013).

Schroeder et al. (2014) identified a series of key issues to address prior to confident use of VIIRS data for AF detection and fire characterisation. Of utmost relevance to FRP retrieval is that the I-Band covering the MWIR spectral region (I4) saturates at 367 K, and because of the small ground footprint of the pre-aggregation I-Band detectors - such a brightness temperature can be reached at the locations of even rather low-to-moderate FRP fires (e.g. ~20 MW or less). Unfortunately, the VIIRS data Quality Flag (QF) currently only shows instances where all the pre-aggregation VIIRS pixels going into the signal averaging calculation are saturated, which is a far less common situation than only a subset of them being saturated. Thus, it is a non-straightforward task to unambiguously identify all I4 Band pixels affected by pre-aggregation saturation, and we address this issue via synergistic use of the 750 m MWIR M13 band data at all such potential locations, as explained in Section 6.

3. Study area

Our 1.1 million km^2 eastern China study region includes the North China Plain and the Yangtze Plain (Fig. 2), encompassing around one

Table 1
VIIRS spectral bands used herein, along with the closest bands of MODIS for reference (from Cao et al., 2013).

VIIRS band	Spectral range (μm)	Spatial resolution @ nadir (m)	MODIS band	Spectral range (μm)	Spatial resolution @ nadir (m)
I1	0.600–0.680	375	1	0.620–0.670	250
I2	0.846–0.885	375	2	0.841–0.876	250
I3	1.580–1.640	375	6	1.628–1.652	500
I4	3.550–3.930	375	20	3.660–3.840	1000
I5	10.500–12.400	375	31 or 32	10.780–11.280	1000
				11.770–12.270	1000
M13	3.973–4.128	750	21 or 22	3.929–3.989	1000
				3.929–3.989	1000

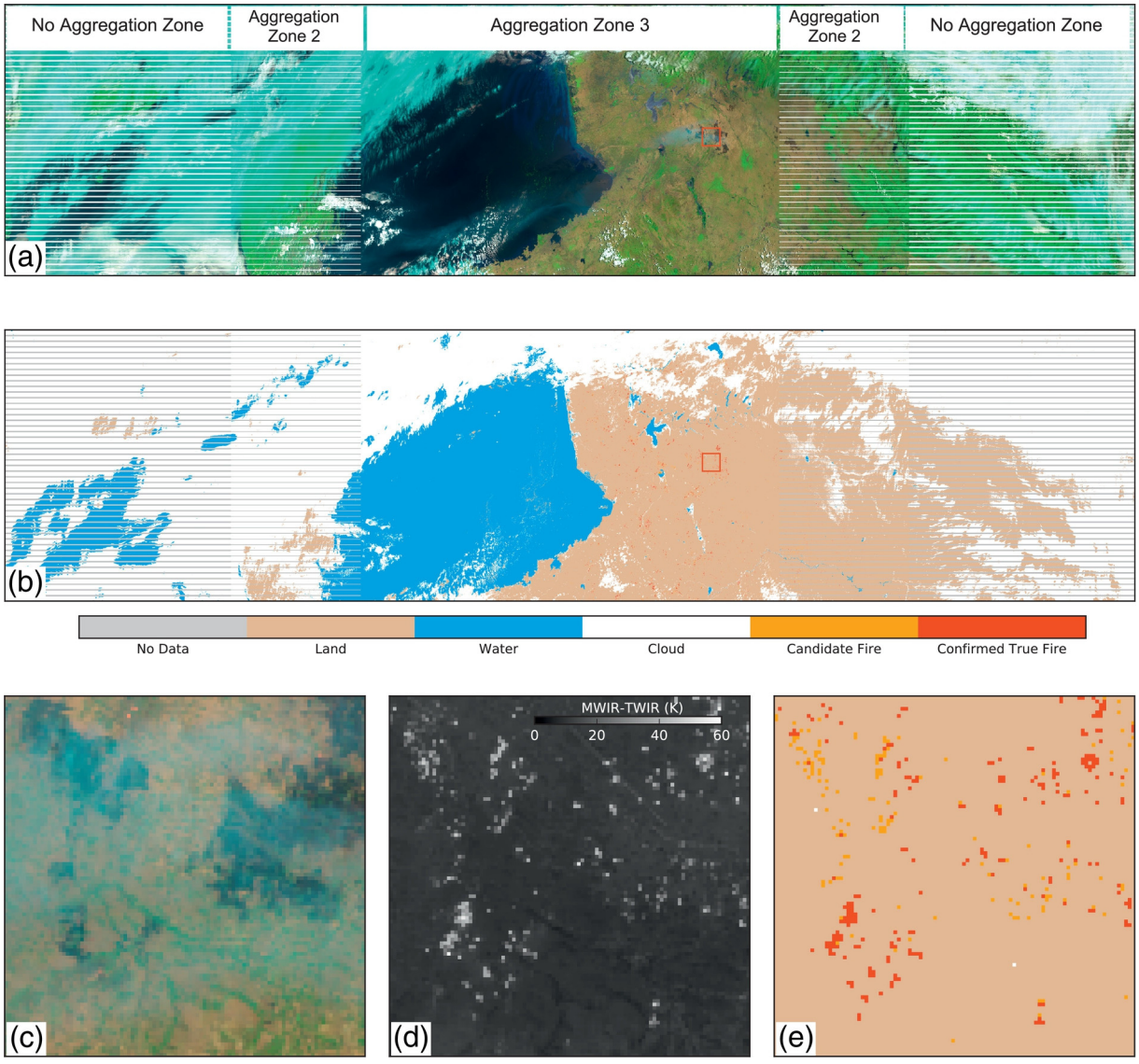

Fig. 1. VIIRS data of eastern China, covering the area outlined in yellow in Fig. 2. (a) VIIRS I-Band false colour composite image (RGB = I3, I2, I1) with the region selected and shown as (c), (d), and (e) outlined in red. (b) cloud/water/candidate thermal anomaly pixel/confirmed thermal anomaly pixel (white/blue/orange/red) derived from I-Band data using the techniques detailed herein. (c) shows the same false colour composite as in (a), but now zoomed on the highlighted region. These data are subset from the first 85-second granule of VIIRS SDR npp_d20150613_t0503225_e0509028. (d) shows the MWIR (Band I4) and LWIR (Band I5) brightness temperature difference image matching (c), and (e) shows the matching cloud/water/candidate fire/confirmed active fire pixel mask output from our active fire detection scheme outlined in Fig. 3. The image is an ascending node scene, with north towards the bottom. (For interpretation of the references to colour in this figure legend, the reader is referred to the web version of this article.)

third of the Chinese population and the area responsible for an estimated 25% of China's crop production (~51% of the national rice yield; NBSC, 2012). Burning typically remains the quickest, simplest and cheapest approach to removing agricultural residues left after harvest of rice, wheat, and other crops, and remains commonplace even though discouraged or forbidden since the late 1990's (Huang et al., 2012). Until recently such crop residues were China's second largest industrial waste product (Qu et al., 2014), and this widespread burning is suspected of contributing significantly to China's air quality problems (Qu et al., 2014). Previous studies show most fields in eastern China support at least two crops per year (Huang et al., 2012; Pan et al., 2013), with winter wheat harvested in June, the stubble burnt shortly after, and the fields then rapidly flooded and rice planted. This rice is harvested in September or October when the fields are also drained, the rice straw burned, and the fields prepared again for wheat planting (Huang et al., 2012).

Being almost solely confined to agricultural fields, the individual crop residue fires themselves may each be quite small, but they occur in extremely large numbers (Huang et al., 2012). Mostly ignited within a few weeks in any particular area (usually twice per year), their cumulative impact on air pollution at these times can seemingly be very high (Huang et al., 2012; Yan et al., 2006). However, whilst 1 km MODIS MOD14/MYD14 AF data indicate their spatial patterns (Fig. 2), and perhaps allow improved quantification compared to MODIS 500 m burned area data alone (which seems to miss large fractions of the activity; e.g. Randerson et al., 2012), the typically small individual size (and thus low FRP) of the fires means that many still remain unaccounted even when using the MODIS AF data (Schroeder et al., 2014). The higher spatial resolution data from VIIRS, which should enable the detection of significantly lower FRP fires, can thus very likely significantly aid their quantification.

4. Active fire detection methodology

4.1. Datasets

We based our algorithm development and testing on VIIRS SDRs covering eastern China between 1st June 2014 and 30th June 2015

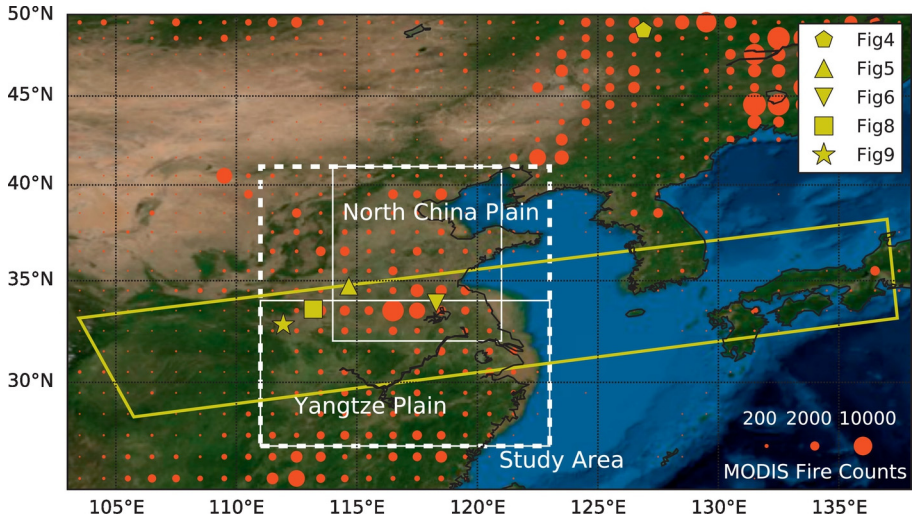

Fig. 2. Eastern China agricultural area (111–123° E, 27–40° N), outlined by the white dashed box. The approximate area of the North China Plain and the Yangtze Plain are demarcated by the solid white boxes. The red circles depict numbers of MODIS active fire pixels detected between 2002 and 2015 per 1° grid cell (see legend lower right). Whilst most fires in the study region are agricultural fires, those towards the north of the wider region include forest fires. Yellow markers show locations of the data of Figs. 4, 5, 6, 8 and 9 (see legend upper right). Yellow outline shows the footprint of the VIIRS swath taken during the 85 s VIIRS SDR used to produce Fig. 1. (For interpretation of the references to colour in this figure legend, the reader is referred to the web version of this article.)

(13 months, covering three burning seasons) and between 12:00 and 15:00 h local solar time by day, and 00:00 to 3:00 by night. An extra VIIRS SDR set for 28th August 2016 was also processed to facilitate comparison of our outputs to the VIIRS global product, which was unavailable for the earlier periods. HDF5 files including all co-registered SDRs were downloaded from NOAA CLASS (https://www.class.ncdc.noaa.gov/), along with the Quality Flag information and common geolocation file. Each 5-min SDR contains four 85-second VIIRS granules (e.g. Fig. 1). For comparison to our VIIRS outputs we used Collection 6 Aqua MODIS MYD14 AF products (Giglio et al., 2016), which closely match VIIRS' overpass time, along with the VNP14IMGTDL_NRT VIIRS I-Band global 'small fire' product based on the algorithm of Schroeder et al. (2014), obtained from https://worldview.earthdata.nasa.gov/ (the Algorithm Theoretical Basis Document and Users' Guide is now available at https://viirsland.gsfc.nasa.gov/Products/FireESDR.html). All data were processed using the UK's JASMIN super-data-cluster (Lawrence et al., 2013).

4.2. VIIRS I-Band regional "small active fire" detection algorithm

Our optimised VIIRS I-Band regional AF detection algorithm has five major steps (Fig. 3), based on a combination of principles taken from the following algorithms: MODIS AF (Giglio et al., 2003, 2016), global VIIRS I-Band (Schroeder et al., 2014), BIRD-HSRS (Wooster et al., 2003; Zhukov and Oertel, 2001; Zhukov et al., 2006), and the Meteosat SEVIRI Fire and Thermal Anomaly (FTA) (Roberts and Wooster, 2008; Wooster

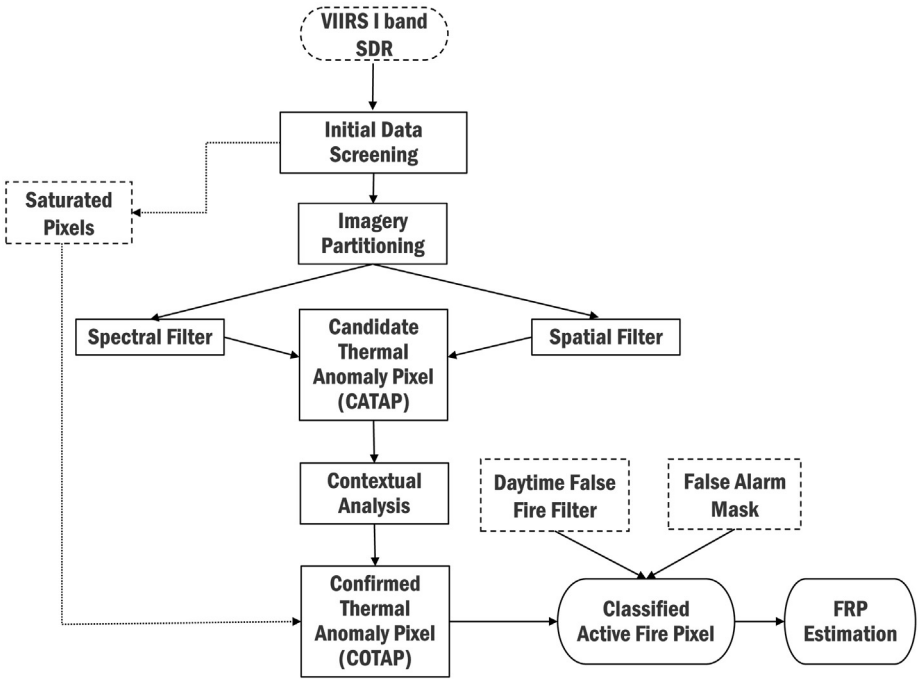

Fig. 3. Workflow of the regionally optimised VIIRS I-Band active fire (AF) detection algorithm developed herein.

et al., 2015). In common with these, our VIIRS algorithm first identifies 'candidate thermal anomaly pixels' whose signals suggest they may possibly contain a fire, and then confirms this via signal comparisons to their surroundings, creating a set of confirmed thermal anomaly pixels. We rely primarily on the VIIRS I4 (MWIR) and I5 (LWIR) spectral channels, with the other three I-Bands used to support cloud/water masking and sunglint discrimination.

Our AF detection algorithm runs at granule level rather than whole VIIRS SDR. In the following description, ρ_i refers to reflectance in VIIRS band i (0 to 1.0), BT_i the brightness temperature (BT) in VIIRS band i (Kelvin), ΔBT_{ij} the BT difference between bands i and j (Kelvin), and QFi the pixel quality flag in VIIRS band i. VIIRS bands are listed in Table 1.

i) Initial data screening

Using its solar zenith angle (θ_s), each VIIRS pixel is classed as day ($\theta_s < 90°$) or night ($\theta_s \geq 90°$), with water and cloud-contaminated pixels removed to reduce computational time in subsequent stages (Schroeder et al., 2014).

For daytime observations, pixels passing six tests taken from Piper and Bahr (2015) are classified as cloud:

$$\rho_1 > 0.08 \quad (1)$$

$$\frac{\rho_1 - \rho_3}{\rho_1 + \rho_3} < 0.7 \text{ AND } \rho_2 > 0.11 \quad (2)$$

$$BT_5 < 300 \text{ K} \quad (3)$$

$$(\max(\rho_3) - \rho_3) \times BT_5 < 410 \text{ K} \quad (4)$$

$$\rho_2/\rho_1 < 2.0 \quad (5)$$

$$\rho_2/\rho_3 > 1.0 \quad (6)$$

where the $\max(\rho_3)$ is the maximum reflectance of VIIRS I3 within the processing scene. The threshold value in (3) is kept at 300 K (cooler than the original implementation) to minimise instances of smoke being classified as cloud.

During night-time passes, a simpler thermal channel cloud threshold is used (Schroeder et al., 2014):

$$BT_4 < 265 \text{ K AND } BT_5 < 295 \text{ K} \quad (7)$$

It is useful to remove water body pixels by day to minimise sunglint impacts, and we use the Schroeder et al. (2014) rapid water mask, with an extra limitation that the I5 BT must lie below 300 K. Without this addition, we found recently burned areas (which are often of low albedo due to their covering of black ash and char) could be incorrectly classed as water, particularly if covered by smoke, as mentioned by Schroeder et al. (2014):

$$\rho_1 > \rho_2 \text{ AND } \rho_2 > \rho_3 \text{ AND } BT_5 < 300 \text{ K} \quad (8)$$

By day, following Schroeder et al. (2014) we also exclude certain radiometrically bright but still fire-free targets, such as sand banks along riverbeds, using:

$$\rho_1 + \rho_2 > 0.6 \text{ AND } BT_5 < 285 \text{ K} \quad (9)$$

AND

$$\rho_3 > 0.3 \text{ AND } \rho_3 > \rho_2 \text{ AND } \rho_2 > 0.25 \text{ AND } BT_4 \leq 335 \text{ K} \quad (10)$$

VIIRS I4 band suffers from saturation over stronger FRP fires, and Schroeder et al. (2014) indicate that complete folding of the digital count (DC) can sometimes occur with recording starting again from a digital count equivalent to 208 K. However, this is far less common than simple saturation is, particularly so over the type of small agricultural fires focused on here. Our algorithm implements the same tests as Schroeder et al. (2014) to identify saturated I4-band pixels:

$$BT_4 = 367 \text{ K AND QF4} = 9 \text{ [both day and night]} \quad (11)$$

AND

$$BT_5 > 290 \text{ K AND QF5} = 0 \text{[daytime] AND } \rho_1 + \rho_2 > 0.7 \text{ [daytime]} \quad (12)$$

Whilst instances of DC "folding" are identified by:

$$\{\Delta BT_{45} < 0 \text{ [both day and night]} \quad (13)$$

AND

$$(BT_5 > 325 \text{ K AND QF5} = 0 \text{ [daytime] OR} \quad (14)$$

$$BT_5 > 310 \text{ K AND QF5} = 0 \text{ [night−time]})\} \quad (15)$$

OR

$$\{BT_4 = 208 \text{ K AND } BT_5 > 335 \text{ K}\} \quad (16)$$

The saturated pixels are excluded from the later contextual analysis tests, but join other confirmed thermal anomaly pixels for step (v) - 'Daytime False Alarm Filter'.

To exclude potential fire affected pixels from inclusion in the background information used in subsequent stages, the pixels most likely to contain fires are identified by:

$$BT_4 > 325 \text{ K AND } \Delta BT_{45} > 20 \text{ K [daytime]} \quad (17)$$

$$BT_4 > 295 \text{ K AND } \Delta BT_{45} > 5 \text{ K [night−time]} \quad (18)$$

ii) Imagery partitioning

This stage excludes 'bowtie deleted' pixels (i.e. the stripes seen in Fig. 1a) from inclusion in the later contextual analysis background windows, ensuring that enough pixels always exist to calculate the background-window statistics no matter where the candidate potential AF pixel lies within the swath. Each granule is partitioned into six sections (the three different aggregation zones either side of nadir shown in Fig. 1a), and in the outermost two sections either side of nadir, 'bowtie deleted' pixels are removed and six new sub-granules constructed. The dimensions of the 'No aggregation Zone' and 'Aggregation Zone 2' are thus changed from 1280 × 1536 and 736 × 1536 pixels to 1280 × 1152 and, 736 × 1344 pixels respectively via this process.

iii) Candidate thermal anomaly pixel (CATAP) identification

This stage selects the candidate pixels to go through the computationally demanding contextual analysis stage. Whilst the low thresholds set in the early algorithm tests enable the maximum number of potential pixels to be included in this set, to avoid unnecessary computational time it is also desirable to remove those extremely unlikely to contain fires. This trade-off is conducted using a combination of spectral and spatial filtering of each sub-image.

To enable maximum sensitivity to low FRP fires, the spectral filter thresholds are based on statistics calculated from blocks of 50 × 50 pixels within each sub-granule (Wooster et al., 2012). The mix of dynamically-adjusted tests, along with fixed thresholding, has also been used in the SLSTR, VIIRS and MODIS Collection 6 AF detection algorithms

(Wooster et al., 2012; Giglio et al., 2016; Schroeder et al., 2014). Within each block (b), the mean brightness temperature of BT_4 and the difference of BT_4 and BT_5 brightness temperature signals ($\overline{BT}_{4b}$ and $\Delta\overline{BT}_{45b}$) are used, and each pixel tested against these to identify it as a candidate thermal anomaly pixel CATAP. For blocks with ≤1% clear land pixels, the fixed threshold of Schroeder et al. (2014) was used but lowered to enable the detection of lower FRP active fires:

$$(BT4>\overline{BT}_{4b}\ \text{OR}\ 320\ \text{K})\ \text{AND}\ (\Delta BT45>\Delta\overline{BT}_{45b}\ \text{OR}\ 10\ \text{K})\ [\text{daytime}] \quad (19)$$

OR

$$(BT4>\overline{BT}_{4b}\ \text{OR}\ 290\ \text{K})\ \text{AND}\ (\Delta BT45>\Delta\overline{BT}_{45b}\ \text{OR}\ 5\ \text{K})\ [\text{night-time}] \quad (20)$$

Roberts and Wooster (2008) introduced use of a spatial high pass (HP) filter to reduce numbers of candidate thermal anomaly pixels unnecessarily selected from larger areas of solar-heated bare ground or other warmed surfaces, reducing computational cost and false alarms. We use a kernel filters (δ_{filter}), growing from size 3 × 3 to 25 × 25 pixels, and locations with filter output exceeding (P) from any kernel filter is retrained.

$$P = HP_{filter} \geq DT \times \delta_{filter} \quad (21)$$

where DT is a function of the solar zenith angle (θ_s):

$$DT = 2.5 - 0.012 \times \theta_s \quad (22)$$

As with the FTA algorithm of Wooster et al. (2015), pixels passing both the spectral and spatial contextual filters are included in the final candidate thermal anomaly pixel set.

iv) Contextual analysis

The contextual analysis stage tests each candidate thermal anomaly pixel against its own background pixel set, in order to confirm whether its signal is sufficiently elevated for it to be considered a confirmed thermal anomaly pixel (COTAP). Background windows sizes extend from 11 × 11 pixels up to a maximum of 31 × 31, until at least 25% of them are considered valid for inclusion and are not themselves cloud covered, water bodies, potential fire pixels or bad quality data. The mean BT of I4 ($\overline{BT}_{4w}$) and I5 ($\overline{BT}_{5w}$), the mean BT difference ($\Delta\overline{BT}_{45w}$) and corresponding standard deviations ($\delta_{4w}, \delta_{5w}, \delta_{45w}$) are then calculated for the selected background window. The absolute I4 and I5 spectral threshold test of Schroeder et al. (2014) have been removed in our regional algorithm, in order to avoid excluding the smallest (lowest FRP) active fires.

Using its background window statistics, a CATAP is confirmed as a COTAP when it meets the criteria below:

Daytime:

$$\Delta BT_{45} > \Delta\overline{BT}_{45w} + 2^{*}\delta_{45w} \quad (23)$$

$$BT_4 > \overline{BT}_{4w} + 3.5^{*}\delta_{4w} \quad (24)$$

$$BT_5 > \overline{BT}_{5w} + \delta_{5w} - 4\ \text{OR}\ \delta'_4 > 5 \quad (25)$$

where δ'_4 refers to the standard deviation of I4 BT of potential fire affected pixels within background window identified using function (17)–(18).

The daytime complementary contextual test from Schroeder et al. (2014), designed to avoid false alarms at desert boundaries is also applied:

$$\rho 2 > 0.15\ \text{AND}\ \overline{BT'_4} < 345\ \text{AND}\ \delta'_4 < 3\ \text{AND}\ BT_4 > \overline{BT'_4} + 6 \times \delta'_4\ [\text{daytime}] \quad (26)$$

where $\overline{BT'_4}$ refers to the average temperature of potential background fires.

A first sun glint rejection test (taken from Roberts and Wooster, 2008), is used to remove any sun-glint induced false alarms, where L4 and L1 refer to the spectral radiance of I-Bands 4 and 1.

$$L4/L1 < 0.018\ \text{for cloud pixels exist within nearby 15 pixels}\ (31 \times 31\ \text{windows}), \quad (27)$$

OR

$$L4/L1 < 0.01\ \text{for cloud pixels not exist within}\ 31 \times 31\ \text{windows}. \quad (28)$$

For the night-time pixels, the criteria for a COTAP changes to:

$$\Delta BT_{45} > \Delta\overline{BT}_{45w} + 3 \times \delta_{45w} \quad (29)$$

$$BT_4 > \overline{BT}_{4w} + 3 \times \delta_{4w} \quad (30)$$

The CATAPs passing all the contextual tests outlined above are set as COTAPs, and passed to the next stage.

v) Daytime false alarm filter

It is possible that the COTAP set contains sunglint-related false alarms, so pixels satisfying the following condition are removed (Schroeder et al., 2014):

$$\theta_g < 15^{\circ}\ \text{AND}\ \rho_1 + \rho_2 > 0.35 \quad (31)$$

OR

$$\theta_g < 25^{\circ}\ \text{AND}\ \rho_1 + \rho_2 > 0.4 \quad (32)$$

where θ_g is the 'glint angle' calculated from:

$$\cos\theta_g = \cos\theta_v \cos\theta_s - \sin\theta_v \sin\theta_s \cos\Phi \quad (33)$$

where θ_g and θ_s are the view zenith and solar zenith angles respectively, and ϕ is the relative azimuth angle (Giglio et al., 2003).

4.3. Cloud mask performance

An appropriate cloud mask is critical for accurate active fire detection (Giglio et al., 2003). As shown in Fig. 1b, our adaptation of Piper and Bahr (2015) successfully identifies pixels with clear cloud-contamination, including over land on the right hand scene edge and over the ocean on the left. Our approach also avoids masking smoke-contaminated pixels in the middle of the land (Fig. 1b–c), where quite a few candidate AF pixels are detected that are most likely real as they accompany large burned areas (Fig. 1c). Fig. 1 also shows that our daytime water mask successfully identifies water bodies, but does not incorrectly mask burned area as water – which was a potential problem identified by Schroeder et al. (2014).

5. Active fire detection output and evaluation

Fig. 4 presents example output from our final, regionally optimised, 'small' active fire detection algorithm (notice these are COTAPs which pass the daytime false alarm filter). In this case, our algorithm identifies almost all (96%) of the AF pixels identified by the global I-Band algorithm of Schroeder et al. (2014), but also a further set of additional detections (15% more). Some clear smoke plumes are associated with the AF pixels detected by both algorithms, but in the imagery alone it is difficult to confidently identify whether our additional detections represent actual active fire locations or not. We therefore employed field validation to gain further understanding and confidence in the AF detection results.

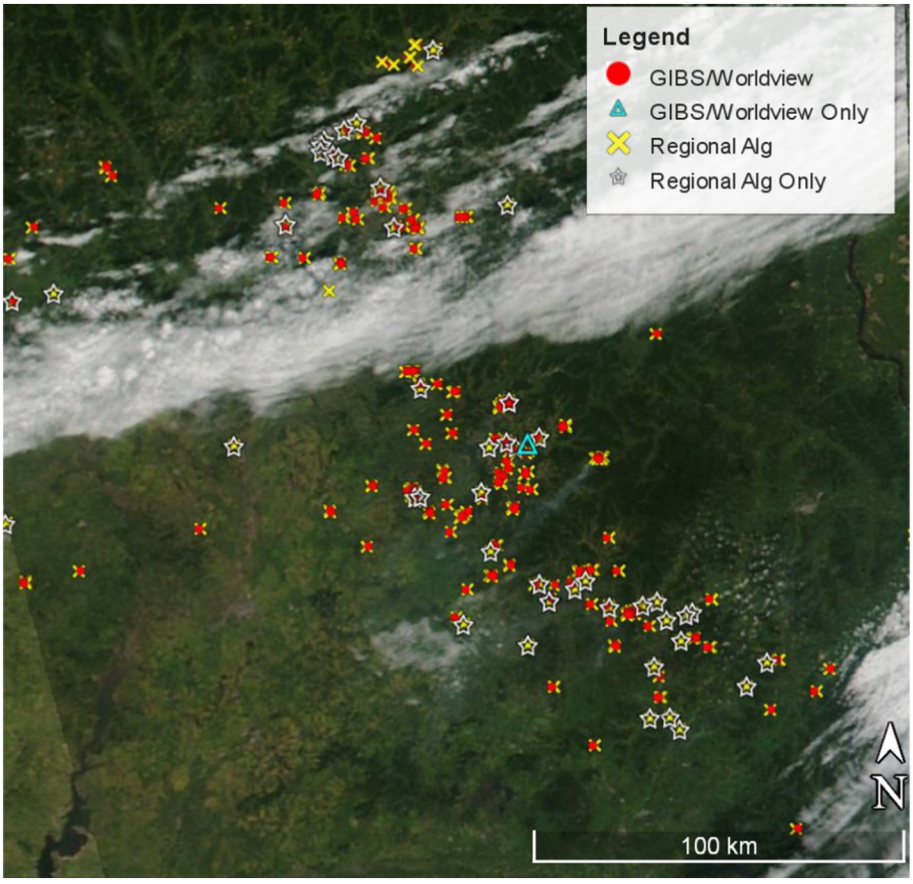

Fig. 4. Active fire pixel detections made on 28 August 2016 from VIIRS, with the scene centre 48.99°N, 126.89°E and a VIIRS true colour composite is used as the basemap. Yellow crosses indicate those AF pixels generated using the regionally optimised VIIRS I-Band AF detection algorithm developed herein, whilst red circles are those output from the global I-Band algorithm of Schroeder et al. (2014) (available from the GIBS/Worldview database). White stars indicate which AF pixel detections were identified only by our regionally optimised I-Band algorithm, and not by the Schroeder et al. (2014) global algorithm. Light blue triangles indicated AF pixels only detected by the global algorithm of Schroeder et al. (2014). (For interpretation of the references to colour in this figure legend, the reader is referred to the web version of this article.)

5.1. Field validation

Field validation (October 2015) involved deploying a small UAV within a few days of a VIIRS confirmed thermal anomaly pixel (COTAP) detection, in order to check for evidence of burning. Thirty COTAPs were examined in total in the Northern China Plain, and for each one recent char and ash were identified clearly in the UAV imagery. Fig. 5 shows one example, where Google Earth Imagery of an agricultural area (34.73° N 114.67° E) taken on 1st October 2015 is shown (Fig. 5a), along with the same scene but with orthomosaiced and geolocated UAV imagery collected six days later overlain (Fig. 5b). Red circles denote the VIIRS I-Band pixel centres which our AF detection algorithm identified as containing fires burning on 5th Oct 2015, and which match recently burned locations in the UAV imagery. Fig. 5d shows more detail, with three different burning patterns seen in the UAV imagery. The large fields on the left show a rather homogeneous covering of black ash and char, indicating a fire that traversed the whole field to burn away crop residues and roots left in the ground (wheat stubble left after harvest is often burned like this). Other fields show a sometimes semi-linear pattern of ash and char, indicating areas where farmers likely gathered up crop residues and burned them in long piles. The rightmost field shows more scattered areas of ash and char, interspersed with apparently unburned areas, indicating perhaps that the farmers had only burned crop roots here. The very patchy and generally quite small nature of the fire-affected areas highlights the great difficulty in mapping burned areas in such agricultural regions, particularly when using relatively coarse spatial resolution imagery of the type provided by MODIS, as pointed out by Randerson et al. (2012).

5.2. False alarm filtering

Schroeder et al. (2014) reported that in eastern China, the global VIIRS I-Band 'small fire' AF detection algorithm shows a high rate of low confidence daytime AF pixels (~40%). This is among the highest proportion seen worldwide, and analysis has shown that many of these low confidence AF pixel detections are in fact false alarms associated with large industrial buildings, having highly reflective and/or warm rooftops and surrounded by more rural landscapes (Fig. 6). Hence, for our regionally optimised algorithm we developed landcover- and hotspot persistence-based spatial filters to identify and remove such occurrences from our algorithm output.

Our landcover-based filter was derived from a combination of 30 m spatial resolution GlobeLand30 global landcover mapping (having an 80% classification accuracy and is derived from 2009 to 2011 Landsat and Chinese land monitoring satellite imagery (http://glc30.tianditu.com/; Chen et al., 2015) and OpenStreetMap (http://www.openstreetmap.org/) data derived from manual surveys, GPS devices, aerial photography, and other free data sources, with layers that include 'places', 'buildings', 'landuse' and 'roads' used here to identify urban areas. We combined GlobeLand30 and OpenStreetMap to generate a binary landcover mask for eastern China at a 0.005° spatial resolution, approximating that of the VIIRS I-Band (Fig. 7a). Cells having a GlobeLand30 crop landcover class cover of ≤40%, or in which any of the four OpenStreetMap 'urban' layers were tagged as 'true', were used to create a spatial mask within which no classified AF pixel detection was allowed to occur. In addition, we also masked as false alarms the thermal anomaly pixels persistently (and unrealistically) detected

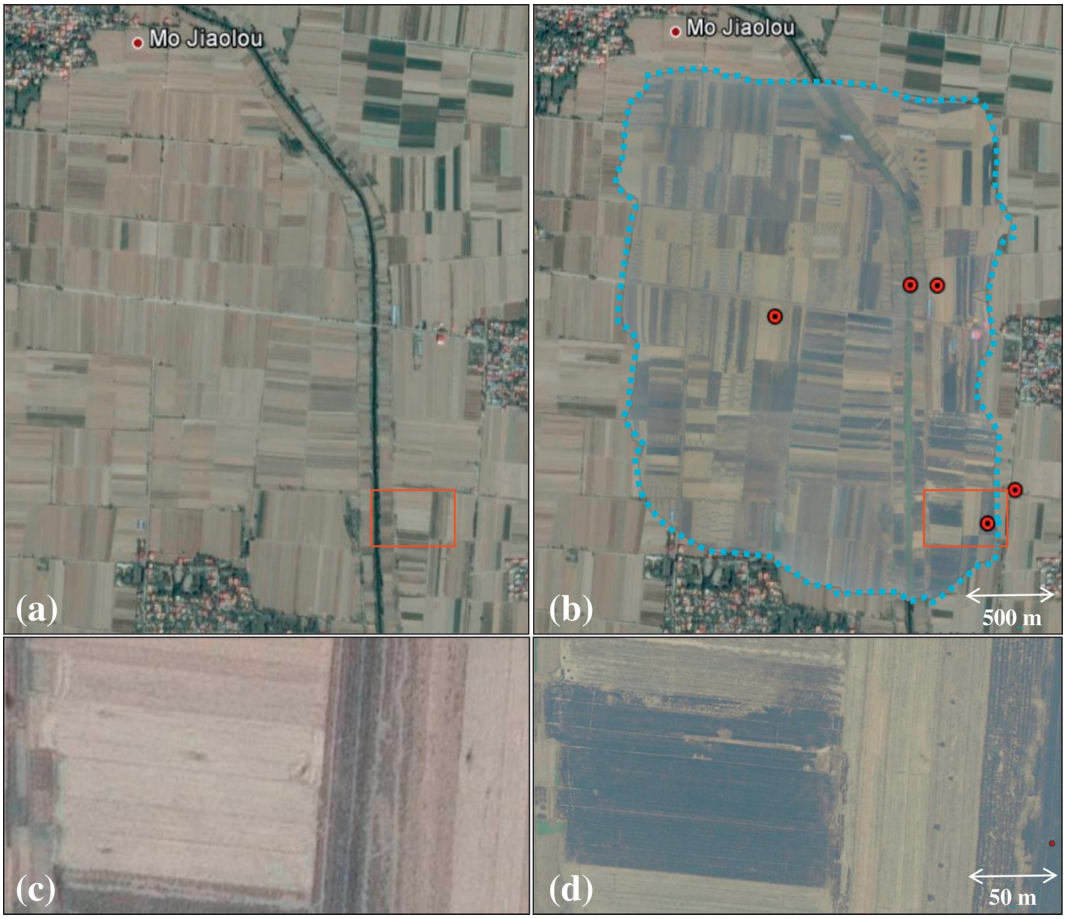

Fig. 5. Validation example taken in Eastern China (34.73° N, 114.67° E). (a) Google Earth imagery dated 1 Oct 2015, with base imagery supplied by CNES/Astrium. (b) mosaiced and geocorrected imagery from our UAV flight (outlined by blue dashed curve) conducted over the area shown in (a) on 7 Oct 2015, one week later than the Google Earth imagery, and with red circles superimposed to show the pixel centres of VIIRS I-Band pixels which our regionally optimised VIIRS I-Band AF detection algorithm detected COTAPs on the afternoon of 5 October 2015. (c) Magnification of the pre-burn area highlighted in (a). (d) Magnification of the post-burn area highlighted in (b), which is the location of a COTAP seen in (a). (For interpretation of the references to colour in this figure legend, the reader is referred to the web version of this article.)

as multiple times in the same locations, and found these again were mostly related to the type of industrial buildings shown in Fig. 6. For this we used a 0.001° spatial resolution mask based on locations where I-Band AF detections were made outside of the burning season four or more times in a single year (Fig. 7b). Fig. 7c illustrates this temporal masks spatial detail for a mixed landuse area, where the mask seems to match up quite well to either urban areas/water bodies (which are assumed to be the sites of repeated false alarms). COTAPs that pass both the spatial and temporal filters are finally classed as AF pixels, and are those used for further analysis and discussion in this study.

Fig. 8 shows an example where confirmed thermal anomaly pixels (COTAPs) identified as 'false alarms' using the masks of Fig.7 are shown in red, and these classified as AF pixels (i.e. that lie outside the masked areas) are in yellow. Classified in this way are both the output from our regional VIIRS I-Band algorithm (smaller polygons reflecting the size of the I-Band pixels), and those generated on the same day and at almost the same time from the MODIS Collection 6 MYD14 product (Giglio et al., 2016). Towards the bottom left of the scene, two clusters of thermal anomaly pixels are detected by both VIIRS and MODIS (along with several more spatially isolated pixels detected only by VIIRS) and each are classified as AF pixels since they are in an agriculturally-dominated area, not one identified as being the location of repeated false alarm detections based on our masking scheme. To the right of the scene centre there are three thermal anomaly pixels initially detected by VIIRS, but classified as confirmed false alarms via our masking and thus not included in the final output AF pixel set. These are all associated with more urbanised landcovers, and whilst not in urban centres they are located at the edges and/or in the suburbs and contain buildings similar to those of Fig. 6. Our procedures correctly remove such thermal anomaly pixels from the final active fire pixel set.

5.3. Comparison to MODIS Aqua active fire detections

Our VIIRS to MODIS AF comparisons were expanded to cover a larger area of eastern China (Fig. 9; 12th June 2015). Here we show the VIIRS I-Band AF detections superimposed on the coarser spatial resolution M-Band imagery. Classified AF pixel locations are indicated by crosses, coloured by FRP (discussed later in Section 6.3). Our VIIRS scheme detects 76 classified AF I-Band pixels, matching to 55 larger M-Band pixels. Far fewer AF pixels (19 in total) are detected by MODIS, and whilst a single MODIS AF pixel may cover multiple I-Band AF pixels, it seems very unlikely that this is the sole cause of the far greater number of VIIRS I-Band AF pixels detections. Rather, the ~10× smaller I-Band pixel area is enabling our algorithm to detect the lower FRP fire pixels that often remain undetected by MODIS, such as in those circled in Fig. 9a.

For the study region of Figs. 2, 10 shows the full 1st June 2014 to 30st June 2015 time-series of classified AF pixel counts made from the VIIRS I-Band (top), along with the AF pixels recorded by MODIS-Aqua (bottom) (day and night-time overpasses). Three burning seasons are covered (June 2014, October 2014 and June 2015), with daytime maxima of ~4000, ~ 2000 and ~3000 AF pixel counts respectively from our VIIRS I-Band scheme and ~700, ~ 500 and ~400 from MODIS. Night-time data show a clear AF peak only in the June burning seasons, with

Fig. 6. Google Earth imagery (33.873° N, 118.294°E) showing the footprints of five false alarm pixels recognized by our I-Band active fire detection algorithm from VIIRS SDR 20140605_t0458444_e0504248 (red polygons with yellow push pins at centre) over large industrial buildings surrounded by a mixture of agricultural lands and rural residential areas. Our false alarm masking approach successfully removes such false detections. (For interpretation of the references to colour in this figure legend, the reader is referred to the web version of this article.)

maxima of ~5000 and ~2000 I-Band AF counts, but only ~140 and ~30 MODIS AF counts. Night-time VIIRS I-Band data of October do still show ~500 AF pixel counts per day, whilst MODIS shows almost none. Overall, our VIIRS I-Band scheme often identifies 5× to 10× more daily AF pixel counts than does MODIS.

6. Fire radiative power (FRP) assessment from VIIRS

Beyond AF pixel detection, fire emissions calculations generally require quantification of the fires radiative power (FRP) output (Wooster et al., 2003, 2005). To minimise impacts from VIIRS I-Band pre-aggregation detector saturation discussed in Section 2.2, we developed an FRP-retrieval scheme to estimate FRP synergistically using both the I-Band and M-Band data.

6.1. FRP estimation

FRP is calculated using the MIR radiance method of Wooster et al. (2003, 2005):

$$FRP = \frac{A}{10^6 \cdot \tau_{MIR}} \frac{\sigma}{a} \left(L_f - \overline{L_b}\right) [MW] \quad (34)$$

where A is the pixel size in m^2, σ is the Stefan–Boltzmann constant (5.67×10^{-8} W m^{-2} K^{-4}), L_f is the VIIRS I4 spectral radiance of the fire pixel (W m^{-2} sr^{-1} μm^{-1}) and $\overline{L_b}$ is the mean background radiance (of the background window), a (3.2146×10^{-9} W m^{-2} sr^{-1} μm^{-1} K^{-4}) is the FRP constant taken from the power-law linking I4 band spectral radiance to the 4th power of emitter temperature (determined using the approach in Wooster et al., 2005), and τ_{MIR} is the VIIRS I4 band atmospheric transmission calculated using the MODTRAN-5 radiative transfer code, standard atmospheric trace gas profiles, and space/time-variable ECMWF total column water vapour and temperature values (http://apps.ecmwf.int/datasets/) as in Wooster et al. (2015).

FRP is estimated for every classified I-Band AF pixel, but because the VIIRS pixel aggregation scheme detailed in Section 2.2 may result in ambiguous I-Band saturation effects, it was also estimated using the M13-Band signal at M-Band pixels within which an I-Band AF detection was made. Due to the 4× larger M-Band pixel area, and greatly increased dynamic range of this channel, only a very few M13 pixel are found to be affected by saturation over active fires (Polivka et al., 2015), and we found none in our study area where the fires are generally relatively small and of low intensity, albeit some can certainly saturate the I4 band.

For the M-band FRP calculation, L_f in Eq. (34) simply uses the M13 spectral radiance, and L_b then becomes that of the M13 band background window, which was allowed to grow from a minimum of 5 × 5 up to 17 × 17 pixels until at least 8 pixels or 1/4 of the window pixels were considered valid for inclusion in the background window set (assessed with a valid M-Band pixel being one where all four constituent I-Band pixels were considered valid via their I-Band classification). The FRP constant a (2.8667×10^{-9} W m^{-2} sr^{-1} μm^{-1} K^{-4}) was calculated as 10.6% lower for M13 than for I4, whilst τ_{MIR} was typically 15% lower for M13 compared to I4 for the same atmospheric profile.

Per-pixel FRP uncertainty (σ_{FRP}; MW) was calculated using standard error propagation as in Wooster et al. (2015):

$$\sigma_{FRP} = FRP \left[\left(\frac{\propto_a}{a}\right)^2 + \left(\frac{\propto_{\tau_{MIR}}}{\tau_{MIR}}\right)^2 + \left(\frac{\propto_{L_b}}{L_f - L_b}\right)^2 + \left(\frac{\propto_{L_f}}{L_f - L_b}\right)^2 \right]^{1/2} \quad (35)$$

This combines the absolute uncertainties ($\propto_a$, $\propto_{\tau_{MIR}}$, $\propto_{L_f}$ and $\propto_{L_b}$) present in the values of the four terms (a, τ_{MIR}, L_f and L_b) of Eq. (35). ($\propto_a/a$) is

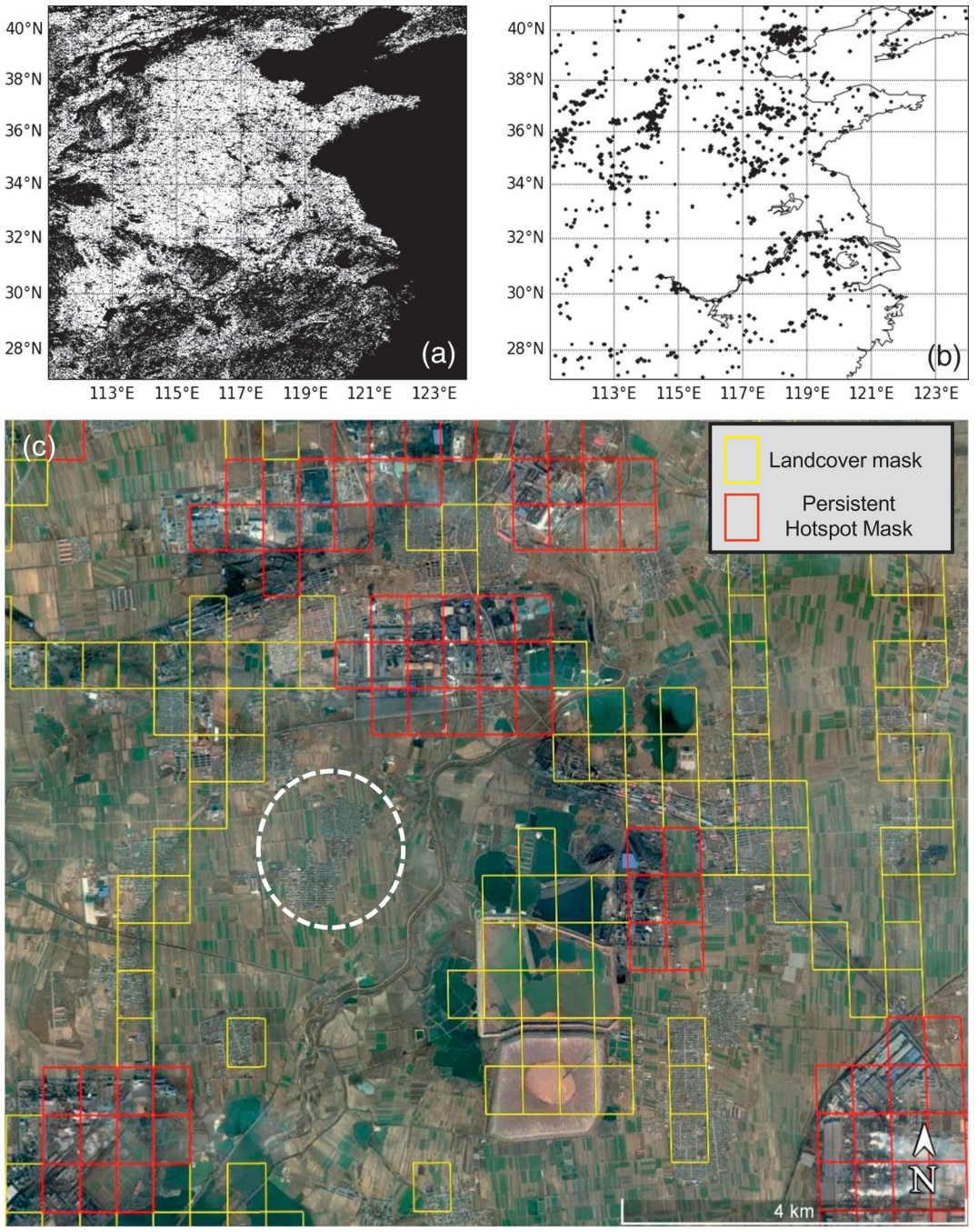

Fig. 7. False alarm mask derived from (a) a binary landcover mask (black pixels) created for eastern China at 0.005° resolution using the GlobeLand30 and OpenStreetMap datasets discussed in the main text, and (b) a map of persistent confirmed thermal anomaly pixel (COTAP) detections, where black pixels indicate locations having four or more COTAP detections in the July 2014 to Sept 2014 and Nov 2014 to May 2015 periods (i.e. outside of the June and October burning seasons), caused by undetected sunglints and industrial heat sources. (c) Google Earth background image (39.588° N, 118.420° E) with locations of mask pixels from (a) and (b) overlain in yellow and red respectively. The white circle outlines an area of urban landuse not included in the current mask, indicating that imperfections still exist in the landcover data and thus that higher quality ancillary data will benefit the algorithm in future. (For interpretation of the references to colour in this figure legend, the reader is referred to the web version of this article.)

equivalent to a 10% uncertainty across the fire temperature range of 650–1350 K (Wooster et al., 2015). $\propto_{\tau_{MIR}}$ contains contributions from both the uncertainty on the actual total atmospheric vertical composition (apart from water vapour), and the water vapour concentration itself (Wooster et al., 2015) (full equations are listed in Appendix A; Eqs. (A1)–(A4)). The absolute uncertainty in the background radiance ($\propto_{L_b}$) is set to the standard deviation of the background window signal in the MWIR band, and the absolute uncertainty in the fire pixel radiance ($\propto_{L_f}$) is set to the sensors radiometric noise in the MWIR channel (0.05 for the VIIRS I4 and 0.007 for M13; Oudrari et al., 2016).

6.2. Comparison of VIIRS and MODIS FRP frequency distributions

Fig. 11 shows the FRP frequency distribution for the study region (June 2014 to June 2015) as calculated from (a, b) the VIIRS I-Band classified AF pixel set, (c, d) the matching VIIRS M-Band data, and (e, f) the corresponding MODIS products (Giglio et al., 2016), which now also use

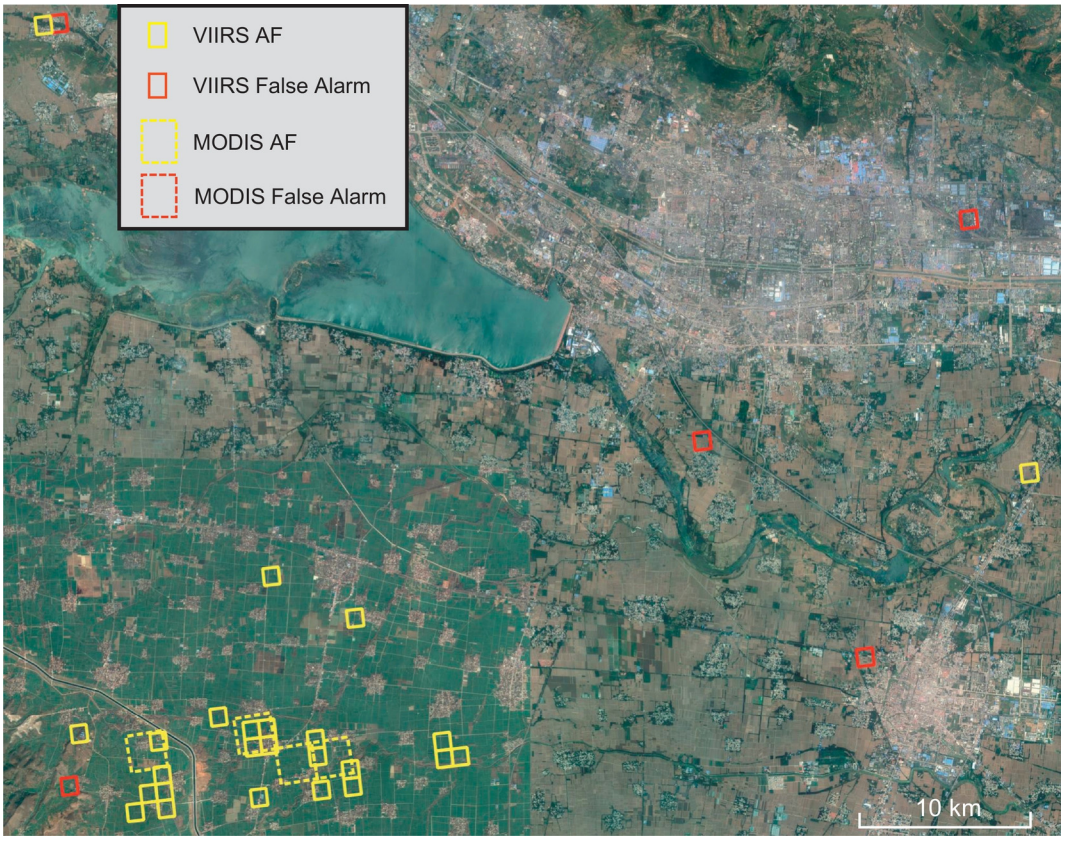

Fig. 8. Locations of confirmed thermal anomaly pixel detections made by our VIIRS I-Band scheme (small polygons) and by MODIS Collection 6 (large dashed polygons). Those classified as false alarms on the basis of the masks shown in Fig. 7 are coloured red, whereas those confirmed as AF pixels are yellow. VIIRS granule is from SDR 20150610_t0555514_e0601318, along with MODIS AF detections from granule A2015161.0545 and a background image from Google Earth. (For interpretation of the references to colour in this figure legend, the reader is referred to the web version of this article.)

Eq. (34) developed by Wooster et al. (2003, 2005) to generate their FRP estimates. We atmospherically corrected the MODIS FRP values using the same MODTRAN-5 based scheme as used with VIIRS.

Data of Fig. 11 approximate a log-normal distribution, being dominated by lower FRP AF pixels and with a long tail of higher FRP AF pixels. For MODIS, the mode (i.e. frequency histogram peak) of the daytime/night-time FRP distributions is 11.8 MW and 7.7 MW respectively, whilst those for VIIRS I-Band are 4.7 MW and 1.5 MW respectively, and for the M-Band 6.3 MW and 2.5 MW respectively. It is important to state that from the M-Band data alone it would often not be generally possible to conclusively detect an AF pixel with an FRP of 2 or 3 MW, as it would raise the 750 m pixels MWIR brightness temperature by only a few Kelvin above background. However, here we are using the I-Band 375 m AF detections to identify the M-Band pixels within which there are actively burning fires, and only using the M-Band data to calculate their FRP and its uncertainty.

Fig. 11 clearly highlights our regional algorithms sensitivity to low FRP fires. However, the VIIRS I-Band observations produce almost no FRP exceeding 30 MW, whereas those from MODIS often extend to around 50 MW and have a highest single-pixel FRP of 1008 MW. These differences result from the VIIRS I-Band pre-aggregation saturation at the higher FRP AF pixels (Section 2.2; and Schroeder et al., 2014), but fortunately the VIIRS M-Band FRP retrievals are unaffected by such saturation and thus extend to the correct FRP maxima.

6.3. Scan angle impacts

In addition to MODIS' difficulty in detecting low FRP AF pixels (<6 to 8 MW) due to its 1 km^2 nadir pixel area (Fig. 11), Freeborn et al. (2011) also demonstrate that because MODIS' pixel areas are ~10× larger at the scan edge than at nadir, so roughly is the minimum FRP detection limit. VIIRS' pixel aggregation scheme (Section 2.2) results in pixel areas varying much less across the swath (Wolfe et al., 2013), which should make the FRP detection limit also more consistent. Fig. 12 confirms this, where for MODIS the minimum but also the maximum, mean and median FRP strongly increase away from nadir, but where the VIIRS I-Band and M-Band derived FRPs show much more uniformity.

Taking the three VIIRS I-Band aggregation zones in turn, a total of 38%, 24% and 38% of all detected AF pixels were found in these regions respectively; far more uniform than with MODIS - where 77% are located close to the swath centre (within ±32° scan angle) and only 10% at scan angles >45° (and the latter is actually an overestimate because of across-track AF pixel duplication caused by the bow-tie effect; Freeborn et al., 2011). Similar bow-tie effect impacts with VIIRS are absent due to the aforementioned SDR zero filling (Fig. 1a).

6.4. Direct VIIRS to MODIS FRP comparisons

As a last step, we directly compared VIIRS and MODIS FRP outputs with 10-min time difference or less, both on a fire pixel cluster basis (i.e. a group of 1 to 11 spatially adjacent MODIS AF pixels, and the matching VIIRS pixels covering the same geographic area), and on a 1° grid-cell basis. The former required manually matching up individual fires, so was applied to a single day only (10th June 2015), whilst the latter was applied across the entire 13-month study period. Given MODIS' FRP scan angle dependence (Fig. 12), we limited comparisons to a maximum MODIS scan angle of 32°, but no limit was placed on VIIRS since Fig. 12 shows no significant VIIRS scan-angle dependencies.

Fig. 13a shows the per-fire cluster comparison, where the VIIRS I-Band typically underestimates FRP compared to 'close-to-swath-centre' MODIS (slope of linear best fit = 0.19) as a result of I4-Band saturation (Section 2.2). This is the same reason the VIIRS I-Band FRPs of Fig. 11 fail

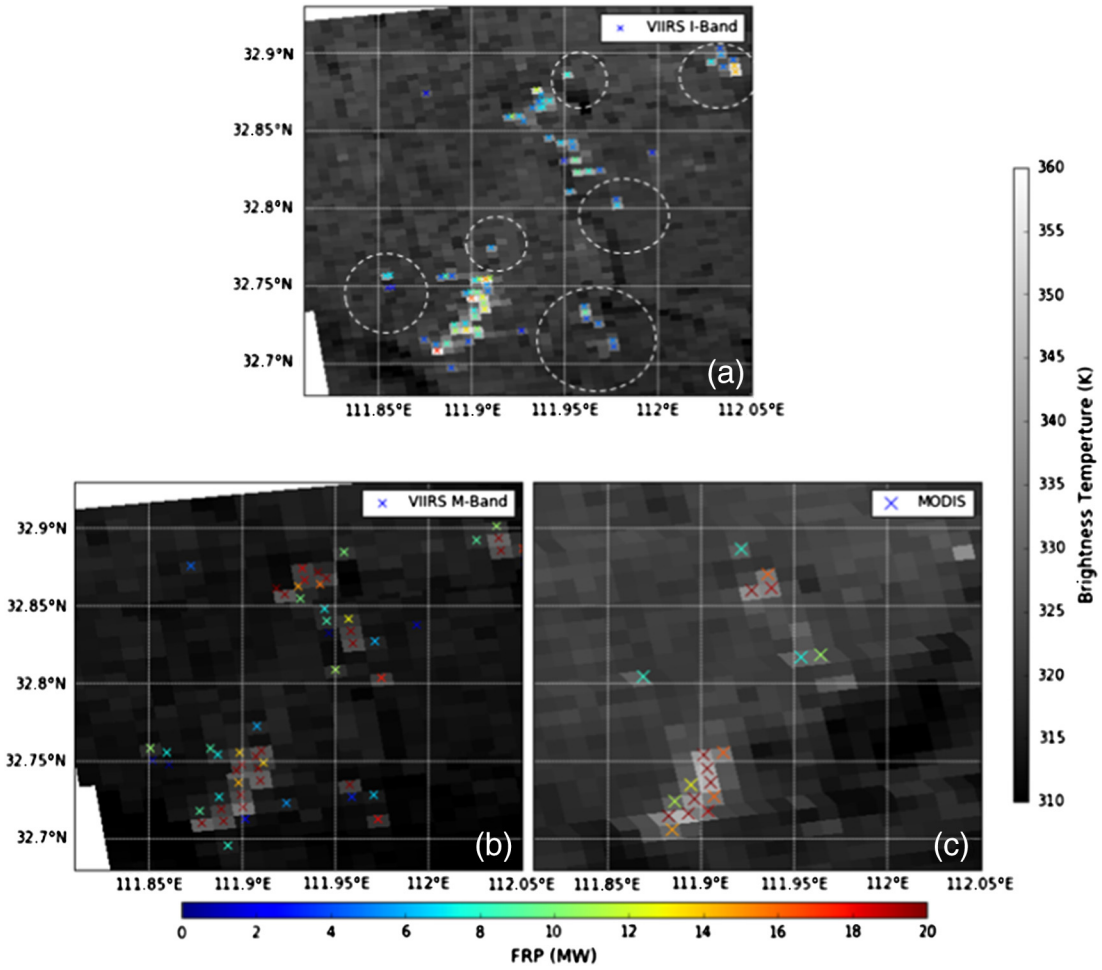

Fig. 9. Active fire (AF) detections made near simultaneously over a 26 km × 26 km region of the study area of Fig. 2 based on different methods and data. Highlighted by the '×' symbols are (a) the VIIRS I-Band AF pixel detections based on the scheme developed herein, superimposed on the source I4-Band MWIR imagery; (b) the VIIRS M-Band pixels containing I-Band detected AF pixels, superimposed on the M13-Band MWIR imagery; and (c) MODIS AF detections, based on the scheme of Giglio et al. (2016). The colour of the crosses depicts the FRP of the detected AF pixel, considered later in Section 6.3. Example active fire pixels detected by our VIIRS I-Band scheme but not by MODIS are circled in (a).

to exceed ~30 MW. VIIRS M-Band FRPs made at the site of the I-Band AF detections (Fig. 13b) show a far better agreement with those from these same MODIS data (slope of linear best fit = 1.01). Those slopes will increase to 0.55 (I-Band) and 1.21 (M-Band) when limiting the data input to those total cluster FRP under 300 MW, indicating the lower impact of I4-Band saturation for smaller fires, as highlighted in Fig. 13a–b.

Fig. 13d and e show, respectively, results of the 1° grid cell based comparisons of VIIRS I-Band FRP's and VIIRS M-Band FRPs (made at the site if the I-Band AF detections) compared to 'close-to-swath-centre' MODIS FRP's. FRP's from VIIRS I-Band and MODIS show a slope increase from 0.19 at the cluster level (Fig. 13a) to 0.64 at the grid-cell level (Fig. 13d). The I-Bands ability to detect many more AF pixels in a grid cell than does MODIS (even close to its swath centre) somewhat counteracts the impact of the I-Band saturation with regard to the grid cells total FRP. However, higher FRP AF pixels will be affected by I-Band saturation, and Fig. 13e shows that when the VIIRS M-Band FRPs measured at the location of the I-Band AF detections are used in place of the I-Band FRP measures themselves, the slope of the linear-best-fit with respect to MODIS increases dramatically (to 1.87). This indicates that nearly half of the study regions' FRP is being emitted by low FRP ("small") fires, undetectable by even 'relatively close-to-swath-centre' MODIS data (i.e. MODIS scan angle ≤32°), a fact also evidenced by the data of Fig.11. Extending the grid-cell comparison to the entire MODIS swath (not shown) increases the slope of the linear-best-fit between the VIIRS M-Band FRPs (assessed at the I-Band-detected AF pixel locations) and MODIS FRPs even more dramatically (to 3.11), because MODIS fails to detect a greater proportion of AF pixels towards the scan edge due to the greatly elevated minimum FRP detection limits away from nadir (shown in Fig. 12). By contrast, Fig. 12 shows that VIIRS AF pixel detection sensitivity is much more constant across the swath due to its unique pixel aggregation scheme.

6.5. Combining VIIRS I- and M-Band FRP measures to optimise FRP retrievals

Though VIIRS I-Band data is clearly extremely useful for detecting low FRP fires, the data of Fig. 13a and d demonstrate that higher FRP fires often saturate the I4-Band, leading to an underestimated FRP compared to simultaneously recorded M-Band data (see Section 2.2). Saturation affecting all pre-aggregation I4-Band measurements is identifiable from the VIIRS SDR Quality Flag data, but that affecting only some pre-aggregation pixels is more difficult to identify (see Appendix B). The VIIRS 750 m spatial resolution M13 data apparently does not suffer saturation effects in our agriculturally-dominated study region, unlike in other areas where much higher FRP fires are more common (e.g. Polivka et al., 2015), and so it can be used for unsaturated FRP retrievals at the location of I-Band detected active fire pixels (as in Figs. 9, 11, 12 and 13). However, where unsaturated I-Band data exist it is better to retrieve FRP from them, because (for the same sub-pixel sized fire) the AF pixel spectral radiance (L_f) is raised more above the background radiance (L_b) in the I-Band than the M-Band, making σ_{FRP} (Eq. (35)) generally much lower for the I-Band FRP than the M-Band FRP. The optimum strategy is thus to combine I-Band and

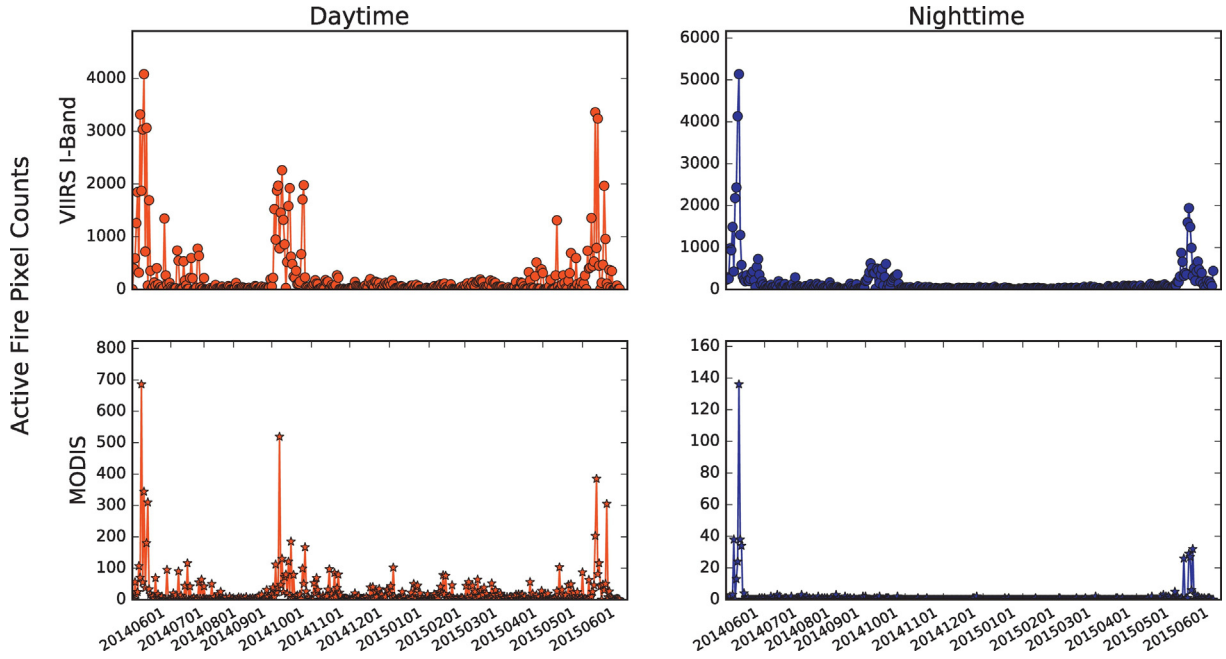

Fig. 10. Daily time-series of AF pixel counts made across the eastern China agricultural region (Fig. 2) between 1st June 2014 and 31st June 2015. Top row shows the daytime and nighttime AF pixel detections made using the VIIRS I-Band scheme developed herein, whereas the bottom row shows those from Aqua MODIS Collection 6 (MYD14). (For interpretation of the references to colour in this figure legend, the reader is referred to the web version of this article.)

M-Band FRP outputs, which we do here to produce a final 'VIIRS-IM' synergy FRP product that selects to record the following FRPs:

(i) For low FRP AF pixels (M-Band FRP ≤ 8 MW), where calculations indicate pre-aggregation I4-Band saturation is almost totally avoided, the algorithm selects whichever of the M-Band and combined I-Band FRPs show lowest FRP uncertainty (according to Eq. (35)). These lowest FRP retrievals, which can extend below 1 MW for the smallest detectable fires, are generally higher for the I-Band than the M-Band, suggesting the likely absence of I4 saturation. This rule selects the FRP output from the VIIRS I-Band data in >90% of cases examined.

(ii) For higher FRP AF pixels (M-Band FRP > 8 MW) whichever I-Band and M-Band FRP is larger is selected for inclusion, because pre-

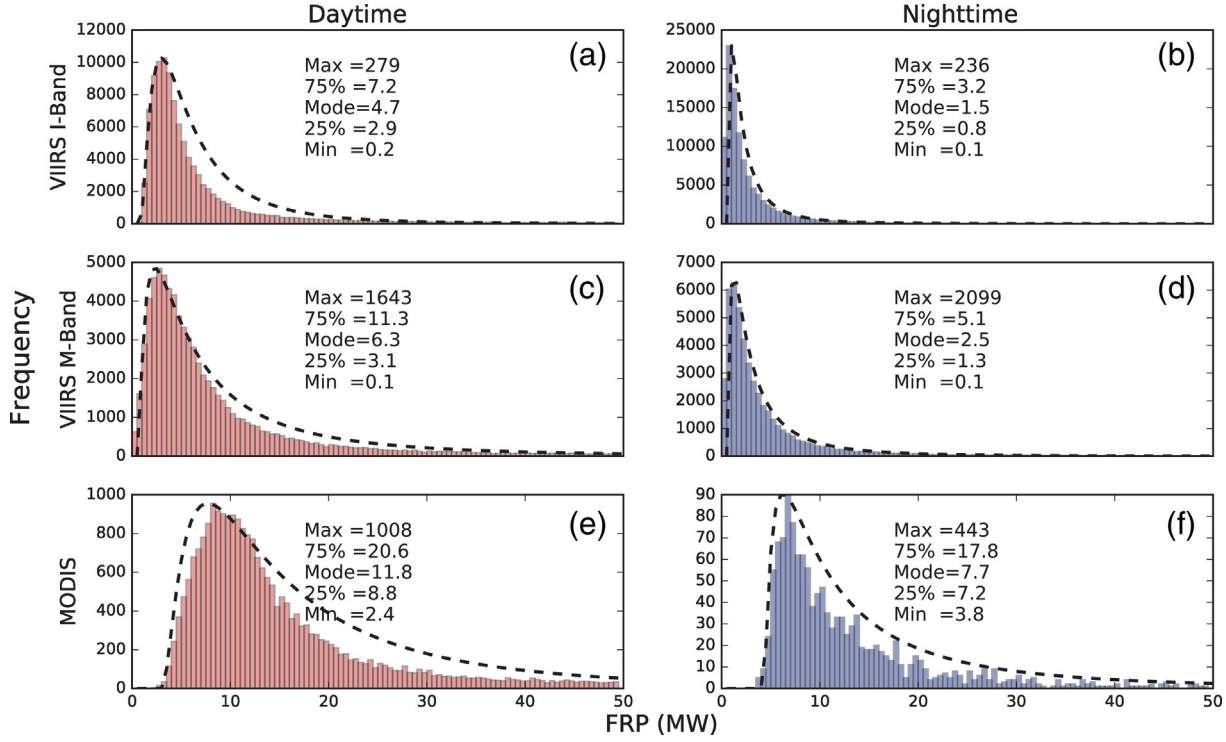

Fig. 11. Frequency distribution of the atmospherically corrected FRP of AF pixels detected over the study region using different data and methods (June 2014–June 2015). AF detections and FRP were derived (a) using the VIIRS I-Band scheme developed herein during the day, and (b) the same scheme but applied at night, (c) from the VIIRS M-Band data recorded at the locations of our I-Band active fire detections by day, and (d) by night, and (e) from MODIS C6 MYD14 by day and (f) by night. All data were atmospherically corrected using MODTRAN-5 as described in the main text, and the dashed lines show log-normal fits to the distribution. The maximum, 75% and 25% percentiles, mode, and minimum of each distribution are also shown.

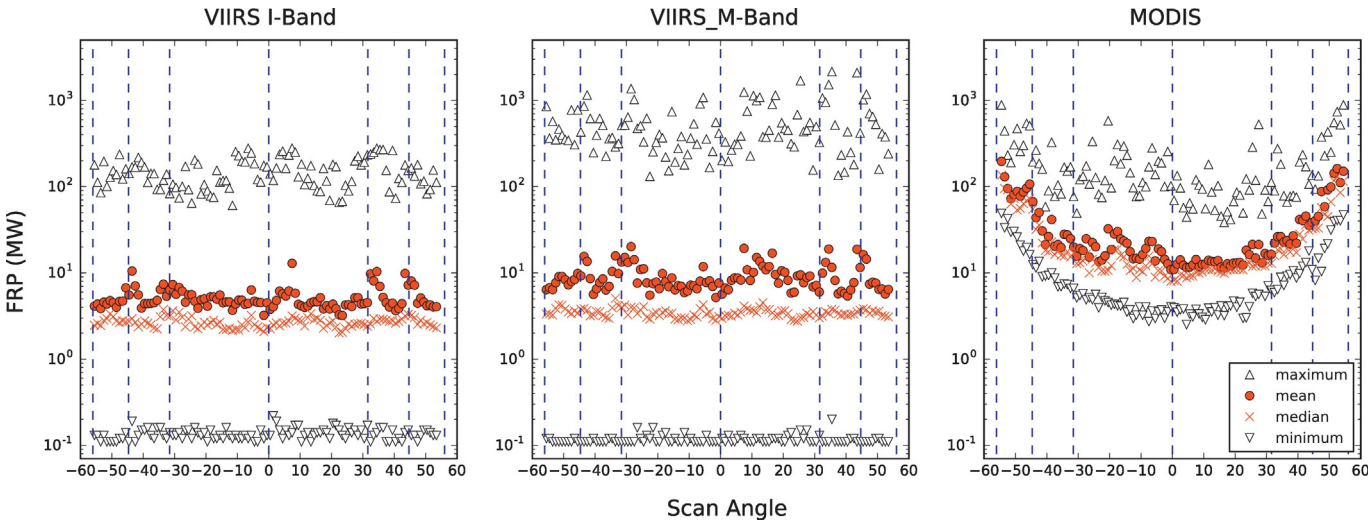

Fig. 12. Variation of maximum, mean, median and minimum per-pixel FRP with scan angle, for the VIIRS I-Band, VIIRS M-Band (calculated using the coincident M-Band radiance for I-Band AF pixels) and MODIS data recorded over our study region (1st June 2014 to 30th June 2015). The blue dashed vertical lines indicate the transition between aggregation zones in VIIRS, and we show them superimposed also on MODIS. The aggregation scheme used by VIIRS to minimise pixel area variations across the swath has very significantly reduced the along-scan variability of these FRP metrics with VIIRS compared to MODIS. (For interpretation of the references to colour in this figure legend, the reader is referred to the web version of this article.)

aggregation I4 saturation will artificially depress the FRP retrievals at certain higher FRP pixels. The clear majority of these AF pixels have their FRP retrieved via the M-Band.

Overall in the 'VIIRS-IM' synergy FRP product developed here, in the 13-month period sampled across the eastern China study area, I-Band-derived FRP contributes 95% of the total FRP in case (i) and M-Band-derived FRP contributes 75% of total FRP in case (ii). Furthermore, in case (ii), the I-Band retrieved FRP's were dominated by FRP's just above the 8 MW limit, because at FRPs much higher than this the I-Band pre-aggregation saturation almost always limits the retrieved FRP to be below the M-Band retrieved FRP.

Across the entire FRP range, the total FRP contributed by small fires (≤8 MW) accounts for around 16% of the total assessed FRP, whereas

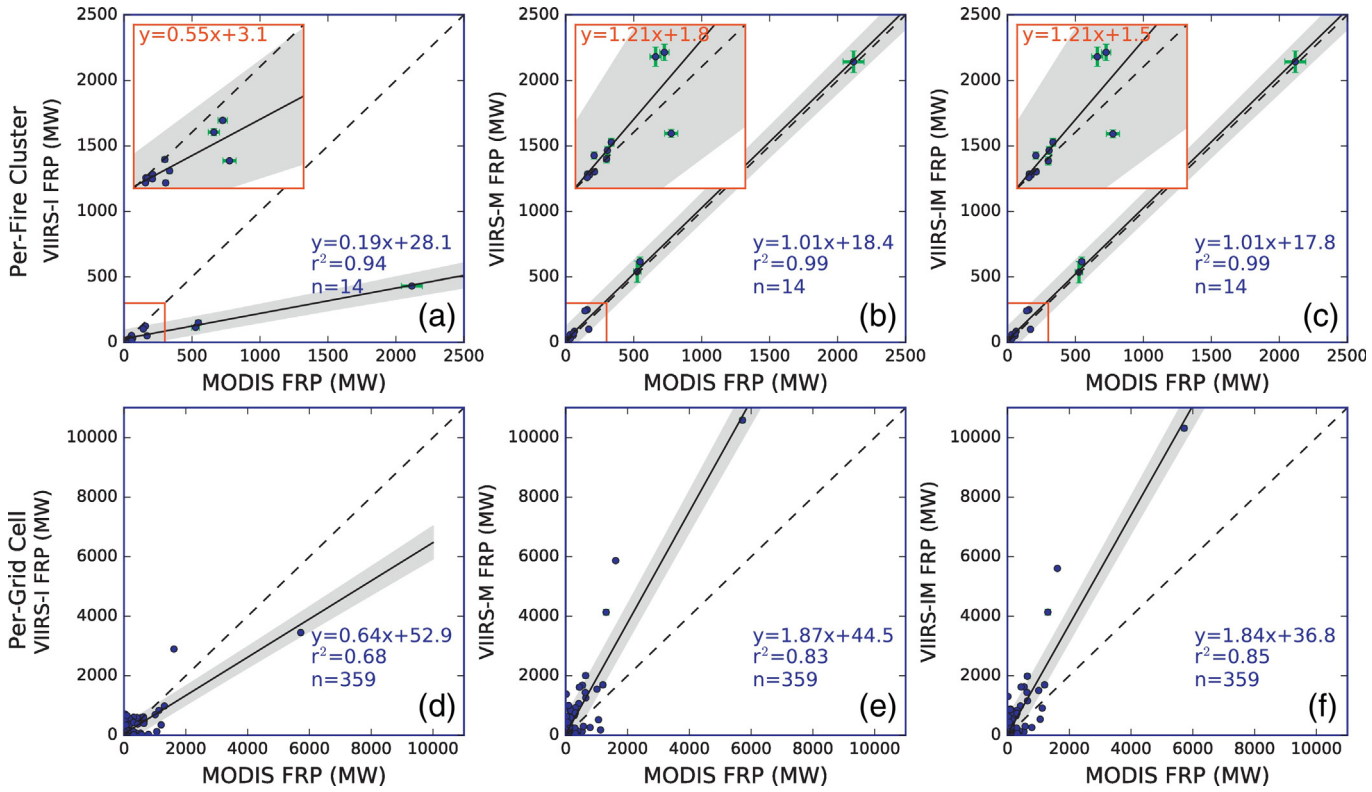

Fig. 13. Direct VIIRS-to-MODIS FRP intercomparisons, conducted using both VIIRS I-Band and M-Band FRP retrievals, and VIIRS-IM 'synergy' FRP product (Section 6.5) at both the scale of individual active fire clusters (a–c), and 1° degree grid cells (d–f). Error bars representing the FRP uncertainty calculated using Eq. (35) are shown in x and y, albeit they are small and difficult to see, especially in d-f. The best fit linear relationships are shown, along with its equation, and the grey shaded area represents the 95% confidence limit on the relationship. The red windows in panels a–c show the highlighted <300 MW data points of main plot with best fit linear relationships and their equations. (For interpretation of the references to colour in this figure legend, the reader is referred to the web version of this article.)

that from larger fires (>8 MW) accounts for the around 84%. As shown in Fig. 13c and f, the slopes of the linear best fits between the VIIRS-IM FRPs and 'close-to-swath centre' MODIS FRPs are similar to those derived with the VIIRS M-Band and MODIS data alone (Fig. 13b and e). Clearly higher FRP AF pixels detected by VIIRS are responsible for the majority of total FRP release, and many of these can in fact also be detected by MODIS when imaged relatively close to the MODIS swath-centre. However, as Fig. 12 indicates, away from the MODIS swath centre the minimum FRP detection limit of MODIS rises dramatically, whereas that for VIIRS does not, meaning that differences between simultaneous VIIRS and MODIS total FRP observations made at the grid cell level increase substantially when more edge-of-swath MODIS data are included in the comparison. Unfortunately for users of MODIS AF data, such edge-of-swath observations are required to be used if daily observations are required.

Fig. 14 compares the spatial pattern of our VIIRS-IM synergy FRP product with that of MODIS FRP data at 0.1° resolution, with all MODIS data now being included rather than just that from close to the swath centre. There is no obvious major difference in the broad spatial distribution, with a large fire-affected area seen bounded by 32–36° N and 114–118° E, and with mostly higher per grid cell FRPs during June than October. This agrees with past suggestions that the central provinces of Shandong, Jiangsu, Anhui and Henan (mainly in the North China Plain) are the source areas of most agricultural fire emissions (Huang et al., 2012; Qin and Xie, 2011; Streets et al., 2003). During June, the most fire-affected areas extend further west and north than in October, including to the west of Henan Province and south of Hebei Province. There are far fewer fires in the Yangtze Plain than in the North China plain, perhaps due to different landscape management practices and increased abilities for agricultural residues to be used in local industries (Liu et al., 2008). Within each grid cell, total FRP is generally higher when assessed using our VIIRS-IM synergy product than when using MODIS, due to VIIRS' greater ability to detect the (very numerous) low FRP fire pixels, and total FRP observed across the study region is larger than that of MODIS by 500% in June 2014, 600% in Oct 2014

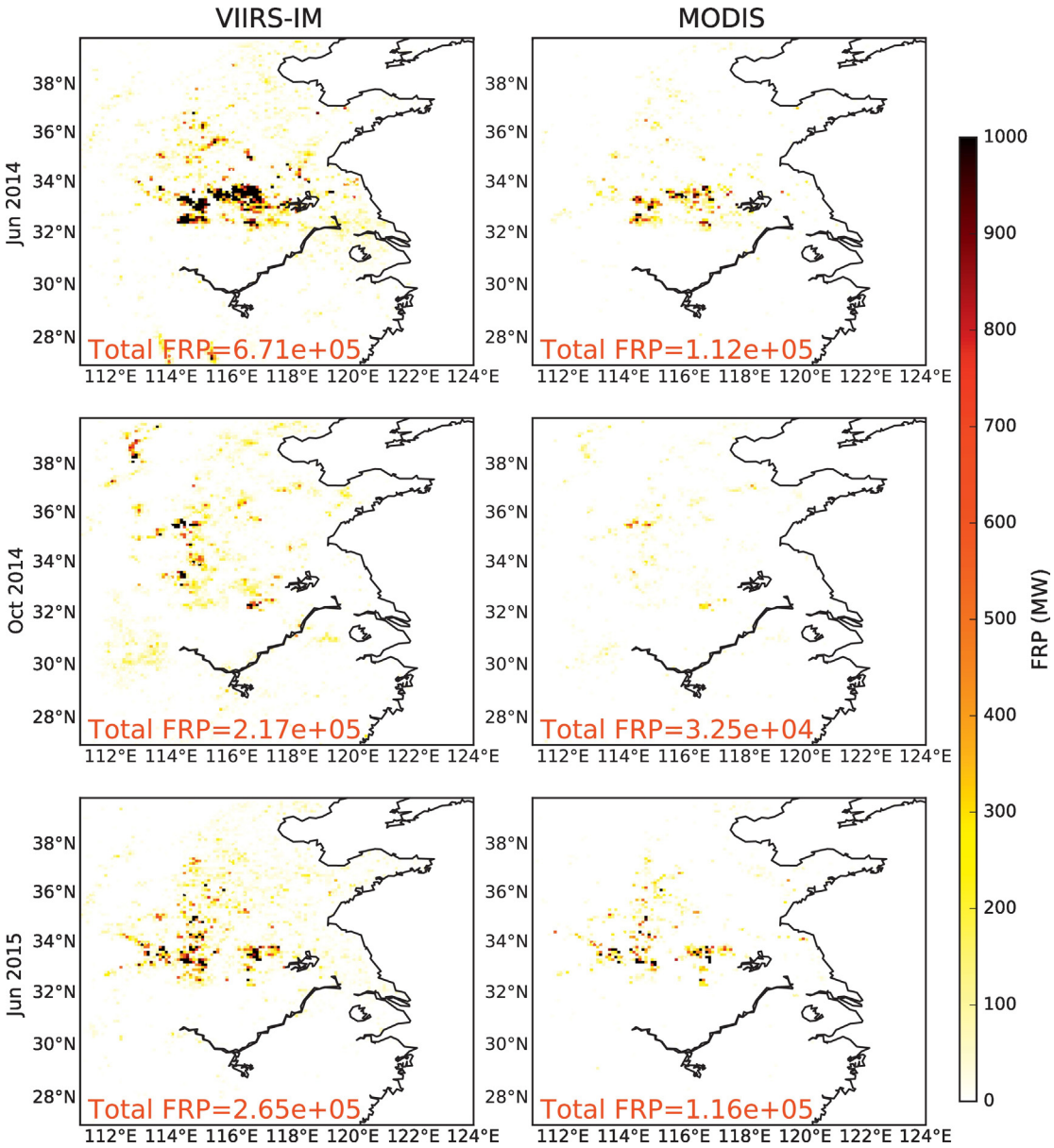

Fig. 14. Spatial distribution and total grid-cell FRP of agricultural fires in eastern China observed during June 2014 (upper row), October 2014 (middle row) and June 2015 (lower row), as assessed using the VIIRS-IM synergy FRP scheme developed here (left column) and MODIS (right column). Total summed regional FRP for each month is also indicated, with VIIRS always significantly higher.

and 100% in June 2015. In the latter case, one particular day (11th June) shows unusually high FRP values, responsible for 62% of the total VIIRS-IM FRP of the whole of June 2015. On this date, the fire-affected area is imaged close to the MODIS swath edge, with large MODIS pixels approaching 10× their area at nadir. Many individual VIIRS AF pixels fall in these large MODIS pixels, and because many are also strongly burning a lot of them trigger MODIS AF detections, even though the MODIS FRP detection limit is significantly raised at near swath edge locations (see Fig. 12). These MODIS AF pixels and their FRP are then replicated along-track due to the MODIS 'bow-tie' effect, which can lead to very significant overestimation of the MODIS-measured. The effect seen on this day therefore contributes very significantly to the total FRP from MODIS for June 2015 being much closer to that from VIIRS-IM than is the case for the other two months, where such burning conditions and sensor viewing geometries were not as fortuitously aligned.

7. Summary and conclusions

We have developed a regional active fire (AF) detection scheme for use with NPP VIIRS, optimising it in this case for the eastern China agricultural region where small (i.e. lower fire radiative power [FRP]) fires dominate due to widespread agricultural residue burning. We have focused primarily on exploitation of 375 m VIIRS I-Band data to detect even very low FRP fires (FRP < 1 MW), and have included detailed procedures to deal with the false alarms that can tend to increase when trying to detect lower FRP fire pixels, and which appear to have been particularly problematic in this area of China during development of the global VIIRS I-Band active fire detection scheme (Schroeder et al., 2014). A small number of AF pixel detections have been validated using pre- and post-fire high spatial resolution imagery, which showed burned areas appearing around the time of the AF detection.

Our VIIRS-based approach shows significant advantages when compared to the simultaneously recorded Collection 6 MODIS MYD14 AF products. The VIIRS approach detects active fires with an FRP-minimum below 0.5 MW, compared to around 6–8 MW for MODIS, and identifies typically 5 to 10× more AF pixels (notwithstanding differences in spatial resolution that mean that sometimes multiple VIIRS AF pixels may be represented by a single MODIS AF pixel). Many studies, including Wooster and Zhang (2004) and Ichoku et al. (2008) have shown that low FRP fires are by far the most common type, indicating that the ability to detect fires below the MODIS FRP detection limit may have a dramatic effect on the total amount of FRP quantified in an area.

It is worth pointing out that combining use of any particular active-fire capable EO data source with an algorithm that includes more liberal thresholds than applied previously does come at the risk of introducing a higher false alarm rate, since a greater range of lower magnitude non-fire phenomena can perhaps exceed the set detection thresholds. This has been countered here via the addition of extra tests, beyond those typically applied in most polar orbiting active fire detection algorithms (for example the spatial filter test), alongside very detailed false alarm screening based on (i) screening out thermal anomalies that are detected in landcover types typically associated with false alarms in this region (i.e. urban areas and manmade structures surrounded by rural landscapes), and (ii) identifying signatures thought largely incompatible with real active fire behaviour (i.e. repeated active fire detections made in the same location, including at times outside of the agricultural burning seasons). The accuracy and representativeness of the ancillary dataset used for the landcover screening is clearly important for the reliability of such approaches, and as further very high spatial resolution data and landcover mapping becomes available to identify such landforms - the accuracy of the approach will improve further. At the present time, it is the case that some urban/industrial areas still fail to be depicted in the current landcover data (Fig. 7c).

Our scheme includes FRP retrieval from the VIIRS M-Band when I-Band data are suspected of being affected by pre-aggregation saturation. Our resulting VIIRS-IM 'synergy' FRP product blends the advantages offered by the VIIRS I-Band sensitivity to small fires with M-Band FRP retrieval over higher FRP fires, and includes appropriate consideration of the waveband and atmospheric transmittance differences between the VIIRS I4 and M13 bands. Over three burning seasons in eastern China, our VIIRS-IM synergy FRP product captures on average 400% more total FRP than does near simultaneous MODIS Collection 6 AF data, even without adjustment for the MODIS 'bow-tie' effect that duplicates MODIS AF pixels towards the swath edge (Freeborn et al., 2011). Our work demonstrates the importance of both VIIRS' ability to detect low FRP fires with the I-Band (see Fig. 11), and its ability to detect active fire pixels with a sensitivity that does not degrade markedly across the swath as does that of MODIS' (see Fig. 12). Our results also prove the key importance of 'small' (i.e. low FRP) fires when quantifying fire emissions in agricultural biomes, but also show the importance of using high quality ancillary data to help mask false alarms. In the most recent implementation of the Schroeder et al. (2014) global 375 m VIIRS active fire product (https://viirsland.gsfc.nasa.gov/Products/FireESDR.html), FRP retrievals for 375 m I-Band pixels are also now made, based on coincident M-Band radiances, and the full data record can be expected soon. We believe our VIIRS-IM Band synergy FRP approach will be highly valuable when applied in other biomass burning regions, particularly those more dominated by low FRP fires, and that working with VIIRS will enable significant improvements in global fire emissions estimation in the coming years.

Acknowledgements

We gratefully thank Lili Wang and her research team for their excellent assistance during fieldwork in eastern China, and Bruce Main for fieldwork preparation and deployment. We thank Wilfrid Schroeder for useful discussions at the start of this work with regard to VIIRS, and gratefully acknowledge the King's China Award and King's Graduate School who funded T. Zhang. NERC Grant's NE/J010502/1 and NE/M017729/1, along with the STFC Newton China Agritech Programme supported aspects of this work. The VIIRS SDR and MODIS data were retrieved from CLASS and Reverb, and are courtesy of the NASA EOSDIS LP DAAC and USGS EROS Centre, South Dakota. Certain map data is copyright of the OpenStreetMap contributors. All data storage and processing was conducted using the UK's JASMIN super-data-cluster system, managed by UK STFC's Centre for Environmental Data Analysis (CEDA). We are grateful to the three anonymous referees for their constructive input.

Appendix A. Variability of atmospheric transmissivity

The uncertainty in atmospheric transmissivity ($\propto_{\tau_{MIR}}$) comes from both the transmission uncertainty due to atmospheric vertical composition apart from water vapour ($\propto_b$), along with the transmission uncertainty associated with the water vapour concentration ($\propto_{H20}$):

$$\propto_{\tau_{MIR}} = \sqrt{\propto_b^2 + \propto_{H2o}^2} \tag{A1}$$

We combined the three equations below, taken from Wooster et al. (2015), to estimate these variables:

$$\propto_b = 10^{-5}\tau_{MIR}\left(710.51117 - 8.37751\theta_v + 0.92238\theta_v^2 - 0.2525\theta_v^3 + 0.00027\theta_v^4\right) \tag{A2}$$

$$\propto_{H20} = \frac{\partial\tau_{MIR}}{\partial U_{H20}} \propto_{U_{H20}} \tag{A3}$$

$$\propto_{U_{H20}} = 0.24287 + 0.11172U_{H20} - 0.00090U_{H20}^2 \tag{A4}$$

Appendix B. FRP underestimation of VIIRS I-Band

Fig. 13c and f (main paper) demonstrate the very significant FRP underestimation that results from use of only the VIIRS I-Band to generate the FRP information, as opposed to both the I-Band and M-Band, and here we discuss the main reasons for these I-Band effects.

A VIIRS I4 pixel has an associated saturation flag set in the VIIRS Quality Flag (QF) data only if all pre-aggregation pixels are themselves saturated. By day, such pixels only account for 3% of the active fire pixel detections made with our I-Band scheme, and by night <1%. However, the summed FRP of these pixels accounts for as high as 9% of the total FRP calculated using the matching VIIRS M-Band pixels, attesting to the significance of dealing with the saturation issue. However, it is also the case that there may be many more cases where saturation only affects some (as opposed to all) the pre-aggregation I4-Band pixels, and these cases are not identified in the QF data (Polivka et al., 2015).

To investigate this, we compared FRP retrievals made from matching I-Band and M-Band pixels. Since each M-Band pixel contains four I-Band pixels, the former might sometimes capture some FRP from I-Band pixels containing fires but which were not detected as such by our I-Band active fire detection algorithm. Therefore, we first selected only those M-Band pixels for which all four constituent I-Band pixels were also identified as containing active fires, but for which no saturation flag was set. We summed the FRP from these I-Band fire pixels and compared them to the matching VIIRS M-Band FRP measure (Fig. A1). For detections made in the VIIRS 'No Aggregation Zone', the linear best fit between the I-Band and M-Band derived FRPs has a slope of 0.69, decreasing to 0.49 for Aggregation Zone 2, and 0.27 for Aggregation Zone 3. The reduction in slope from 'No Aggregation Zone' to 'Aggregation Zone 2' indicates that perhaps 20% ((0.49-0.69)/1) of the FRP underestimation might be due to some (but not all) of the constituent I-Band pixels being saturated before aggregation, a situation that becomes even worse in Aggregation Zone 3 where twelve original I-Band pixels contribute to the I-Band FRP measure to be compared to that from the M-Band (as opposed to the eight I-Band observations in Aggregation Zone 2). However, results for Aggregation Zone 3 can be separated into two groups, whose linear best fits to the matching M-Band FRP data have slopes of 0.1 and 0.84 respectively (likely representing matchups with and without significant I-Band pre-aggregation detector saturation). FRP underestimation due to I-Band pre-aggregation saturation could seemingly therefore be as high as 74% in VIIRS Aggregation Zone 3. Therefore, this comparison shows in Fig. A1 highlights the importance of implement a dual FRP retrieval using both I-Band and M-Band.

References

Cao, C., Xiong, J., Blonski, S., Liu, Q., Uprety, S., Shao, X., ... Weng, F., 2013. Suomi NPP VIIRS sensor data record verification, validation, and long-term performance monitoring. J. Geophys. Res.-Atmos. 118 (20).

Chen, J., Chen, J., Liao, A., Cao, X., Chen, L., Chen, X., He, C., Han, G., Peng, S., Lu, M., Zhang, W., 2015. Global land cover mapping at 30m resolution: a POK-based operational approach. ISPRS J. Photogramm. Remote Sens. 103, 7–27.

Freeborn, P.H., Wooster, M.J., Roberts, G., 2011. Addressing the spatiotemporal sampling design of MODIS to provide estimates of the fire radiative energy emitted from Africa. Remote Sens. Environ. 115, 475–489.

Freeborn, P.H., Cochrane, M.A., Wooster, M.J., 2014. A decade long, multi-scale map comparison of fire regime parameters derived from three publically available satellite-based fire products: a case study in the Central African Republic. Remote Sens. 6 (5), 4061–4089.

Giglio, L., Descloitres, J., Justice, C.O., Kaufman, Y.J., 2003. An enhanced contextual fire detection algorithm for MODIS. Remote Sens. Environ. 87, 273–282.

Giglio, L., Csiszar, I., Justice, C., 2006. Global distribution and seasonality of active fires as observed with the Terra and Aqua Moderate Resolution Imaging Spectroradiometer (MODIS) sensors. J. Geophys. Res. 111, G02016.

Giglio, L., Csiszar, I., Restás, Á., Morisette, J.T., Schroeder, W., Morton, D., Justice, C.O., 2008. Active fire detection and characterization with the advanced spaceborne thermal emission and reflection radiometer (ASTER). Remote Sens. Environ. 112, 3055–3063.

Giglio, L., Randerson, J.T., van der Werf, G.R., Kasibhatla, P.S., Collatz, G.J., Morton, D.C., DeFries, R.S., 2010. Assessing variability and long-term trends in burned area by merging multiple satellite fire products. Biogeosciences 7, 1171–1186.

Giglio, L., Schroeder, W., Justice, C.O., 2016. The collection 6 MODIS active fire detection algorithm and fire products. Remote Sens. Environ. 178, 31–41.

Huang, X., Li, M., Li, J., Song, Y., 2012. A high-resolution emission inventory of crop burning in fields in China based on MODIS thermal anomalies/fire products. Atmos. Environ. 50, 9–15.

Ichoku, C., Martins, J.V., Kaufman, Y.J., Wooster, M.J., Freeborn, P.H., Hao, W.M., Baker, S., Ryan, C.A., Nordgren, B.L., 2008. Laboratory investigation of fire radiative energy and smoke aerosol emissions. J. Geophys. Res.-Atmos. 113, D14S09.

Kaiser, J.W., Heil, A., Andreae, M.O., Benedetti, A., Chubarova, N., Jones, L., Morcrette, J.J., Razinger, M., Schultz, M.G., Suttie, M., van der Werf, G.R., 2012. Biomass burning emissions estimated with a global fire assimilation system based on observed fire radiative power. Biogeosciences 9, 527–554.

Lawrence, B.N., Bennett, V.L., Churchill, J., Juckes, M., Kershaw, P., Pascoe, S., Pepler, S., Pritchard, M., Stephens, A., 2013. Storing and manipulating environmental big data with JASMIN. Big Data, 2013 IEEE International Conference on, pp. 68–75.

Liu, H., Jiang, G.M., Zhuang, H.Y., Wang, K.J., 2008. Distribution, utilization structure and potential of biomass resources in rural China: with special references of crop residues. Renew. Sust. Energ. Rev. 12, 1402–1418.

National Bureau of Statistics of China (NBSC), 2012. China Statistical Yearbook. China Statistics Press, Beijing.

Oudrari, H., McIntire, J., Xiong, X., Butler, J., Ji, Q., Schwarting, T., Lee, S., Efremova, B., 2016. JPSS-1 VIIRS radiometric characterization and calibration based on pre-launch testing. Remote Sens. 8 (1), 41.

Pan, X.L., Kanaya, Y., Wang, Z.F., Komazaki, Y., Taketani, F., Akimoto, H., Pochanart, P., 2013. Variations of carbonaceous aerosols from open crop residue burning with transport and its implication to estimate their lifetimes. Atmos. Environ. 74, 301–310.

Piper, M., Bahr, T., 2015. A rapid cloud mask algorithm for Suomi NPP VIIRS imagery EDRs. Int. Arch. Photogramm. Remote. Sens. Spat. Inf. Sci. 40 (7), 237.

Polivka, T.N., Hyer, E.J., Wang, J., Peterson, D., 2015. First global analysis of saturation artifacts in the VIIRS infrared channels and the effects of sample aggregation. IEEE Geosci. Remote Sens. Lett. 12, 1262–1266.

Qin, Y., Xie, S.D., 2011. Historical estimation of carbonaceous aerosol emissions from biomass open burning in China for the period 1990–2005. Environ. Pollut. 159, 3316–3323.

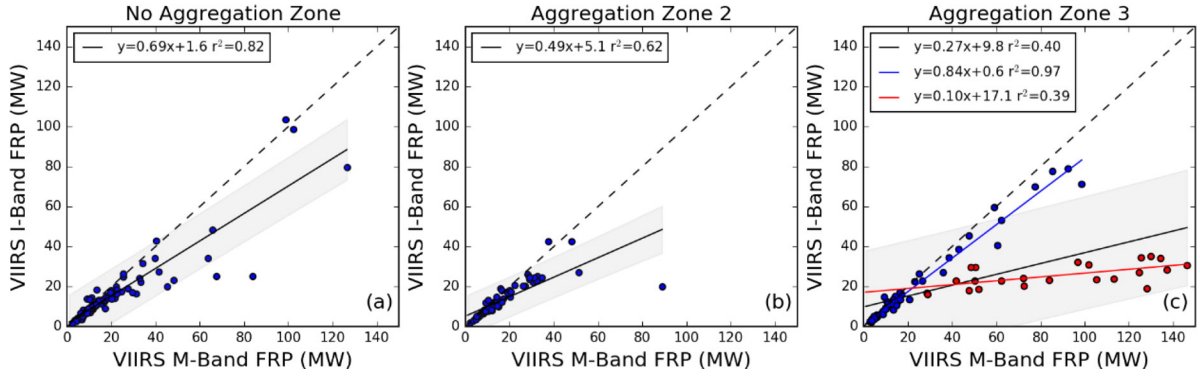

Fig. A1. Comparison of FRP values derive from matching VIIRS I-Band and M-Band observations of active fire pixels detected in the three VIIRS aggregation zones. Linear best fits and the 1:1 line are also shown. In Aggregation Zone 3 two different patterns are seen and linear best fits are applied to each. These likely represent data where pre-aggregation zone I-Band saturation does not occur or is minimal (slope of 0.84) and where it does (slope of 0.1).

Qu, L., Zhang, T., Lu, W., 2014. Assessing the potential of crop residue recycling in China and technology options based on a bottom-up model. Front. Environ. Sci. Eng. 8, 570–579.
Randerson, J., Chen, Y., Werf, G., Rogers, B., Morton, D., 2012. Global burned area and biomass burning emissions from small fires. J. Geophys. Res. Biogeosci. 2005–2012, 117.
Roberts, G.J., Wooster, M.J., 2008. Fire detection and fire characterization over Africa using Meteosat SEVIRI. IEEE Trans. Geosci. Remote Sens. 46, 1200–1218.
Roberts, G., Wooster, M.J., Perry, G.L., Drake, N., Rebelo, L.M., Dipotso, F., 2005. Retrieval of biomass combustion rates and totals from fire radiative power observations: application to southern Africa using geostationary SEVIRI imagery. J. Geophys. Res.-Atmos. 110 (D21).
Robinson, J.M., 1991. Fire from space: global fire evaluation using infrared remote sensing. Int. J. Remote Sens. 12 (1), 3–24.
Roy, D.P., Frost, P.G.H., Justice, C.O., Landmann, T., Le Roux, J.L., Gumbo, K., Makungwa, S., Dunham, K., Du Toit, R., Mhwandagara, K., Zacarias, A., Tacheba, B., Dube, O.P., Pereira, J.M.C., Mushove, P., Morisette, J.T., Santhana Vannan, S.K., Davies, D., 2005. The Southern Africa Fire Network (SAFNet) regional burned-area product-validation protocol. Int. J. Remote Sens. 26, 4265–4292.
Roy, D.P., Ju, J., Lewis, P., Schaaf, C., Gao, F., Hansen, M., Lindquist, E., 2008. Multi-temporal MODIS–Landsat data fusion for relative radiometric normalization, gap filling, and prediction of Landsat data. Remote Sens. Environ. 112, 3112–3130.
Schroeder, W., Oliva, P., Giglio, L., Csiszar, I.A., 2014. The New VIIRS 375 m active fire detection data product: algorithm description and initial assessment. Remote Sens. Environ. 143, 85–96.
Streets, D., Yarber, K., Woo, J.-H., Carmichael, G., 2003. Biomass burning in Asia: annual and seasonal estimates and atmospheric emissions. Glob. Biogeochem. Cycles 17.
Wolfe, R.E., Lin, G., Nishihama, M., Tewari, K.P., Tilton, J.C., Isaacman, A.R., 2013. Suomi NPP VIIRS prelaunch and on-orbit geometric calibration and characterization. J. Geophys. Res.-Atmos. 118, 11,508–511,521.
Wooster, M.J., Zhang, Y.H., 2004. Boreal forest fires burn less intensely in Russia than in North America. Geophys. Res. Lett. 31 (20).
Wooster, M.J., Zhukov, B., Oertel, D., 2003. Fire radiative energy for quantitative study of biomass burning: derivation from the BIRD experimental satellite and comparison to MODIS fire products. Remote Sens. Environ. 86, 83–107.
Wooster, M.J., Roberts, G., Perry, G.L.W., Kaufman, Y.J., 2005. Retrieval of biomass combustion rates and totals from fire radiative power observations: FRP derivation and calibration relationships between biomass consumption and fire radiative energy release. J. Geophys. Res.-Atmos. 110, D24311.
Wooster, M., Xu, W., Nightingale, T., 2012. Sentinel-3 SLSTR active fire detection and FRP product: pre-launch algorithm development and performance evaluation using MODIS and ASTER datasets. Remote Sens. Environ. 120, 236–254.
Wooster, M.J., Roberts, G., Freeborn, P.H., Xu, W., Govaerts, Y., Beeby, R., He, J., Lattanzio, A., Fisher, D., Mullen, R., 2015. LSA SAF Meteosat FRP products – part 1: algorithms, product contents, and analysis. Atmos. Chem. Phys. 15, 13217–13239.
Yan, X., Ohara, T., Akimoto, H., 2006. Bottom-up estimate of biomass burning in mainland China. Atmos. Environ. 40, 5262–5273.
Zhukov, B., Oertel, D., 2001. Hot Spot Detection and Analysis Algorithm for the BIRD Mission. Algorithm Theoretical Basic Document, DLRBerlin.
Zhukov, B., Lorenz, E., Oertel, D., Wooster, M., Roberts, G., 2006. Spaceborne detection and characterization of fires during the bi-spectral infrared detection (BIRD) experimental small satellite mission (2001–2004). Remote Sens. Environ. 100 (1), 29–51.

3.3 DATA VALIDATION

This Section provides details of two periods of fieldwork conducted to help assess the performance of the active fire detection algorithm described in the paper included in this Chapter (Zhang *et al.*, 2017, Section 3.2). The first field campaign was performed during the early stage of algorithm development (June 2014) at a time when the smoke emissions sampling was being conducted in China (Chapter 4), whereas the second was performed during the algorithm testing phase (October 2015).

3.3.1 FIELDWORK IN JUNE 2014

During fieldwork in June 2014 (also see Section 4.2, Methodology: Sampling Approach and Data Analysis Methods), field visits were conducted to confirm whether a subset of active fire detections made using the developing VIIRS I-band active fire detection algorithm were real or not, and if not what potentially maybe causing the presumed false alarms. Since this was not main purpose of this particular field visit, only three locations close to the site of the ongoing smoke measurement campaign were actually examined.

Prior to visiting the field, an early version of the active fire detection algorithm described in Section 3.2 was augmented with an e-mailing function that sent out the results from each VIIRS overpass. With the help of this enhancement, the code containing the algorithm could automatically download new VIIRS imagery from the previous day, process it to identify the location of actively burning fires, and then email those fire detections that were within a set distance of the field site to the field team. A GPS (Trimble Juno) was then used by the field team to locate the detected active fire positions on the ground, which enabled confirmation as to whether a fire had or had not taken place to be made (based on a visual assessment of the location).

Three fire locations named 140607_A, 140610_A, 140610_B (Fig. 3.1), detected in two separate VIIRS overpasses captured over two days were checked in the field via the procedure described above. The latter two fire locations from imagery collected on 10th June 2014 were found to be false alarms, caused most likely by large scale factories having the type of blue metal roof seen in Fig. 6 of the published paper included in this Chapter. However, local farmers did confirm that with regard to 140607_A, an agricultural fire had indeed been conducted on 7th June 2014 to clear wheat residue from a field. Due to the ongoing field activities related to smoke emissions sampling (see Section 5.2), it was not possible to

check this location until five days later (12th June 2014), and ground photographs collected then and shown in Fig. 3.2 indicate that the field had already been ploughed and partly flooded by that time, thus providing limited information with which to confirm the area had been recently burned. Though it seems likely this was the case based on the farmers reports and the fact that a small part of the unflooded area showed apparent evidence of burning (Fig. 3.2).

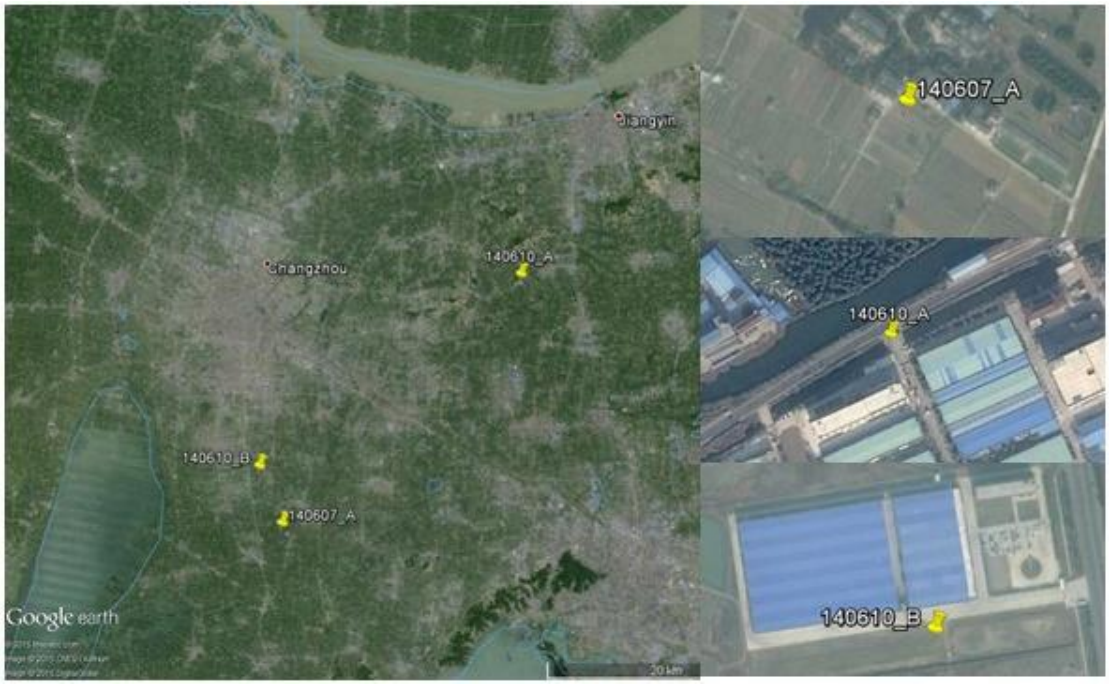

Figure 3.1: Three locations near Changzhou City (31.811° N, 119.974° E), Eastern China, where fires have been identified by the implemented VIIRS active fire detection algorithm (yellow pins, algorithm details see in Section 3.2) but where two of these are expected to be false alarms. Detection 140607_A is located inside an agricultural area, but 140610_A and 140610_B appear to both be industrial areas with large buildings whose roofs which might be causing sunglint induced false alarms.

The most useful information resulting from this very limited "field validation" exercise was the increased awareness of how important a landcover map could be to help discriminate false alarms from true active fire detections. Simply by checking whether a detected active fire pixel was located on agricultural land or not was considered a good strategy to perform this discrimination. Google Earth was used to perform the first tests, in order to gain an idea of the relative proportion of 'true' and 'false' active fire detections. This test was performed for fires on 26th September 2013, the date of highest active fire occurrence in the September 2013 burning period. Visual checks, considering the size of the VIIRS I-Band pixels (so only identifying an area as "farmland" when all land in a radius of 200 m from the detected fire pixel centre is agricultural land) led to the results shown in Table 3.1. A similar procedure was also performed for the

MODIS-Aqua active fire product of the same day, increasing the radius to 500 m to account for the larger MODIS pixel area.

Figure 3.2: Photo taken five days later in site 140607_A after active fire detection by VIIRS. Red rectangle shows the small burned scar while most part of this field has already been ploughed and flooded.

For VIIRS I-Band-detected active fire pixels, Table 3.1 shows that only around half are considered to be fully located on agricultural land. False alarm rates are at least 10%, since 10% of active fire detections are located fully in industry/village/urban areas. This level of commission error is approximately similar to that of other active fire detection algorithms (e.g. Wooster *et al.,* 2015; Roberts *et al.,* 2015), but in addition to this around 40% of the VIIRS AF detections were located in areas where there is a mix between agricultural and industry/village/urban landscovers, and these AF detections may or may not be false alarms. It is almost certain that some of them are, so the true commission error is very likely to be higher than 10%. However, despite the apparently quite high false alarm rate, VIIRS still appears to perform better than MODIS-Aqua. Only 15% of the AF pixels detected by MODIS-Aqua are located on fully agricultural land, whereas over 80% are located in mixed areas or in industry/village/urban areas. Furthermore, MODIS also detected far fewer AF's overall than VIIRS due to its much coarser pixel area (Table 3.1)

Table 3.1: Identification of landcover using Google Earth for hot spots detected by VIIRS and MODIS-Aqua on Sep.26, 2013.

	VIIRS		MODIS-Aqua	
	Samples	Percentage (%)	Samples	Percentage (%)
Agricultural land	396	49	25	15.2
Forest	2	0.3	1	0.6
Industry	69	8.6	3	1.8
Village or Urban area	9	1.1	-	-
Mixed above	325	41	136	82.4
Total	801		165	

The early version of the VIIRS AF detection algorithm assessed during the June 2014 fieldwork did not include most of the false alarm screening described in the published paper (Section 3.2), only that which attempts to remove sunglint affected pixels. What was concluded from the June 2014 fieldwork and the testing using Google Earth was that in China's agricultural areas there exist many more opportunities for false alarms than just sunglints from clouds and water, a fact actually highlighted (but not solved) by Schroeder et al. (2014). The main reason for the high rate of false alarms appears to be the rooftops of large industrial buildings, which either heat up by day and/or reflect sunlight preferentially in one direction leading to possibly stronger sunglint-induced false alarms that are not picked up by the sunglint tests (perhaps because the roofs are not flat and so the glints are not occurring at the expected angles). These findings indicated the need for a false alarm discrimination procedure based on landcover information, the details of which will be introduced in Section 3.4 and the evaluation of conducted in Section 3.5.

3.3.2 FIELDWORK IN OCTOBER 2015

The purpose of the fieldwork performed in October, 2015 (also see in Section 3.2, Active Fire Detection Output and Evaluation: Field Validation) was to help confirm the final performance levels of the completed AF detection algorithm used with the VIIRS I-Band, via the detection of evidence of burning at identified AF pixel locations. By this time, the AF detection algorithm already included a landcover-based false alarm filter based on the findings in Section 3.3.1. False alarm occurrences related to the aforementioned industrial buildings were therefore expected be reduced.

During this fieldwork, the main evidence was collected by deploying a small UAV carrying a digital camera at the sites of the AF detections made by VIIRS. Fig. 5 in Section 3.2 shows one such validation

example, with areas of black ash and char seen on the land surface shortly after the VIIRS-based AF detection (they were not there in the Google Earth imagery captured a few days before). A magnification of part of the previous Fig.5 (Section 3.2) is shown here as Fig. 3.3, and the red polygon shown in the left is the footprint of a VIIRS AF pixel. At right are two zoomed images in the areas highlighted with yellow polygons at left, and both lie within the VIIRS AF pixel area. Both these highlighted areas show large black burn scars where ash and char have been laid down by recent fires. They also show the three different burning patterns discussed in Section 3.2, homogeneous covering, semi-linear and scattered patterns of ash and char.

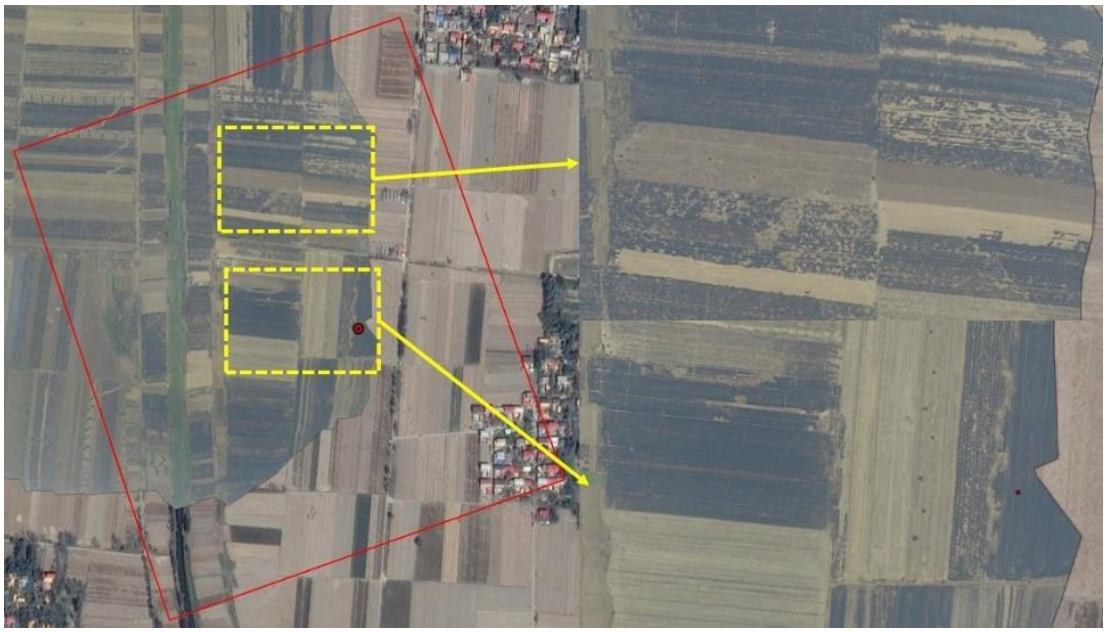

Figure 3.3: Zoomed example of Fig. 5 in Section 3.2. At left show a red polygon which is the footprint of the VIIRS AF pixel (it is the AF detection shown at the bottom right of the original Fig. 5b). At right are two zoomed images in the areas highlighted with yellow polygons at left.

Though some studies have found that low-albedo, burned areas created by fires that occurred previously can trigger false active fire detections (Li *et al.*, 2000), this was not the case for the agricultural fires shown in Fig. 3.3. At the sites imaged by the UAV, active fires were only detected on one day (5th Oct 2015), and there were no repeat detections. The Google Earth imagery (that showed the areas as unburned) was taken on 1st Oct 2015, and the UAV deployed on 7th Oct 2015 when clear 'burn scars' showing fresh ash and char were visible. If the active fire detections were false alarms caused by the presence of the low-albedo burn scars (rather than actively burning fires themselves) then they would very likely be seen more than once in the same place over this time. Furthermore, due to the relatively low fuel loads usually associated with agricultural residue fires, the ash represents a very thin and non-continuous layer

on top of the soil (Fig. 3.4), and would therefore not be expected to get particularly hot via solar heating. Thus the VIIRS-based AF detections definitely appear to have been correct identifications, related to fires that occurred during the 1st -7th October period.

Figure 3.4: Image of ash and char taken right after corn residue burning. The ash represents a very thin and non-continuous layer on top of the soil, indicating relatively low fuel loads associated with agricultural residue fires.

As indicated in Section 3.2, a total of 30 detected AF pixels were checked during this October 2015 fieldwork. Recent char and ash were identified close to the pixel centre of each of the 30 AF detections, confirming these as likely correct identifications and highlighting the advantages of the landcover filter in greatly reducing the false alarms that would likely have been present should such a filter not have been developed and applied subsequent to the June 2014 field campaign.

It is worth to note that a full active fire detection omission and commission statistics will need to be based on independent validation data, which requires large scale ground-based fieldwork, higher spatial resolution satellite or airborne data, or simultaneous active fire data from a sensor operating at even higher spatial resolution whose detection accuracy is already know. This is not covered by this thesis, and these kind of data at the moment are lacking, not only for the VIIRS regionally optimised active fire detection algorithm but also the global algorithm of Schroeder et al. (2014). Currently in this very limited field validation, thirty of the "classified active fire pixels" have been checked, and very recent burn scars found for all of them – indicating that the active fire pixel detections were correct. However, errors of omission potentially still exist in the dataset produced by this study, as they do in most active fire datasets.

3.4 SRF WEIGHED LANDCOVER PROPORTION CALCULATION

This Section provides the full details of the land-cover based method used in both the estimation of the agricultural area ratio of each detected fire pixel, and the false alarm discrimination used to classify some of these fire detections as being caused by non-fire phenomena in Section 3.2 (published as Zhang *et al.*, 2017). The primary aim of this land-cover based procedure was to calculate the proportion of agricultural land within each VIIRS pixel initially detected as an active fire, based on a 30-m spatial resolution landcover map (Fig. 3.5).

The manual examination conducted using the VIIRS-detected active fire pixels and Google Earth in Section 3.3.1 indicated the need for false alarm checks, probably based on landcover information because the false alarms were not identified by sunglint tests and appeared to be associated with large industrial buildings surrounded by more rural landscapes. A 30-m spatial resolution global land cover data map derived from Landsat ETM+ and Chinese land monitoring satellite data was used (GlobeLand30, http://www.globallandcover.com/, Fig. 3.5; Chen *et al.*, 2015). These data have 10 classes, and were derived from imagery collected in 2009-2011. Within each VIIRS-detected active fire pixel, the calculated agricultural land proportions, as well as the spatial and temporal mask shown in Fig. 7 (Section 3.2), were used together to identify every active fire pixel as a false alarm or true fire pixel.

Figure 3.5: Global view of GlobeLand30-2010 product (Chen *et al.*, 2015), includes 10 land cover types, namely cultivated land, forest, grassland, shrubland, wetland, water bodies, tundra, artificial surfaces, bareland, permanent snow and ice.

Satellite imager pixels do not typically have top-hat response functions, and the spatial response function (SRF) maps out the sensitivity of the detector to spectral radiance signals coming from different locations within the pixel footprint (Huang *et al.,* 2002; Lin *et al.,* 2011; Wolfe *et al.,* 2013). These SRFs therefore need to be considered when providing a metric that denotes the effective landcover fraction of any particular pixel, since for example a patch of "urban" land lying towards the edge of a pixel that is mostly covered by agricultural landcover is likely to have less impact on the overall pixel-integrated spectral radiance than if it lay at the pixel centre. This was shown by Townshend et al. (2000) in the context of landcover mapping, and it was shown there that consideration of the sensor SRF can reduce by half the standard error of landcover mapping procedures. Clearly then, a more reliable metric of the contribution of a particular landcover type to the pixels signal can be provided if the SRF is considered compared to if it is not.

In whiskbroom systems like VIIRS and MODIS, a scan mirror sweeps out the projection of the detector(s) onto the Earth's surface, and this signal is integrated for a finite period of time to provide each pixels output signal. This typically results in a spatial response function (SRF) that peaks at the pixel centre and lowers to zero at the two pixel edges (i.e. where the integration time for that pixel starts and stops; Wolfe *et al.,* 2013). According to the full width at half maximum height (FWHM) definition, with MODIS and VIIRS this SRF pattern causes approximately 25% of the radiance of any particular pixel to contribute also to the neighbouring pixels in the along scan direction, half to the left and half to the right hand pixel (Huang *et al.,* 1998; Wolfe *et al.,* 2013). In the along-track direction however the SRF is almost top-hat in nature, and with VIIRS there is no along-track overlap as overlapping pixels (due to the 'bow tie effect') have been deleted in the level 1b product (see Fig.1 of Section 3.2).

Use the SRF with the 30m landcover map shown in Fig. 3.5 allows for a more detailed consideration of the response of pixels to the particular landcovers that lies within them, taking account of where the landcover is located within the pixels. To do this, the SRF map for VIIRS I-Band pixels was calculated from the appropriate along-scan and across-track line spread function (LSF), available on the NOAA National Calibration Centre website (http://ncc.nesdis.noaa.gov/VIIRS/index.php). For VIIRS, the LSFs in the along-track direction can be considered squares (Robert *et al.,* 2013), with their width the same as the horizontal sampling interval (HIS), while the LSF values in the along-scan direction for the 32 detectors of each I-band cannot. Separate LSF values were obtained for each of the 32 detectors, and averaged to get a mean LSF in this direction (Fig. 3.6a) since the standard error of the mean LSF compared to the actual LSF at all points was within 1%. The SRF map shown in Fig. 3.6b gives the

spatial response for the area covered by the equivalent of 2×2 VIIRS pixels, where the red rectangle is the central pixel location (FWHM). The ground cover in the pixel on the scan line subsequent to and prior to that of the central pixel does not impact on the signal of the central target pixel, but that within the left and right pixels along the scan does. Therefore, only these central, left and right pixels are used for the landcover proportion calculation within any particular pixel.

The area of each VIIRS-detected active fire pixel to be examined is projected onto the 30m spatial resolution landcover map to perform the calculation. At the edge of a VIIRS pixel potentially only part of some landcover map grids are covered during projection. Therefore, a sub-pixel strategy is used whereby the area covered by each non-georectified VIIRS pixel is split into a series of 10 m × 10 m cells, and each cell treated as a point (using central latitude/longitude) in the next step of the landcover identification procedure. The number of subpixel cells varies as the VIIRS pixels move away from nadir such that the pixel size grows, from 370 m × 388 m at nadir to 789 m × 800 m at edge of swath. This growth is far less than with MODIS, due to VIIR's unique pixel-averaging scheme (Section 3.2). The MODIS Geolocation Algorithm Theoretical Basis Document (ATBD) provides a method of interpolation to determine the location of any point [Z(x,y)] inside a nominal pixel, using a bi-quadratic equation:

$$z(x,y) = \sum_{i,j=0}^{2} a_{ij} x^i y^i \qquad (3.1)$$

This method can be applied to calculate the latitude/longitude of a point location (x,y) given its nominal pixel location (i, j) within a 3 x 3 grid block. The coefficients a_{ij} are generated using the matrix provided by ATBD.

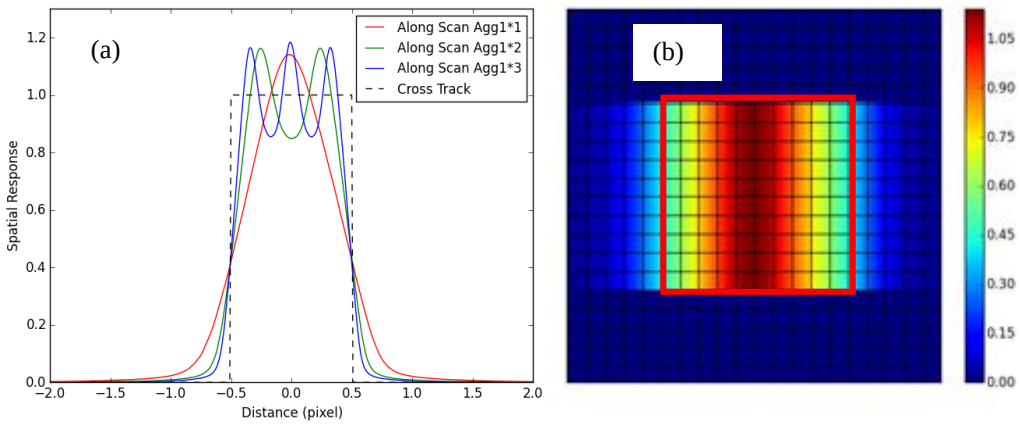

Figure 3.6: Information related to the VIIRS spatial response function (SRF). (a) VIIRS I4 band spatial response data in the along-scan and across-track directions. The details of three aggregation zones (along scan agg 1 *1/2/3) can be

seen in Section 3.2. (b) SRF map based on along and across-track spatial response for the area covered by the equivalent of 2×2 VIIRS pixels, where the red rectangle is the central pixel location (FWHM).

Fig. 3.7 illustrates the final process applied to determine land cover metric for each detected active fire pixel. The geographic location of any sub-pixel location can be calculated as long as the geolocation information for the 3×3 pixels surrounding that pixel are known. The model developed for MODIS can be applied to VIIRS as long as the 3×3 pixel block is within a single scan line and the same aggregation scheme region (either Aggregation zone 2, 3 or no aggregation zone, Fig. 1 of Session 3.2; but not at a location that crosses two regions) (Nishihama, pers. comm.). When applying the scheme to the vast majority of VIIRS pixels, the target pixel is selected as the central pixel of the 3×3 pixel array. However, for pixels at the edge of scan or at the boundary of an aggregation scheme region, a nearby pixel is chosen to ensure that the 3×3 pixel array is located within one scan line and one aggregation scheme only. Note the 3×3 pixel array here is only to calculate the geolocation of those sub-pixels, and is not used in the later landcover proportion estimation.

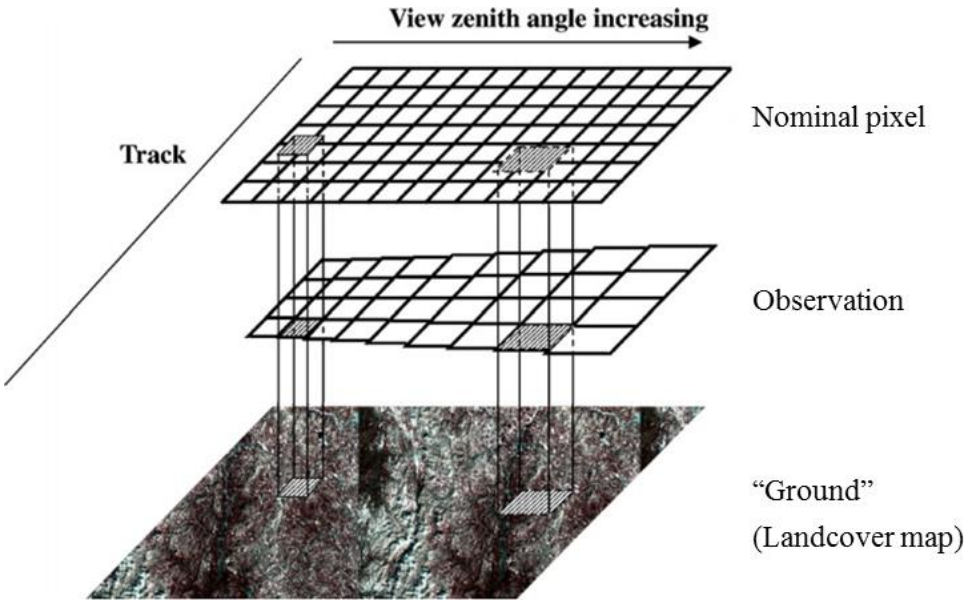

Figure 3.7: Schematic illustration of the procedure developed herein for determining the landuse metric for help in identifying true active fires and false alarms. The original pixel is split to obtain a series of 10 m × 10 m sub-pixels (only a few are shown in this illustration for clarity). The geolocation of each sub-pixel with respect to the landcover map is then calculated at the observation level from a 3×3 pixel array. Finally, at the "ground" level, the land cover data are found for each sub-pixel. Figure is taken from Tan *et al.*, (2006).

Then for each 10 m sub-pixel cell, the land cover type (for example, agricultural land) is taken from the 30 m landcover map. Fig. 3.8 illustrates how the inclusion of the SRF information impacts on the final metric of 'land cover proportion' in a pixel. Suppose the original land cover map simply provides the

information as to whether each sub-pixel is agricultural land or not, where 0 (blue) is 'False' and 1 (red) is 'True'. Clearly, the central set of 10 m sub-pixels are more important in determining the final output than are the sub pixels more distant from the centre, and the SRF weights gradually decrease away from the centre to reflect this. After classification of all sub-pixels, a weighted average metric is calculated from the multiplication of the resulting land cover array and the normalized spatial response function (SRF) map. For each pixel, the sum of all the weighted land covers within the pixel should still be 1.

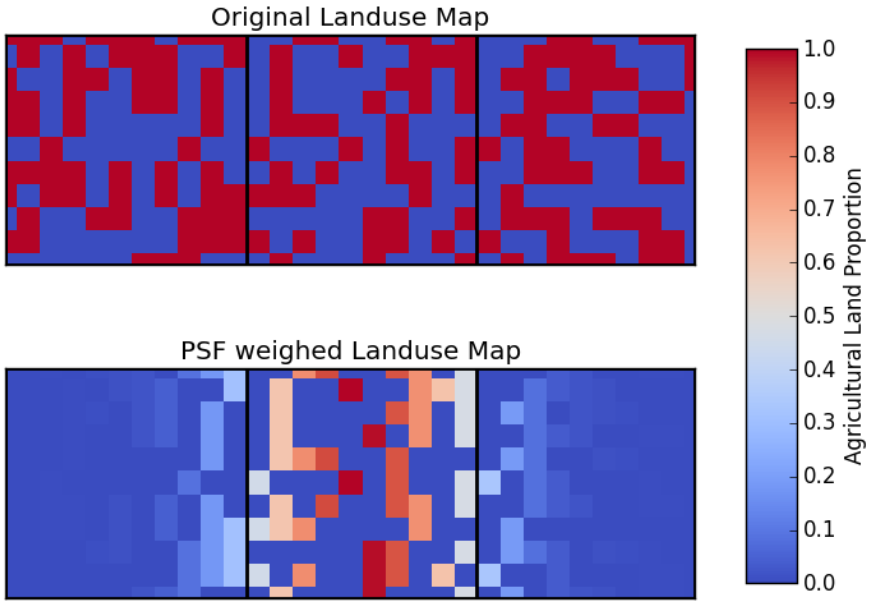

Figure 3.8: Illustration of the spatial response function (SRF) approach to determining the land cover metric for a pixel in this study, with the 30 m land cover map shown at top for the area of the (central) target pixel and its two neighbouring along scan pixels, and the multiplication of the SRF by the land cover map at bottom.

3.5 FALSE FIRE ALARM RATIOS

This Section provides details of the performance of the spatial and temporal 'false alarm' masking procedure introduced in Section 3.2 (Fig. 7ab). The filtered results of this study were compared with that from the global VIIRS algorithm of Schroeder et al. (2014) to assess the potential benefit of using high quality ancillary data to help mask out what appear to be false fire detections resulting from primarily industrial buildings. The same method has also been applied to data from MODIS-Aqua to evaluate the potential ratio of false fire detections within the official MOD14 MODIS active fire product across Eastern China. The metric used was the percentage of detected active fire pixels being filtered out from

the total number of original AF detections). When applyed to other two products, only spatial ‘false alarm’ mask are used.

3.5.1 False Fire Results in This Study

As shown in Fig. 3.9, the total monthly VIIRS I-Band detected AF pixel counts that are believed to be false alarms can be 20000 - 50000 during the summer burning seasons (note that forest or grassland fires have been excluded from false alarms, as is also the case for Fig. 3.12), similar to the number of AF detections believed to truly represent real active fires. The ratio of false alarms to total confirmed thermal anomaly pixels is thus 40% to 79%, with a mean of 62 ± 10%. 41 ± 18% of those false alarms were identified by spatial filter and the rest were identified by temporal filter as shown in Fig. 3.9. The false alarms ratio decreases a little (57 ± 16%) when using the total FRP instead of pixel counts to calculate the false alarm contribution. Take the summer burning seasons as an example, the contribution of false alarms in terms of FRP was 16 - 30%, compared to 43 - 52% when calculated using fire pixel counts from 2012-2015. This comparison indicates that most false alarms show relatively low FRP measures. Fig. 7c from Section 3.2 showed that some urban/industrial areas still fail to be depicted in the current landcover data, and thus these areas can still generate AF detections that are not screened out as false alarms. Better quality ancillary landcover data are expected in the future to minimise this occurrence, but since most false alarms show low FRPs the impact of failing to screen out a relative few is not considered hugely significant.

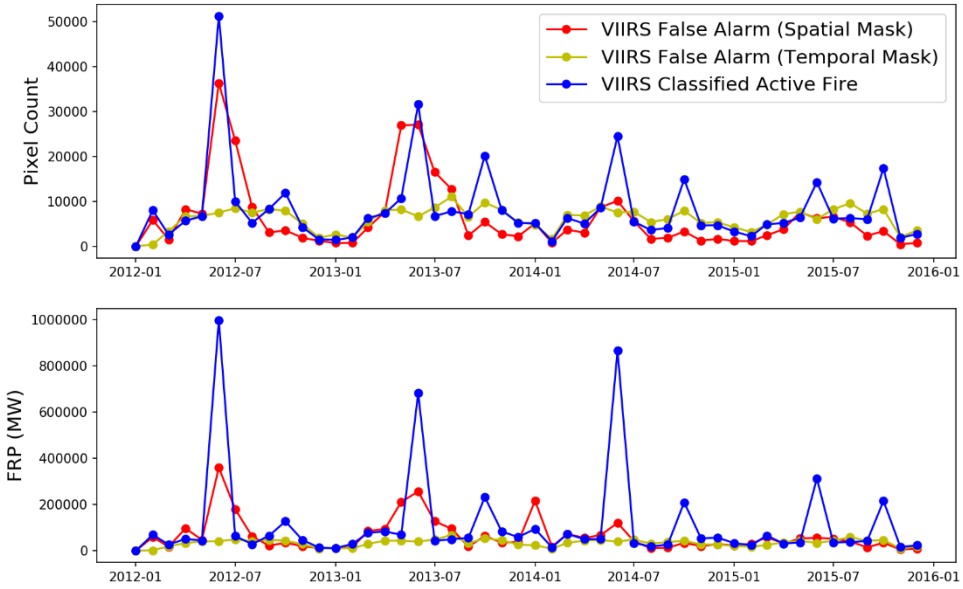

Figure 3.9: Time series of VIIRS monthly pixel count (upper) and FRP (bottom) in Eastern China, break down by false alarm filtered by spatial mask (red), temporal mask (yellow), and classified active fire (blue) using the spatial and temporal mask introduced in Section 3.2 (Fig. 7ab).

3.5.2 Comparison to VIIRS Global Algorithm Results

The regional VIIRS I-Band AF detection algorithm developed here has been show to be sensitive to false alarms generated by urban/industrial features (and these represent 63 ± 10% of the detected AF pixel counts as shown in Fig. 3.4). This phenomena is not unique to VIIRS, but most existing AF detection algorithms do not include such high spatial resolution false alarm masking procedure based on landcover information (Giglio *et al.*, 2016; Schroeder *et al.*, 2014). For comparison to the VIIRS I-Band data produced here, the global I-Band active fire detection algorithm results of Schroeder et al. (2014) were used (obtained from the data stored in NASA Worldview).

Fig 3.10 shows a comparison of outputs from the algorithm developed herein (Section 3.2) to those from VIIRS global I-Band algorithm (using imagery taken on 2nd August 2016, with the centre scene located in Beijing). The red dots refer to the VIIRS global algorithm output, which shows a total of 24 AF hotspots (some of them are very close to each other, and perhaps might be a single detection in the original data but split into two in the PNG data downloaded from Worldview). The regional VIIRS algorithm output is shown as the coloured pins, with 35 of the identified thermal anomalies discounted by the masking procedure developed here as false alarms, and 8 classified as true active fires. Since the imagery is taken outside of the agricultural burning season, and in a high density, populated urban area, in fact all the AF pixels detected by both algorithms shown in Fig. 3.5 are likely to be false alarms.

This direct comparison shows that the regionally optimized algorithm developed in this PhD – which included use of more liberal thresholds in order to detect the lowest FRP fires, did indeed lead in this case to the detection of more false alarms in the initial thermal anomaly detection stage compared to the global algorithm of Schroeder et al. (2014, 11 more in the case shown in Fig. 3.5; assuming all the detections are in fact false alarms). However, the error of commission (8 out of 42 detections = 19%) is in fact lower than that of the global algorithm of Schroeder et al. (2014, 24 out of 24 detections = 100%) with the help of the spatial and temporal masking procedure developed herein.

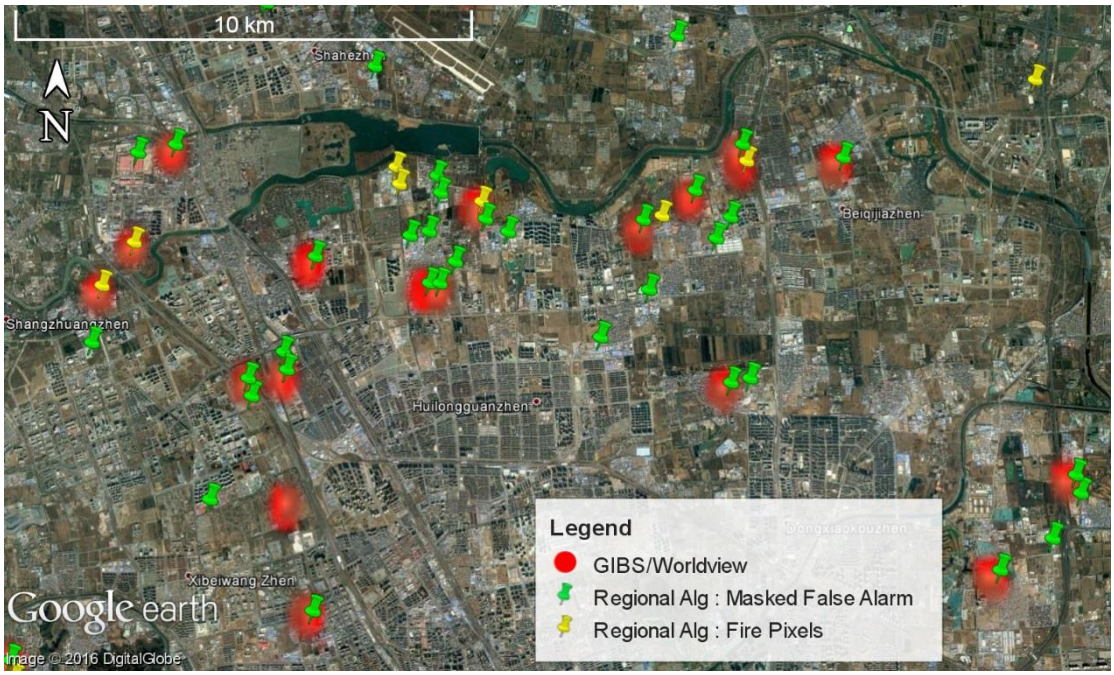

Figure 3.10: Active fire (AF) pixel detections made on 2nd August 2016 from VIIRS, with the scene centre 40.098°N, 116.362°E near Beijing City and a google earth imagery is used as the basemap. Yellow and green pins indicate those masked false alarm and classified AF pixels generated using the regionally optimized VIIRS I-Band AF detection algorithm developed herein (Section 3.2), whilst red circles are those output from the global I-Band algorithm of Schroeder et al. (2014, available from the GIBS/Worldview database).

3.5.3 Comparison to False Fire Alarm Ratio of MODIS-Aqua

Similar to the VIIRS global I-band product of Schroeder et al. (2014), investigations showed that the widely-used, and more spatially coarse, MODIS active fire product of Giglio et al. (2016) was also found to be impacted by a high rate of unscreened false alarm. Fig. 3.11 shows an example recorded on the 12th August 2015 using the 1 km MODIS-Aqua MYD14 AF product close to Shanghai (different date and location from the VIIRS case showed in Fig. 3.10 since those relatively small false alarms in Fig. 3.10 have not been detected by MODIS). A total of 16 AF pixels were detected by the MODIS algorithm, all

of which are likely to be false alarms linked with industrial areas and manmade structures, similar the false alarms shown in Fig.6 of Section 3.2 and in Fig 3.10.

Figure 3.11: Active fire (AF) pixel detections made on 12st August 2015 from MODIS-Aqua, with the scene centre 30.875 °N, 121.350°E near Shanghai City and a google earth imagery is used as the basemap.

The spatial and temporal mask used in this study was also applied to the MODIS MYD14 AF detection data, in order to evaluate its potential false alarm rate and compare them to those found with VIIRS in this study. Since the pixel size of MODIS-Aqua is significantly coarser than the VIIRS I-Band (giving a 10× larger pixel at nadir), MODIS was expected to be less sensitive to the signatures of the industrial buildings that appear commonly responsible for the VIIRS false alarm detections (Fig. 6 in Section 3.2). However, the monthly time-series shown in Fig. 3.12 produced using the same landcover-based filtering approach (without the temporal filter as that should be generated using MODIS long time series data in this case) as used with VIIRS but now applied to MODIS indicate that false alarms accounted for 48 ± 18% (mean ± 1sd) of total detected MODIS AF pixels in this area, a value only 14% lower than that from the VIIRS regional I-Band algorithm developed here and applied to the same location and period (62 ± 10%; though note that these false alarm detections with VIIRS are then filtered out using the landcover and temporally-based filtering scheme). Both VIIRS and MODIS show false alarms, expressed as total pixel counts or FRP, are higher in May to August than the rest of the year. This seasonal pattern implies perhaps that the phenomena causing the false alarms are related to solar position (warm weather, and/or a

stronger solar beam of a particular direction), which favours heating of the large industrial building roofs (Fig. 6; Section 3.2). However, the ratio of MODIS' suspected false alarms to total AF detections during June, the most intensive burning month, was relatively low - ranging from 24 - 31% for pixel count and 16 - 22% for FRP, similar to what is observed in the VIIRS regional algorithm results. This is because many more true fires have been detected during more intensive burning period.

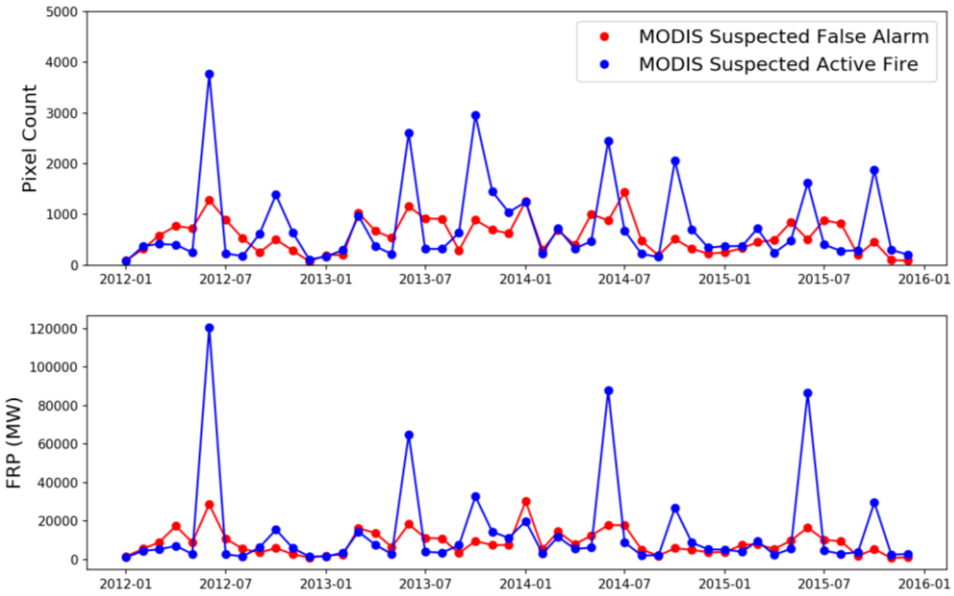

Figure 3.12: Time series of MODIS-Aqua (Collection 6) monthly pixel count (upper) and FRP (bottom) in Eastern China, break down by false alarm and classified active fire using the spatial mask introduced in Section 3.2 (Fig. 7a).

CHAPTER 4: *IN SITU* MEASUREMENTS OF SMOKE EMISSION FACTORS ASSOCIATED WITH AGRICULTURAL RESIDUE BURNING IN EASTERN CHINA

4.1 INTRODUCTION

Estimates of fuel consumption derived from FRP-based (or burned area based) measurements need to be combined with emission factors (EFs) if they are to be converted into smoke emission estimates. However, as described in Chapter 2, there have been a relatively limited number of *in situ* measurement of crop residue burning EFs in China. The goal of the research reported in this Chapter was therefore to perform the *in situ* measurements needed to calculated the EFs of key species associated with crop residue burning in Eastern China, and to report these EFs and compare them to those in the existing literature.

The Chapter is comprised of the following section (Section 4.2) which is a published paper describing the first *in situ* measurement campaign and its results, focusing on trace gas, $PM_{2.5}$ and black carbon. This paper also describes the design and deployment of a bespoke sampling system use for *in situ* measurements of smoke, with further building and testing details of this system described in Section 4.3. A second *in situ* measurement campaign and its results are then described in Section 4.4, which included use of an improved measurement system. Finally, a mathematical model deployed within the procedure used to calculate the EF's from the smoke concentration measurements is introduced in Section 4.5.

The author of this thesis is the first author of the published paper, and designed and conducted the fieldwork experiment along with M. Wooster and B. Main. D. Green was involved in designing and testing the smoke sampling system, whilst B. Main helped in its construction. The thesis author undertook all the data analysis and drafted the first version of the paper, to which the co-authors then suggested edits.

4.2 NEW FIELD-BASED AGRICULTURAL BIOMASS BURNING TRACE GAS, PM2.5, AND BLACK CARBON EMISSION RATIOS AND FACTORS MEASURED *IN SITU* AT CROP RESIDUE FIRES IN EASTERN CHINA

Atmospheric Environment 121 (2015) 22–34

Contents lists available at ScienceDirect

Atmospheric Environment

journal homepage: www.elsevier.com/locate/atmosenv

New field-based agricultural biomass burning trace gas, $PM_{2.5}$, and black carbon emission ratios and factors measured *in situ* at crop residue fires in Eastern China

Tianran Zhang [a], Martin J. Wooster [a, b, *], David C. Green [c], Bruce Main [a]

[a] King's College London, Earth and Environmental Dynamics Research Group, Department of Geography, Strand, London, WC2R 2LS, UK
[b] NERC National Centre for Earth Observation (NCEO), UK
[c] King's College London, Environmental Research Group, MRC-PHE Centre for Environment and Health, London, SE1 9NH, UK

HIGHLIGHTS

- A new sampling system was designed to measure CO, CO_2, $PM_{2.5}$ and black carbon (BC) *in situ* during field based fires.
- A linear mixing model was generated to quantify the combustion phase contribution to the measurement of each species.
- New 'fire averaged' CO, CO_2, $PM_{2.5}$ and BC emission factors are reported for Chinese agricultural fires in different fuel types.
- Intense flaming processes with visible clouds of soot was found for the rapeseed residue bonfire in particular.

ARTICLE INFO

Article history:
Received 27 December 2014
Received in revised form
22 April 2015
Accepted 7 May 2015
Available online 14 May 2015

Keywords:
Agricultural residue fires
Eastern China
Emission factor
Black carbon
FTIR
Biomass burning

ABSTRACT

Despite policy attempts to limit or prevent agricultural burning, its use to remove crop residues either immediately after harvest (e.g. field burning of wheat stubble) or after subsequent crop processing (e.g. "bonfires" of rice straw and rapeseed residues) appears to remain widespread across parts of China. Emission factors for these types of small but highly numerous fire are therefore required to fully assess their impact on atmospheric composition and air pollution. Here we describe the design and deployment of a new smoke measurement system for the close-range sampling of key gases and particles within smoke from crop residue fires, using it to assess instantaneous mixing ratios of CO and CO_2 and mass concentrations of black carbon (BC) and $PM_{2.5}$ from wheat stubble, rice straw, and rapeseed residue fires. Using data of our new smoke sampling system, we find a strong linear correlation between the $PM_{2.5}$ mass and BC, with very high $PM_{2.5}$ to BC emission ratios found in the smouldering phase (up to 80.7 mg m^{-3}.(mg m^{-3})$^{-1}$) compared to the flaming phase (2.0 mg m^{-3}.(mg m^{-3})$^{-1}$). We conclude that the contribution of BC to $PM_{2.5}$ mass was as high as 50% in the flaming phase of some burns, whilst during smouldering it sometimes decreased to little over one percent. A linear mixing model is used to quantify the relative contribution of each combustion phase to the overall measured smoke composition, and we find that flaming combustion dominated the total emission of most species assessed. Using time series of trace gas concentrations from different fire cases, we calculated 'fire integrated' trace gas emission factors (EFs) for wheat, rice and rapeseed residue burns as 1739 ± 19 g kg^{-1}, 1761 ± 30 g $kg^{-1}$and 1704 ± 27 g kg^{-1} respectively for CO_2, and 60 ± 12 g kg^{-1}, 47 ± 19 g kg^{-1} and 82 ± 17 g kg^{-1} respectively for CO. Where comparisons were possible, our EFs agreed well with those derived via a simultaneously-deployed open path Fourier transform infrared (OP-FTIR) spectrometer. These EFs, and the linear best fit relationships between both $PM_{2.5}$ and BC mass and the CO_2 and CO measurements, were used to generate particulate EFs, which varied over the 5.8 −20.3 g kg^{-1} and 0.25–2.89 g kg^{-1} range respectively. We note a particularly high 2.89 g kg^{-1} BC emission factor for the rapeseed bonfires, reflective of intense flaming combustion that gave off visible clouds of soot. These field-measured EFs offer a different perspective than is obtained when burning in laboratory combustion chambers, and are suitable for combining with landscape-scale fuel consumption estimates to provide atmospheric modelling inputs of emissions from these types of crop residue fires.

* Corresponding author. King's College London, Earth and Environmental Dynamics Research Group, Department of Geography, Strand, London, WC2R 2LS, UK.
E-mail address: martin.wooster@kcl.ac.uk (M.J. Wooster).

http://dx.doi.org/10.1016/j.atmosenv.2015.05.010

1. Introduction

1.1. Agricultural residue burning

Agricultural residues (sometimes called agricultural waste) represent the by-products of crop production, for example the wheat stubble remaining after harvest, the rice straw cut at grain harvest, or the rapeseed material remaining after harvest and pressing. Methods to remove or dispose of these residues prior to the next harvest include their use as mulch for the succeeding crop, a substrate for composting, fuel for biogas or power generation, and use as animal feed or bedding (Ponnamperuma, 1984). However, the viability of these uses depend on local circumstances, and in many still developing economies agricultural residues are often removed via *in situ* burning, which in areas without well-developed large scale agricultural mechanisation is generally the quickest, simplest and cheapest approach, and also possibly provides some nutrients back into the soil prior to the next planting (Jiang et al., 2012; Smith et al., 2007). Though each individual crop residue burn may be quite limited in area, their widespread nature across extremely high numbers of fields worldwide means that such fires actually contribute significantly to the overall global landscape-scale burning totals (Akagi et al., 2011; Andreae and Merlet, 2001; Randerson et al., 2012). Korontzi et al. (2006) for example estimated that agricultural fires may constitute 30–40% of all fire detections made using the MODIS burned area products, though the true amount is highly uncertain since many of the individual agricultural burns maybe too small to detect using this particular Earth observation approach (Randerson et al., 2012). Smoke emissions from these agricultural fires have significant impacts however, particularly in areas such as East Asia where such burning appears extremely commonplace (Streets et al., 2003).

China has the largest agricultural enterprise worldwide (Frolking et al., 1999) and Xiao et al. (2003) estimate around 1.4 million km^2 of the country is given over to crop production. Until recently, crop residues have been the second largest industrial waste product produced in China (Qu et al., 2014). Whilst field burning of these residues has been largely forbidden in China since the late 1990's, and there are state-sponsored efforts to collect and burn the material in power stations or otherwise recycle it, much of the material is still burned *in situ*. Indeed, such field-based burning of crop residues remains extremely widespread across large parts of China (Huang et al., 2012; Zhang et al., 2008). Streets et al. (2003) used total crop production figures to estimate that perhaps 110 million tonnes of agricultural residue is burned annually in China. This represents around 60% of the total biomass burned in the country (the remainder being primarily grassland and forest fires), and around half of all the agricultural burning believed to occur across Asia. However, all these figures remain very tentative estimates, due to uncertainties in the quantities of dry matter left after harvest, and the relatively poor current understanding of how much residue material is burnt in the field per unit of dry matter residue produced via the different agricultural practices (since, as stated above, some residues are used for other purposes). Whilst very accurate assessments of overall agricultural biomass burning totals may remain elusive therefore, inventories based on satellite remote sensing are continually improving (van der Werf et al., 2010) and it is clear that China remains one of the countries in which agricultural burning is most widespread.

The majority of China's agriculture is located in Eastern China, where the vast majority of crop residue burning also apparently occurs (Huang et al., 2012; Streets et al., 2003). Merged satellite and ground based aerosol optical depth (AOD) data show that Henan, Jiangsu and Anhui provinces are the three main sources of smoke soon after the spring harvest (e.g. Huang et al., 2012; Xue et al., 2014, Fig. 1). In these areas, most fields support at least two crops per year, for example with wheat being grown over winter, harvested in June and the stubble often burned before the fields are rapidly flooded via irrigation networks and rice is planted. The rice is harvested in October, and the fields are then drained, the rice straw often burned, and the fields prepared again for wheat (Huang et al., 2012). The intensity of this agricultural cycle, the difficulties and costs associated with crop residue collection in the many non-mechanised farming areas, the lack of other significant uses for certain of the residues types in many parts of the country, together with a sometimes unclear overall management plan to guide the large-scale alternative crop residue utilisation, leads to many farmers burning the residues *in situ*, as demonstrated in Fig. 1 (Qu et al., 2014).

1.2. Agricultural residue fire emissions

Agricultural residue burning releases smoke containing a wide variety of trace gases (e.g. CO_2, CO, CH_4, NH_3 and NO_x), along with BC and organic carbon (OC) aerosols. These can have significant environmental effects both locally and at large distances downwind, even affecting densely populated urban areas well outside of the agricultural areas themselves (Chan and Yao, 2008; Zhang et al., 2011). Simulation modelling of emissions transport in the Yangtze River Delta region attributed up to 37% of $PM_{2.5}$, 70% of OC and 61% of BC to the smoke from agricultural residue fires in neighbouring provinces, hundreds of km away (Cheng et al., 2014), and in Beijing for example, severe episodes of crop residue burning are estimated to contribute perhaps 50% of the OC aerosols making up the city-wide haze (Duan et al., 2004), worsening the existing air quality problems (Li et al., 2010; Du et al., 2011). There remains, however, an increasing need to better understand the exact gaseous and aerosol species makeup of smoke emitted from crop burning fires, so that their contributions can be better quantified in emissions inventories, and such impacts better assessed.

To estimate the total emissions of each smoke constituent, estimates of crop residue fuel consumption must be multiplied by an emissions factor (EF; g kg^{-1}) for each emitted species, representing the amount of that species emitted per unit of dry fuel burned (Andreae and Merlet, 2001). As with other biomass fires, the EFs of crop residue burns most likely depend on the physical properties of the fuel (e.g. packing density, fuel diameter, moisture content) and the fire characteristics (e.g. the relative proportions of flaming or smouldering phase combustion) (Andreae and Merlet, 2001; van der Werf et al., 2010; Wooster et al. 2011). Current knowledge regarding agricultural residue burning emissions factors has primarily been based on laboratory studies (e.g. Andreae and Merlet, 2001; Zhang et al., 2008), where fire behaviour can be somewhat different to those of real landscape-scale fires (Delmas et al. 1995; Wooster et al., 2011). Furthermore, field-based EFs measured in one region, for example a largely mechanized harvesting area in Mexico, may differ markedly from those appropriate to the more manually farmed areas in another country, even if the actual crop type (e.g. wheat) is the same (Akagi et al., 2011). Due to their major impact on air quality, there is a special concern on emitted particles, including the amount of black carbon as opposed to other aerosols (Cheng and Lin, 2013). Particulate emission from fires appears quite dependent on the amount of flaming and smouldering combustion occurring (Reid et al., 2005), so field measurements of emitted particles should ideally be performed in parallel with CO and CO_2 measurements in order to better quantify particulate emission factors during different fire phases (in which the ratio of these two key gases can vary markedly).

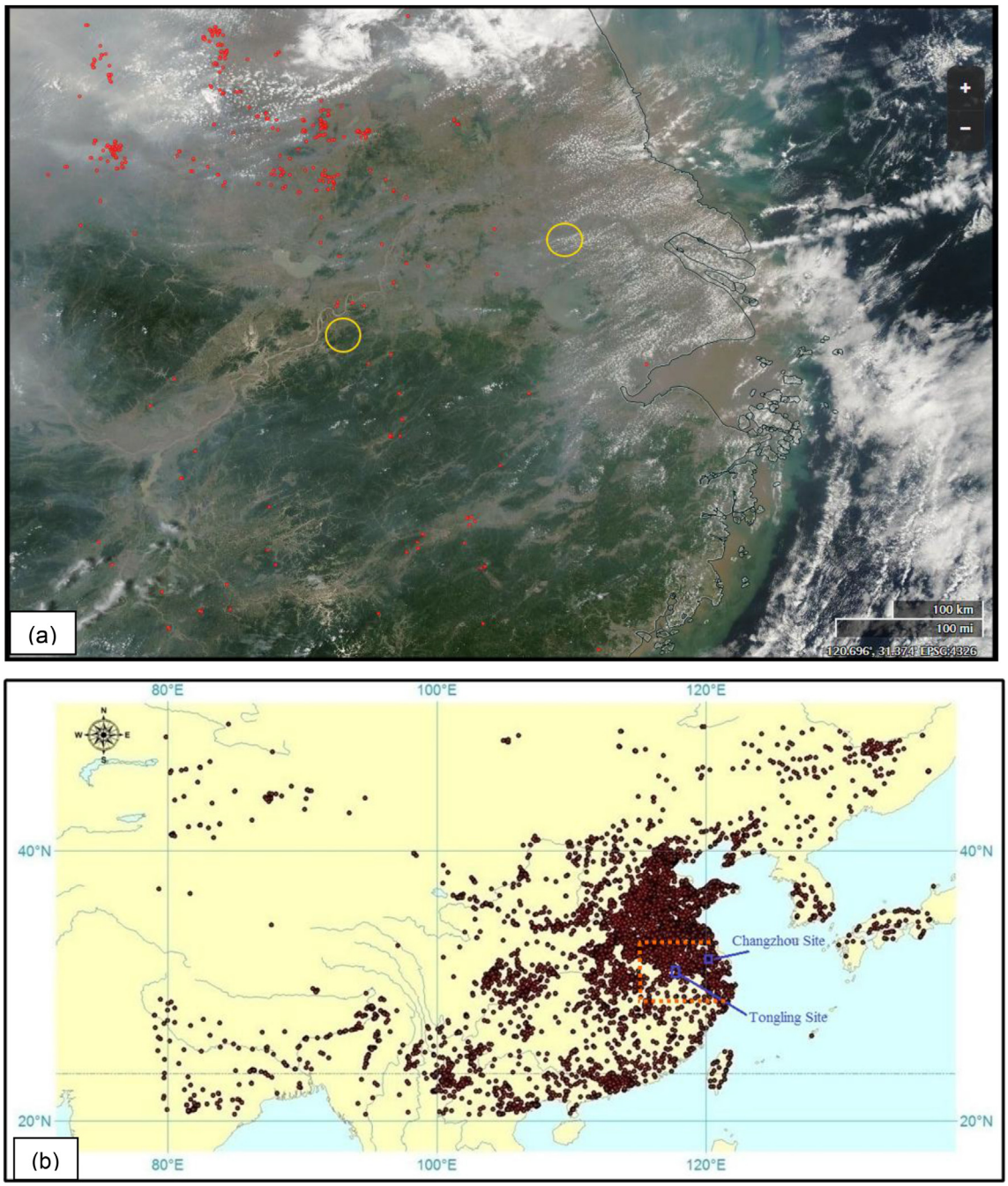

Fig. 1. Fire activity in China during the period of the fieldwork, with the sites close to the cities of Changzhou and Tongling marked. (a) Aqua MODIS true colour composite of part of eastern China taken on 11 June 2014, with MOD14/MYD14 Terra and Aqua active fire detections of that day overlain in red and the fieldwork sites circled (Giglio et al., 2003). Smoke from the fires can be clearly seen in this image, which is adapted from the NASA Worldview system (b). Distribution of actively burning fires detected across China throughout June 2013, as detected by the same MODIS active fire products, and with the area imaged in (a) outlined along with the two fieldwork sites. The widespread nature of burning in both the fieldwork area and throughout much of China at this time is readily apparent. (For interpretation of the references to colour in this figure caption, the reader is referred to the web version of this article.)

The work described here reports our recent work in developing and deploying a field-based smoke emissions measurement approach in eastern China, using this to assess the trace gas and particulate makeup, and ultimately the emissions factors, of smoke from the burning of wheat stubble, rice straw, and rape-seed residues, three of the most frequently burned crop residues in China. We compare results to simultaneous measurements obtained from an open path Fourier transform infrared (OP-FTIR) spectrometer, first used to derive such EFs in savannah regions (Griffith et al., 1991; Wooster et al., 2011). To our knowledge this is the first time these approaches have been used together on agricultural residue fires, and if proved viable such field-derived datasets representative of real *in situ* burning conditions can be expanded to other areas of agricultural burning.

2. Methodology

2.1. Sampling box design, build and test

For this work, we designed and deployed a new smoke sampling system for the close range, *in situ* measurement of the mixing ratios of CO and CO_2 and the mass and BC content of $PM_{2.5}$ in smoke from agricultural fires. The aim was that these measurements could then be used to calculate the emission ratios (ERs) and EFs of these species, disaggregated by combustion phase (flaming/smouldering), and also these could be combined to deliver a 'fire integrated' EF measure appropriate for the entire burn and for use with measures of fuel consumption to provide new estimates of the total emissions released (e.g. Andreae and Merlet, 2001; Wooster et al., 2011). Details of sampling system design and test are presented in the Supporting Information, and summarized below.

A single inlet design using a $PM_{2.5}$ size selective impaction inlet (BGI miniPM® inlet 5011, 5 l min^{-1}) provided both gas and aerosol samples to a range of different instruments all housed in a wheeled peli case (see Fig. 2). A flow splitter (TSI 3708) isokinetically divided the airstream and aerosols into three pathways. Pathway 1 was drawn by a TSI Dustrak; and the eluent flow, now particle-free, was used to provide the CO and CO_2 gas sensors with an ambient sample. Pathway 2 was drawn by a Casella Apex Pro pump; and PM2.5 then collected on a filter. Pathway 3 was drawn by a combination of a Casella Apex pump and a microAeth AE51 (Cheng and Lin, 2013) to measure black carbon.

Electrochemical and NDIR sensors are typically characterised by non-zero response 'lag' times, generally specified via a T90 metric (Roberts et al., 2012), and these details are provided in the Supporting Information. To minimise measurement impacts from the combination of lag times and the rapidly changing trace gas mixing ratios experienced during *in situ* smoke plume measurements (Reid et al., 2005), the outputs from the gas sensors were averaged over 20s for trace gas emission ratio (ER) derivation. This averaging period was further increased to 120s when comparing the gas and aerosol measurements, and such averaging is commonly used in plume investigations when relying on different instruments to target diverse species whose concentrations will later be used to derive emissions ratios (e.g. Reid and Hobbs (1998); Roberts et al., 2014).

2.2. Sampling approach

Fieldwork took place in Eastern China in June 2014, coinciding with the main harvest and burning time in this part of China (Fig. 1a), which the MODIS Active Fire product (Giglio et al., 2003) confirms (Fig. 1b). Smoke emissions from *in situ* burning were measured in four different fields close to the two cities marked in Fig. 1, Changzhou City (31.75°N, 128.11°E) and Tongling City (30.84°N, 117.65°E). Wheat, rice and rapeseed residues were used, burned in their most common way (spreading fires for wheat and bonfires for the other two fuels; Fig. 3). Each burn took 6–30 min to complete, depending on the field size and shape, fuel load, and wind velocity (Table 1). Though wheat is normally burned as stubble in spreading fires, samples of wheat stubble of ~5 kg mass were also burned as a bonfire to help assess the specific emissions related to the flaming and smouldering phases of its combustion (see Table 1, Fire 3a and Fire 3b).

During the spreading fires, smoke was mostly advected horizontally, allowing the sampling system described in Section 2.1 to appropriately capture the ground-level plume. For the bonfires, the inlet of the sampling box was fit into one end of a 100 mm pipe attached to a pump that drew smoke into the pipe a significant distance ahead of the sampling box inlet. The pipe inlet end was linked to a >5 m long lightweight pole that was easily controlled to allow the pipe to capture smoke from the vertically rising smoke (Fig. 3b).

A portable MIDAC open-path Fourier transform infrared (OP-FTIR) spectrometer and IR emitting lamp was deployed co-incident with the smoke sampling system on some of the fires, in order provide comparison trace gas assessments based on the methods described in Wooster et al. (2011). Further details of all measurement approaches employed are provided in the Supporting Information.

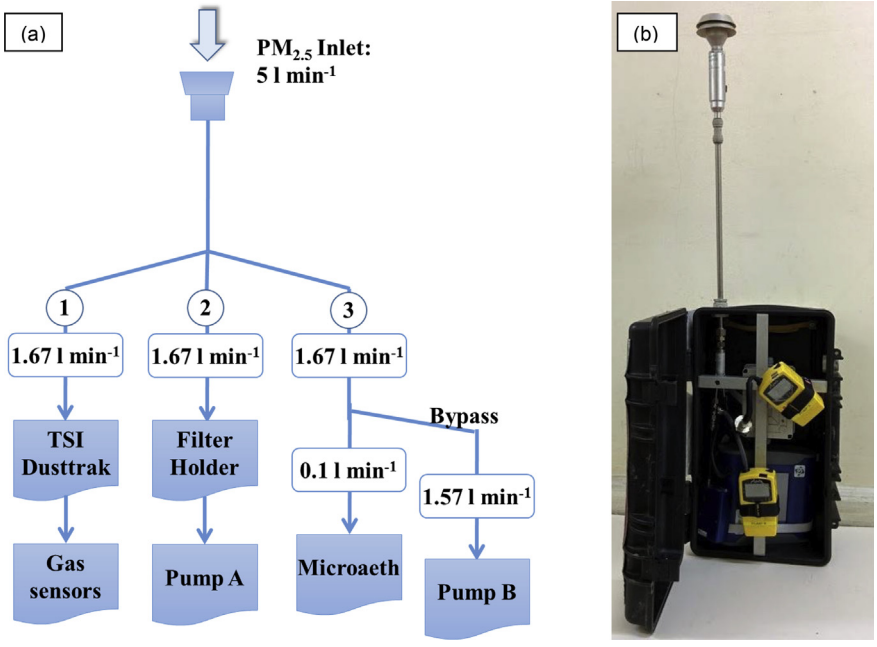

Fig. 2. Design of the smoke sampling system developed and deployed herein with (a) flow rates, and (b) completed sampling system contained in its pelicase shown.

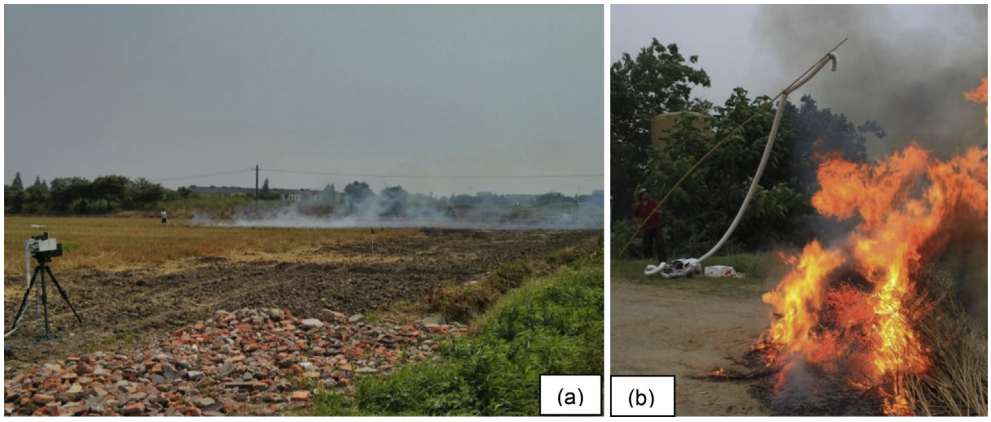

Fig. 3. Photographs of two of the agricultural fires studied herein. (a) was taken during Fire No. 4, which is a spreading wheat stubble fire. The wind was blowing from west to the east (left to right in the photo), the smoke sampling box is standing downwind inside the ground level smoke plume, whilst the FTIR spectrometer was located north of the fire viewing southward to measure the spectra of the IR lamp that was behind the smoke plume and around 20 m away. (b) was taken during Fire No. 9 on a rapeseed residue bonfire. The inlet of the smoke sampling box was fitted into one end of the large diameter sampling pipe, and a pump used to pull the smoke into the pipe so that it could be captured by the sampling system inlet. Visible clouds of soot can be seen in the smoke plume emanating from the top of the flames.

Table 1
Detail of the fires and their mean excess CO, CO_2 mixing ratios and excess BC, $PM_{2.5}$ mass concentrations as measured in China during the June 2014 field campaign.

							Mean gas/particle measurement			
Fire no.	Fire code	Site[a]	Fuel	Fire type	June	Fire duration (minutes)	ΔCO (ppm)	ΔCO_2 (ppm)	ΔBC (mg m^{-3})	ΔPM2.5 (mg m^{-3})
1	0610run1	A	Wheat	Spreading	10th	6	25	493	0.25	2.1
2	0610run2	A	Wheat	Spreading	10th	28	8	138	0.15	1.7
3	0610run3	A	Rice	Bonfire	10th	8	22	374	0.20	3.2
4	0613run1	B	Wheat	Spreading	13th	23	28	452	0.39	4.9
5	0614Run1	B	Wheat	Spreading	14th	22	28	641	0.63	5.5
6a	0614Run2_f	B	Wheat	Bonfire	14th	5	1	–	0.15	0.4
6b	0614Run2_s	B	Wheat	Bonfire	14th	10	51	–	0.06	8.6
7	0615run1	B	Wheat	Spreading	15th	22	34	928	0.46	6.9
8	0615run2	B	Wheat	Spreading	15th	29	8	171	0.05	2.9
9	0616Run1	C	Rapeseed	Bonfire	16th	10	33	605	0.54	3.9
10	0616Run2	C	Rapeseed	Bonfire	16th	7	8	264	0.19	1.1
11	0616Run3	C	Rapeseed	Bonfire	16th	9	65	622	0.37	3.8
12	0616Run4	C	Rice	Bonfire	16th	14	7	197	0.06	1.5
13	0616Run5	C	Rice	Bonfire	16th	16	20	532	0.22	4.5
14	0618run1	D	Rice	Bonfire	18th	24	23	1117	0.20	12
15	0619run1	D	Rapeseed	Bonfire	19th	14	89	1317	0.89	13

[a] Site A was close to Changzhou City, whilst sites B, C and D were close to Tongling City (Fig. 1).

2.3. Emission factor calculation methodology

The EFs (g kg^{-1}) of the trace gases present in the smoke were calculated using the carbon mass balance method used by Yokelson et al. (1999) and many others:

$$EF_x = 1000 F_c \frac{MM_x}{MM_c} \frac{C_x}{C_t} \quad (1)$$

Where F_c is the mass fraction of carbon in the fuel (0.5 ± 0.05; Yokelson et al., 1999), MM_x is the molecular mass of trace gas species x (limited to CO and CO_2 when considering data from the small gas sensors present in the smoke sampling system of Fig. 2, but expandable to other gases when considering the data from the FTIR system [as per Wooster et al., 2011]). MM_c is the molecular mass of carbon (0.012 kg mol^{-1}), and where $\frac{C_x}{C_t}$ is the ratio of the number of moles of species x divided by the total number of moles of carbon (assessed over key emitted carbon containing species). Further details of this calculation are provided in the Supporting Materials. We also calculated the modified combustion efficiency (MCE), commonly used as an indicator of the relative magnitude of flaming and smouldering phase combustion (Ward and Radke, 1993):

$$MCE = \frac{1}{(1 + ER_{CO/CO_2})} \quad (2)$$

To derive the EFs of the aerosol components ($EF_{PM2.5}$ and EF_{BC}; g kg^{-1}) we developed a new approach using the EF of a reference gas and the abundance ratio of the aerosol and gas in question ($S_{particle/gas}$; mg m^{-3} ppm^{-1}), derived from the slope of the linear best fit between the excess mass concentration measures of the aerosol species ($PM_{2.5}$ or BC) and the excess mixing ratio of the reference gas (either CO_2 or CO) recorded in the same sample over the same averaging period:

$$EF_{aerosol} = aS_{aerosol/gas} EF_{\text{gas}} \quad (3)$$

where a is a factor included for unit conversion (having the value of 0.909 ppm (mg m^{-3})$^{-1}$ when using CO_2 as the reference gas, and 0.556 ppm (mg m^{-3})$^{-1}$ when using CO).

3. Results

3.1. Gas and aerosol measurements

The mean trace gas and aerosol abundances in the smoke recorded by the sampling system for each fire are listed in Table 1, expressed as excess measures via subtraction of the pre-fire values. The recorded excess trace gas mixing ratios, ΔCO_2 and ΔCO, varied between 138–1317 ppm and 1–89 ppm respectively, whist the mean excess mass concentrations of $PM_{2.5}$ and BC varied between 1.1–13 mg m^{-3} and 0.06–0.89 mg m^{-3} respectively. Since the inlet of the sampling system was always located within 20 m of the fire emissions source, these values are directly representative of the agricultural burning, uninfluenced by any other emissions source and without any major atmospheric processing. The abundances appear significantly higher than those obtained at greater distances from the source fire (e.g. Yang et al., 2008; Zhang et al., 2013).

We use time series of measurements from two fires (Fire No. 4 and Fire No. 11) to demonstrate the performance of our smoke sampling system. In spreading wheat Fire No. 4 (Table 1), Fig. 4 indicates multiple peaks in the gas and aerosol time series, caused by the contributions of several discrete 'plumes' being sampled over the course of the fire (e.g. as the wind changed, the fire front spread across the field, and the sampling box was moved to keep well within the smoke). A clear difference in the width of the peaks between the gas and aerosol measurements can be seen in these time series, with the aerosol signals being noticeably sharper. As an example, several peaks can be seen before 17:14 h (local time) for all constituents, but are more distinguishable in the $PM_{2.5}$ and BC data than in the CO_2 and CO records. This difference is reflective of the significant lag times of the gas measurements compared to the particulate measurements, resulting from the combination of the T90 sensor response times and the placement of the gas sensors in the smoke sampling system measurement tube array (see Section 2.1 and Supporting Information). This lag effect delays the CO_2 and CO measurement peaks, changing their shape somewhat relative to the matching aerosol measures. For example, around the times of the multiple plumes sampled by the system in the last third of the time series, the $PM_{2.5}$ and BC data show five discrete spikes, ending around 17:25:13 h. By contrast, the CO electrochemical sensor shows a less well resolved response, with the individual plumes less discernible, whilst the faster response NDIR CO_2 sensor (K30) more clearly discerns at least three individual peaks. Thus the instantaneous aerosol and trace gas data cannot simply be combined as is, but rather must be time-averaged for use in ER and EF estimation, as discussed in Section 2.1. A somewhat similar approach was recently demonstrated by Roberts et al. (2014) when using different electrochemical sensors to derive emission ratios of volcanic plumes.

The second example, Fire No. 11 (piled rapeseed residue 'bonfire') at first showed intense flaming activity similar to that seen in Fig. 3b, and then smouldered for some time (changing its dominant combustion phase around 17:32 h local time in Fig. 5, when CO mixing ratios started to substantially increase). During the flaming phase of this burn, the modified combustion efficiency (MCE) is ≥ 0.95, indicating efficient and near complete combustion. The first four $\Delta PM_{2.5}$ measurement peaks are 39, 22, 21 and 39 mg m^{-3}, which each contain 7%, 10%, 12% and 6.6% of black carbon (peaks of 2.2–2.9 mg m^{-3}). After 17:32 h, BC abundance substantially reduces, with only a single plume exceeding 1 mg m^{-3} after that time. However, $PM_{2.5}$ abundance shows increasing peak magnitudes after this time, up to 54 mg m^{-3}, and consequently the BC to $PM_{2.5}$ ratio of the smoke decreases to around 1% over this period. This indicates that high BC to $PM_{2.5}$ ratios are seen in the flaming stage, and generally much lower ratios characterise the smouldering phase, a finding which agrees with prior research indicating that the BC fraction of emitted aerosol differs between the phases of crop residue burns (Li et al., 2009). Reid and Hobbs (1998) report this effect more generally for biomass fires, and we find the effect to be more apparent in this crop residue bonfire (Fig. 5) than in the spreading fire (Fig. 4), since in the latter case whilst flaming combustion dominates in the moving headfire, a trailing 'smoking zone' is typically also present that is dominated by areas of still smouldering combustion (Wooster et al., 2011). Thus,

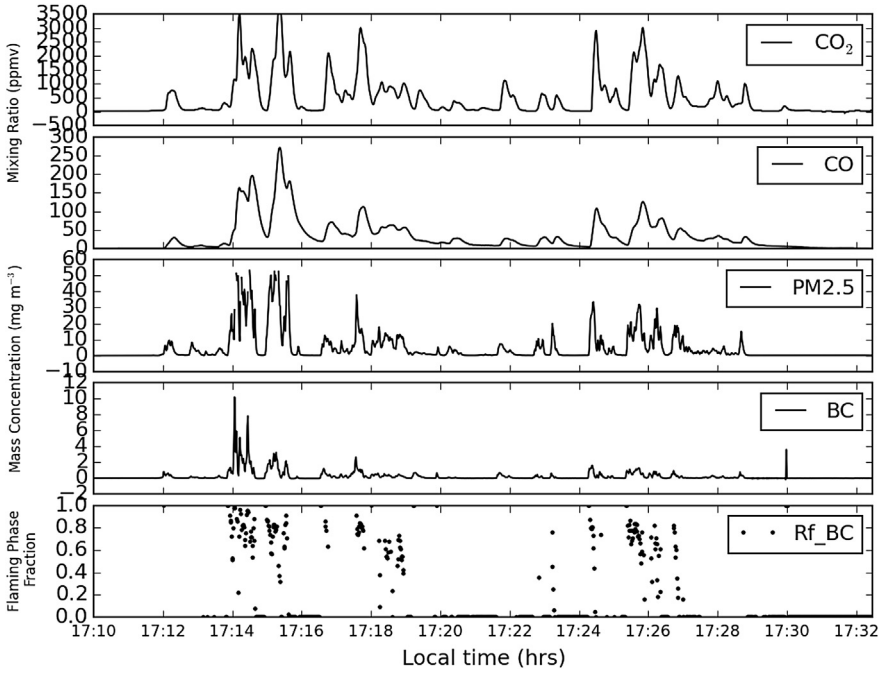

Fig. 4. Time series of excess CO_2 and CO mixing ratio (ppmv), and $PM_{2.5}$ and BC mass concentrations (mg m^{-3}) for Fire No. 4, with the proportion of flaming combustion contributing to the BC mass concentrations being measured also shown (RF[BC] from Equation 8). Wheat stubble was used as the fuel for this spreading fire, as shown in Fig. 3a.

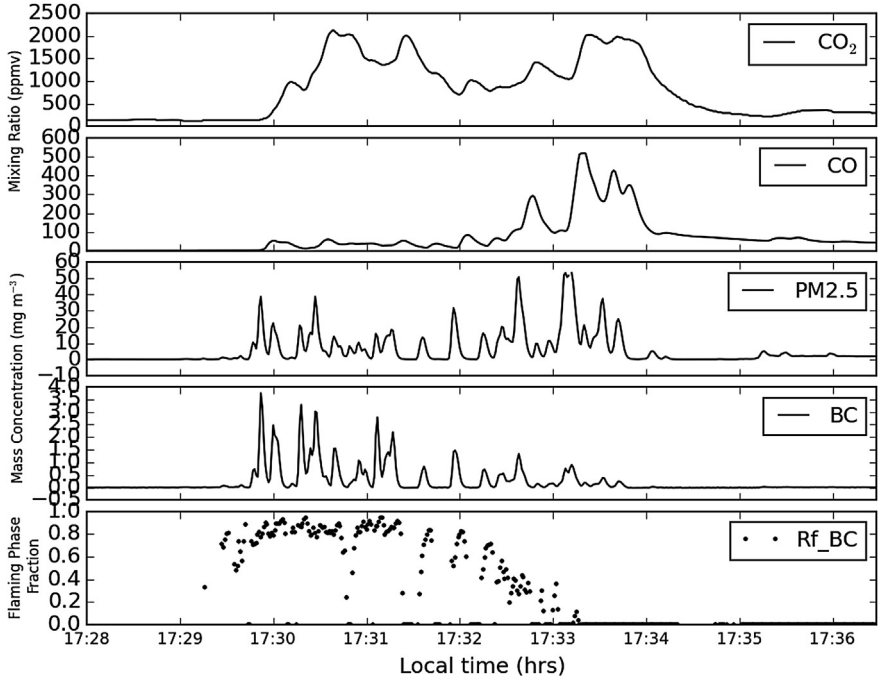

Fig. 5. Time series of CO_2 and CO mixing ratio (ppmv), $PM_{2.5}$ and BC mass concentrations (mg m^{-3}) for Fire No. 11, with the proportion of flaming combustion contributing to the BC mass concentrations being measured also shown (Rf[BC] from Equation 8). Rapeseed residue was used as fuel for this burn, burned in a bonfire similar to that shown in Fig. 3b.

whilst the ground-level plume of a spreading fire typically contains a mix of smoke from both combustion phases (Lacaux et al., 1996; Wooster et al., 2011), the bonfire style of burning may more clearly commence with almost fully flaming combustion and end with almost solely smouldering activity.

3.2. Emission ratios and combustion phases

Section 3.1 has highlighted that different $PM_{2.5}$ to BC emission ratios are seen during the flaming and smouldering phases of the sampled agricultural residue fires. During the wheat residue bonfire (Fire No. 6) the abundances of BC and $PM_{2.5}$ during the flaming (Fire No. 6a) and smouldering (Fire No. 6b) phases of this fire were thus analysed individually (Fig. 6).

In both the flaming and smouldering phases (Fig. 6a and 6b respectively), we find strong positive correlations between $PM_{2.5}$ and BC. In the flaming phase, a $PM_{2.5}$ to BC mass concentration ratio of 2.0 mg m^{-3} (mg m^{-3})$^{-1}$ is seen (r = 0.97), whilst for the smouldering phase the ratio is much higher at 80.7 mg m^{-3} (mg m^{-3})$^{-1}$. The smouldering phase correlation coefficient is slightly lower (r = 0.92), possibly contributed to by the relative difficulty in sampling smoke from purely smouldering activity, since small pockets of flaming combustion still often exist close to the fuel surface during smouldering-dominated periods (Hays et al., 2005). This comparison of flaming and smouldering dominated burning presented in Fig. 6 nevertheless further highlights the very large difference in the emission ratio of $PM_{2.5}$ to BC for these two combustion phases, which can be also found in the

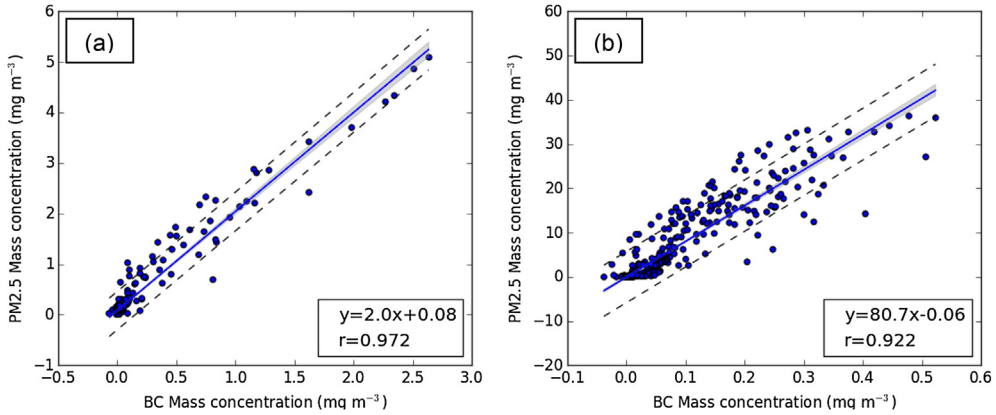

Fig. 6. Linear relationship between $PM_{2.5}$ and BC mass concentrations for (a) pure flaming phase combustion (Fire No. 6a) and (b) pure smouldering phase combustion (Fire No. 6b). Fire details are listed in Table 1, and wheat stubble is the fuel in both cases, burned as a bonfire. The blue line represents the least squares linear best-fit, which is then taken as the $PM_{2.5}$ to BC emission ratio for the 'pure' combustion phases in this fuel type, along with the 95% confidence intervals on the slope (grey filled polygon) and on the prediction (dashed line). These slopes are thus taken as the emission ratio for wheat undergoing flaming combustion [S_f; mg m^{-3} (mg m^{-3})$^{-1}$ and smouldering combustion [S_s; mg m^{-3} (mg m^{-3})$^{-1}$] respectively. (For interpretation of the references to colour in this figure caption, the reader is referred to the web version of this article.)

spreading fire data shown in Fig. 4 as discussed above. Our data indicate that the contribution of BC to $PM_{2.5}$ rises high as 50% during the flaming phase, whilst during smouldering phase it can decrease to little over one percent. Prior studies have indicated that, in general, vegetation fires with more intense flaming combustion, generating higher temperatures, are more likely to be oxygen limited and can thus produce much larger amounts of soot-based (BC) aerosols than does smouldering dominated burning (Martins et al., 1998; Reid and Hobbs (1998); 2005; Chakrabarty et al., 2006). Our findings imply that, even though total $PM_{2.5}$ abundances appear higher in the smouldering phase plume, most of the BC maybe emitted from agricultural residue fires during the flaming phase, particularly so since in these types of fine fuels most of the fuel consumption often occurs during flaming activity when combustion rates are much higher than in the (perhaps longer duration) smouldering phase (as discussed for savannahs by e.g. Wooster et al., 2011).

Using our finding of a very significantly different $PM_{2.5}$ to BC emission ratio for flaming combustion [S_f; mg m^{-3} (mg m^{-3})$^{-1}$, from Fig. 6a] and smouldering combustion [S_s; mg m^{-3} (mg m^{-3})$^{-1}$ from Fig. 6b] allows us to develop a simple linear mixing model to quantify the relative amounts of each combustion phase contributing to the smoke being sampled. We assume that the ratios represented in Fig. 6a and b represent that from the pure flaming and pure smouldering phase activity respectively, and that these ratios are valid for all the wheat residue fires assessed. Details of the mixing model can be found in the Supporting Information, and are summarized below.

For both BC and $PM_{2.5}$, we assume that the total excess mass concentration measured (ΔM_t; mg m^{-3}) is a linear combination of the instantaneously measured excess mass concentration due to flaming (ΔM_f; mg m^{-3}) and smouldering (ΔM_s; mg m^{-3}) phase combustion:

$$\Delta M_t(PM_{2.5}) = \Delta M_f(PM_{2.5}) + \Delta M_s(PM_{2.5}) \quad (4)$$

and

$$\Delta M_t(BC) = \Delta M_f(BC) + \Delta M_s(BC) \quad (5)$$

And we relate the excess mass concentration of each aerosol type produced from flaming and smouldering combustion using the emission ratios S_f and S_s taken from Fig. 6a and 6b:

$$\Delta M_f(PM_{2.5}) = S_f \Delta M_f(BC) \quad (6)$$

$$\Delta M_s(PM_{2.5}) = S_s \Delta M_s(BC) \quad (7)$$

Then, for BC, the instantaneous flaming phase fraction $R_f(BC)$ [mg m^{-3}. (mg m^{-3})$^{-1}$] representing (at any particular time) the proportion of total sampled BC mass that has come from flaming phase combustion [i.e. $\frac{\Delta M_f(BC)}{\Delta M_t(BC)}$] can be expressed as a function of four known quantities, namely the total sampled excess mass concentration of PM2.5 and BC, $\Delta M_t(PM_{2.5})$ and $\Delta M_t(BC)$ respectively, and the $PM_{2.5}$ to BC emission ratios for flaming and smouldering combustion (S_f and S_s respectively):

$$R_f(BC) = \frac{S_s - [\Delta M_t(PM_{2.5})/\Delta M_t(BC)]}{\left(S_s - S_f\right)} \quad (8)$$

Where the term in square brackets equates to the instantaneous ratio of the excess amount of PM2.5 and BC, which can easily be derived from the measured timeseries (e.g. those shown in Figs. 4 and 5 for Fire No. 4 and 11 respectively for example). Exactly same approach can be used to derive the $PM_{2.5}$ instantaneous

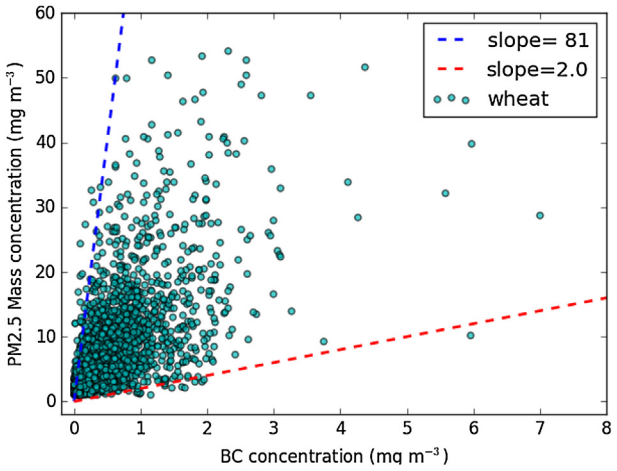

Fig. 7. Scatterplot showing $PM_{2.5}$ and BC mass concentrations from all wheat fire samples, with the emission ratios from pure flaming and smouldering phase combustion shown in Fig. 6 (S_f and S_s respectively) overlain.

flaming phase fraction, $R_f(PM_{2.5})$, and also the flaming phase fractions of the gases CO and CO_2.

However, when analysing rice and rapeseed fires, unlike for wheat we did not directly collect samples of pure flaming and pure smouldering smoke for these fuels from which we could directly obtain the flaming and smouldering emission ratios, S_f and S_s. However, Fig. 7 plots the excess mass concentration of $PM_{2.5}$ and BC for our spreading wheat fires, and based on the observation of clear flaming and smouldering boundaries in these data, which appear quite well characterised by the $PM_{2.5}$ to BC flaming and smouldering ERs (S_f and S_s respectively) derived from the wheat bonfire data shown in Fig. 6a and 6b (and plotted on Fig. 7 as red and blue lines respectively), we applied a 'boundary detection' approach to the spreading wheat fire measurements. The idea here is to pilot use of this approach for the derivation of S_f and S_s, such that it can be applied in cases where obviously "pure" samples of flaming and smouldering smoke are unavailable, for example in the case of the rice and rapeseed residue burns sampled here. Based on 95% confidence intervals, the highest and lowest 2.5% of the $PM_{2.5}$ to BC ratio shown in Fig. 7 were selected, and a linear best fit applied to these 'boundary' data to estimate the $PM_{2.5}$ to BC emission ratios for flaming and smouldering combustion of wheat, at 1.9 mg m^{-3} (mg m^{-3})$^{-1}$ and 58.1 mg m^{-3} (mg m^{-3})$^{-1}$ respectively (yielded with correlation coefficients (r) of 0.82 and 0.88 respectively; Table 2). These particulate ERs are close to those obtained via our sampling of explicit flaming and smouldering smoke (with a scaling factor of 1.3) from wheat combustion separately (i.e. those shown in Fig. 6a and 6b respectively), thus demonstrating the viability of the 'boundary detection' approach (See Supporting Information for more details of this comparison). The same 'boundary detection' approach was then applied to the rice and rapeseed residue aerosol data (Fig. 8), and was also used with the CO_2 and CO data of all three agricultural residue fuels (Fig. 9) to derive a flaming and smouldering phase emission ratio (ppmv.(ppmv)$^{-1}$) for each trace gas (reported in Table 2). An averaging period of 120 s was selected to compare the aerosol and trace gas data, as discussed in Section 2.1, and the derived flaming phase fractions, $R_f(x)$, of the two flaming-dominated compounds (CO_2 and BC) were found to show similar trends (Fig. 10).

Based on the time-series of $R_f(x)$ calculated for each sampled gas and aerosol species, the fire-integrated flaming-fraction $F(x)$ was also estimated, for each type of fire and each combustion product. For example, for wheat the fire-integrated fraction of black carbon

Table 2
Trace gas (CO/CO_2) and particulate ($PM_{2.5}/BC$) emission ratios (ERs) for discrete flaming and smouldering phase combustion, as derived from the 95% confidence interval 'boundary detection' approach applied to the data of each fuel type (see Section 3.2). The correlation coefficients (r) for each linear best fit used in the calculation of the emissions ratios are also reported.

Fuel		$PM_{2.5}/BC$		CO/CO_2[a]	
		ER ($mg\ m^{-3}$. $mg\ m^{-3}$)	r	ER ($ppmv.ppmv^{-1}$)	r
Wheat	Flaming	1.9	0.82	0.0184	1.00
	Smouldering	58.1	0.88	0.46	0.98
Rice	Flaming	7.3	0.88	0.0043	0.85
	Smouldering	66.3	0.81	0.21	0.81
Rapeseed	Flaming	0.50	0.90	0.0186	0.95
	Smouldering	47.5	0.74	0.17	0.97

[a] Calculated from 20s averages to account for the different response times of the two trace gas sensors (Table 2).

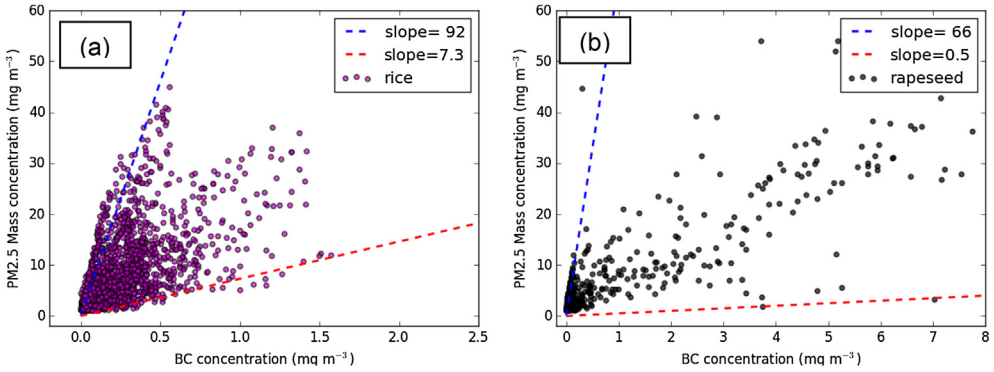

Fig. 8. Scatterplot of $PM_{2.5}$ and BC mass concentrations from (a) all rice, and (b) all rapeseed fires, with the $PM_{2.5}$ to BC emission ratios for 'pure' flaming and 'pure' smouldering overlain (as derived from the 95% confidence interval method discussed in Section 3.2).

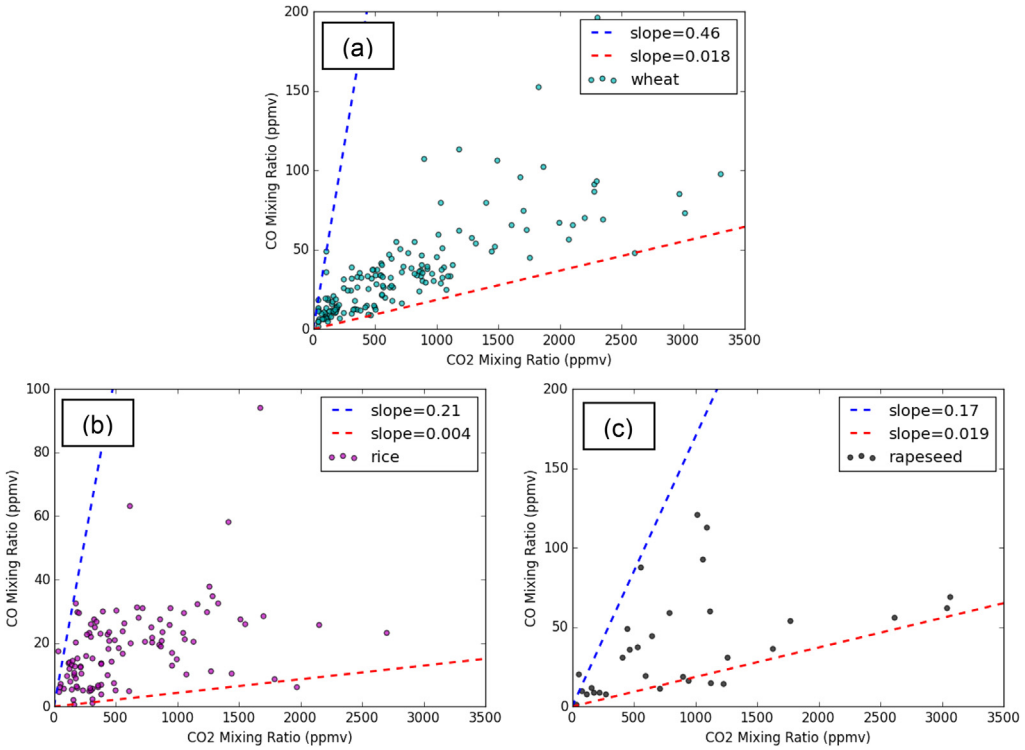

Fig. 9. Scatterplot of CO and CO_2 mixing ratio measures from (a) all wheat, (b) rice, and (c) rapeseed fires, with the CO and CO_2 emission ratios for 'pure' flaming and 'pure' smouldering overlain (as derived from the 95% confidence interval method discussed in Section 3.2).

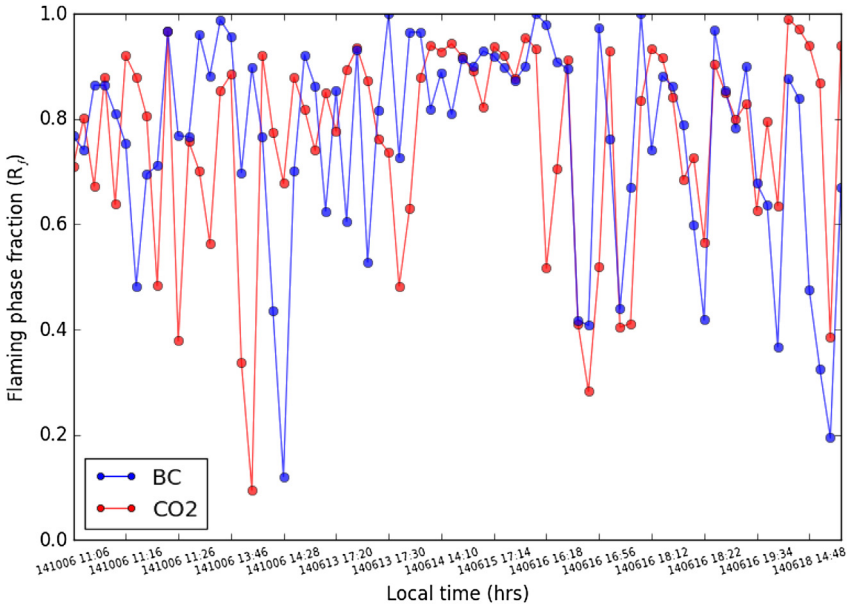

Fig. 10. Time series of flaming phase fraction (R_f) for the two flaming-dominated compounds (BC and CO_2), representing the estimated proportion of the samples of these compounds measured by the smoke sampling system that has come from flaming phase combustion, derived as discussed in Section 3.2.

emitted by flaming combustion was calculated as:

$$F(BC) = \frac{\sum M_t(BC) R_f(BC)}{\sum M_t(BC)} \quad (9)$$

Where $M_t(x)$ is the mass concentration (for aerosol), or mixing ratio (ppmv) for gas, of the target species recorded over the 120 s averaging period. The corresponding fire-integrated fractional contribution of the smouldering phase to the production of the same species was then calculated as $[1 - F(x)]$. Table 3 presents the results of this calculation, where the flaming stage is confirmed to dominate in terms of BC (and CO_2) production.

3.3. Emission factor determination

3.3.1. Trace gases

The trace gas time series for each burn, discussed in Section 3.2 and consisting of n discrete measurements after the 120 s averaging, were used to calculate a timeseries of instantaneous emission ratios, $ER_t(x)$ and then emission factors, $EF_t(x)$. 'Fire integrated' EFs were then calculated by weighting each instantaneous EF by the corresponding instantaneous excess abundances $(\Delta CO_2 + \Delta CO)_t$ of the two primary trace gases that make up more than 95% of the emitted carbon, used as a measure of the amount of smoke being produced by the fire at measurement time t. This weighting approach has been used previously in laboratory burns, and was recently applied by Paton-Walsh et al. (2014) in an open burning situation. See Lacaux et al. (1996) and Wooster et al. (2011) for previous examples of such 'Fire integrated' trace gas EFs calculations):

$$\textit{Fire integrated } EF(\textit{species } x) = \frac{\sum_{t=0}^{n} EF_t(x)(\Delta CO_2 + \Delta CO)_t}{\sum_{t=0}^{n} (\Delta CO_2 + \Delta CO)_t} \quad (10)$$

Our 'fire integrated' EF_{CO_2} (Table 4) for the spreading wheat residue fires is 1739 ± 19 g kg^{-1}, somewhat higher than the 1470 g kg^{-1} and 1558 g kg^{-1} reported previously for Chinese wheat residues (Li et al., 2007; Zhang et al., 2008), though these latter measures are based on laboratory fires rather than field sampling. The difference may reflect the fact that laboratory fires usually comprise of piles of fuel that burn initially in flaming combustion, but which may have a longer and most significant smouldering phase than does a typical spreading fire measured in the field, and this supports the view that laboratory fires may behave differently to more 'natural' *in situ* combustion cases, and that care must be taken when combining and comparing these different types of measurement (Delmas et al., 1995; Wooster et al., 2011; Yokelson et al., 2013). Our field-measured fire integrated CO_2 emissions factors for wheat are, however, very close to the 1787 g kg^{-1} for wheat also measured in the field in an Indian agricultural area by Sahai et al. (2007). We also find that the fire integrated EF_{CO2} for our field-measured rice and rapeseed burns are similar to that of our wheat burns, at 1761 ± 30 and 1704 ± 27 g kg^{-1} respectively. By contrast, our fire integrated carbon monoxide emissions factor varies quite widely amongst the three crop residues studied, with

Table 3
Fire-integrated flaming (F) and smouldering (1-F) fractions defining the relative contribution of flaming and smouldering phase combustion to the total amounts of CO, CO_2, $PM_{2.5}$ and BC sampled by the smoke sampling system for each of the three fuel types. See Section 3.2 for details.

Fuel		CO_2	CO	$PM_{2.5}$	BC
Wheat	Flaming (F)	0.93	0.36	0.59	0.91
	Smouldering (1-F)	0.07	0.64	0.41	0.09
Rice	Flaming (F)	0.88	0.13	0.36	0.79
	Smouldering (1-F)	0.12	0.87	0.64	0.21
Rapeseed	Flaming (F)	0.60	0.14	0.75	0.96
	Smouldering (1-F)	0.40	0.86	0.25	0.04

Table 4
Trace gas (CO_2 and CO) emission factors (EFs) with uncertainties, calculated from the data of the smoke sampling system for the three agricultural residue fuels, using the time series of EFs weighted by the excess CO_2 +CO abundances (see Section 3.3.1). Shown for comparison are the equivalent EF values calculated from the OP-FTIR data using the techniques of Wooster et al. (2011) (from Fire No. 7).

Sampling box species emissions factor (g kg^{-1})				OP-FTIR
Fuel		EF_f	EF_f uncertainty	EF_{FTIR}
Wheat	CO_2	1739	19	1723
	CO	60	12	66
Rice	CO_2	1761	30	–
	CO	47	19	–
Rapeseed	CO_2	1704	27	–
	CO	82	17	–

wheat (60 ± 12 g kg^{-1}) and rice (47 ± 19 g kg^{-1}) having a lower EF_{CO} than rapeseed (82 ± 17 g kg^{-1}). From the information discussed in Section 3.2, and from Table 3, the CO from the rapeseed residue bonfires indeed appears to be sourced from a higher proportion of smouldering combustion (0.86) than does that from the spreading wheat fires (0.64), which may help explain the higher EF_{CO} of rapeseed compared to wheat. However, the rice residue bonfires have an even lower EF_{co} than rapeseed residue, but are reported to have had a very similar smouldering combustion contribution (0.87). The explanation for this requires further study, but may result from differences in combustion rates between the same combustion phase of different burns, and a similar pattern was observed in previous research (Zhang et al., 2008). Overall, our fire integrated EF_{CO} values appear comparable to the 60 g kg^{-1} obtained for wheat (laboratory combustion) by Li et al. (2007), but significantly lower than those reported by some another laboratory studies (141 g kg^{-1} for wheat and 64 g kg^{-1} for rice; Zhang et al., 2008).

Our FTIR data allowed the determination of EFs for one of the spreading wheat residue fires using a completely independent approach to the smoke sampling system (Fire No. 7, with Equation (2) adjusted to take in account of the increased number of carbonaceous gases (CO_2, CO, methane [CH_4] and formaldehyde [CH_2O]) easily available to be probed using the IR spectroscopy). The OP-FTIR method samples a transect through the plume, representing at any one time a significantly larger proportion of the total smoke production compared to the point based smoke sampling system (Fig. 3a), and also suffers no lag time effects between the measurements of different gases (Wooster et al., 2011). The OP-FTIR derived fire integrated EFs of 1723 g kg^{-1} for CO_2 and 66 g kg^{-1} for CO, included in Table 4, are close to the values derived from the smoke sampling system for the same wheat fuel and well within the reported uncertainty ranges derived from those data. We obtain fire integrated EFs for CH_4 and CH_2O as 2.1 and 1.2 g kg^{-1} respectively using the OP-FTIR method, with these gases accounting for less than 1% of all gaseous emitted carbon and thus indicating the validity of deriving CO_2 and CO EFs from measurements of only those two gases when using the smoke sampling system and Equation (2). The FTIR method can be used to probe many more gaseous species than just these four, though the relatively short pathlengths and thus low abundances of lesser species make this more difficult in this case, and we focus here on the main carbonaceous gases only.

3.3.2. Particulates

To estimate aerosol EFs, linear best fit relationships between both $PM_{2.5}$ and BC and CO_2 and CO were derived from two minute averages of the smoke sampling system measures, as discussed in Section 2.1. Fig. 11 shows the results for wheat (and Figs. S2 and S3 in the Supporting Information for rice and rapeseed residues), and these aerosol-to-trace gas ERs were used alongside the EFs of the relevant gases in Equation (3) to derived the particulate emissions factors.

The particulate EF calculations were undertaken based on both the aerosol-to-CO_2 and aerosol-to-CO emission ratios shown in Fig. 11. We determine $EF_{PM2.5}$ for wheat as 10.0 ± 1.2 g kg^{-1} when using CO_2 as the reference gas, and 6.1 ± 1.3 g kg^{-1} when using CO. For comparison to other measurements derived using a similar technique to that used here, Cachier et al. (1995) recorded simultaneous CO_2 and total particulate matter (TMP) abundances in smoke from savannah fires, and using these data estimated EF_{TPM} for flaming processes as 5.7 ± 2.3 g kg^{-1}, with more than 90% of the mass of TPM being sub-micron in size. This value is comparable with our findings. Cachier et al. (1995) found a considerably higher smouldering phase EF_{TPM} (34.5 ± 12.5 g kg^{-1}), but note that most fuel is burned in the flaming phase, as is the case with our spreading wheat fires.

We suggest our $EF_{PM2.5}$ based on the CO measurement maybe more representative, since the correlation of PM2.5 was higher with CO rather than CO_2 (see Fig. 11). However, as discussed in Section 3.2, the flaming phase fraction (R_f) of BC correlates better with CO_2 (Fig. 10) as they were both flaming phase dominated, and so the EF_{BC} based on CO_2 (0.70 ± 0.09 g kg^{-1} for wheat) is considered a potentially better estimate. The US Environmental Protection Agency (EPA) quote $EF_{PM2.5}$ for wheat burning in the US as 6–10 g kg^{-1}, depending on burning conditions, as previous research found that $PM_{2.5}$ emissions would decrease by over 80% as MCE increased from 92% to nearly 98% (Dhammapala et al., 2007). This EPA suggested range almost exactly brackets the $EF_{PM2.5}$ findings we report from our Chinese wheat residue field burns in Table 5. Akagi et al. (2011) summarizes global crop residue burning EFs from a variety of past studies, calculating an average $EF_{PM2.5}$ of 6.26 g kg^{-1}, and an average EF_{BC} of 0.75 g kg^{-1} for different agricultural crop species, values again quite close to those reported here. Our EF_{BC} for wheat straw is, though, somewhat higher than that from some prior laboratory studies conducted in China (0.43–0.49 g kg^{-1}; Li et al., 2007; Zhang et al., 2008), and again may reflect the increased amount of flaming combustion seen in spreading field-based fires than in the typical 'piled fuel' situations used within laboratories. Our field-based burns show an EF_{BC} of 0.56 g kg^{-1} for rice residue, a little lower than for the spreading wheat fires, but the rapeseed residue fires developed a very high EF_{BC} of 2.89 g kg^{-1} with a fraction of 0.96 contributed by flaming (Table 3), reflective of the intense flaming combustion processes involved (Fig. 3b) that gave off visible clouds of soot in the plume.

4. Summary and conclusions

Crop residue fires in eastern China are believed to contribute significantly to regional air pollution (Chan and Yao, 2008). To study closely the gas and particle emissions from these burns in the field during agricultural burning periods, we have developed and

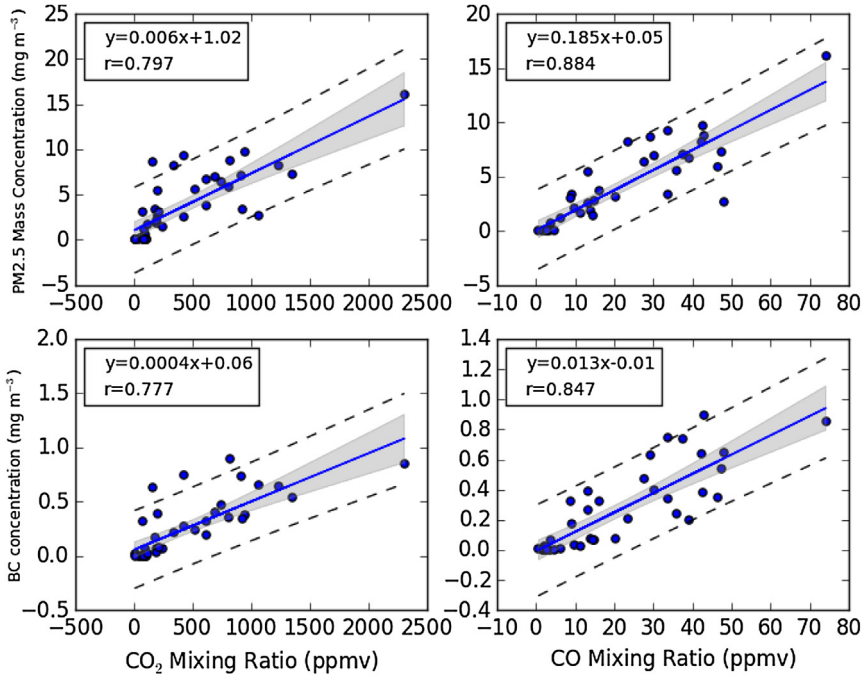

Fig. 11. Scatterplot of $PM_{2.5}$ and BC mass concentrations to excess CO_2 and CO measures from all wheat residue fires, with data presented as 120 s averages. The blue line represents the least squares linear best-fit to the data, taken as the relevant particulate to gas emission ratio for this fuel type, along with the 95% confidence intervals on the slope (grey filled polygon) and on the prediction (dashed line). (For interpretation of the references to colour in this figure caption, the reader is referred to the web version of this article.)

deployed a new portable smoke sampling system for the simultaneous close range measurement of trace gases (CO and CO_2) and aerosols ($PM_{2.5}$ mass and BC). We have used the system to derive gas and particle emission ratios and emissions factors for a series of crop residue fires sampled in eastern China in June 2014. Most prior research on smoke from these types of fuels have either been based on laboratory measurements, and/or have relied on filter-based sampling that provides only the total sampled mass from whole combustion. Our system offers the advantage of allowing continuous *in situ* measurements of smoke generated by naturally behaving agricultural fires (e.g. fires spreading across agricultural fields and field-measured 'bonfires'), which is important as field-burns may well behave quite differently to burns conducted under laboratory conditions (Delmas et al., 1995). Our sampling system allows us to study both inter and intra-fire variability between combustion phases and between different fires and fuels, and we use the data collected along with a new approach (summarised in Eq. (4)) to obtain 'fire-integrated' emission factors for particulates as well as gases.

We studied the combustion of three types of common Chinese agricultural residues (wheat, rice and rapeseed), both spreading fires and bonfires. For all we found quite different trace gas emission ratios during flaming and smouldering periods, and also different BC to $PM_{2.5}$ mass ratios. BC represented a much higher proportion of the total $PM_{2.5}$ generated by these burns during the flaming combustion phase, up to 10 × more in the case of rapeseed, and the CO to CO_2 emission ratio was significantly lower, up to 50 × less in the case of rice residue. The full set of ERs are shown in Table 2, and using the carbon mass balance method we calculated the individual CO_2 and CO trace gas 'Fire integrated' EFs for each fuel type (Table 4). Using these, and the measured ratios of aerosols (BC and $PM_{2.5}$) to trace gases (CO_2 and CO), we estimated the EFs for each type of particulate as well (Table 5). We also probed the wheat fires using open path FTIR spectroscopy (Wooster et al., 2011), and confirmed a very similar set of trace gas EFs for this fire type compared to those derived using our smoke sampling system (Table 4). We find our emission factors to be reasonably similar to those reported by prior studies, but our results from spreading wheat fires are characteristic of more flaming-dominated burning than are most previously reported laboratory measurements (Li et al., 2007; Zhang et al., 2008). This may reflect the increased amount of flaming combustion seen in more 'natural' spreading fires than in typical 'piled fuel' laboratory burns. Our rapeseed residue bonfires showed a very high EF for BC, at up to 2.89 g kg^{-1}, reflective of the intense flaming combustion processes involved that gave off visible clouds of soot.

All our EFs are derived from measures made within 10–20 m of the fires themselves, which were burnt in the field as Chinese farmers do. They are therefore representative of fresh smoke without photochemical processing, and can be regarded as primary EFs for these types of fire. For the aerosols, chamber-based examination of photochemical processing is suggested for future work, since higher EFs maybe expected after hours of atmospheric processing (Akagi et al., 2011). We anticipate combining our EFs with estimates of the amounts of the various residues burned, producing updated agricultural emissions inventories for use in air quality modelling (e.g. Li et al., 2010; Cheng et al., 2014).

Table 5
Particulate emission factors of $PM_{2.5}$ and BC (with uncertainties), derived separately from the ratio of particles to the two measured trace gases (i.e. data of Figure 11) and the CO_2 and CO emission factors listed in Table 4.

	$PM_{2.5}$ emissions factor (g kg^{-1})		BC emissions factor (g kg^{-1})	
	Based on CO_2	Based on CO	Based onCO_2	Based on CO
Wheat	10.0 ± 1.2	6.1 ± 1.3	0.70 ± 0.09	0.43 ± 0.10
Rice	20.3 ± 1.5	9.6 ± 4.3	0.56 ± 0.04	0.25 ± 0.11
Rapeseed	16.9 ± 2.6	5.8 ± 1.3	2.89 ± 0.70	1.01 ± 0.27

Acknowledgements

Within China we gratefully thank Mr. Wu and his family for their assistance, and Mr. Zhang and his family for aiding the fieldwork in Changzhou and Tongling City. We thank Dr. Hefeng Zhang for his suggestions, and Dr Tarjda Roberts for very useful thoughts with regard to sensor use. We thank Dr John Saffell and Mr Wah On Ho of Alphasense Ltd for very helpful discussions. We acknowledge the King's China Award and King's Graduate School who funded T. Zhang. M Wooster is supported by the NERC National Centre for Earth Observation, and NERC Grant NE/J010502/1 funded the field component of this research.

Appendix A. Supplementary data

Supplementary data related to this article can be found at http://dx.doi.org/10.1016/j.atmosenv.2015.05.010.

References

Akagi, S., Yokelson, R., Wiedinmyer, C., Alvarado, M., Reid, J., Karl, T., Crounse, J., Wennberg, P., 2011. Emission factors for open and domestic biomass burning for use in atmospheric models. Atmos. Chem. Phys. 11, 4039–4072.

Andreae, M.O., Merlet, P., 2001. Emission of trace gases and aerosols from biomass burning. Glob. Biogeochem. Cycles 15, 955–966.

Cachier, H., Liousse, C., Buat-Menard, P., Gaudichet, A., 1995. Particulate content of savanna fire emissions. J. Atmos. Chem. 22 (1–2), 123–148.

Chakrabarty, R.K., Moosmüller, H., Garro, M.A., Arnott, W.P., Walker, J., Susott, R.A., Hao, W.M., 2006. Emissions from the laboratory combustion of wildland fuels: particle morphology and size. J. Geophys. Res. Atmos. (1984–2012) 111 (D7).

Chan, C.K., Yao, X., 2008. Air pollution in mega cities in China. Atmos. Environ. 42, 1–42.

Cheng, Y.H., Lin, M.H., 2013. Real-time performance of the microAeth® AE51 and the effects of aerosol loading on its measurement results at a traffic site. Aerosol Air Qual. Res. 13 (6), 1853–1863.

Cheng, Z., Wang, S., Fu, X., Watson, J.G., Jiang, J., Fu, Q., Chen, C., Xu, B., Yu, J., Chow, J.C., Hao, J., 2014. Impact of biomass burning on haze pollution in the Yangtze River delta, China: a case study in summer 2011. Atmos. Chem. Phys. 14, 4573–4585.

Delmas, R., Lacaux, J.P., Brocard, D., 1995. Determination of biomass burning emission factors: methods and results. Environ. Monit. Assess. 38, 181–204.

Dhammapala, R., Claiborn, C., Jimenez, J., Corkill, J., Gullett, B., Simpson, C., Paulsen, M., 2007. Emission factors of PAHs, methoxyphenols, levoglucosan, elemental carbon and organic carbon from simulated wheat and Kentucky bluegrass stubble burns. Atmos. Environ. 41, 2660–2669.

Du, H., Kong, L., Cheng, T., Chen, J., Du, J., Li, L., Xia, X., Leng, C., Huang, G., 2011. Insights into summertime haze pollution events over Shanghai based on online water-soluble ionic composition of aerosols. Atmos. Environ. 45, 5131–5137.

Duan, F., Liu, X., Yu, T., Cachier, H., 2004. Identification and estimate of biomass burning contribution to the urban aerosol organic carbon concentrations in Beijing. Atmos. Environ. 38, 1275–1282.

Frolking, S., Xiao, X., Zhuang, Y., Salas, W., Li, C., 1999. Agricultural land-use in China: a comparison of area estimates from ground-based census and satellite-borne remote sensing. Glob. Ecol. Biogeogr. 8 (5), 407–416.

Giglio, L., Descloitres, J., Justice, C.O., Kaufman, Y.J., 2003. An enhanced contextual fire detection algorithm for MODIS. Remote Sens. Environ. 87 (2), 273–282.

Griffith, D.W.T., Mankin, W.G., Coffey, M.T., Ward, D.E., Riebau, A., 1991. FTIR remote sensing of biomass burning emissions of CO_2, CO, Ch_4, CH_2O, NO, NO_2, NH_3 and N_2O. In: Levine, J. (Ed.), Global Biomass Burning: Atmospheric, Climatic, and Biospheric Implications. MIT Press, pp. 230–240.

Hays, M.D., Fine, P.M., Geron, C.D., Kleeman, M.J., Gullett, B.K., 2005. Open burning of agricultural biomass: physical and chemical properties of particle-phase emissions. Atmos. Environ. 39, 6747–6764.

Huang, X., Li, M., Li, J., Song, Y., 2012. A high-resolution emission inventory of crop burning in fields in China based on MODIS thermal anomalies/fire products. Atmos. Environ. 50, 9–15.

Jiang, D., Zhuang, D., Fu, J., Huang, Y., Wen, K., 2012. Bioenergy potential from crop residues in China: availability and distribution. Renew. Sustain. Energy Rev. 16, 1377–1382.

Korontzi, S., McCarty, J., Loboda, T., Kumar, S., Justice, C., 2006. Global distribution of agricultural fires in croplands from 3 years of moderate resolution imaging spectroradiometer (MODIS) data. Glob. Biogeochem. Cycles 20, GB2021.

Lacaux, J.-P., Delmas, R., Jambert, C., Kuhlbusch, T.A.J., 1996. NOx emissions from African savanna fires. J. Geophys. Res. 101, 23585–23596.

Li, W., Shao, L., Buseck, P., 2010. Haze types in Beijing and the influence of agricultural biomass burning. Atmos. Chem. Phys. 10, 8119–8130.

Li, X., Wang, S., Duan, L., Hao, J., Li, C., Chen, Y., Yang, L., 2007. Particulate and trace gas emissions from open burning of wheat straw and corn stover in China. Environ. Sci. Technol. 41, 6052–6058.

Li, X., Wang, S., Duan, L., Hao, J., Nie, Y., 2009. Carbonaceous aerosol emissions from household biofuel combustion in China. Environ. Sci. Technol. 43, 6076–6081.

Martins, J.V., Artaxo, P., Liousse, C., Reid, J.S., Hobbs, P.V., Kaufman, Y.J., 1998. Effects of black carbon content, particle size, and mixing on light absorption by aerosols from biomass burning in Brazil. J. Geophys. Res. Atmos. (1984–2012) 103, 32041–32050.

Paton-Walsh, C., Smith, T.E.L., Young, E.L., Griffith, D.W.T., Guérette, É.A., 2014. New emission factors for Australian vegetation fires measured using open-path Fourier transform infrared spectroscopy–part 1: methods and Australian temperate forest fires. Atmos. Chem. Phys. 14 (20), 11313–11333.

Ponnamperuma, F.N., 1984. Straw as a source of nutrients for wetland rice. Org. Matter Rice 117–136.

Qu, L., Zhang, T., Lu, W., 2014. Assessing the potential of crop residue recycling in China and technology options based on a bottom-up model. Front. Environ. Sci. Eng. 8, 570–579.

Randerson, J.T., Chen, Y., Werf, G.R., Rogers, B.M., Morton, D.C., 2012. Global burned area and biomass burning emissions from small fires. J. Geophys. Res. Biogeosci. (2005–2012) 117 (G4).

Reid, J., Koppmann, R., Eck, T., Eleuterio, D., 2005. A review of biomass burning emissions part II: intensive physical properties of biomass burning particles. Atmos. Chem. Phys. 5, 799–825.

Reid, J.S., Hobbs, P.V., 1998. Physical and optical properties of young smoke from individual biomass fires in Brazil. J. Geophys. Res. Atmos. (1984–2012) 103 (D24), 32013–32030.

Roberts, T.J., Braban, C.F., Oppenheimer, C., Martin, R.S., Freshwater, R.A., Dawson, D.H., Griffiths, P.T., Cox, R.A., Saffell, J.R., Jones, R.L., 2012. Electrochemical sensing of volcanic gases. Chem. Geol. 332, 74–91.

Roberts, T.J., Saffell, J.R., Oppenheimer, C., Lurton, T., 2014. Electrochemical sensors applied to pollution monitoring: measurement error and gas ratio bias-a volcano plume case study. J. Volcanol. Geotherm. Res. 281, 85–96.

Sahai, S., Sharma, C., Singh, D.P., Dixit, C.K., Singh, N., Sharma, P., Singh, K., Bhatt, S., Ghude, S., Gupta, V., 2007. A study for development of emission factors for trace gases and carbonaceous particulate species from in situ burning of wheat straw in agricultural fields in India. Atmos. Environ. 41, 9173–9186.

Smith, P., Martino, D., Cai, Z., Gwary, D., Janzen, H., Kumar, P., McCarl, B., Ogle, S., O'Mara, F., Rice, C., Scholes, B., Sirotenko, O., Howden, M., McAllister, T., Pan, G., Romanenkov, V., Schneider, U., Towprayoon, S., 2007. Policy and technological constraints to implementation of greenhouse gas mitigation options in agriculture. Agric. Ecosyst. Environ. 118, 6–28.

Streets, D., Yarber, K., Woo, J.-H., Carmichael, G., 2003. Biomass burning in Asia: annual and seasonal estimates and atmospheric emissions. Glob. Biogeochem. Cycles J. 17.

van der Werf, G.R., Randerson, J.T., Giglio, L., Collatz, G.J., Mu, M., Kasibhatla, P.S., Morton, D.C., DeFries, R.S., Jin, Y., van Leeuwen, T.T., 2010. Global fire emissions and the contribution of deforestation, savanna, forest, agricultural, and peat fires (1997–2009). Atmos. Chem. Phys. 10, 11707–11735.

Ward, D.E., Radke, L.F., 1993. Emissions measurements from vegetation fires: a comparative evaluation of methods and results. Fire Environ. Ecol. Atmos. Clim. Imp. Veg. Fires 13, 53–76.

Wooster, M.J., Freeborn, P.H., Archibald, S., Oppenheimer, C., Roberts, G.J., Smith, T.E.L., Govender, N., Burton, M., Palumbo, I., 2011. Field determination of biomass burning emission ratios and factors via open-path FTIR spectroscopy and fire radiative power assessment: headfire, backfire and residual smouldering combustion in African savannahs. Atmos. Chem. Phys. 11, 11591–11615.

Xiao, X., Liu, J., Zhuang, D., Frolking, S., Boles, S., Xu, B., Li, C., 2003. Uncertainties in estimates of cropland area in China: a comparison between an AVHRR-derived dataset and a Landsat TM-derived dataset. Glob. Planet. Change 37 (3), 297–306.

Xue, Y., Xu, H., Guang, J., Mei, L., Guo, J., Li, C., Mikusauskas, R., He, X., 2014. Observation of an agricultural biomass burning in central and east China using merged aerosol optical depth data from multiple satellite missions. Int. J. Remote Sens. 1–13.

Yang, S., He, H., Lu, S., Chen, D., Zhu, J., 2008. Quantification of crop residue burning in the field and its influence on ambient air quality in Suqian, China. Atmos. Environ. 42, 1961–1969.

Yokelson, R.J., Goode, J.G., Ward, D.E., Susott, R.A., Babbitt, R.E., Wade, D.D., Bertschi, I., Griffith, D.W.T., Hao, W.M., 1999. Emissions of formaldehyde, acetic acid, methanol, and other trace gases from biomass fires in North Carolina measured by airborne Fourier transform infrared spectroscopy. J. Geophys. Res. Atmos. (1984–2012) 104, 30109–30125.

Yokelson, R.J., Burling, I.R., Gilman, J.B., Warneke, C., Stockwell, C.E., de Gouw, J., Akagi, S.K., Urbanski, S.P., Veres, P., Roberts, J.M., Kuster, W.C., Reardon, J., Griffith, D.W.T., Johnson, T.J., Hosseini, S., Miller, J.W., Cocker III, D.R., Jung, H., Weise, D.R., 2013. Coupling field and laboratory measurements to estimate the emission factors of identified and unidentified trace gases for prescribed fires. Atmos. Chem. Phys. 13, 89–116. http://dx.doi.org/10.5194/acp-13-89-2013.

Zhang, H., Hu, D., Chen, J., Ye, X., Wang, S.X., Hao, J.M., Wang, L., Zhang, R., An, Z., 2011. Particle size distribution and polycyclic aromatic hydrocarbons emissions from agricultural crop residue burning. Environ. Sci. Technol. 45, 5477–5482.

Zhang, H., Ye, X., Cheng, T., Chen, J., Yang, X., Wang, L., Zhang, R., 2008. A laboratory study of agricultural crop residue combustion in China: emission factors and emission inventory. Atmos. Environ. 42, 8432–8441.

Zhang, Y., Shao, M., Lin, Y., Luan, S., Mao, N., Chen, W., Wang, M., 2013. Emission inventory of carbonaceous pollutants from biomass burning in the Pearl River Delta Region, China. Atmos. Environ. 76, 189–199.

4.3 SMOKE SAMPLING SYSTEM BUILD, TESTING AND FIELD DEPLOYMENT

This Section provides further details of the smoke sampling system used in the fieldwork described in the published paper included as Section 4.2.

4.3.1 SAMPLING SYSTEM DESIGN

The principal measurement objectives of the smoke sampling system shown in Fig. 2 of Section 4.2 was to quantify the mixing ratios of CO and CO_2 in the sampled smoke, along with the mass concentrations of $PM_{2.5}$ and the amount of that mass which was composed of black carbon. This was designed to cover the full lifetime of the field-scale fires, at a relatively high temporal resolution in order to both be able to derive 'fire averaged' emissions factors and look at EF differences over time due, potentially, to changes in fire behaviour or phase (e.g. flaming to smouldering). The system needed to be sufficiently robust and portable and with an internal power supply to allow effective mobile use in the field.

A summary of instruments/sensors used within the smoke sampling system can been seen in Table 4.1, along with some of their key characteristics such as the sensor response time. A single inlet design was used to provide both gas and aerosol samples to a range of different instruments, all housed in a wheeled peli case (see Figure 2, Section 5.2). A single $PM_{2.5}$ size selective impaction inlet (BGI miniPM® inlet 5011, 5 l min^{-1}) was used, since the majority of aerosols from agricultural crop burning are predominantly those sized in the accumulation mode or smaller, with a size range reportedly of 100 to 1000 nm (da Rocha *et al.,* 2005; Hays *et al.,* 2005; Zhang *et al.,* 2011). This design also helped minimise interference from soil and mineral dust re-suspension, which certainly was observed at some measurement sites on windier days. A flow splitter (TSI 3708) isokinetically divided the airstream and aerosols in up to four pathways, though here only three pathways were used (one pathway was blocked), entailing a flow rate of 1.67 l.min^{-1} through each (5.0 l.min^{-1} total flow). This setup is configurable such that one to four pathways can be used as long as the total flow remains at 5 l.min^{-1} to ensure an accurate separation of $PM_{2.5}$ in the inlet. Conductive tubing with a minimum of bends was used to connect all aerosol instrumentation; all tubing was also kept as short as possible to minimise residence times. All flows were

calibrated in the laboratory using a flowmeter (BIOS Defender 530, MesaLabs) traceable to national standards; flows were further checked before and after every sample using a portable flowmeter (TSI 4040) in the field.

Table 4.1: Summary of instruments/sensors used within the smoke sampling system.

Instrument / Sensor	Targeted Species	Measurement Range	Sampling Rate (Hz)	Response* Time (s)
TSI Dusktrak DRX 8533	$PM_{2.5}$		1	1
MicroAeth AE51	BC		1	1
Alphasense CO-AX	CO	0 – 400 ppm	1	< 30
Alphasense CO-AF	CO	0 – 400 ppm	1	< 23
Alphasense H_2-AF	H_2	0 – 200 ppm	1	< 35
Alphasense CO_2-NDIR	CO_2	0 - 5000 ppm	1	< 40 s
SenseAir CO_2-K30	CO_2	0 - 5000 ppm	1	2

* Obtained from lab measurements made using stable target gas concentrations

Pathway 1 was drawn by a TSI Dusrtrak, set to 1.67 l min^{-1}; and the eluent flow, now particle-free, was directed to the gas sensors. Pathway 2 was drawn by a Casella Apex Pro pump set to 1.67 l min^{-1}; and $PM_{2.5}$ was collected onto a 25 mm Tissuequartz™ (PALL Life Sciences) filter. This filter was stored at 4° C after sampling and subsequently analysed using thermal/optical analysis (Sunset Labs) to allow later analysis of elemental and organic carbon composition. Pathway 3 was drawn by a combination of a Casella Apex pump (1.57 l min^{-1}) and a microAeth AE51 black carbon meter (0.1 l min^{-1}). As the flow rate required for the microAeth was lower than that required to maintain the isokinetic separation, a second Casella pump was mounted next to draw the bypass flow away as excess flow.

Each individual instrument was chosen to be compact and battery powered, able to operate for several hours without charging. The TSI (Dusttrak DRX Aerosol Monitor 8533) was used to measure $PM_{2.5}$ mass concentrations, since its broad measurement range (0.001-150 $mg.m^{-3}$) could cope with close proximity to the fire without an obvious requirement to pre-dilute the smoke being sampled. As size selection was undertaken using the size selective inlet, only the Dusttrak DRX $PM_{2.5}$ measurements were used, and indeed the higher size PM values were almost identical to these as the larger particles had been filtered out in the inlet. Measurements were made at 1 Hz and stored in the on-board logger, with the manufacturers documentation stating a measurement resolution ±0.1% of the reading at 0.001 $mg.m^{-3}$. All raw Dusttrak DRX measurements of smoke $PM_{2.5}$ mass concentrations were adjusted to be relevant to smoke using the equation provided by Preble *et al.* (2014) and reported in published paper included as Section 4.2, the calibration equation ($PM_{corrected} = 1.10 \times PM^{0.78}$) being calculated from cookstove smoke

and being necessary because the 'raw' Dusttrak factory calibration is conducted with Arizona road dust, having a density, size distribution and shape very different to smoke particles. Further fieldwork and laboratory testing was conducted later to enhance the calibration for smoke, which will be introduced in Section 4.4.

A microAeth AE51 was used to measure BC, with measurements also made at 1 Hz and stored onboard. The AE51 pump was set at a constant 0.1 $l.min^{-1}$, and the measurement range was 0-1 mg BC m^{-3} at a resolution of 0.001 µg BC m^{-3}. The microAeth AE51 filter strip was replaced every second fire, though this actually resulted in the filter saturating on a small number of occasions and in the second field campaign replacement after every fire was used. Hagler *et al.*, (2011) reported microAeth AE51 instrument noise at this sampling frequency, and developed an optimized noise-reduction procedure (https://aethlabs.com/dashboard) to reduce the occurrence of negative values and which was applied here to all AE51 data.

CO was measured using two small sensors supplied by Alphasense Ltd, the CO-AF and CO-AX electrochemical sensors. Similar sensors have been used previously for example to characterise volcanic plumes (e.g. Roberts *et al.,* 2012; 2014). The CO-AF has some cross sensitivity to H_2, which is also a potential product released during biomass burning (Cofer *et al.,* 1998), and so this gas was consequently also measured using an H2-AF sensor (also from Alphasense Ltd), and these measures used to adjust those of the CO-AF sensor (Roberts *et al.,* 2012). The CO-AX, has much less of a H_2 sensitivity, but a more significant temperature sensitivity, and so the output from this sensor adjusted for gas temperature using data from thermocouples placed in the internal sample airstream of the sampling system. All these sensors have associated circuitry which produces a current between 4 (0 ppm) and 20 (maximum ppm) mA, corresponding to the mixing ratio of the target gases and logged as voltages by two Hobo data loggers (U12-006) across a 100 ohm resistor (one for each sensor). To ensure that the gas sensors were exposed to a homogenous sample, and to simplify the physical and electrical connections inside the pelicase, the gas sensors were fitted into a tube shape container so that the top of each sensor was exposed to the smoke-contaminated airstream passing across the array of sensors. A filter membrane fitted to the top of each sensor allowed gas molecules to diffuse across into the sensor interior. In addition to the CO and H_2 measurements made using the electrochemical sensors, an Alphasense nondispersive infrared (NDIR) sensor was used to assess CO_2, whilst a second NDIR sensor (K-30 from SenseAir, Sweden) was placed downstream of the Alphasense sensors to provide a second CO_2 measure (logged using a third hobo logger). This downstream setting of the K-30 was necessary because of its larger size and irregular

shape compared to the Alphasense sensors, which makes it very difficult to fit into the same tube as these other sensors. Power to all these trace gas sensors was supplied by a single 12V sealed lead-acid battery.

4.3.2 TRACE GAS SENSOR PERFORMANCE ANALYSIS

Electrochemical and NDIR sensors are typically characterised by a T90 response time (also called 'lag time') (Roberts *et al.,* 2012). This represents the time (in seconds) it takes for the sensor to respond to a change in target species concentration, and reach an recorded output of 90% of the new true concentration. A low T90 is of course expected for a fast response sensor. By testing the lag time of the sensors inside and outside of the sensor array tube used in the field, two lag effects were identified - the first associated with the T90 times of the sensors themselves (with the manufactures reported values shown in Table 4.1) and the second associated with their placement in the smoke sampling system and the particular exposure to the sample airflow.

The T90 response time effect of the individual sensors, as reported by Roberts *et al.* (2012), was assessed outside of the smoke sampling system using CO and CO_2 calibration gases at a range of mixing ratios; and the results shown in Table 4.2. Secondly, when the gas sensors were fitted into the single tube array inside the sample box, similar use of calibration gases showed the sensors taking significantly longer than these initial T90 time to respond to changes in the incoming concentration. Despite designing a relatively compact tube to hold the gas sensor array, the volume of the tube was found to be quite large for the flow setting of 1.67 l min^{-1}, and the exchange volume time calculated at 14 seconds.

The combined impact of the volume exchange times and the basic T90 sensor response time was further investigated using simulations based on the equations of Roberts *et al.* (2014), which describe how such sensors respond to changes in the relevant trace gas mixing ratio (see Eqn. 4.2 of Section 4.5).

Table 4.2: Volume exchange times for the smoke sampling box, along with T90 response times of the trace gas sensors deployed here, derived during laboratory testing.

	Time (secs)
Tube Array Volume Exchange Time	14
CO_2_NDIR	12
CO_2_K30	8
CO_AF	23
CO_AX	40

Figure 4.1 shows one such simulation for the Alphasense CO-AF sensor, using a 14 second exchange time for the array volume and a 23 second T90 sensor response time (as reported in Table 4.2). Here, the simulation is for a target gas with a mixing ratio of 2000 ppmv being fed into the system for 100 seconds, followed by 250 seconds of "clean air" with zero target gas presence. The time series of the actual instantaneous concentration of the target gas within the tube containing the gas sensor array is shown, along with the lagged concentration reported by the sensor. From this simulation, the overall response time for the modelled sensor system can be calculated as 40 seconds, even longer than the sum of the exchange volume time and the measured sensor T90 time (shown in Table 4.2 for all sensors). Fig. 4.1 shows the reported concentrations lagging behind the true concentrations, and since the different sensors had different T90 response times (Table 4.2), this had to be taken into account during any emissions ratio calculation where data from different sensors was combined.

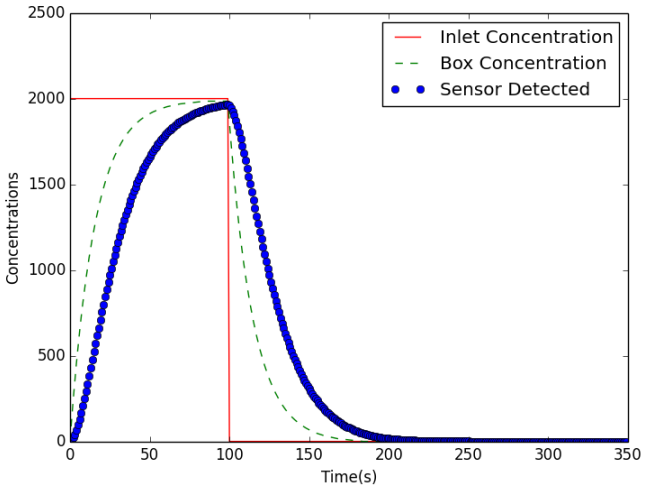

Figure 4.1: Demonstration of the sensor lag time effect in relation to the carbon monoxide CO_AF sensor used herein. Red line shows a simulated input of CO gas, green dash line shows the simulated time series of the gas mixing ratio within the tube holding the array of sensors inside the smoke sampling system, and the blue dotted line shows the detected mixing ratio as measured by the CO_AF sensor. The tube containing the sensors takes time to fill completely with the gas, whilst the CO_AF sensors non-zero T90 response time (Table 4.2) means its reported trace gas mixing ratio lags somewhat behind the true mixing ratio present in the tube.

4.3.3 Laboratory Testing Sensors Lag Time Effects and Impacts

Laboratory tests were conducted to further investigate the lag time effect. In this test, two different sensor containers are used, together with five different sensors (Table 4.3) to check the relation of total lag time, gas exchange time, and basic sensor lag time. A new sensor box with a smaller exchange volume, and consequently, smaller exchange time, was also investigated for deployment in a second field campaign,

building on that of the first campaign detailed in Section 4.2. Three scenarios were envisioned for the sensor box to be deployed in this second campaign: (i) fit sensors in the large tube from original sampling box used in the fieldwork of Section 4.2, (ii) fit sensors in the new smaller box and, (iii) directly expose each (one by one) to the gas flow. For the former two scenarios, five different sensors were fitted inside the sampling system, including three CO_2 sensors (one Alphasense NDIR, and two K30 NDIR) and two CO sensors (CO_AF and CO_AX). The total lag time of the different scenarios tested for the different sensors is summarised in Table 4.3. The results show that the total lag time is close to the sum of exchange time and sensor lag time, but usually a little higher. For example, the CO_AX total lag time in large tube is as high as 57s, 7s higher than the sum (50s) from the two individual lag time contributions.

Table 4.3: Total lag time derived during laboratory tested, using three fittings with different volume exchange time (large tube from sampling box, small box and directly exposure to gas flow) and five different sensors with different T90 response times.

Fitting	Sensor	Exchange time (s)	Sensor lag time (s)	Total lag time (s)
Large tube	NDIR	10	12	23
	K30	10	8	18
	K30_2	10	8	18
	CO_AF	10	23	37
	CO_AX	10	40	57
Small box	NDIR	5	12	17
	K30	Sensor Error (contact with box edge)		
	K30_2	5	8	13
	CO_AF	5	23	29
	CO_AX	5	40	47
Directly exposure	NDIR	0	12	12
	K30_2	0	8	8
	CO_AF	0	23	23
	CO_AX	0	40	40

The experimental results reported in Table 4.3 were also compared to the simulated lag times of the kind shown in Fig. 4.2. The simulated results indicated that for tests with exchange times and sensor lag times below 20 secs, the total lag time is close to the sum of the two individual lag times. However, the total lag time increases by significantly more when the exchange time and/or sensor lag time is higher than 20 secs, similar to the findings of the laboratory testing. This the laboratory testing confirmed that use of a smaller tube to minimise the exchange volume times might help lessen the lag time issues associated with these data (see Section 4.4), and further analysis and discussion are included in Section 4.5.

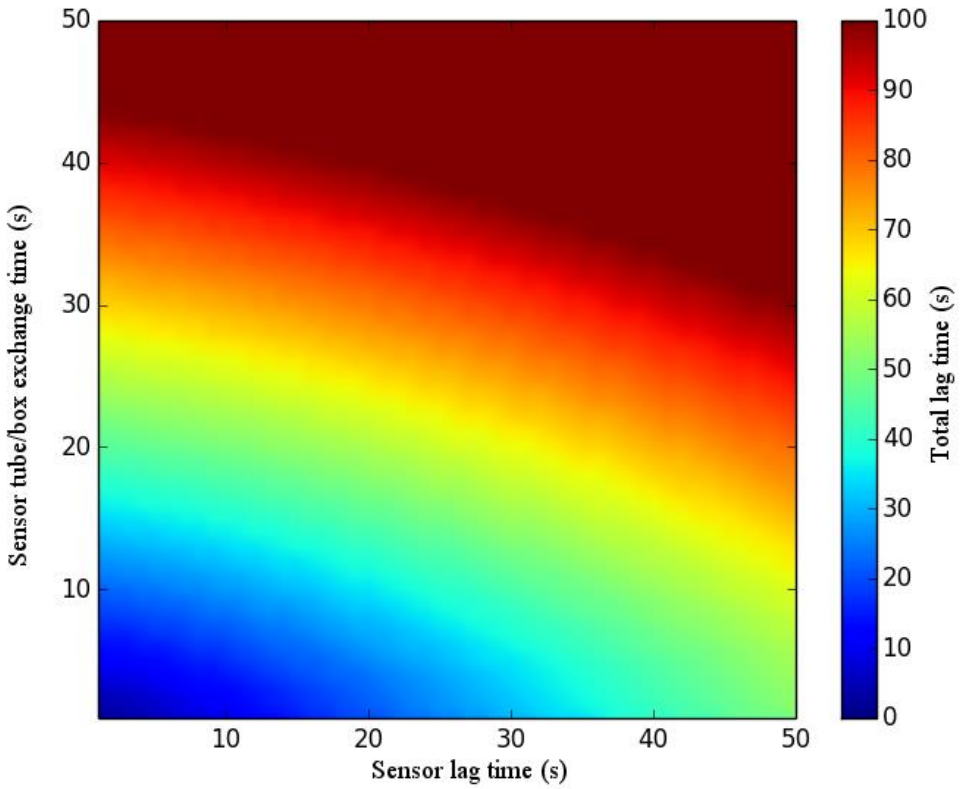

Figure 4.2: Simulated total lag time using different exchange time and sensor lag time (see Eqn. 4.2 and details in Section 4.5).

4.3.4 AVERAGING METHOD FOR REMOVING LAG TIME EFFECT

Roberts *et al.* (2014) previously used a sensor response model to evaluate the impact of different sensor T90's on emissions ratio calculations, based on sensors very similar to those deployed in this study. By inverting this model, it is theoretically possible to recover the instantaneous 'actual' target gas mixing ratio the sensor is exposed to using the measured outputs, and these actual mixing ratios could then be used to calculate instantaneous emissions ratio from measurements of sensors having different T90 times. When testing this approach with real data however, the output time-series was found to contain significant and unrealistic fluctuations ('noise'), so the method was not used for the analysis herein. Further lag time model simulation will be introduced in Section 4.5, but in the first field campaign described in Section 4.2 the measured signals from the sensors were simply averaged over set periods of time, which has been suggested as a simple but effective way to combine data impacted by different lag times in order to calculate emissions ratios (Roberts *et al.*, 2014).

The investigation of the sampling systems performance with respect to the trace gas measurements concluded with the fieldwork data analysis focusing on the CO and CO_2 datasets recorded by the sensors

showing the shortest lag times (Table 4.1: CO_AF, CO_2_K30). To minimise the impact of the combination of the remaining lag times and the rapidly changing trace gas mixing ratios experienced during *in situ* plumes measurement (Reid *et al.*, 2005), the outputs from the gas sensors in Section 4.2 were in the end averaged over 20 seconds for derivation of trace gas emission ratios, and this averaging period increased to 120 seconds when comparing gas and aerosol measurements.

4.3.5 Sampling Approach For First Field Campaign

In the fieldwork described in Section 4.2, fires close to Changzhou City (31.75°N, 128.11°E) and Tongling City (30.84°N, 117.65°E) were conducted primarily in the afternoons, and the ambient air temperature during the daytime measurements was 20 - 35 °C, with 40% to 60% relative humidity. Emissions from the post-harvest residues of wheat, rice and rapeseed were targeted, and fuel moisture prior to burning was assessed using a Moisture Analyser Balance (Ohaus MB23) that weighs a small sample of the vegetation whilst it is heated to drive off water. Five samples were measured for each fire, and all were found to be very dry. The moisture content of the wheat and rice residue was 9 - 10%, and that of rapeseed was even drier at 8 - 9 %.

The agricultural residue fires were burned in different ways, in areas of up to 10 m × 15 m. Local people helped to ensure the burning was conducted in the way normally undertaken by Chinese farmers. The majority of the wheat stubble residue was burned *in situ* in the field as a spreading fire, since June is the time that this crop type is normally harvested and burned in this way in Eastern China. The field containing the wheat stubble was ignited in the upwind corner as is done normally, and the headfire allowed to spread across the whole field generating flame lengths of a few tens of cm to around 1.5 m (Figure 3a, Section 4.2). These burns took between 6 and 30 minutes to complete, depending on the field size and shape, wind speed and direction (Table 1, Section 4.2). Samples of wheat of ~ 5 kg mass were also gathered from the same area and burned as a bonfire, to help better assess the specific emissions related to the separate flaming and smouldering phases of its combustion (see Table 1, Fire 6a and Fire 6b, Section 4.2). The other two crop residues types (rice, rapeseed) were burned in similar, albeit larger, bonfires as the residues of these fuels are normally collected, piled and burned in this way by local farmers (Figure 3b, Section 4.2). Flames reached ~ 8 m high in some of these intensely burning bonfires, helped by the dry, fine nature of the rice and rapeseed residues, and the high fuel loads contained in the piles that were designed to replicate what is seen normally in these types of field fire (e.g. Knapp, 2009).

Eighteen fires were conducted in all, and in all but one was significant smoke sampled and the measurements used for further analysis as reported in Table 1 of Section 4.2.

The smoke from the spreading agricultural residue fires had relatively little thermal buoyancy, probably due to the low fuel loads, generally slow fire spread rates and thus low fire intensities (Figure 3a, Section 4.2). In these cases the smoke was mostly advected horizontally, allowing the sampling system to appropriately capture samples from the ground-level plume. The system could be easily moved if the flames came too close, or when the wind direction changed and prevented smoke being sampled effectively. If the sampling system was very close to the smoke source, the likelihood of saturation of one or more of the measurement instruments was substantially increased, so the system was kept at least 5 m away from the fire front at all times, and mostly 10 - 20 m away (see Fig. 4.3). Since we are primarily interested in trace gas and particulate emission ratios, rather than absolute concentrations, the different dilutions of the plume experienced at different distances from the fire had no significant impact on our results. Our main requirement for the measurements was to obtain unsaturated, but significantly elevated, concentrations of each smoke constituent studied – whose measurements could later be combined into emissions ratios.

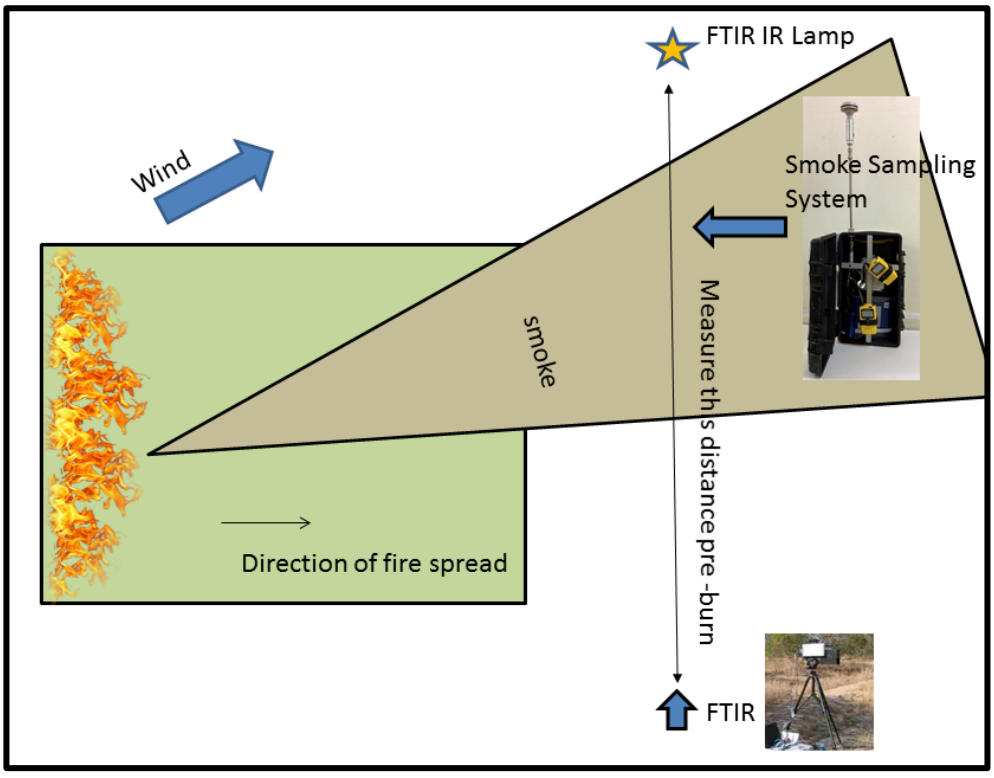

Figure 4.3: Illustration of instruments display during *in-situ* spreading fire measurements in China. The smoke sampling system was kept downwind but at least 5 m away from the fire front. The FTIR and lamp were displayed at two ends outside of the smoke affected downwind area but with the path in-between crossing the smoke sampling system.

For the bonfires, smoke usually rose fairly vertically above the fires, which burned much more intensely and with much higher flame lengths than for the spreading fires (e.g. Figure 3b, Section 4.2). To capture a sample of this vertically rising smoke, a larger suction pump was connected to a ~10 m long, ~ 50 cm diameter flexible aluminium pipe. The inlet of the sampling box was fit into one end of the pipe a significant distance ahead of the pump location, and the other end linked to a > 5 m long lightweight pole which could be easily controlled to move in and out of the vertically rising smoke (Figure 3b, Section 4.2). The pump was then used to pull smoke from the vertically rising plume down the sampling line and across the inlet of the smoke sampling system. A distance of one or two meters between the fire and the end of the sampling line was found necessary to keep the aerosol concentration in the unsaturated measurement range. Nevertheless, during some of the most strongly burning fires (e.g. Fire No. 9, see Figure 5, Section 4.2), saturation was found in the TSI dusttrak, microAeth and K30 measurements, and these observations were therefore excluded from emission ratio (and EF) calculations.

A second remote sensing based measurement approach focused on trace gas assessment was deployed co-incident with the smoke sampling system on some of the agricultural residue fires (see Fig 4.3). The method was based on a portable MIDAC open-path Fourier transform infrared (OP-FTIR) spectrometer and an IR emitting lamp, with the use of the same system in biomass burning trace gas assessment being described in detail by Wooster *et al.* (2011). The only difference between the deployment described by Wooster *et al.* (2011) and that used here is the much shorter (10 to 30 m) path lengths used in China (Figure 3a), which allowed use of a lightweight and more portable IR source. Yokelson *et al.* (2013) describe recent use of a similar approach, using it as part of an integrated ground-based, laboratory and airborne measurement campaign to probe numerous compounds emitted by biomass fires in north American fuels, whilst Smith *et al.* (2011) performed an accuracy assessment of the approach covering the primary gases investigated here using OP-FTIR (CO_2, CO and CH_4) and found estimates of 5% uncertainty on the final trace gas mixing ratio retrievals.

Prior to each agricultural residue fire targeted via the OP-FTIR spectroscopy, the spectrometer was turned on at least 30 minutes before ignition, allowing time for the Stirling cycle cooler to stabilise the system temperature at a sufficiently low level to provide low-noise spectra. The spectrum from the IR lamp was then measured by the spectrometer every second at 0.5 cm^{-1} spectral resolution, across a 600 – 5000 cm^{-1} wavenumber range. IR absorbing trace gases in the smoke caused absorption features in the spectra that were later used to identify both the chemical species involved and their path averaged volume mixing ratios, according to the optimal estimation retrieval techniques described in Wooster *et al.* (2011). Pre-fire

spectra without the presence of the IR lamp were subtracted from the fire measurement spectra prior to the trace gas retrieval procedure, in order to ensure they were adjusted for the impact of instrument self-emission, as described in Müller *et al.* (1999) and Wooster *et al.* (2011). This OP-FTIR based approach was found to be very well suited to the analysis of the ground-level emissions from the spreading agricultural residue fires (Figure 3a, Section 4.2), but the vertically rising smoke from the bonfires (e.g. Figure 3b, Section 4.2) proved difficult to target, and the path-averaged volume mixing ratios on those fires were generally considered too low to provide reliable OP-FTIR retrievals.

4.3.6 MIXING MODEL

The simple linear mixing model was based on the Eqn. 4 to 7 of Section 4.2. Eqn. 8 was then used for spreading wheat residue fires to examine variations in the flaming phase fraction (R_f). Taking Fire No. 4 as an example (0613run1; Table 1, Section 4.2) Fig. 4 (Section 4.2) presents the time series of $PM_{2.5}$ and BC mass concentrations along with the output of the mixing model. From the former we can see that the first few plumes arriving from this fire (around 17:14 hrs) BC contributed more to the sampled $PM_{2.5}$ mass than the for later plumes. The mixing model shows the flaming phase fraction of BC mostly lies between 0.5 and 1.0 for the earlier plumes that existed around 17:14 hrs, indicating that 50 - 100% of the sampled BC are from flaming combustion. This is realistic, since at the start of these spreading fires the vast majority of the smoke is being generated by the headfire, whilst the 'smoking zone' behind the fire front is relatively limited in area since the headfire has not yet had significant time to spread. For the later plumes, between 17:22 hrs and 17:27 hrs, the flaming phase fraction of BC (R_f) tends to be somewhat lower, with a reduced maximum of ~ 0.8. This is consistent with a larger area 'smoking zone' having been generated behind the spreading headfire, and this larger area contributing more to the overall smoke being sampled at these later times. These results confirm that during these spreading burns, apart from a period right at the start of the fire when flaming phase combustion is very dominant, as with savannah fires the sampled smoke is a mixture of that generated by the flaming front and the smouldering 'smoking zone' (Lacaux *et al.*. 1996). However, even in the smouldering dominated plumes, flaming phase combustion appears to still account for over 20% of the overall BC contribution, which agrees with our observations that smouldering-only combustion is very limited in this type of spreading agricultural residue burning, in which fuels are fine, not closely packed, and of low moisture content, thus supporting an efficient and

rapid combustion process. Once the headfire is extinguished therefore, it is not long before combustion totally ceases.

We did not collect samples of pure flaming and pure smouldering smoke for the rice and rapeseed residues, but based on the observation of clear flaming and smouldering boundaries in the spreading wheat fire data of Figure 7 (Section 4.2) we applied a boundary detection approach to the spreading fire measurements of the wheat fires in order to pilot its use in the derivation of emission ratios before application to the rice and rapeseed residue burns, as described in Section 4.2. Based on the 95% confidence interval, the highest and lowest 2.5% of the $PM_{2.5}$ to BC ratio shown in Figure 7 (Section 4.2) was selected, and a linear best fit applied to only these 'boundary' data. The resulting $PM_{2.5}$ to BC emission ratio for flaming combustion [1.9 mg m^{-3}.(mg m^{-3})$^{-1}$] is within 5% of that derived from the bonfire case of a wheat burn (S_f, Figure 6a), whilst the result for smouldering $PM_{2.5}$ to BC emission ratio [58.1 mg m^{-3}.(mg m^{-3})$^{-1}$] is 30% lower than the emission ratios (S_s) derived from the bonfire case of smouldering wheat. The latter difference can again perhaps be related to the relative difficulty in sampling pure smouldering combustion during the spreading fires, since as discussed above the spreading fires do not really support smouldering-only combustion. A scaling factor of 1.3 was therefore used to adjust the value of the $PM_{2.5}$ to BC ratio derived from this confidence interval methodology when used in the flaming phase fraction calculations for the other fuels. The equivalent values of S_f and S_s (mg m^{-3}. (mg m^{-3})$^{-1}$ for the rice and rapeseed residues are shown in Figure 8 in Section 4.2, plotted onto the instantaneous $PM_{2.5}$ and BC mass concentrations. As expected, in a similar manner to the measurements from the spreading wheat fire, the derived emission ratio boundaries correctly bracket the limits of the instantaneous measurements.

The same methodology applied to the aerosol measurements to derive the flaming phase fraction (Section 4.2) was also used with the CO_2 and CO data of all three agricultural residue fuels to derive the same metric, but now for the trace gas rather than aerosol measures. Unlike the data provided by the aerosol systems however, due to the lag times of the CO and CO_2 sensors noted in Section 4.3.3, the instantaneous measurements from the two gas sensors cannot be considered as simultaneous records of the true trace gas mixing ratio. We therefore calculated and compared 20 second averages as discussed in Section 4.3.4, with this averaging period selected as a compromise between the response times of the CO_AF and K30 CO_2 sensors (Table 4.2) and the requirement to keep a significant number of data points for the ER derivation. For the wheat fuels, the CO to CO_2 emission ratio for flaming phase combustion was calculated as 0.018 (ppmv.ppmv^{-1}), and 0.46 (ppmv.ppmv^{-1}) for the smouldering phase combustion

(representing an MCE of 0.98 and 0.68 respectively). The derived emission ratios quite appropriately represent the boundaries seen on the CO to CO_2 scatter plots, be it from wheat, rice or rapeseed fires (Figure 9 of Section 4.2).

4.3.7 EMISSION FACTOR CALCULATION

The EFs in $g.kg^{-1}$ of the trace gases present in the smoke were calculated using the carbon mass balance equation of Yokelson *et al.,* (1999, Equation 1, Section 4.2).

The ratio of the number of moles of species *x* divided by the total number of moles of carbon ($\frac{C_x}{C_t}$) for use in Eqn.1 was calculated as (Ward and Radke, 1993):

$$\frac{C_x}{C_t} = \frac{{ER_x}/{CO_2}}{\sum_{j=1}^{n}\left(NC_j ER_{\frac{j}{CO_2}}\right)} \qquad (4.1)$$

Where the summation is over the carbon containing gases and the [$ER_{x/y}$] is the so-called emission ratio [ER] of two compounds that is derived from the gradient of the linear best fit to the measured excess abundance of species [*x*] when plotted against the excess abundance of reference species [*y*] measured in the same sample (Yokelson *et al.*; 1999). In terms of trace gas measurements, CO_2 is commonly the reference species for 'flaming dominant' compounds, and CO for 'smouldering dominant' compounds (Andreae and Merlet, 2001).

Wooster *et al.* (2011) and Yokelson *et al.,* (2013) recently describe the use of the carbon mass balance technique with data from OP-FTIR systems, and we use it here with both those data and that from the smoke sampling system described above. The main gaseous carbon containing compounds in vegetation fire smoke are CO_2, CO, methane (CH_4) and non-methane hydrocarbons (NMHC). Since aerosols comprise only a few percent of the emitted carbon (Andreae and Merlet, 2001), and methane and NMHCs are reported to account only around 2% for all carbonaceous gases emitted from wheat or maize straw combustion in China (Li *et al.,* 2007), we conclude that the vast majority of the carbon is present in the form of CO_2 and CO and so is measured by the trace gas sensors of our smoke sampling system. Delmas *et al.* (1995) also show that CO_2 and CO account for the vast majority of the total gaseous carbon flux from agricultural residue burning, a median of 99%, whilst Yokelson *et al.* (1999) confirm that EFs are underestimated by only 1 or 2 % when neglecting the aerosol components. We therefore conclude that the

measurements of CO_2 and CO made using our smoke sampling system can provide the information necessary for calculating the emissions factors of these two gases via the carbon mass balance approach outlined above. A comparison of the EFs derived using this CO_2 and CO measurement approach to those derived from the OP-FTIR system, where further carbon-containing species can be accounted, is also possible using the same carbon mass balance approach, but now considering these additional gaseous constituents (see Section 4.2).

The particulate EFs are calculated from the aerosol/gas emissions ratios shown in Fig. 4.4 and 4.5 (as well as in Fig. 11 from Section 4.2) using Eqn.3, and the results summarised in Table 5 of Section 4.2.

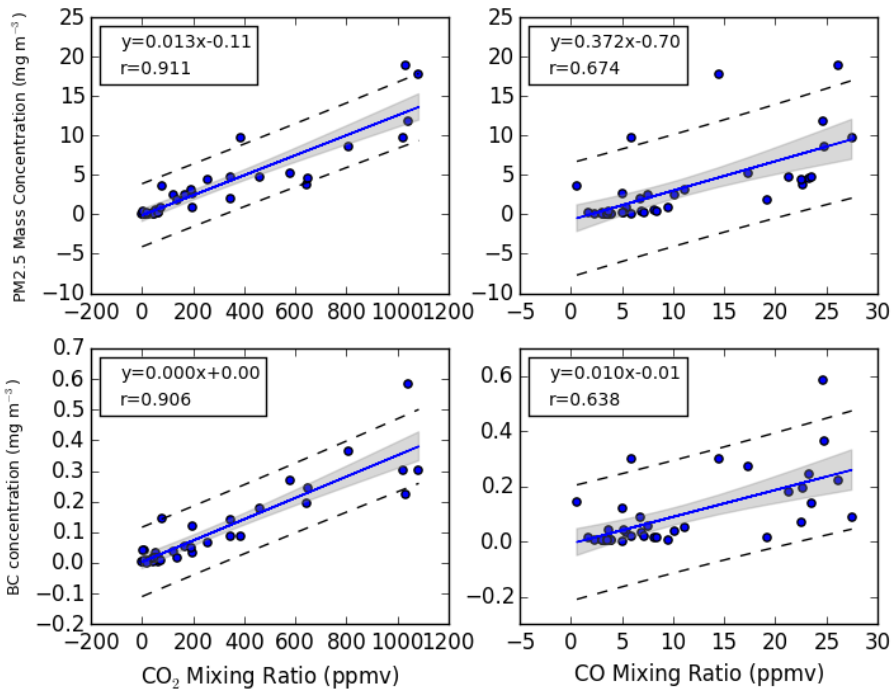

Figure 4.4: Scatterplot of $PM_{2.5}$ and BC mass concentrations to CO_2 and CO mixing ratio measures from all rice residue fires listed in Table 1 (Section 4.2), with data presented as 120 s averages. The blue line represents the least squares linear best-fit to the data, taken as the relevant particulate to gas emission ratio for this fuel type, along with the 95% confidence intervals on the slope (grey filled polygon) and on the prediction (dashed line).

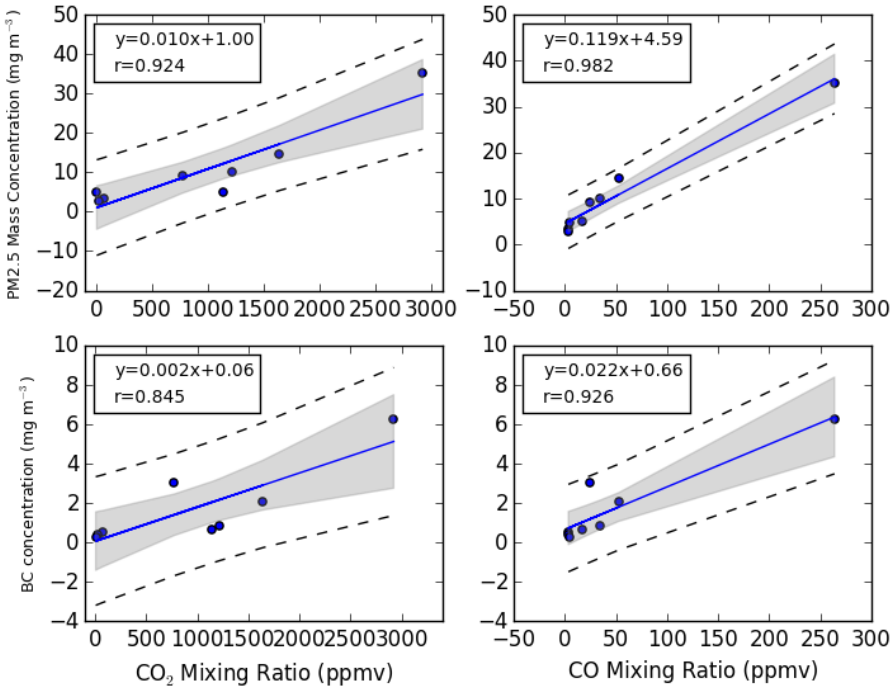

Figure 4.5: Scatterplot of $PM_{2.5}$ and BC mass concentrations to CO_2 and CO mixing ratio measures from all rapeseed residue fires (listed in Table 1 of Section 4.2), with data presented as 120 s averages. The blue line represents the least squares linear best-fit to the data, taken as the relevant particulate to gas emission ratio for this fuel type, along with the 95% confidence intervals on the slope (grey filled polygon) and on the prediction (dashed line).

4.4 UPDATED SMOKE SAMPLING SYSTEM CALIBRATION AND EXTRA FIELDWORK RESULTS

This section introduces further laboratory testing and fieldwork testing of the smoke sampling system, conducted after the first field deployment detailed in Section 4.2.

4.4.1 UPDATED SMOKE SAMPLING SYSTEM

With the issue of the sensor lag time discussed in Section 4.2 and 4.3, improvement of smoke sampling system was considered important subsequent to its first field deployment. This was conducted in two ways. Firstly minimisation of the gas exchange time, in this case by limiting the volume of the box containing the sensors. The other was to introduce a parallel sampling system with a quicker and uniform response time for all trace gases, since the lag time can vary a lot for the different low-cost small sensors, and this can cause some difficulties (see Table 4.1, Section 4.3).

Fig 4.6 shows the updated smoke sampling system, which consists of two main sampling boxes rather than the single one used for the first fieldwork. The first box is an updated version of previous smoke sampling box used for the fieldwork described in Section 4.2. The fitted gas sensor system inside has been designed to have a less than five second gas exchange time, replacing the old tube with its 14 second gas exchange time (Section 4.3.3). An aluminium and glass frame has also been fitted into the sampling box, providing better support to all the equipment inside. The filter holder has also been moved to outside of the sampling box, though the link to the sampling system follows original flow (see Fig. 2a, Section 4.2). This change is to reduce the need to open the box when changing filters during fieldwork, which is much more convenient. The second sampling box (yellow one in Fig 4.6) is actually an ultra-portable analyser working on the principle of the absorption of laser radiation in an IR cavity, and is an adapted Los Gatos Research (LGR) ultra-portable greenhouse gas analyser (μGGA) that provides CO as well as CO_2, CH_4 and H_2O mixing ratios. It delivers data at 1 Hz, though the flow time through the internal measuring cell will introduce an approximately 10 second response time for the analyser (but which is the same for all species measured). An external pump with a higher flow rate can be used to reduce the response time to less than 2 seconds when required (the silver pump next to the keyboard in Fig. 4.6).

Figure 4.6: Deployment of updated smoke sampling system in the field, including two main parts, LGR ultra-portable greenhouse gas analyser which provided CO_2, CO, CH_4 and H_2O measurements (closed yellow box at top) and the new smoke sampling box which provided CO_2, CO, $PM_{2.5}$ and BC measurements (opened orange box in the middle).

4.4.2 TEST IN A NORTHUMBERLAND MOORLAND FIRE

The first test of this updated sampling system occurred in May 2015 at an experimental moorland fire conducted in Northumberland, UK. Fig. 4.7 shows the time series of the four trace gas mixing ratios recorded by the LGR analyser downwind of the fire, which lasted around 20 min. All mixing ratios/concentrations show here are excess measures, calculated via subtraction of pre-fire ambient background values. The whole burning process is been divided into 7 plumes (P1 to P7) identified by different colours in Fig. 4.7. It is very clear the plumes 1-2, which occurred at the beginning of fire, were dominated by flaming process with both high concentrations of CO_2, CO and CH_4. After the mixing stage shown as plume 3, the fire appears to be dominated by smouldering emission in plumes 4-7. The time series of particulate mass concentrations are also shown in Fig. 4.7. In Section 4.2, a very large difference in the $PM_{2.5}$ to BC ratio was noted between flaming and smouldering combustion of wheat residue burning (2.0 vs 80.7 respectively). Similar patterns are seen here, for example in plumes 1 and 2, which are considered as being generated by primarily flaming stage combustion, high $PM_{2.5}$ and BC values are observed. Whilst during the plumes expected to have been generated by primarily smouldering stage combustion (plumes 4 - 7), only high mass concentrations of $PM_{2.5}$ are observed (with peak values ranging from 30 - 60 mg m^{-3}), whilst BC mass concentrations were all below 1.0 mg m^{-3} in these smouldering stage plumes.

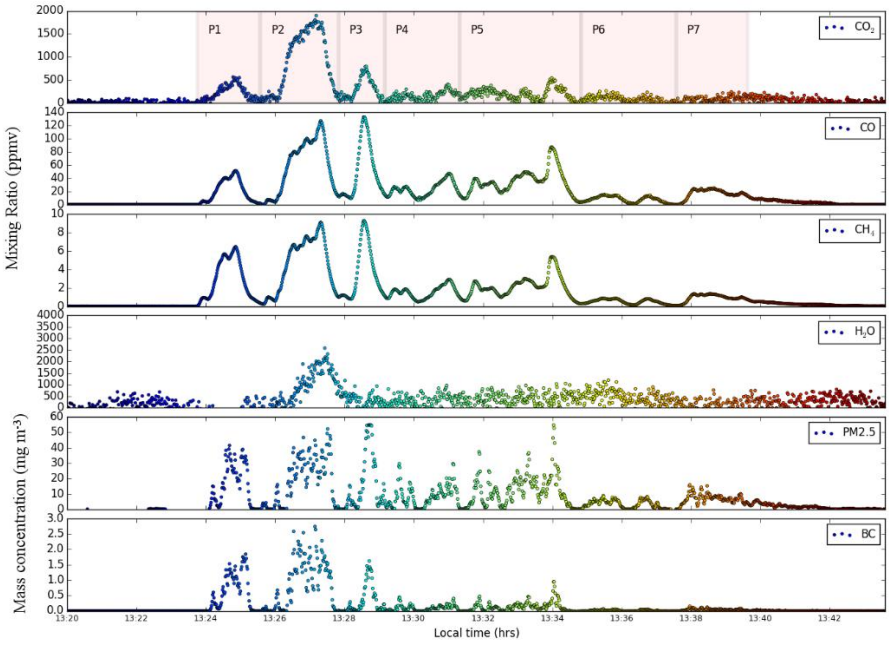

Figure 4.7: Time series of gas mixing ratios (CO_2, CO, CH_4 and H_2O; ppmv) measured by LGR analyser and particulate mass concentrations of $PM_{2.5}$ and BC ($mg.m^{-3}$) from smoke sampling box, coloured by time. The time series data have been divided into 7 plumes (P1-P7), which status were gradually changing from being dominated by flaming to smouldering process.

Fig 4.8 shows the correlation of CO, CH_4, $PM_{2.5}$, and BC with CO_2, with the same colour scheme used as in Fig 4.7 for the different plumes. Fig 4.8 a-b shows clearly two different fire stages based on the trace gas data alone, with the uppermost (higher slope) CO/CO_2 and CH_4/CO_2 ratios coming from smouldering phase smoke and the lower from flaming stage smoke. However, introduction of the particulate mass concentration measures (Fig 4.7 c-d) makes the scatterplots show less of a clear relationship, though with some potential indication still of two patterns that may match those shown in the trace gas scatterplots of Fig 4.7 a-b. This lack of a clear scatterplot linear relationship in Fig 4.7 c-d is put down to the fact that the internal pump of the LGR analyser was used, which as mentioned in Section 4.4.1 delivers a long exchange time (of 10 sec). This appears to cause significant problems when matching the LGR-measured trace gas data to the particulate data ($PM_{2.5}$ or BC) coming from the other sampling box.

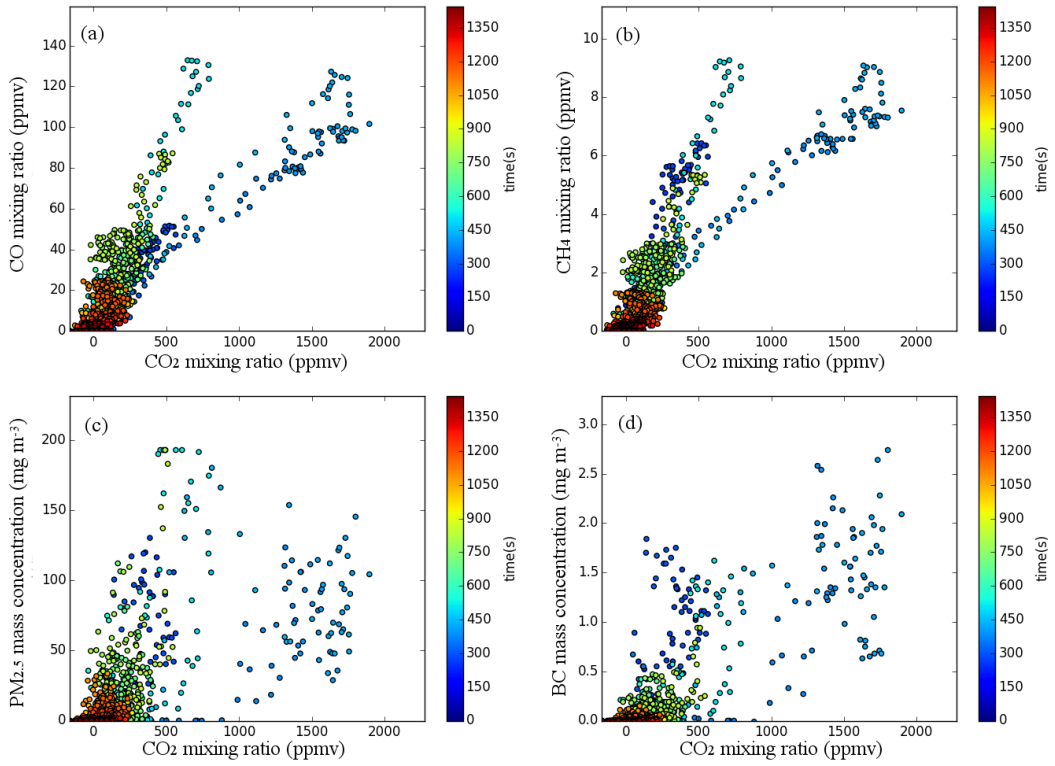

Figure 4.8: Directly comparison of CO_2 mixing ratio to (a) CO and (b) CH_4 mixing ratios, and (c) $PM_{2.5}$, (d) BC mass concentrations using the same data from Fig. 4.7, coloured by time (seconds count from the start of fire).

This test highlighted the great advantage of LGR analyser for the trace gas measurements, which reduced the difference in lag times between the CO_2, CO and CH_4 time-series down to zero and thus enabled very effective determination of the trace gas emission ratios from the relevant scatterplots (Fig. 4.8a, b).

However, the internal pump of the LGR appears insufficient when delivering trace gas data to be combined with the particulate matter data from the second sampling system. It appears a faster, external pump is needed to speed up the flow rate through the LGR.

4.4.3 TESTING USING CROP RESIDUE COLLECTED IN CHINA

Though a filter holder has been designed to fit in the smoke sampling box (Fig.2, Section 4.2), and this was used to collected a few filter samples during the first period of fieldwork in China, the total mass on those filter samples was insufficient for accurate quantification. This is because the flow (1.67 $l.min^{-1}$) used for sampling lead to insufficient particles being collected during each fire that was sampled. Therefore, as already stated, the $PM_{2.5}$ mass concentrations taken from the DustTrak in Section 4.2 were calibrated using the equation provided by Preble et al (2014), calculated from (biomass) cookstove smoke emissions. However different aerosols may scatter the laser light used by the DustTrak in different ways, and cookstove smoke may have some different characteristics to landscape fire smoke, and so calibration of the Dusttrak for the smoke of crop residue fires was considered desirable for future field campaigns.

To provide this, a test was conducted using crop residues collected in China and burned in the UK, and the results were also compared to smoke from other fuel (Indonesian peat) to determine how transferrable the calibration factors determined using one type of landscape fire fuel are to very different types. Similar to the method of deployment used for the bonfire measurements in Eastern China (described in Fig. 3b, Section 4.2), we fitted the inlet of the smoke sampling box into the end of an aluminium laminated pipe which attached to a pump (Fig. 4.9). Instead of piling all the fuel at bottom of the burn container and then igniting it, the fuel was fed to the fire continually to better simulate the smoke from a spreading fire in the field which has access to continual new fuel and sufficient oxygen for sustained flaming combustion. Alongside the DustTrak, for this test a Thermo Fisher Partisol Sequential Air Sampler was deployed, which collects filter samples at a high flow of 16.7 $l.min^{-1}$, ten times the flow of our smoke sampling system. This potentially allows us to collect sufficient particles on the filters to perform the calibration. The LGR analyser was also deployed so it can be used to collect trace gas data from the smoke.

Figure 4.9: Deployment of Partisol Sequential Air Sampler, smoke sampling box and LGR analyser in crop residue bonfire tests, designed primarily to provide a DustTrak calibration for this type of smoke.

Fig. 4.10 shows the results from this calibration test, with two samples unfortunately contaminated by rain drop when opening the Sampler to check the filter. That happened during the first two wheat burns and therefore those results being removed (see Table 4.4). With the limited samples, results from wheat and corn were categorised as same group "crop residue". The slope of the linear best fit calibration line through the data is $y = 4.6x + 0.62$ with $r^2 = 0.43$. The relatively high variation is probably due to mixing status of flaming and smouldering during sampling. The slopes of crop residues samples are, however, much higher than that for the peat burn (1.45), probably because the more flaming dominated crop residue burns produced more black carbon (as discussed in Section 4.2), whereas the smouldering dominated peat fires produce larger organic aerosols. The DustTrak sensitivity to particles below 300 nm in size is likely to be less than that at larger particle diameters, and sensitivity stops at 100 nm particles. Much of the black carbon produced by flaming combustion maybe below 100 nm in diameter, and so will be missed by the DustTrak but will be present on the filter, thus increasing the ratio of PM2.5 mass captured on the filter to that measured by Dusttrak compared to the peat-fire smoke where larger OC aerosols dominate.

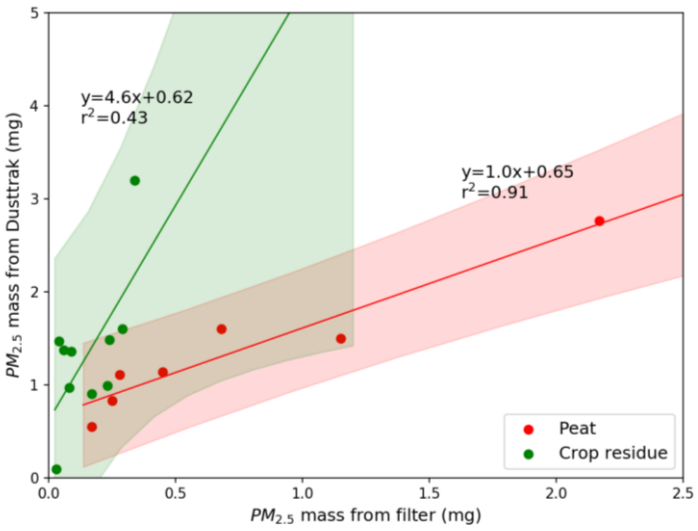

Figure 4.10: Correlations of $PM_{2.5}$ mass measured by Dusttrak and filter from Chinese crop residue (wheat and corn) and peat burning samples. The best fit linear relationships are shown, with the shaded area representing the 95% confidence limit on the relationship.

Table 4.4: Emission ratios and emission factors estimates calculated from the tests using the setup shown in Fig 4.9. The emissions factors of $PM_{2.5}$ have been calculated two ways using the same method of Table 5, Section 4.2.

	Fuel	Duration(s)	Emission Ratio		Emission Factor ($g.kg^{-1}$)				
			PM_{25}/CO_2*1000	PM_{25}/CO	CO_2	CO	CH_4	PM_ CO_2	PM_ CO
1	Wheat	307	42±3.2	1.1±0.039	2147±176	53±6	1.9±0.35	50±6	50±6
2	Wheat	456	37±17	0.81±0.15	2121±175	69±12	1.7±0.27	43±20	49±13
3	Wheat	312	8.6±0.62	1.1±0.14	2218±182	11±1	0.12±0.02	11±1	10±2
4	Wheat	241	16±1.3	0.49±0.17	2177±179	36±11	0.66±0.11	19±2	15±7
5	Corn	409	15±3.2	0.42±0.098	2194±180	25±9	0.65±0.29	18±4	9±4
6	Corn	298	9.9±2.9	0.74±0.023	2208±181	17±5	0.37±0.14	12±4	11±5
7	Corn	317	11±0.69	0.56±0.16	2198±180	23±5	0.41±0.13	13±1	11±4
8	Corn	464	14±3.4	0.41±0.16	2195±180	24±7	0.84±0.23	17±4	9±4
9	Corn	342	14±0.58	0.49±0.12	2189±180	28±5	0.44±0.08	17±2	12±4

Using the CO_2, CO, CH_4 measurements from LGR analyser and the particulate information from smoke sampling system, the emission ratios and emission factors were calculated for these test fires using the methods explained in Section 4.2. Table 4.4 shows the resulting EFs, with the wheat EF_{CO2} (2121-2218 $g.kg^{-1}$) being significantly higher than that reported in Section 4.2 based in the *in situ* field measurements of smoke made in China (1739 $g.kg^{-1}$, Table 4). This likely indicated that the burning conditions in these tests were more favourable for flaming combustion compared to those seen with spreading fires in the field. Section 4.2 stated the importance of measuring emission factors by deploying instruments *in situ* in real field burns, due to the fact that the burning conditions and this the smoke characteristics can be quite different from those of laboratory or other forms of 'atticful' burning situations, and that is exactly is found here. The other important finding is the similarity of $EF_{PM2.5}$ calculated from the emission ratio of $PM_{2.5}$ with CO_2 (and EF_{CO2}) as explained in Section 4.2, and $PM_{2.5}$ with CO (and EF_{CO}). This

improvement is believed to compared to results shown in Figure 4-5, Section 4.2, stems from the high performance of the introduced LGR analyser.

4.4.4 FIELDWORK IN JUNE 2016

Further to the developments described above, an extra period of fieldwork in June 2016 was performed around Tongling city, Eastern China – the same city used for the first fieldwork described in Section 4.2. The main purpose was to re-investigate the crop residue burning emissions factors now using the LGR analyser at an *in situ* burning site in China, to compare the results with those obtained using the low-cost small sensors of the smoke sampling box described above and in Section 4.2. Due to local fire prohibition policy enforcement operating at the time, only bonfire burning was able to be studied at this time, not spreading fires.

This fieldwork was initially planned to collect the gas concentrations of smoke from wheat, corn and rice residue burning. However, the LGR analyser failed after the first day and only samples from wheat residue fires were able to be collected.

The time series of excess gases mixing ratios (i.e. after ambient background concentrations have been deducted) can be seen in Fig. 4.11. Very high mixing ratios were found for CO_2 (up to 6000 ppmv), CO (up to 1000 ppmv) and CH_4 (up to 175 ppmv) using the LGR. MCE varied from 0.75-0.92 during main burning process from 14:29-14:35 pm, indicating this burning is more smouldering compared to the samples collected in Section 4.2 (Table 1), which is likely to be caused by the different style of burning in bonfires compared to spreading fires.

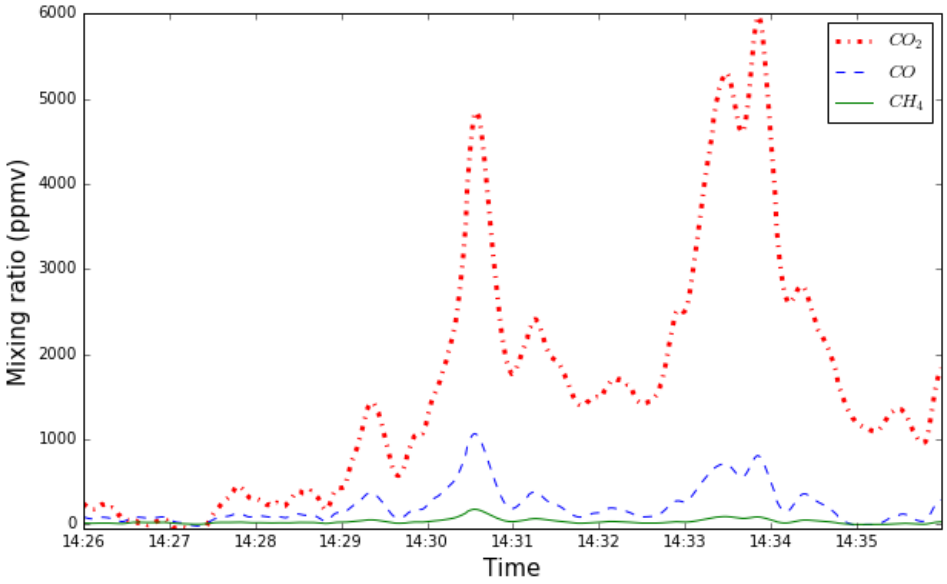

Figure 4.11: Time series of CO_2, CO and CH_4 mixing ratios measured by LGR analyser during June 2016 fieldwork in China.

Scatter plots of CO/CO_2 and CH_4/CO_2 are shown in Fig. 4.12, along with the best fit linear relationships. Using the emission ratios (mol.mol^{-1}), which are the slopes of the CO/CO_2 (0.130) and CH_4/CO_2 (0.017) linear best fires, emission factors were calculated using the Eqn. 4.1 from Section 4.3.7. These are 1593, 135 and 9.3 g.kg^{-1} for CO_2, CO and CH_4 respectively. The emission factor of CO_2 is 8.4% lower than that for the most similar fuel burnt in the first fieldwork period (Table 4, Section 4.2), which is likely a result of the wheat sample here being burned in a bonfire rather than a spreading fire, as described above. Smouldering dominated burning leads to somewhat lower CO_2 emissions than flaming fires, and much higher CO emissions. In fact, the CO to CO_2 emission ratio of 0.130 mol.mol^{-1} lies between the pure smouldering (0.46) and flaming (0.018) emission ratios for wheat burning we proposed in Fig. 9, Section 4.2. Therefore, we believe the results reported in Section 4.2 have been shown to be somewhat repeatable here, using the updated and more capable sampling system. The emission factors calculated in Section 4.2 will therefore be used in Chapter 5 for production of the final emissions inventory of Eastern China.

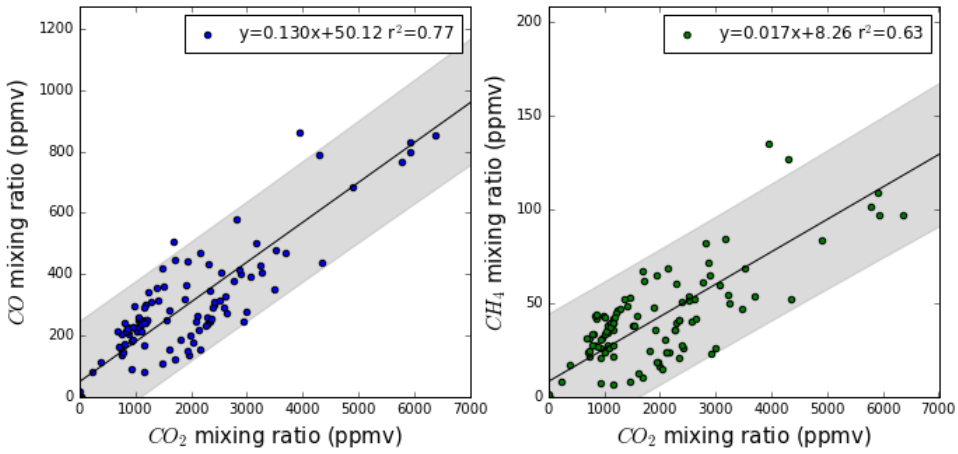

Figure 4.12: Directly comparison of CO_2 to CO (left) and CH_4 (right) mixing ratios using samples from June 2016 fieldwork. The best fit linear relationships are shown, along with its equation, and the grey shaded area represents the 95% confidence limit on the relationship. The slopes of the equations, which are emission ratios, will be used for emission factor estimation.

4.5 LAG TIME MODEL

4.5.1 LAG TIME EFFECT

The problems introduced by having sensors characterised by different lag times when measuring trace gas concentrations for the calculation of emission ratios and emission factors has been introduced in both Section 4.2 and 4.3. There it was shown that electrochemical and NDIR sensors are typically characterised by significant response 'lag' times, generally specified via a T90 metric (Roberts *et al.*, 2012) as below.

$$I_{Sensor}(t) = [X] \cdot s_{Sensor} \cdot (1-F) + I_{Sensor}(t-1) \cdot F + I_{SensorBaseline}(t) \quad (4.2)$$

Where sensor's 1Hz output, $I_{Sensor}(t)$ (ppmv), is a function of the actual gas mixing ratio, [X(t)], the sensor sensitivity (S_{Sensor}, ascertained by the final sensor reading after 600 s exposure), the 'slowness factor' (F), the sensor output of the previous second ($I_{Sensor}(t-1)$, ppmv), and the sensor baseline ($I_{SensorBaseline}(t)$, ppmv). The sensor baseline was found to be typically constant and near-zero for sensors used in this study (Table 4.1, Section 4.3).

The slowness factor is the function of T90, which is response time for the sensor to reach 90% signal is simply related to the exponential time-constant. This can normally be obtained from the sensor manual, or assessed in the laboratory using standard gas with a known mixing ratio (Section 4.3.3).

$$T_{90} = -Ln(0.1)\cdot\tau = -Ln(0.1)\cdot\frac{(t_2 - t_1)}{-Ln(F)} = \frac{Ln(0.1)}{Ln(F)} \quad (4.3)$$

Many studies have used a simple temporal shift between the measurements from the different sensors to try to match them up for the emissions ratio calculation (e.g. Chen *et al.*, 2007; Hörtnagl *et al.*, 2010). Even though such a temporal shift could potentially allow an improved correlation coefficient to be obtained than existed without such a shift, and thus the fitting of an improved linear best fit with a lower uncertainty, recent work by Roberts et al. (2014) shows that this can come at the expense of introducing incorrect changes in the slope of the relationship from which the emissions ratio is calculated. Roberts et al. (2014) show that averaging or integrating over particular time-periods of data is likely a better approach to take.

To compare the results from the temporal shifting and temporal averaging approaches, a simulation was conducted - illustrated in Fig. 4.13 and based on Eqn.4.2-3. In this example, 'Environmental' refers to the true concentrations in the environment, with several Gaussian distribution modes (with added noise) to simulate a few plumes being assessed by the sampling system during fieldwork. 'Detected' refers to the measured concentration recorded by the sampling system. A slope of 1.0 is expected in the ideal case when lag time equals to zero. Here a 40-sec lag time was introduced to simulate the CO_AX sensor (Table 4.1, Section 4.3) In the bottom plots we show the scatterplot of the 'environmental' vs. detected datasets, with original data(b), and output from temporal shifted method (c, 'modified') and averaging method ('average'). In the modified plot the 'detected' data has been temporally shifted to maximise the correlation coefficient (r).

Subsequent to the temporal shift (Fig 4.16b), an improved correlation is seen and the slope of the linear best fit to the data is around 1.16, nearly 20% higher than the true slope of 1.0 that we would hope to gain (i.e. with the temporal shift perfectly correcting for the sensor lag effect). In contrast to this, the slope of the data processed with the temporal averaging method is almost equal to 1.0 (Fig. 4.16c). Whilst the concentrations are lowered by the temporal averaging, as long as the slope is correct then the estimated emission factors results will also be correct. This supports the use of temporal averaging to minimise the measurement impacts from the combination of different sensor lag times and the rapidly changing trace

gas mixing ratios experienced during *in situ* smoke plume measurements (Reid *et al.*, 2005). This supports the use in Section 4.2 of the temporal averaging method for trace gas emission ratio and emissions factor derivation, albeit with the price of sacrificing the number of data points.

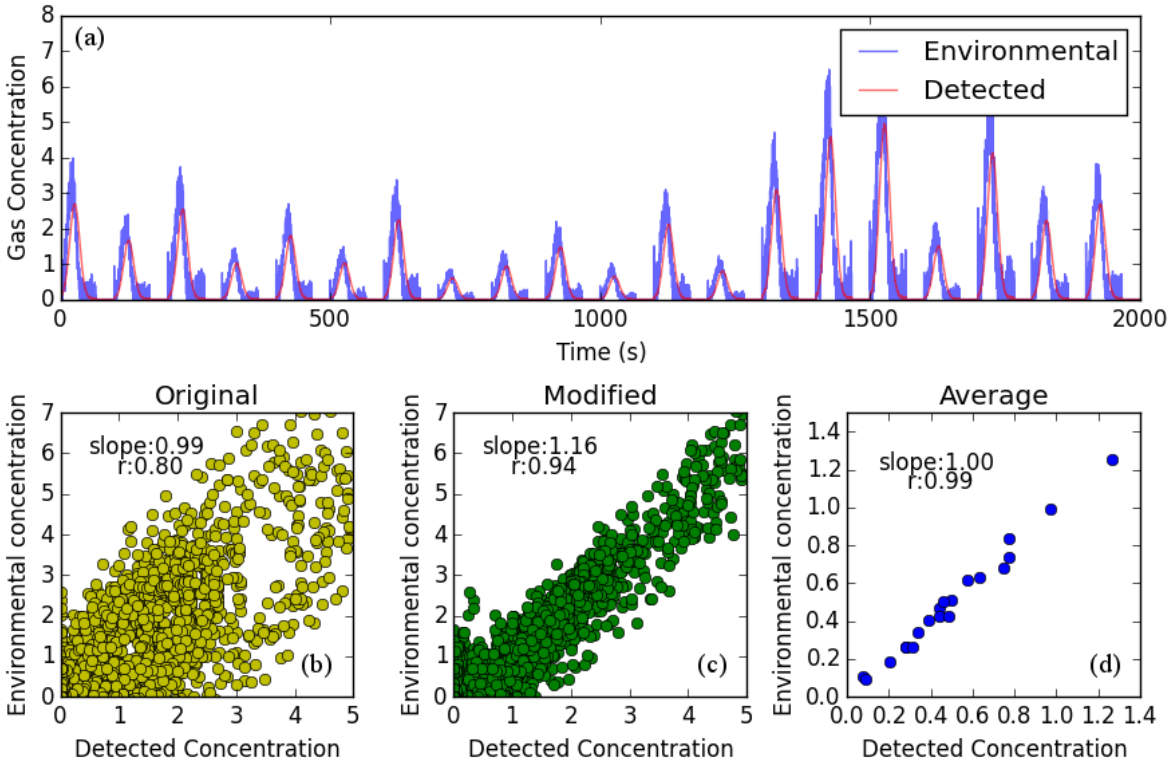

Figure 4.13: (a) Time series of environmental and detected gas concentrations from simulation results. Bottom row of scatter plots show the correlations of environmental and detected gas concentrations under different calculation scenarios, with (b) original data, (c) output modified by temporal shift and (d) averaging results.

4.5.2 Forward Lag Time Model

The average interval used in the averaging method of Section 4.2 is 20s to different gas, up to 120s for gas and aerosol, which will lead to a problem of insufficient data for emission ratio calculation when the fire duration is below 10min (at least 5 points for linear fit). Also, as shown in Fig. 4 and 5 in Section 4.2, each plume in the rapid change *in situ* fieldwork can be as short as tens of seconds. In the averaging method, a few plumes will be potentially averaged as one point, losing the information of fire phases (flaming or smouldering).

An alternative way is desirable for such short sampling with rapid gas/aerosol concentration change. In this section the function 4.3-4.4 are used to explore the possibility of deriving the 'real' concentrations from sensor output which has been impacted by lag time effect, which is to use a slow response sensor results to simulate its performance without the lag time effect.

The CO_2 data from burning case 1 of UK tests (Table 4.4, Section 4.4.3) is used in this study. As shown in Fig. 4.14a, the time series curve of NDIR data is more smooth compare to that from LGR analyser. Three main peaks can be found during whole 300s sampling period of NDIR results while more small peaks show up in LGR results. The main difference can be seen at the peak(s) during 50-100s, where LGR shows a bi-mode and NDIR only shows single mode with wider width. This comparison shows NDIR results are highly impacted by lag time effect, leading to the mixture of this bi-mode into one mode.

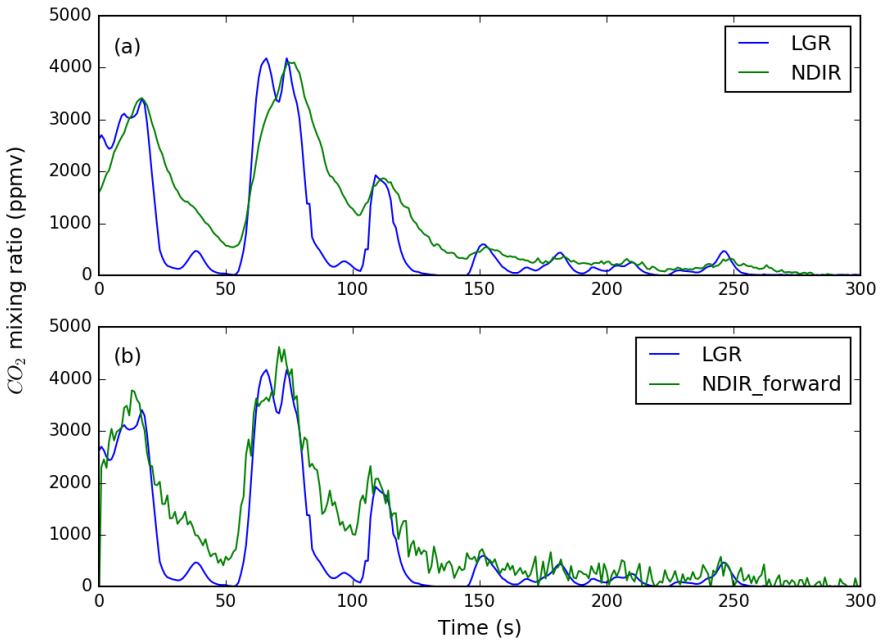

Figure 4.14: Time series of CO_2 mixing ratios: (a) Comparison of results from LGR analyser and NDIR sensor of smoke sampling box; (b) Comparison of results from LGR analyser and NDIR sensor output from forward lag time model. Data is from the burning case 1, Table 4.4.

In the forward lag time model, the T90 derived in lab test (12s, Table 4.3) is applied to NDIR.

The simulated results from NDIR (NDIR_forward) is compared with LGR output in Fig. 4.14b. Though not perfect, the curve of simulated results is much closer with LGR output. For example, in the 50-100s period, the modelled results show a flat curve before reaching the near 5000 ppmv peak, indicating the big mode is combining two modes as what we found in LGR output. The flat distribution between 140-250s in the original results also change towards a few modes as those in LGR results. However, such forward simulation also introduces large unrealistic noise in those CO_2 mixing ratios, making it almost impossible to directly compare with CO data and calculate the emission ratio. Therefore, the forward lag time model of using slow response data to simulate fast response data is not a practical way.

4.5.3 REVERSED LAG TIME MODEL

Instead, smooth data can be derived when using fast response data to simulate the sensor's 'slow' output if a larger T90 is given. Though absolute values of output data series will change here, the emission ratio between two species will stay same if they are being simulated at the same slowness level.

When simulating the slow output, the T90 should be the T90 of slow response sensor deduct that of quick response sensor. Fig. 4.14 gives the example of reversed lag time model using the same dataset of Fig. 4.13. In this case, the T90 is 9s, using that of NDIR (12s) deduct by LGR CO_2 laser (3s). Unlike the noisy results from forward lag time model (Fig. 4.14b), the output of reversed lag time model using LGR data showing here is very smooth. The shapes of two big modes between 50-150s from these two set of data are almost same except the modelled LGR results are a bit lower. The linear correlation can be found between NDIR data and modelled LGR data with a function of $y = 0.839x-156$ and the R square is as high as 0.92. The slope not equals to 1 and the intercept value could be the result of equipment' different response to certain gas concentrations.

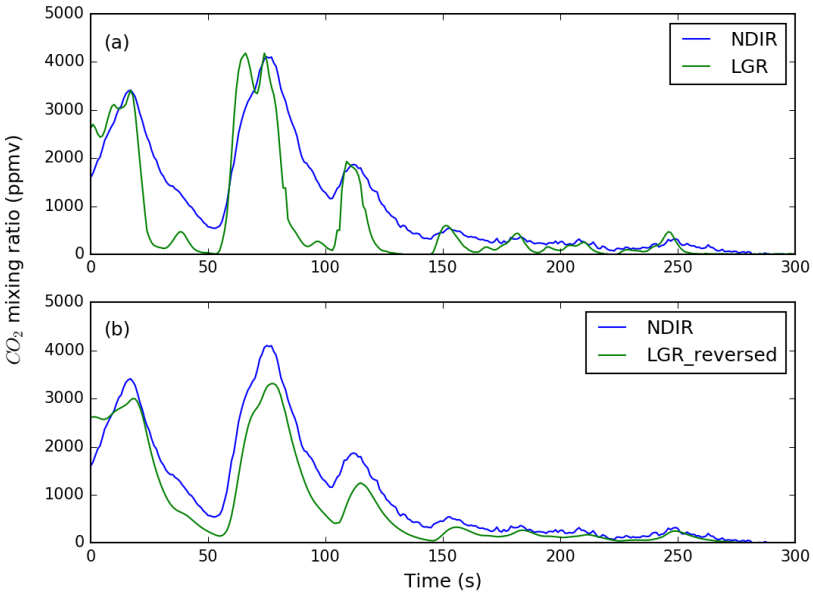

Figure 4.15: Time series of CO_2 mixing ratios: (a) Comparison of results from NDIR sensor of smoke sampling box and LGR analyser; (b) Comparison of results from NDIR sensor of smoke sampling box and modified output of reversed lag time model using LGR analyser data. Data is from the burning case 1, Table 4.4.

For the sensors with unknown T90, a 'best linear fit' method is used for generating the difference of two sensors. Here two sets of equipment/sensors are used as example. One is CO and CO_2 from LGR analyser used as reference, assuming they don't have any lag time effect when using the external pump with larger

flow (see Section 4.4.1). The other one is CO and CO_2 from AQ sensors, which CO_2 is known as a slow sensor with unknown T90. Four different gas samples have been fed into these two sampling sets. The scatter plots, as well as best fit lines with functions of CO_2 and CO for different gas samples measured by LGR and AQ can be seen in Fig. 4.16a-b. The LGR results have shown four linear fit lines with R squares all over 0.9. Meanwhile AQ results have shown very strong lag time effect.

In the computation experiment, the fast response data (CO from AQ sensor in this case) will be used. The simulation ran for fast sensor data using T90 from 1s to 120s and calculate the correlation coefficient of each output plume (each gas sample in this case) with slow sensor plume data. The mean value of correlation coefficient of all plumes was recorded. The lowest T90 of mean correlation coefficient which is higher than 0.9 was chosen as simulated T90, if it exists. Otherwise T90 with highest mean correlation coefficient was used. Using the simulated T90, the corresponded 'slow' output of fast sensor can be calculated, which could be directly compare with the slow sensor data for emission ratio calculation.

The modelled results can be seen Fig. 4.16c. A very high T90 of 74s has been generated from the 'best linear fit' method, which explained the serious lag time effect shown in Fig. 4.16b. However, the emission ratios (slopes of the linear fit equations) from four gas samples are -3.4, 7.3, 19.2 and -8.4, very close to those from LGR analyser (-3.6, 8.4, 20.3, -7.9).

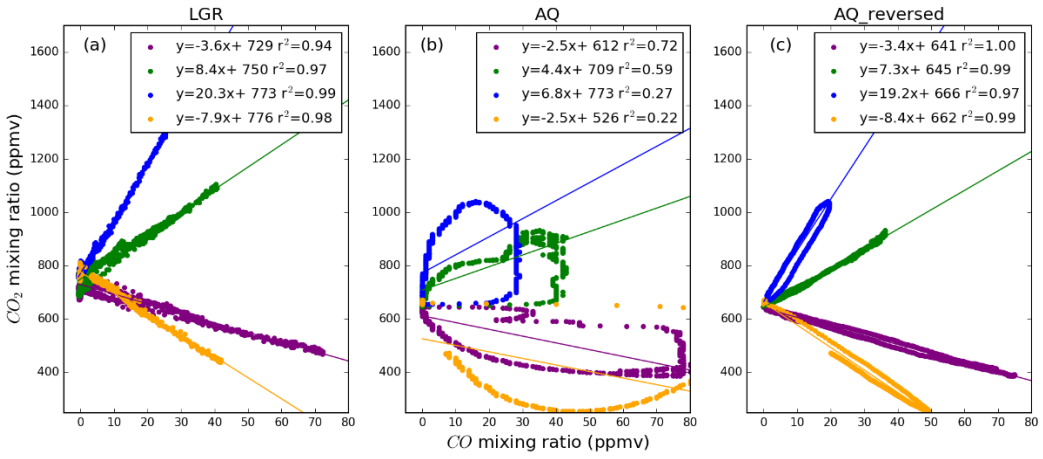

Figure 4.16: Directly comparison of CO_2 and CO mixing ratios from, (a) LGR analyser, (b) original AQ sensors' measurements, (c) reversed lag time model output using AQ sensors' measurements. The best fit linear relationships are shown, along with its equation.

4.5.4 SUMMARY OF LAG TIME MODEL

The reversed lag time model has proved its potential of improving data quality from sensors which are suffering lag time effect due to their slow response. The simulation example from Fig. 4.16 further shows this model could still work well without knowing the exact sensor lag time by introducing a 'best linear fit' method. For studies only focusing on the relative ratio of two species rather than their actual concentration, similar like the emission factors estimation in this study, this model could potentially have been applied. However, when applying it to rapid change data collected from field, bad performance might occur for mixed plumes. This is because different plumes could have different emission ratio depending on the mixture status of flaming and smouldering, which might cause confusion in the 'best linear fit' method. Here it is recommended to let the equipment/sensors expose under ambient air for a few seconds to create breaks of each plume when trying to use the lag time model for future research.

CHAPTER 5: ESTIMATING AGRICULTURAL RESIDUE BURNING FUEL CONSUMPTION AND SMOKE EMISSIONS IN EASTERN CHINA USING NEW REMOTE SENSING

5.1 INTRODUCTION

This Chapter combines outputs from Chapters 3 and 4 related to agricultural residue burning fires in Eastern China, firstly to generate a gridded daily biomass consumption product (meeting Objective 2 from Section 2.7), and then to produce a smoke emissions inventory (meeting Objective 4 from Section 2.7). It does this via a combination of active fire locations and FRP retrievals, mapped across the region using data from the NPP VIIRS sensor (Chapter 3), and fire emission factors derived from *in situ* measurements of smoke using the newly developed smoke sampling system (Chapter 4).

5.2 METHODOLOGY FOR FIRE RADIATIVE ENERGY, FUEL CONSUMPTION AND SMOKE EMISSIONS ESTIMATION

5.2.1 VIIRS-IM FRP PRODUCT AND OTHER INPUT DATASETS

The gridded daily biomass consumption product for Eastern China was generated primarily using the VIIRS-IM FRP product developed in Chapter 4. Fig 5.1 shows the FRP time series derived from this product for Eastern China (the area shown in Fig. 2, Section 3.2), using the earliest VIIRS data currently available at the time of writing (February 2012 - December 2015). Since January 2012 is outside the local agricultural burning season, these data essentially cover 4 full years of fire season(s), and should be sufficiently long-term to allow meaningful comparisons to be made with other biomass combustion datasets. This includes the GFAS and GFED global inventories reviewed in Chapter 2.

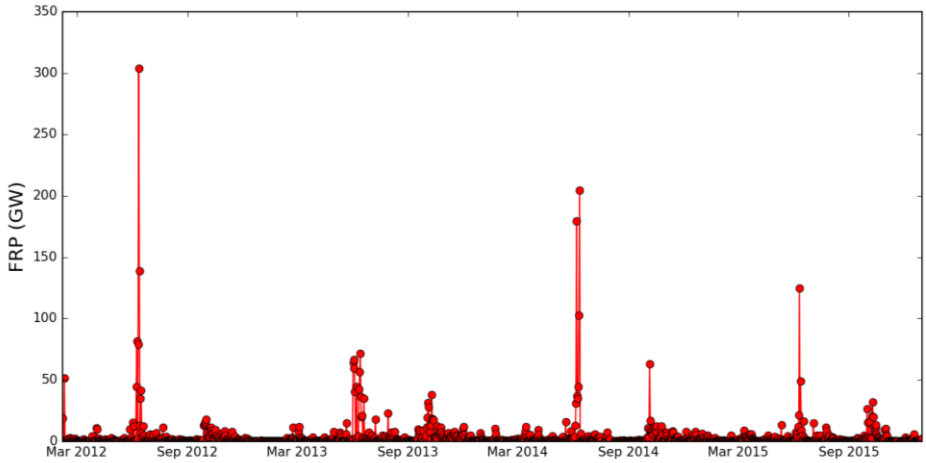

Figure 5.1: Time series of total daily FRP recorded from fires across Eastern China using the VIIRS-IM FRP product algorithm developed in Chapter 3, shown here from Feb. 2012 to Dec. 2015. The seasonality of fire activity is clearly seen, with FRP peaks of around 50 and 300 GW respectively corresponding to the times of agricultural burning in this region (Huang *et al.*, 2012).

FRP is well related to fuel consumption rate, as shown in Wooster *et al*. (2005) and detailed in Chapter 3. As described in Chapter 3, VIIRS provides observations of any particular location twice per day, and thus the VIIRS-IM FRP product can be used to estimate fuel consumption rates at these times only. A key benefit of VIIRS compared to MODIS is that the performance degradation in the FRP retrievals made far away from nadir appears far less for VIIRS than for MODIS, due to the VIIRS pixel aggregation (see Figure 12, Section 3.2). Thus the full swath of VIIRS can be used to obtain good quality, twice daily FRP retrievals and thus fuel consumption rates. Further information is required to estimate the fire radiative energy (FRE) however, because this is the temporal integral of the FRP over a particular time-period (Wooster *et al.*, 2015). FRE has been shown proportional to the total biomass burned (Freeborn *et al.*, 2011; Roberts *et al.*, 2009), building on the fact that FRP is proportional to biomass combustion rate (Kaiser *et al.*, 2012; Wooster *et al.*, 2005). Wooster *et al.*, (2005) show the linear FRE-to-fuel consumption relationship for the type of 'small straw fire' representative of those involved in agricultural residue burning in Eastern China. This relationship (fuel consumption [kg] = 0.37 [±0.015] × FRE [MJ]) will be applied to FRE-estimates derived from the temporal integration of the VIIRS-IM FRP dataset in order to estimate daily biomass consumption.

However, to perform the conversion between the twice daily VIIRS-IM FRP data and daily-integrated FRE, information on the fire diurnal cycle is required (Ellicott *et al.*, 2009; Roberts *et al.*, 2005). This information was obtained from Himawari-8, a Japanese geostationary meteorological satellite launched on 7th October 2014. These data have recently been used to derive active fire detections and FRP across

Asia by Xu *et al.*, (2017) upon which the thesis author was a co-author (including in Appendix A of this thesis). Himawari-8 cannot be used directly to calculate the FRE for each day of the 3 years of the study period however, because (i) it only provides data from early 2015 onwards, and (ii) its relatively coarse spatial resolution (2 km at the sub satellite point) means it misses many smaller agricultural fires, which is a significant issue as the comparison between MODIS and VIIRS showed in Section 4.2. Xu *et al*. (2017) included in Appendix A details further how the Himawari-8 active fire detection processes misses a significant number of fires compared to simultaneous MODIS observations, due to its coarser pixel size. However, where such fires are concentrated in sufficient numbers, Himawari-8 does detect their signature and can map their changing total FRP output over the day to derive the fire diurnal cycle, as explained below.

5.2.2 BENEFITS OF HIMWARI-8

Himawari-8 is the first of a new generation of three axes stabilised geostationary weather satellites, and is located above the equator at 140° east to view primarily Asia (Kurihara, Murakami & Kachi, 2016; Xu *et al.*, 2017). Himawari-8 carries the Advanced Himawari Imager (AHI), which scans the full disk of Asia and Australia every 10-minutes. The active fire detection and FRP algorithm whose output is used here is described fully in Xu *et al*. (2017) (included as Appendix A).

For the Eastern China region during the June 2015 burning season, Fig. 5.2 shows the times series of FRP derived from Himawari-8 and from VIIRS-IM (Chapter 3). The similar trends seen in the two datasets derived from these different systems provide confidence that they are responding to the same (or at least similar) fire activity. However, the Himawari-8 FRP values are many times lower than those of the VIIRS-IM FRP product because of its much coarser pixel area (4 km^2 pixels at nadir, and coarser at these latitudes) means that it will typically fail to detect isolated agricultural fires and will only detect those that are burning alongside many others within the same pixel.

This same issue affects all geostationary fire products (e.g. that derived from Meteosat SEVIRI; Wooster *et al.*, 2015) and means that such datasets typically need to be combined with other remotely-sensed FRP data to bias adjust them for the impact of the 'undetected' small fires (Freeborn *et al.*, 2009). The fire situation in Eastern China makes this particularly important, because in such agricultural regions the vast majority of fires are small, and of rather low intensity (as shown in Fig. 11, Section 3.2). This type of active fire detection bias can also be seen in the differences in the total FRP of the region measured at

approximately the same time by MODIS and VIIRS-IM (Fig. 11, Section 3.2), where VIIRS-IM measures an FRP often around four times greater than MODIS – thus indicating that many agricultural fires lie even below the MODIS active fire detection limit (but are detected by the higher spatial resolution VIIRS product).

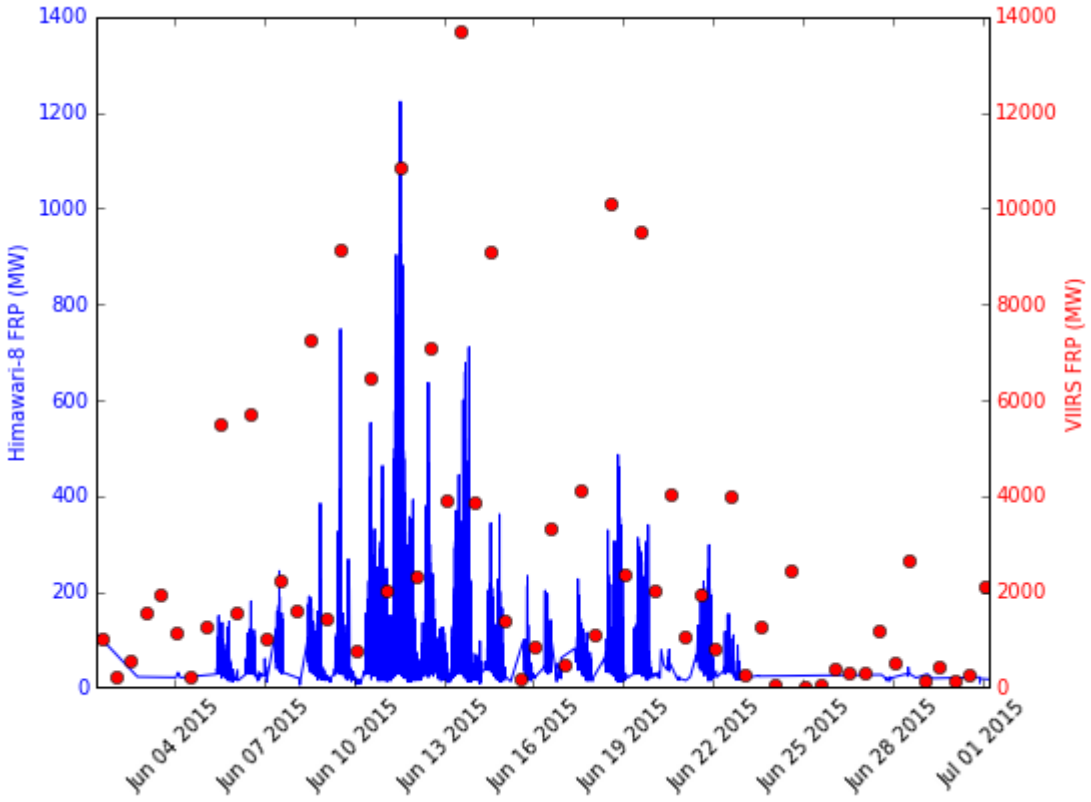

Figure 5.2: Time series of spatially summed FRP in Eastern China retrieved from Himawari-8 (blue lines) and VIIRS (red points) in June, 2015. VIIRS provides typically two observations per day, and Himawari 144 observations per day at 15-min frequency.

Whilst the FRP retrievals made from Himawari-8 may not be that representative of the total FRP of the region due to this issue, the detections made in areas where many fires are burning at the same time (which enables a confident detection to be made) can be used to derive the regionally representative diurnal cycle of fire activity. This represents the relative variation in fire activity of a region over a 24 hour cycle (Kaiser *et al.*, 2012; Roberts *et al.*, 2005). When this diurnal cycle is combined with the total FRP estimates coming from the high spatial resolution VIIRS-IM FRP product twice a day, the combination can be used to provide an estimate of the total FRE being emitted by the agricultural burning across the whole day. Converting this FRE estimate to total fuel consumption is expected to provide the best estimate of daily fuel consumption currently available for the region.

5.2.3 USAGE OF HIMWARI-8 AND VIIRS-IM

Two months of Himawari-8 data were used to specify the fire diurnal cycle, collected in June 2015 and October 2015 (i.e. across two burning seasons), and these data were combined with the four years of VIIRS-IM FRP data shown in Fig. 5.1.

5.2.4 DATA GRIDDING AND CLOUD CORRECTION

The data from the VIIRS-IM product were aggregated into 0.1° grid cells for the analysis. Unlike the daily average FRP calculation of GFAS, which weights the individual FRP observations by their view zenith angle to downgrade the importance of far off-nadir MODIS observations (Kaiser *et al.*, 2012), the VIIRS-IM FRP data were used directly since Chapter 3 showed a very limited view zenith angle dependence of the FRP values (Section 3.2). For a VIIRS observation, the total observed FRP (F) within each 0.1° grid cell j was calculated from the FRP sum of all active fire pixels (i) within the grid cell:

$$F_j = \sum_{i \in j} F_i \qquad (5.1)$$

Total agricultural area (A) within the grid is calculated similarly:

$$A_j = \sum_{i \in j} A_i \qquad (5.2)$$

The VIIRS-IM product has been shown to be relatively insensitive to smoke because such plumes are relatively transparent at MWIR wavelengths (Section 3.2). However, adjustment for meteorological cloud cover is required to take into account actively burning fires hidden from view of the sensor. For partially cloud covered grid cells, it is assumed that the active fire distribution under cloud is the same as under clear sky areas, as has been assumed by Kaiser *et al*. (2012) in GFAS and in previous research (Streets *et al.*, 2003). However, since agricultural fires will only occur on or close to agricultural land, a factor (ω_{j-ac}) was introduced to avoid over-compensating for cloud-cover in non-agricultural areas. This factor is calculated from:

$$\omega_{j-ac} = 1 + \frac{R_{j-agrc}}{R_{j-agrL}} \times \frac{R_{jc}}{1-R_{jc}} \qquad (5.3)$$

Where R_{j-agrc} and R_{j-agrL} refer to the ratio of agricultural area covered and not covered by cloud respectively, and R_{jc} refers to the cloud coverage of grid j expressed as a fraction (0 to 1.0). This cloud cover information is obtained from pixels classified as cloud by the VIIRS I-Band active fire detection algorithm (see details in Section 3.2).

Subsequently, the gridded and cloud corrected FRP areal density (FRP_j, MW.km^{-2}) was calculated using:

$$FRP_j = \omega_{j-ac} \frac{F_j}{A_j} \quad (5.4)$$

Note that grids covered by cloud with a fraction of 0.99 or more are removed from contributing any FRP areal density in order to avoid anomalies resulting from large ω_{j-ac} ratios.

Fig. 5.3 shows for a single day of the fire season (4 June 2013) the spatial distribution of FRP areal density calculated from the VIIRS-IM product, before and after the cloud cover adjustment. On this day, intensive agricultural fire activity was detected across a large region of Eastern China, but there is also significant cloud cover. Cloud cover fractions in some grid cells exceed 0.3 (30%), and some reach 0.5. After cloud cover adjustment, the mean (and total) grid-cell FRP across the area increased by 11.5%.

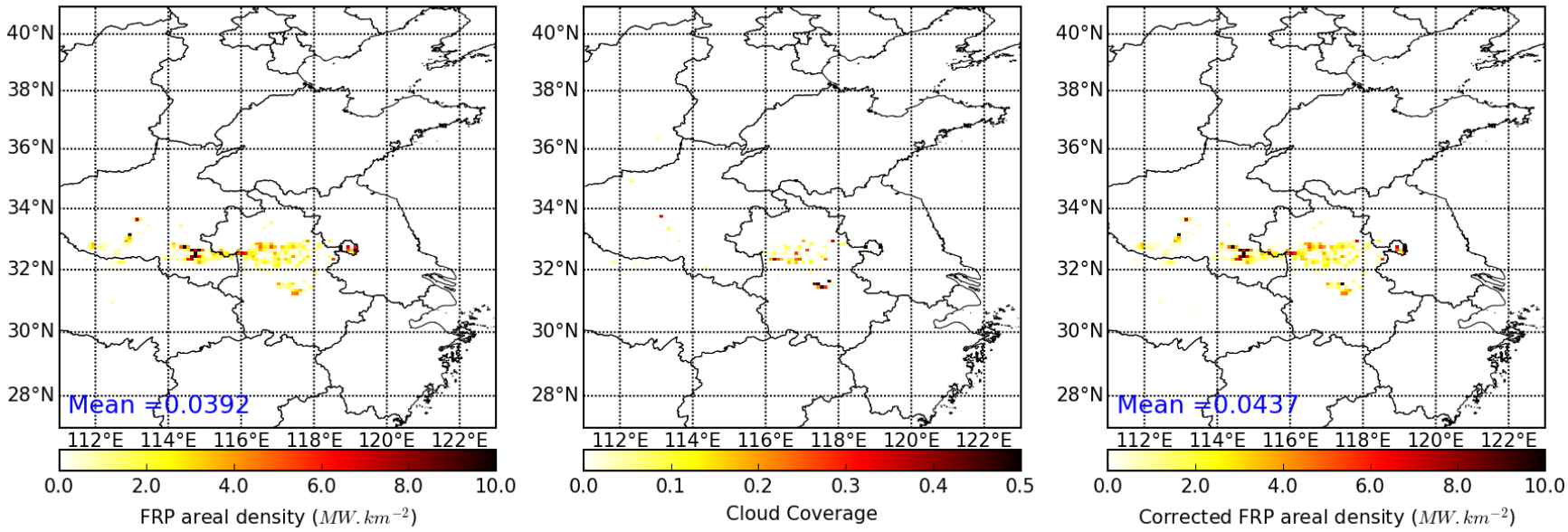

Figure 5.3: An example of the gridded FRP areal density processing conducted using VIIRS SDR (Sensor Data Record) 20130604_t0553424. This shows the spatial distribution of FRP areal density before (left) and after (right) the cloud cover correction. The middle plot shows the fraction of each grid cell covered by cloud. The mean FRP recorded across Eastern China before and after cloud correction is also shown in the blue text.

Fig. 5.4 shows a comparison of the total VIIRS-IM FRP 4-year time-series before cloud correction, along with the mean cloud cover fraction, mean correction ratio (ω_{j-ac}, Eqn. 5.3) and total additional FRP added after cloud-correction. A few FRP peaks are seen in the latter time-series, with values ranging from 2000 - 8000 MW, during which total FRP reaches around 20,000 – 160,000 MW and mean cloud coverage ranges from 0.5% - 1.5% per grid cell. The additional FRP accounts for only 4.4% of total post-cloud corrected FRP, indicating the impact of the cloud-correction procedure is small but significant over the time series.

Figure 5.4: Time series of daily total FRP before cloud correction, mean cloud coverage, mean correction ratio (ω_{j-ac} calculated using Eqn. 5.3), and additional FRP after cloud correction per VIIRS scene in Eastern China from 2012-2015.

5.2.5 Diurnal Cycle and Daily FRE Generation

FRP data from the Himawari-8 FRP product of Xu *et al.*, (2017) were gridded to the same 0.1° grid cell resolution as the VIIRS-IM dataset, and converted to normalised FRP values in order to minimise the impact of day-to-day variations in the amount of fire activity. The hourly normalised FRP ($FRPn_{h,j}$) of grid cell j was then calculated from the hourly FRP ($FRP_{h,j}$) using:

$$FRPn_{h,j} = \frac{FRP_{max,j} - FRP_{h,j}}{FRP_{min,j} - FRP_{h,j}} \quad (5.5)$$

$FRP_{max,j}$ and $FRP_{min,j}$ refer to the maximum and minimum hourly FRP observed in a day (MW). Note the h here is local solar hour (UTC/GMT +8 hours). The durnal cycle runs from 0 to 23 local solar hour

everyday. When applied to the data of June 2015, a number of diurnal cycles can be generated for different days in different grid cells. Instead of using the simple mean of these diurnal cycles, a FRP-weighting method was applied to calculated the weighted mean via the sum of the daily FRP values ($FRP_{sum,j}$), such that the days showing most fire acitvity provided the greatest contribution to the calculation:

$$FRP_{n_w} = \frac{\sum FRP_{sum,j} * FRPn_{h,j}}{\sum FRP_{sum,j}} \quad (5.6)$$

Fig. 5.5 shows the results of this processing, where in Eastern China the weighted mean fire diurnal cycle can be seen to have a a bi-modal distribution. The first peak occurs around 13:00 local solar time, and extends from around 08:00 to 18:00 (daytime), while a smaller second night-time peak is apparent at around 21:00 local time (and shows a height of only around 20% of the normalised FRP value of the first peak).

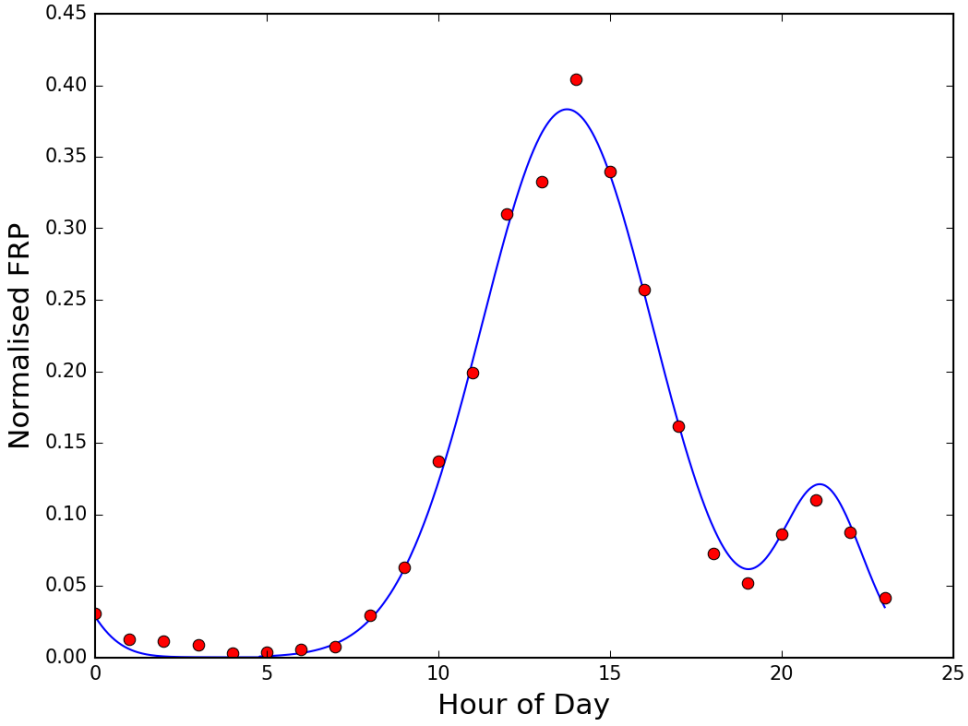

Figure 5.5: Time series of hourly normalised FRP derived from Himawari-8 FRP data generated from the algorithm of Xu *et al*. (2017) over Eastern China for the 0.1-degree date of June 1st to 30th, 2015. The blue curve shows the best fit of sum of two Gaussian distributions.

Whilst the first FRP peak shown in Fig. 5.5 occurs around the time of the afternoon VIIRS overpass, facilitating in principle the relatively easy blending of the VIIRS-IM and Himawari-8 FRP data, the bi-modal nature of the fire diurnal cycle distribution raises a problem, since the nighttime VIIRS overpass

occurs around 01:00 – 03:00 am local solar time, far later than the second peak seen in the Himawari-8 derived data of Fig. 5.5. To tackle this issue two approaches were considered.

The first approach was to generate a VIIRS-to-Himawari-8 ratio using observations from the two sensors made within a short time period of one another (e.g. 15-min). This ratio could then be multiplied by the Himawari-8 FRP time-series in order to bias-correct it for the omission of small isolated agricultural fires. Fig. 5.6 provides an example of this approach applied to the 0.1º grid cell data of June 2015. Two different linear functions were used, one for the daytime ($y = 1.67x + 100$) and one for the nighttime ($y = 4.38x - 68.6$) data. The slope of the latter is higher than the former, indicating more small fires were missed at night. This makes sense, as fewer fires are burning at night and they are this more dispersed and more likely to fail to be detected by Himawari-8 compared to VIIRS.

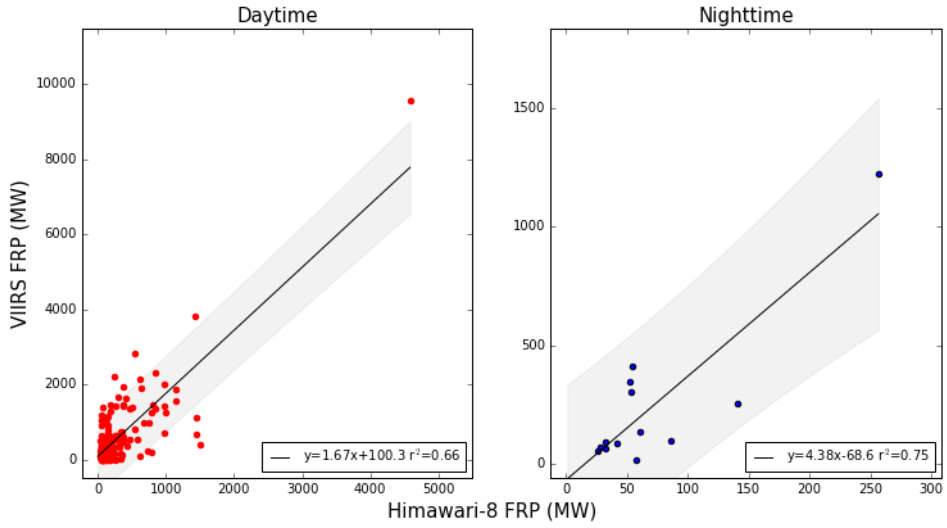

Figure 5.6: Direct VIIRS-to-Himawari-8 FRP data intercomparisons for 0.1º grid cells observed over Eastern China during June 2015, separated into daytime (left) and nighttime (right). The best fit linear relationships are shown, with the grey shaded area representing the 95% confidence limit on the relationship. Both relations are strongly driven by a single high FRP point.

The fact that the relationships shown in Fig. 5.6 are each largely driven by a single high FRP point reduces confidence in its applicability, and the fact that Himawari-8 data are only available from January 2015 anyway and thus unavailable for the period of most of the VIIRS record makes the approach of perhaps limited use.

The second approach tested to blend the Himawari-8 FRP diurnal cycle and the instantaneous twice-daily VIIRS-IM FRP data followed the method detailed in Andela *et al*. (2015). This introduced an approach to

fit the diurnal cycle with an optimally fitted Gaussian fuction to represent the FRP variation across the day, with a fitted baseline to represent the nighttime fire activity:

$$\tilde{\rho}(t) = \rho_{base} + (\rho_{peak} - \rho_{base})e^{-\frac{(h_t - h_{peak})^2}{2\sigma^2}} \quad (5.7)$$

Where ρ_{peak} and ρ_{base} refer to the nighttime and daytime observed FRP (MW), h_{peak} (h) is the hour in the day when FRP reaches maximum in the diurnal cycle, and σ (h) is the width of the main diurnal peak. Using this method, given a certain time of day (h_t) it is a simple process to estimate the resulting FRP value ($\tilde{\rho}(t)$, MJ). The advantage is that the nighttime FRP observations from VIIRS that are located far outside of the main diurnal peak can be directly treated as a constant baseline value (ρ_{base}), and this can be used to counteract the problem of not being able to obtain any information around the time of the second FRP peak seen in Fig. 5.5 from VIIRS.

To evaluate the daily FRE generated using the FRP time-series produced using this methodology, a simulation was conducted to compare results from using Eqn. 5.8 to that from a full consideration of a bimodal distribution. In the first simulation (S1), the FRP derived from Himawari-8 at the VIIRS daytime and nighttime overpass times are used as ρ_{peak} and ρ_{base}in Eqn. 5.7, whilst in the second simulation (S2) the bimodal distribution shown in Fig. 5.5 is described as the sum of two Gaussian fuctions:

$$\tilde{\rho}S2(t) = \sum \rho_{peaki} e^{-\frac{(h_t - h_{peaki})^2}{2\sigma_i^2}} \quad (5.8)$$

Where σ_i from each peak i in Fig. 5.5 (2.39±0.053 for σ_1 and 1.24±0.12 for σ_2 during June, 1.63±0.041 for σ_1 and 0.60±0.077 for σ_2 during October) are used here, h_{peaki} (h) is the hour in day when FRP reaches maximum of two peaks in the diurnal cycle (14.0 for h_{peak1} and 21.2 for h_{peak2} during June, 14.2 for h_{peak1} and 18.4 for h_{peak2} during October). The ρ_{peaki} are the daily Himawari-8's observations during those two peak maximum time.

Fig. 5.7 and 5.9 show the results of the simulations using data from two burning seasons in Eastern China: June and October 2015, whilst Fig. 5.8 shows the details of a week long simulation in June from 9th to 16th.

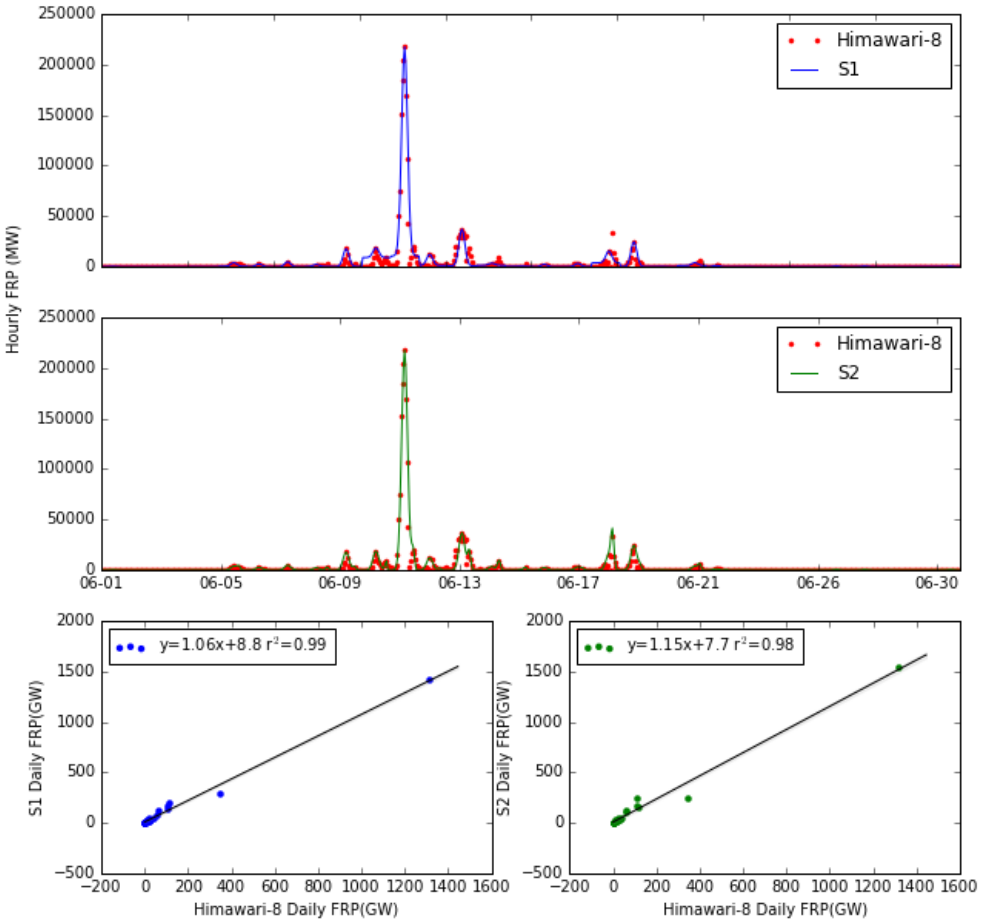

Figure 5.7: Hourly time series of FRP from two simulations: S1 (top row, blue line) and S2 (middle row, green line), along with observed FRP values from Himawari-8 (red dots) during June 2015. The bottom two scatter plots show a direct comparison of the summed daily FRP values from S1 (blue, left) and S2 (green, right) to those from Himawari-8. The best fit linear relationship is shown in each case, along with its equation and the coefficient of determination between the two datasets.

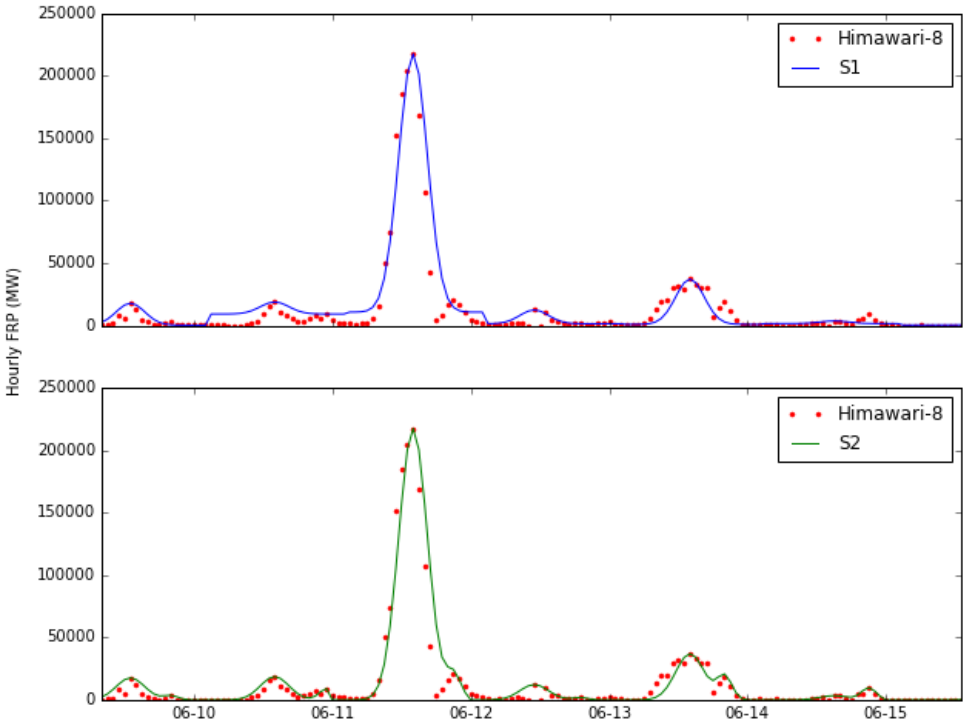

Figure 5.8: Zoomed version of time series plots shown in Fig. 5.7. Hourly time series of FRP from the two simulations: S1 (top row, blue line) and S2 (middle row, green line), along with observed FRP values from Himawari-8 (red dots) during 9th-16th June 2015.

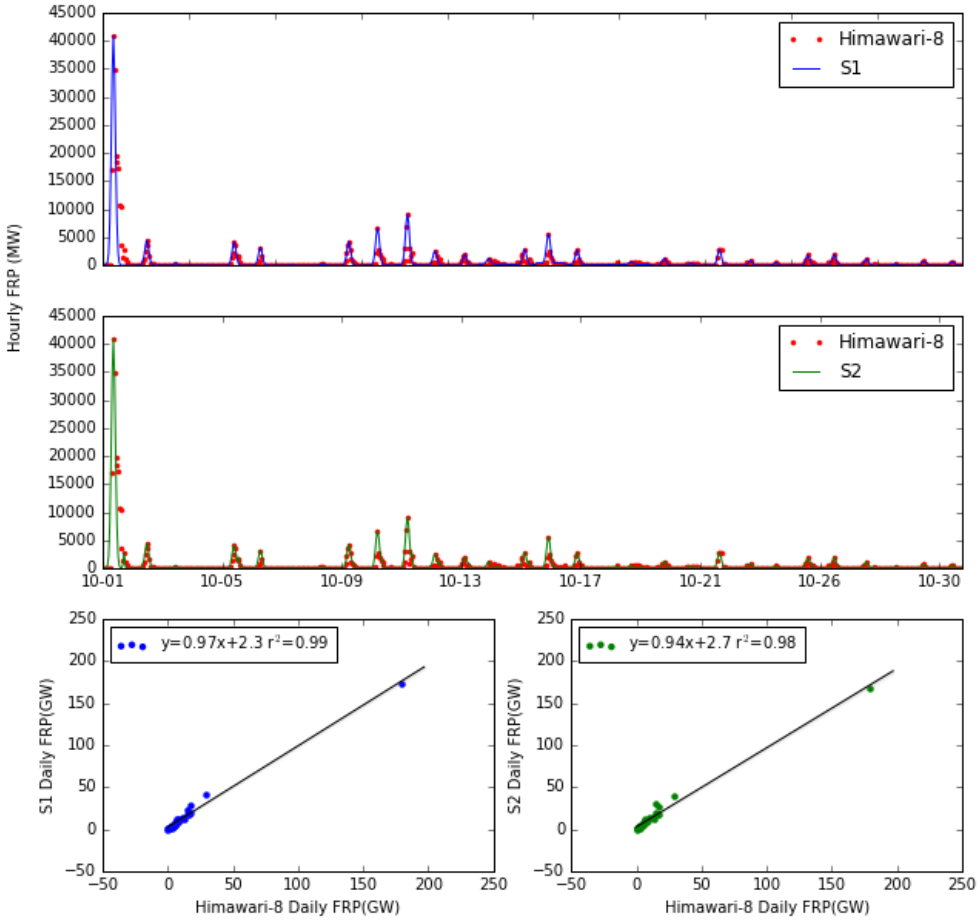

Figure 5.9: Hourly time series of FRP from two simulations: S1 (top row, blue line) and S2 (middle row, green line), along with observed FRP values from Himawari-8 (red dots) during October 2015. The bottom two scatter plots show a direct comparison of the summed daily FRP values from S1 (blue, left) and S2 (green, right) to those from Himawari-8. The best fit linear relationship is shown in each case, along with its equation and the coefficient of determination between the two datasets.

In Fig. 5.7, the upper time-series shows a comparison of the simulation results from S1 and S2 with the original FRP data from Himawari-8 in June. Fig. 5.8 shows only one week data from Fig. 5.7, which gives zoomed view of the genereal similar distributions of S1 and S2 from 9th to 16th, June 2015. S1 shows a slightly overestimated baseline on 10 June and underestimation of values near the second peak on 13 June. Meanwhile S2 shows good correlation with original observations on 13 June but a slight overestimation on 11 June. Nevertheless, the main purpose of this simulation is to compare FRE rather than hourly FRP change across the dirnual cycle. In Fig. 5.7 and 5.9 the summed hourly FRP derived from the simulation is compared to the sum of direct observations from Himawari-8, at same temporal frequency. The slopes of the linear best fit to these data, of 1.06 and 1.15 for S1 and S2 in June, and 0.97 and 0.94 in October, suggesting that S1 is performing better in both June and October. The absolute errors

of S1 and S2 are however within 10% of each other. Since simulation S1 demonstrated the best results in this comparison, Eqn. 5.8 taken from Andela *et al.* (2015) was finally used to combine the Himawari-8 and VIIRS-IM FRP data in this study.

The daily FRE generated from the combination of VIIRS FRP data and the Himawari-8 derived diunal cycle was compared with that generated from the Himawari-8 FRP data and the VIIRS-to-Himawari-8 FRP ratio shown in Fig. 5.6. These two FRE time-series are shown in Fig. 5.10a, and show very similar distributions, with three peaks on 11th, 13th and 17th June 2015. A strong linear correlation exists between these two FRE datasets, seen in Fig. 5.10b, with a linear best fit of $y = 0.85x - 19.0$. The similar results generated using the two different approaches to calculate the daily FRE confirm their robustness, and support the use of Eqn. 5.8 for the remainder of the study.

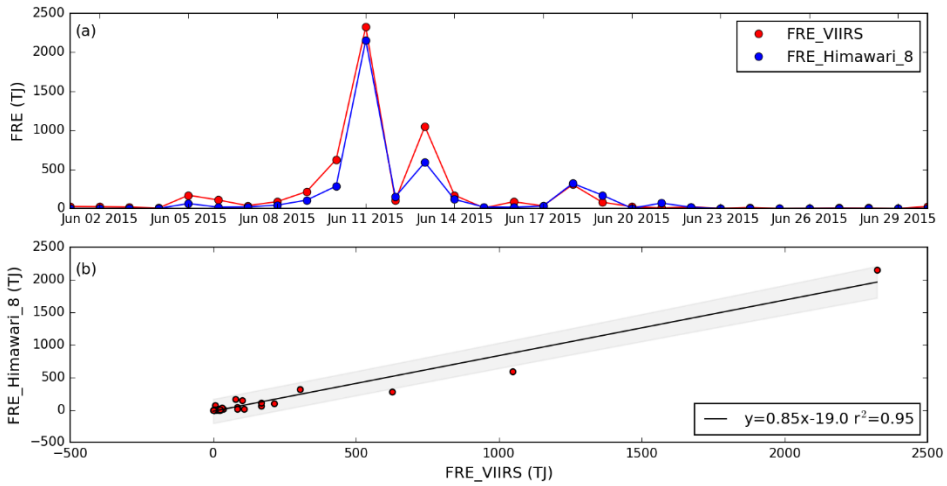

Figure 5.10: Time series of daily FRE (a) generated from VIIRS (using VIIRS FRP and Himawari-8 diunal cycle from Eqn. 5.8) and Himawari-8 (using Himawari-8 FRP and VIIRS-to-Himawari-8 ratio from Fig. 5.6) of Eastern China in Jun, 2015. Scatter plot (b) shows a directly daily FRE intercomparison using the same data. The best fit linear relationships are shown, along with its equation, and the grey shaded area represents the 95% confidence limit of the relationship.

Fig. 5.11 gives examples of mapped daily FRE areal density, ouput from use of the appraoch of Andela *et al.* (2015) with inputs of the daytime and nighttime cloud adjusted FRP from the VIIRS-IM product as the peak value and baseline values in Eqn. 5.8 respectively. The width of the main peak of the diunual cycle ($\sigma = 2.48$ hrs) is taken from the Himawari-8 derived diurnal cycle, shown in Fig. 5.5. If there are multiple VIIRS-IM Product observations for a particular 0.1^{o} grid cell during either the day or night, the maximum FRP is used in the implemenation.

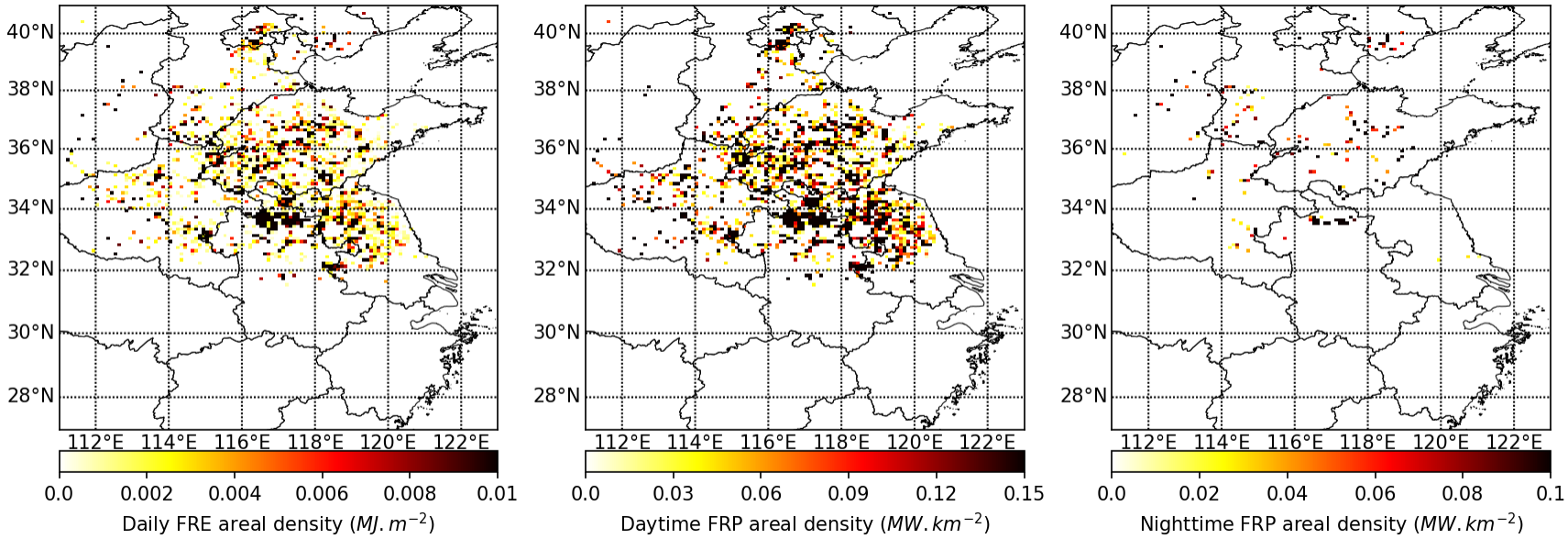

Figure 5.11: Spatial distribution of daily gridded FRE areal density (left) calculated for 13 June 2015 across Eastern China, using Eqn. 5.8 with daytime areal density (middle) and nighttime FRP areal density (right, both cloud corrected).

5.2.6 COMBUSTION RATE

The 0.368 (±0.015) kg MJ^{-1} conversion factor between fuel consumption and FRE reported by Wooster *et al*. (2005) from outdoor experimental tests with small straw fires is used here, because these fires are similar to those present in Chinese agricultural fields (Section 2.2). In the GFAS system described by Kaiser *et al*. (2012) a constant but much higher rate was initially used (1.37 kg MJ^{-1} in GFASv0), though this was later adjusted in GFASv1.0 to a landcover dependent factor ranging between 0.13 and 5.87 $kg.MJ^{-1}$ to improve consistency between GFAS' combustion estimates with those of the burned-area based GFED inventory (Kaiser *et al.*, 2012). In agricultural landcover types the GFAS conversion factor derived via this comparison to GFED was 0.29 $kg.MJ^{-1}$, indicating that the conversion factor between FRE and biomass combustion derived via comparison between GFAS FRP and GFED fuel consumptions is a little lower than the factor derived via small-scale experiments. However, the GFED inventory is based on the MODIS burned area product, which is not very effective in capturing small are agricultural fires (see Section 2.5-2.6). Furthermore, undetected 'small fires' in the MODIS active fire based GFAS inventory will cause underestimation of FRP in such regions (Ichoku and Kaufman, 2005). By contrast, the VIIRS-IM product can detect active fires down to around 1-2 MW, compared to MODIS' 8 MW minimum, as detailed in Chapter 3. Thus using the VIIRS I-band data as the main driver of the active fire detection process here, is likely to provide a far more truthful FRE measure for use in producing the biomass consumption product than is obtained by using MODIS.

5.2.7 CONVERSION TO SMOKE EMISSIONS

As detailed in Chapter 2, bottom-up biomass burning emissions calculations aiming to quantify the amount of a particular species [x] released to the atmosphere require use of an emission factor [EFx] that represents the amount [g] of chemical species [x] emitted per kg of dry fuel burned. Though the differences in fire emission characteristics, and thus in emissions factors, occur during the different combustion stages of a fire have long been recognised, most commonly a single "fire averaged" emission factor is used to represent the typical EF of fires in particular landcover types (Wooster *et al.*, 2011).

The emission factors used herein were calculated from the series of *in situ* measurements conducted in agricultural areas of Eastern China during this research (see Table 4 & 5 in Chapter 4). The EFs are reported in Table 5.1, and do not include those of corn because the fieldwork occurred in summer and corn waste burning is conducted in the autumn. Therefore, the emission factors of agricultural fires taken

from Andreae and Merlet (2001), as used in GFAS (Kaiser *et al.*, 2012), were used to represent the corn emissions factors. In fact, the EFs for CO_2 and CO (1308 and 92 $g.kg^{-1}$ respectively) present in Andreae and Merlet (2001) are not totally dissimilar to corn EFs based on fieldwork conducted in a rural area in Shandong, China (1350 and 53 $g.kg^{-1}$, Li *et al.*, 2007) (at least in terms of the CO_2 EF).

Table 5.1: Emission Factors from agricultural residue burning in Eastern China used in this study (unit: g kg^{-1}) and derived from measurements conducted for this research, apart from that of corn, which was taken from Andreae and Merlet (2001), as used in GFAS (Kaiser *et al.*, 2012).

	Emissions Factor ($g.kg^{-1}$)		
	Wheat	Corn	Rice
CO_2	1739±19	1308±14	1761±30
CO	60±12	92±18	47±19
$PM_{2.5}$	6.1±1.3	8.3±1.8	9.6±4.3
Black Carbon	0.70±0.09	0.42±0.05	0.56±0.04

5.2.8 CULTIVATION HARVESTING MAP

To identify the fuel type (wheat, corn or rice residue) of the agricultural residue fires being detected, a "cultivation rotation" map was used. This was generated from a global monthly crop area dataset (MIRCA2000, Portmann *et al.*, 2010) representing monthly irrigated and rainfed crop areas assessed around the year 2000. The dataset covers all major food crops, and is stored at a spatial resolution of 0.08°, equivalent to 9.2 km × 9.2 km at the equator. The three main grain crops in China are rice, corn and wheat, and this was used with the MIRCA2000 dataset to generate the cultivation harvesting map used for the fuel type classification (Fig. 5.12). This map was then used with the EFs from Table 5.1 to select the appropriate emissions factor for use at a particular location and time of year.

The monthly cultivation rotation map was converted from its original spatial resolution to that of the 0.1° grid cells matching the biomass combustion product developed in Section 5.3.7. Where there was more than one crop type in a grid cell for a particular month, the crop type with the maximum cultivated area was used. During data processing, once a monthly cultivation rotation map grid cell changed from "growing" to "empty", the cell is flagged as "harvested". After initial processing of the entire dataset, the algorithm finds all cells flagged as "harvested" and extends the same flag for the particular grid cell one month earlier and after this date. This is done because harvest time varies from year to year, depending on the weather. For example, grid cells in the south of Eastern China have been flagged as "rice harvested" in October during the first algorithm pass, but the actual harvest time could potentially be in September or even beyond the end of October - and so active fires detected between September to November in these

grid cells seem likely to be burning rice straw. Thus those grid cells in south of Eastern China are flagged as “rice harvested” for all three of these months.

The final 0.1º monthly cultivation rotation map is shown in Fig. 5.12, and shows that during the summer harvesting season (May - July), wheat dominates across Eastern China, while in the autumn harvest season (September - October), rice dominates in the southern area, while rice and corn can both be found in the north. When using this map to identify the fuel type being burned, some grid cells (dark blue in Fig. 5.12) have no crop information because of no record from MIRCA2000 database. In these cases, the spatially closest pixel with a crop type is be used to define the crop type, which accounts for between 26% to 34% of total yearly FRE from 2012 to 2015. During January and December, there is certainly no harvesting, in which case the identified fires might be false alarms, and these are omitted from the final fire emissions calculation. However, false alarms during December are not always the case, which will be further discussed in Chapter 6.

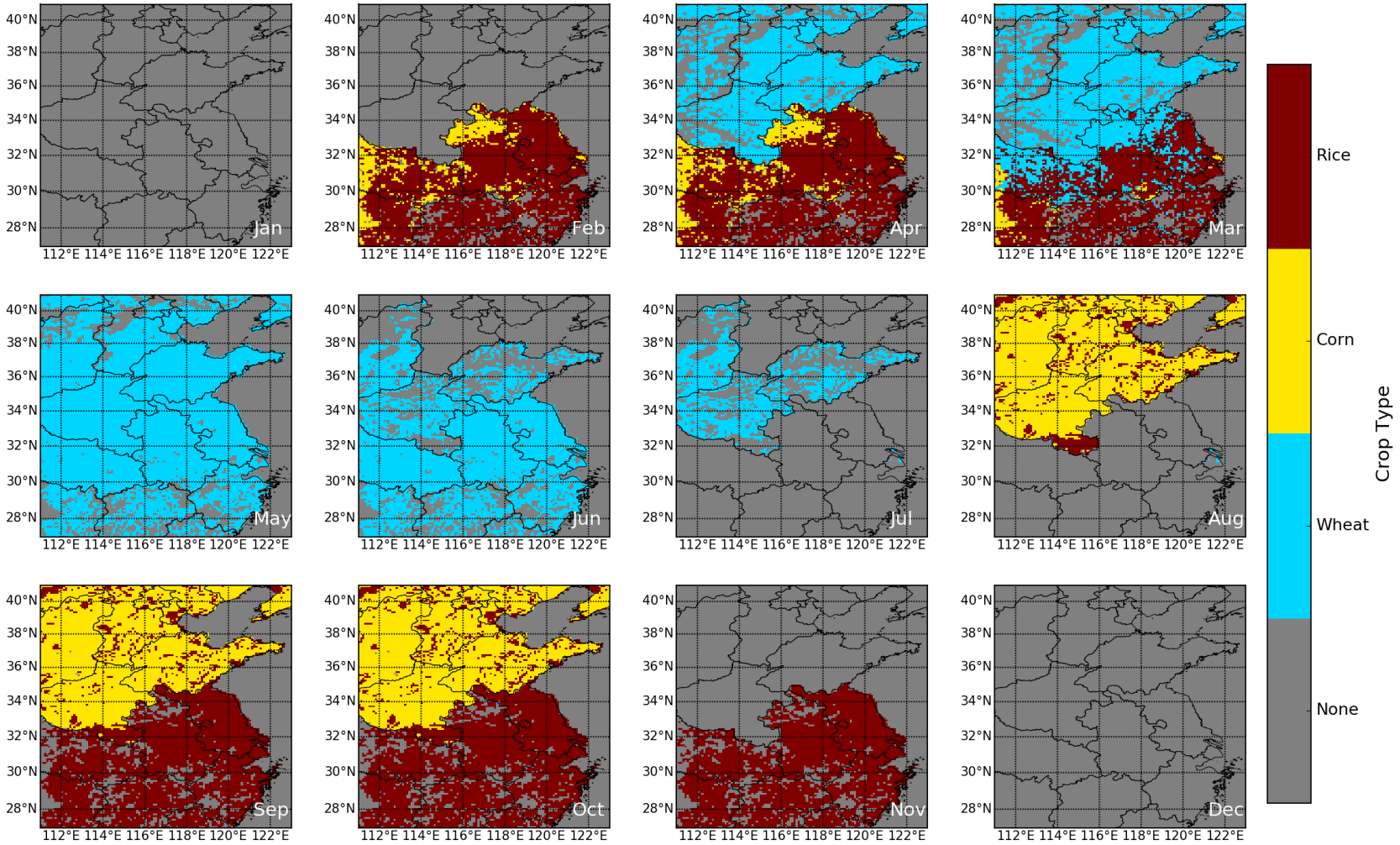

Figure 5.12: Monthly harvest map (0.1×0.1º map) of Eastern China generated from MIRCA2000 rotation cultivation datasets, which will be used to identify the fuel type of each grid cell and apply corresponding emission factors from Table 5.1 during fire emission estimations.

5.3 RESULTS

This Section examines the characteristics of the FRE generated using the combined VIIRS-IM and Himawari-8 FRP data, as described in Section 5.2. In addition, it will examine the dry matter combustion estimates produced from the FRE data, and compare it to the GFED and GFAS inventories (see the review in Section 2.6). Both GFEDv4.0 and GFEDv4.1s (with small fire burned area boosting) will be used for this comparison, as well as the up-to-date GFAS version 1.2.

5.3.1 TEMPORAL AND SPATIAL DISTRIBUTION OF FRE IN EASTERN CHINA

Fig. 5.13 shows an example of the spatial distribution of daily gridded FRE areal density present during the most intensive day of burning for each of the four summer burning seasons examined (2012 - 2015). The mean values of those grids with detected active fires range from 0.023 to 0.081 $MJ.m^{-2}$. This is of a similar magnitude to GFAS, which has mean values ranging from 0.003 - 0.015 $MJ.m^{-2}$. The higher values present in the VIIRS-IM derived FRE data are very likely the result of the better small fire sensitivity of VIIRS sensor compared to the MODIS sensor used in GFAS (Chapter 3), a subject further discussed in Section 5.3.2.

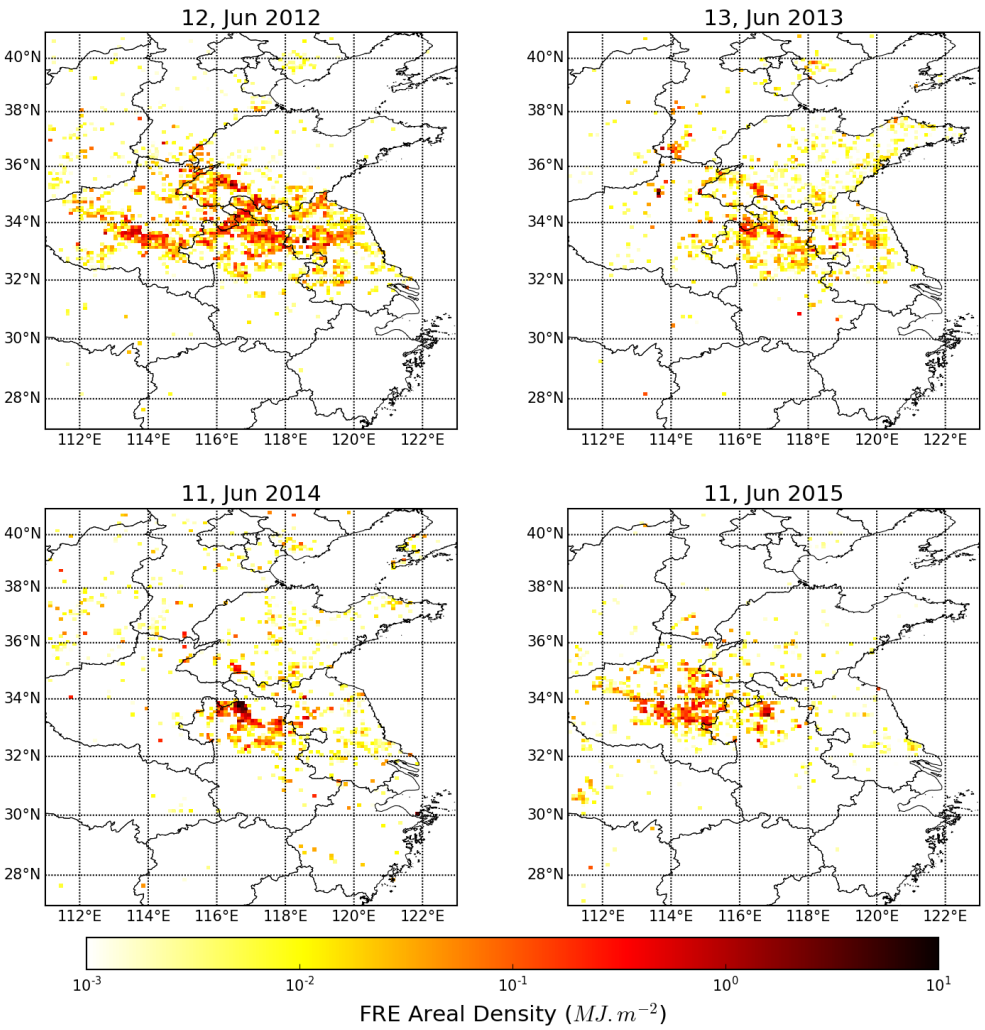

Figure 5.13: Example of spatial distribution of daily FRE areal density (calculated per 0.1° grid cell) from the day with highest total daily FRE of the four summer burning seasons in 2012-2015.

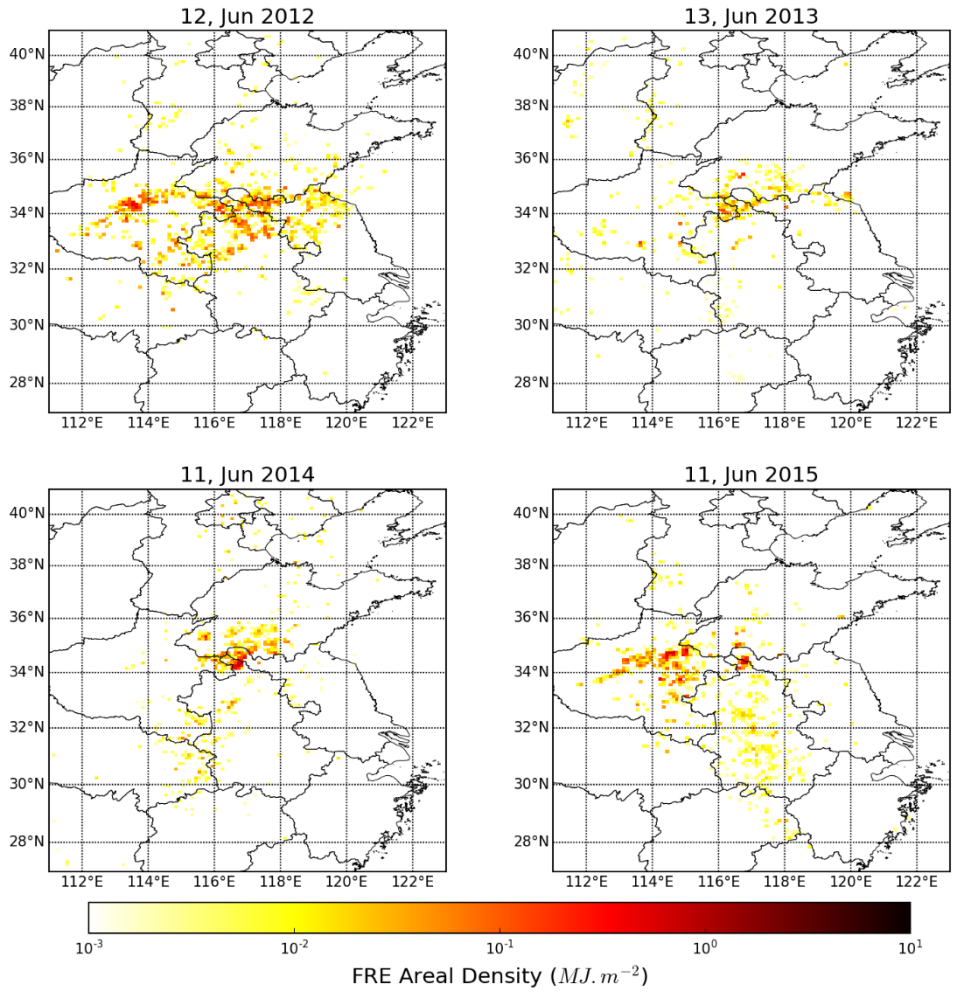

Figure 5.14: Estimated daily FRE areal density (MJ.m^{-2}) from GFAS on the same days shown in Fig. 5.13 (Kaier *et al.*, 2012).

Fig. 5.15a shows the time series of daily mean FRE areal density (0.1° grid cell resolution) in Eastern China from February 2012 to December 2015. A very strong seasonal variation is seen, with major peaks in May-June and much smaller peaks in September-October. In fact, the smaller peaks are a combination of a few fluctuations lasting from October until December, and this will be further discussed in Chapter 6. Fig. 5.15b shows the same data, but broken down by crop residue type using the mapped information shown in Fig. 5.12. This breakdown shows that the strong seasonal difference comes from the harvesting of the different crop types (also see in Fig. 5.12 and Section 5.2.8). Wheat residue burning dominates the May - June burning season, whilst corn and rice are the primary contributors in September - October. Over the whole 4 year period, wheat crop residues contributed 65 % of total FRE, whilst corn and rice residues contributed 17 % and 18 % respectively.

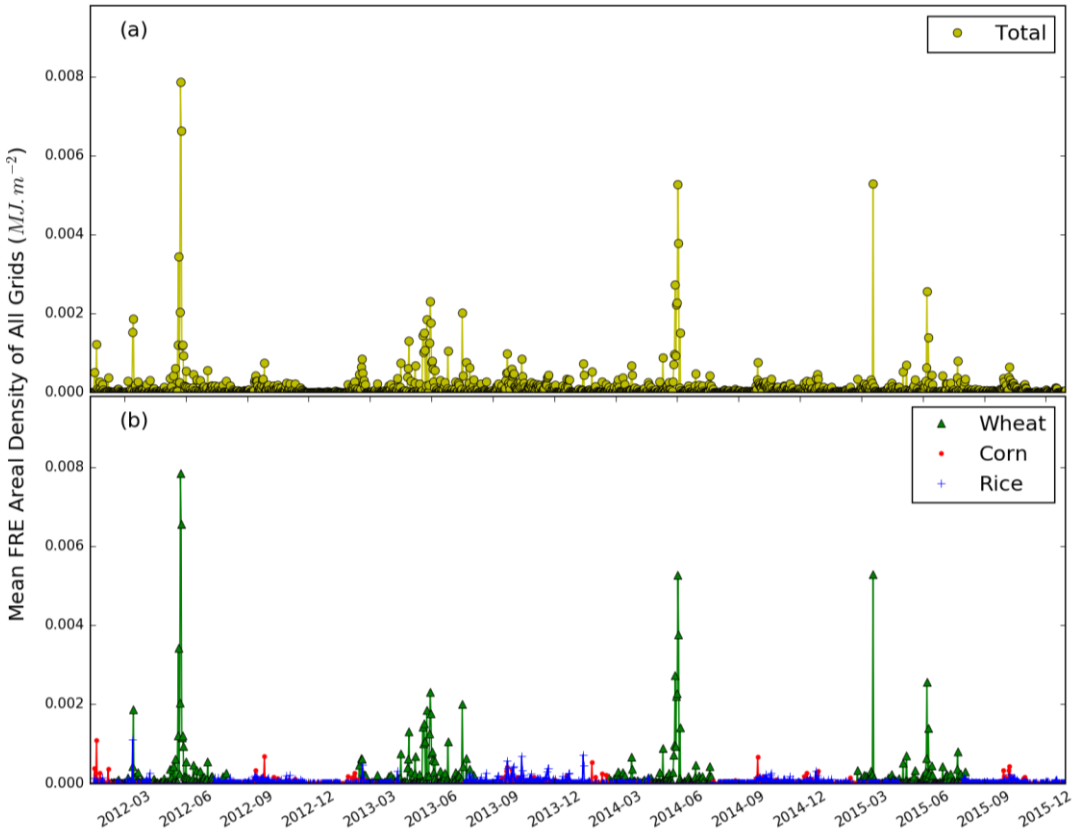

Figure 5.15: Time-series of mean daily FRE areal density (calculated per 0.1° grid cell) from 2012-2015. (a) Total FRE, and (b) break down by crop residue type (wheat, corn and rice) according to the method described in Section 5.2.8.

A distinct pattern showing two individual burning seasons can also been seen in the spatial distribution of FRE (Fig. 5.16). During the summer burning season (May - June), most burning is located along a latitudinal line around 34° N, extending from 112° E to 120° E near the coast. In the autumn burning season, the area of burning is much smaller and more evenly distributed. There is still a focus located between 32° N and 34° N, starting from 112° E and stopping close to 119° E longitude. However, in the southwestern direction within 112 - 114° E and 29 - 32° N we see a region that only appears to undergo substantial burning in the autumn. This is located in the centre of Hubei Province, a province that contributes around 12% of the total rice yield of the whole of China (NBSC, 2015). The FRE contributed from this area also accounts for between 10 and 18% of the total FRE seen in the autumn burning season of different years, and according to the breakdown by residue burning type as much as 26 to 39% of total FRE related to rice residue fires during this season.

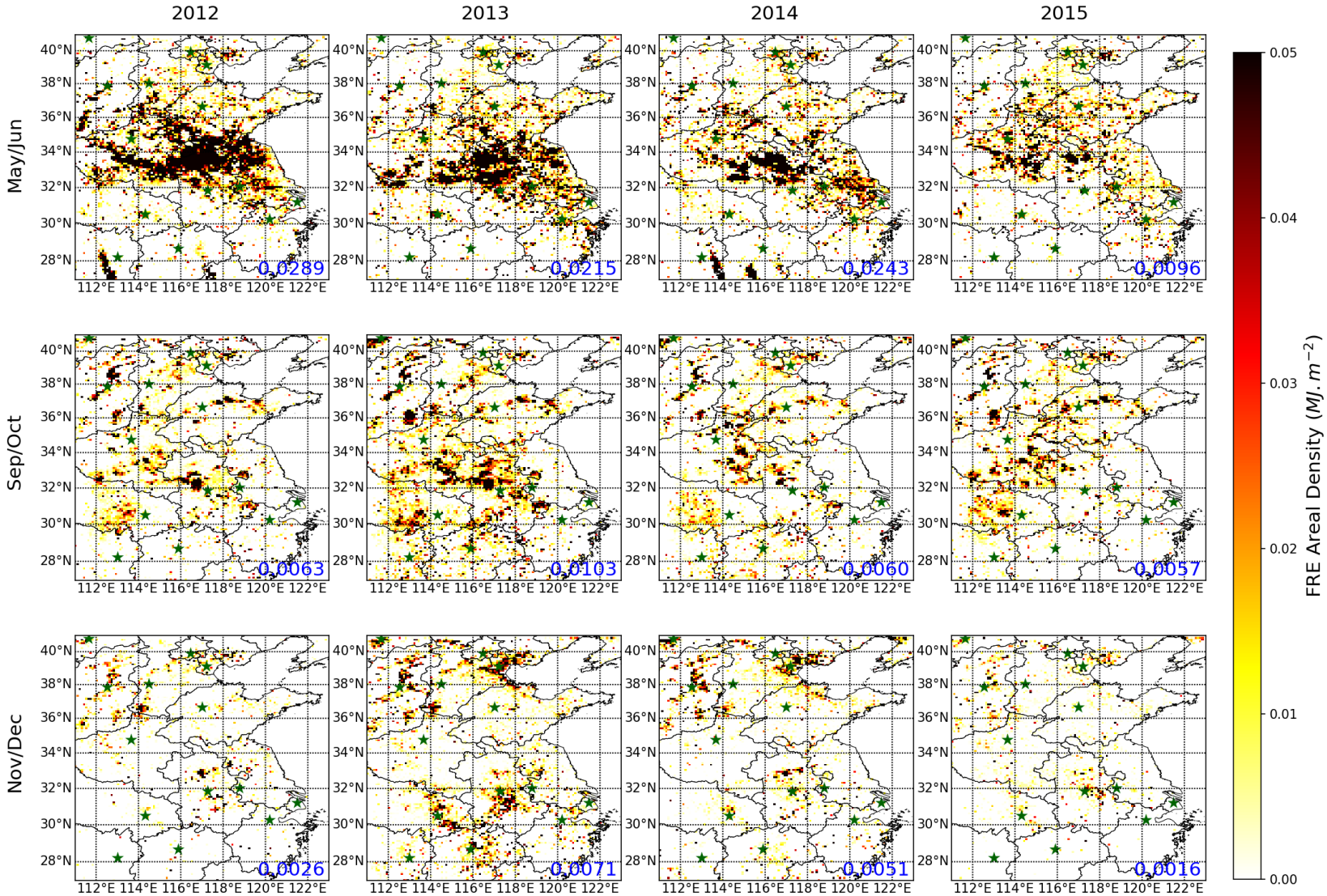

Figure 5.16: Spatial distribution of grid-cell FRE areal density (MJ.m^{-2}, 0.1 deg grid cells) for agricultural fires in Eastern China from 2012 to 2015 (top to bottom rows) split by fire season: summer (May-June, left column), autumn (Sep-Oct, middle column) and winter (Nov-Dec, right column). Mean regional FRE for each season is indicated in blue text, and the capital city location of each province is shown as a green star.

5.3.2 Comparison with GFAS Fire Radiative Energy

A comparison was conducted between the VIIRS-generated FRE data produced herein and that output from the Global Fire Assimilation System (GFAS) of Kaiser *et al.* (2012). Both these are based on an active fire detection/FRP methodology and have the same output grid cell size (0.1° latitude and longitude). Fig. 5.17 shows a comparison of one month of daily mean FRE areal density, generated from this study and from GFAS. Since the grid cell size is the same, and thus the amount of landmass in each matching grid cell, the FRE areal density values from MODIS and VIIRS have the same ratio as the original FRE values (i.e. those not divided by the grid cell area).

The two time-series shown in Fig. 5.17 demonstrate similar trends, but with generally lower values for GFAS than for the VIIRS-IM product developed here. During the two highest FRE days (11th and 13th June 2015) GFAS shows a very clear underestimation compared to VIIRS, with values 2× to 4× lower. The large uncertainty is from averaging all grid cells within Eastern China.

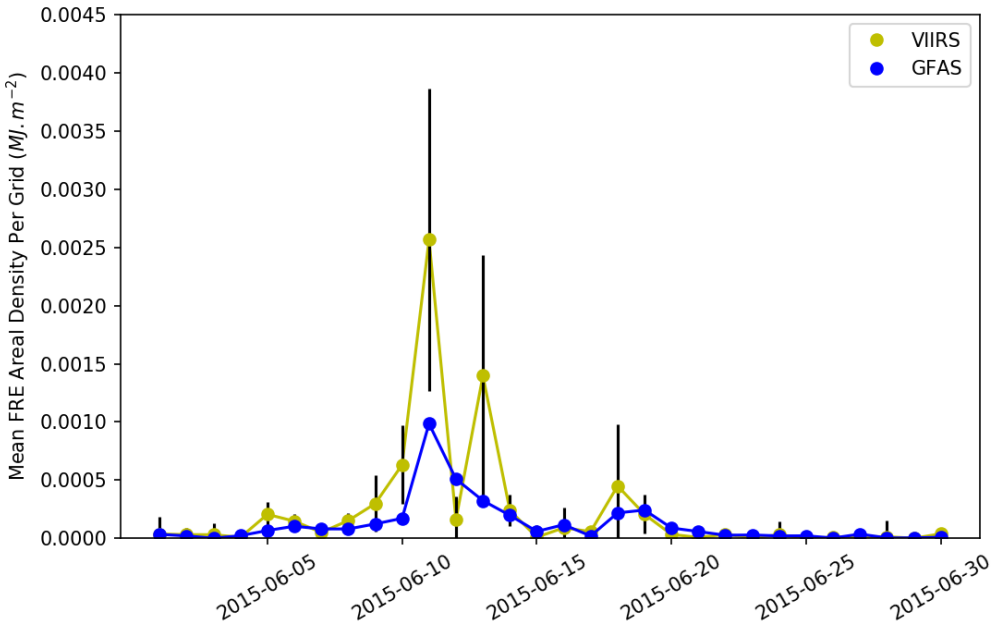

Figure 5.17: Comparison of daily mean FRE areal density (with standard deviation) generated from the VIIRS-IM product developed in this study and the global fire assimilation system (GFAS) described in Kaiser *et al.* (2012). Daily data for June 2015 over Eastern China (0.1° grid cells).

Building on the type of comparison shown in Fig. 5.17, a scatterplot of the mean FRE areal density per grid cell calculated from the four years of data is compared between VIIRS and GFAS in Fig. 5.18. VIIRS and GFAS show a positive correlation in their FRE areal density values, though with varying coefficients of variation (r^2) ranging from 0.30 to 0.77. This variability is likely to be contributed to by

various aspects of the methodologies used to produce the two inventories, including (i) the satellite overpass time differences (up to over an hour difference) which will mean the data are recorded at different points on the diurnal cycle; (ii) the fact that GFAS weights the FRP measures by viewing angle which is unnecessary for VIIRS (Section 3.2); (iii) the use in GFAS of the weighted mean of all MODIS overpasses available per day (multiplied by the number of seconds in 24 hours) to enable a representative FRE to be captured, whilst the VIIRS-IM based approach developed here uses the real fire diurnal cycle characteristic for the region (taken from Himawari-8). The differences may also of course be related to the different minimum FRP detection limits of the NPP-Suomi VIIRS and Aqua/Terra MODIS sensors, and the proportion of the residue fires that fall below these limits at different times.

The mean slope of the FRE areal density data coming from VIIRS and from GFAS is 3.19 ± 0.90 $J.m^{-2}/J.m^{-2}$, indicating that GFAS provides substantially lower estimates of FRE areal density than does the VIIRS-IM product developed here. The lowest slope occurs for 2015, with a value of 2.04. This is significantly influenced by one high FRE areal density value from GFAS, suspected to be anomalously due to duplicated active fire detections coming from MODIS' edge-of-swath observations made on this particularly fire-affected day during the summer burning season, a point already discussed in Section 3.2 in relation to this particular observation.

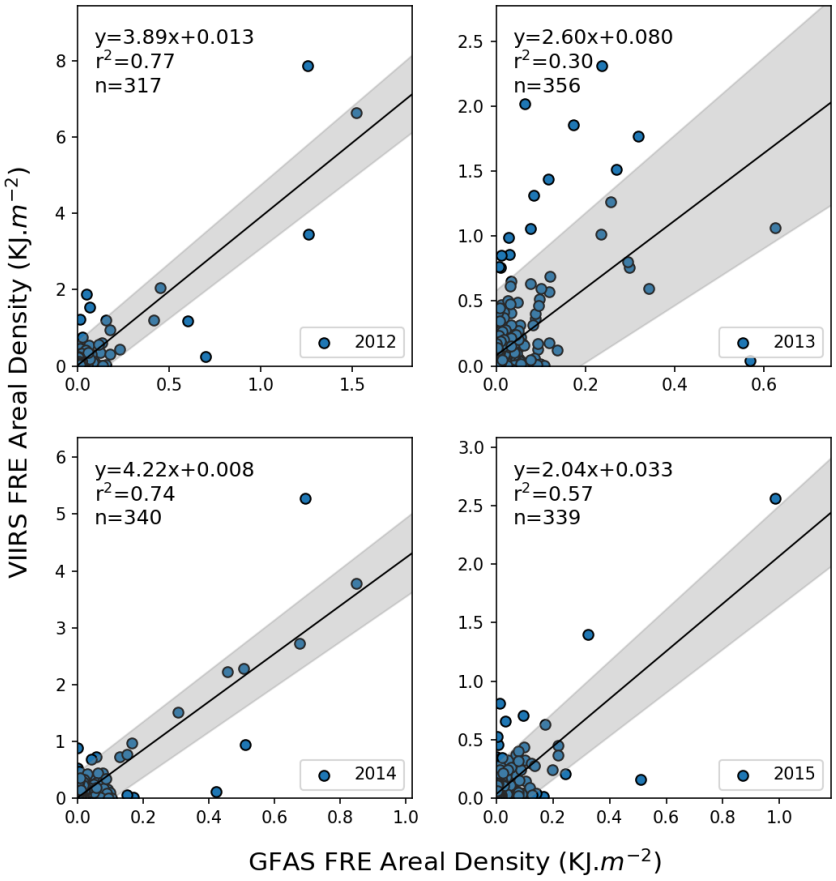

Figure 5.18: Direct VIIRS-to-GFAS FRE areal density intercomparisons retrieved from the two datasets at 0.1º degree grid cells from 2012-2015 (a-d). The best fit linear relationships are shown, along with its equation, and the grey shaded area represents the 95% confidence limit on the relationship.

5.3.3 Comparisons to GFAS and GFED Dry Matter Burned Metrics

Dry matter burned (DMB) is used as a metric here, which is a common and direct output of all three fire emissions inventories being compared (GFAS, GFED and the VIIRS-IM method developed herein). The version of GFED used here is version 4.1, as described in Giglio *et al*. (2013) which is the most current version at the time of writing (May 2017). The version of GFAS used is version 1.2, which is an updated version of that described in Kaiser *et al*. (2012, updated mainly in terms of the spatial resolution [0.1°]) which is the most recent version at the time of writing (May 2017). The use of the DMB as the comparison variable removes differences that could come from the different inventories use of varying gaseous or particulate emission factors in the final fire emissions calculation, and enables a directly comparable metric to be used. Comparisons between the monthly DMB estimates are shown in Fig. 5.19. All three inventories (GFAS, GFED and VIIRS-IM) show a clear peak during the summer burning season, but GFAS and VIIRS show a much sharper peak in June, while GFED's summer burning season extends one month earlier (May) and later (July). VIIRS-IM shows a DMB peak during June ranging from 3.30 to

11.2 Tg, whilst GFED shows lower values of 1.89 - 5.34 Tg and GFAS rather similar to GFED at 2.00 to 4.30 Tg. It should be remembered that GFAS' FRE to dry matter burned (DMB) calculation is calibrated using GFED, and so these two databases are essentially driven to give similar monthly totals, as explained in Kaiser *et al.* (2012). It can be seen from Fig 5.19 that VIIRS' DMB estimates are in general approximately 100% to 400% higher than those of the same period reported by GFAS and GFED. As detailed in Chapter 3, VIIRS has the ability to detect far smaller (and lower FRP) fires than can MODIS, due to its fine spatial resolution I-band observations that are based on much smaller area thermal channel pixels (375 m x and y pixel sizes at nadir) than those of the MODIS sensor (1000 m x and y pixel sizes at nadir). This results in often significantly higher per-scene FRP totals being generated by VIIRS-IM compared to MODIS, due to additional active fires being detected by VIIRS that are below the MODIS detection limit (see Fig. 13, Section 3.2). This feeds into far higher FRE estimates from the VIIRS-IM inventory than come from the use of MODIS within GFAS for the same time period, again as a result of VIIRS' ability to detect lower FRP fires, and also because the near-nadir minimum FRP detection limit is more consistently maintained across the VIIRS swath than with MODIS due to the VIIRS unique pixel aggregation scheme (see Section 3.2).

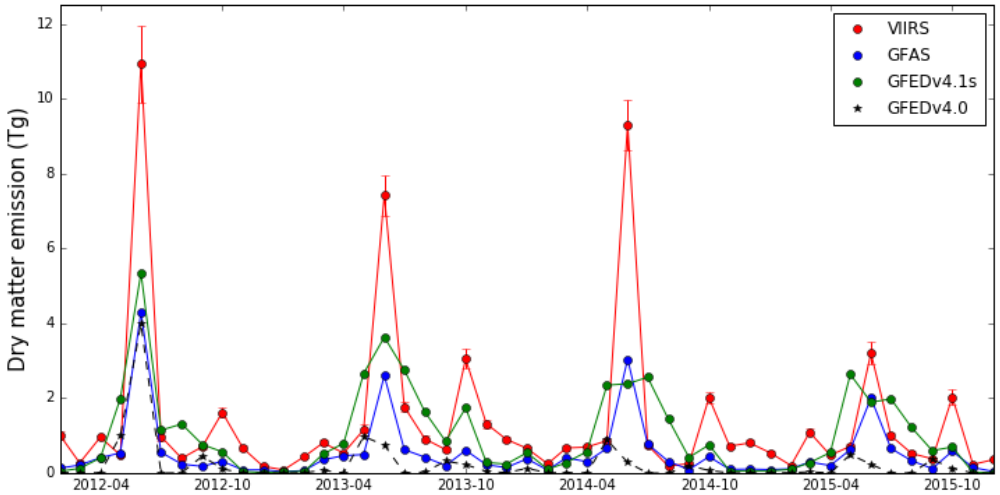

Figure 5.19: Monthly time-series of total dry matter burned (DMB) retrieved using the VIIRS-IM FRP product developed in Chapter 3 (with standard deviation shown as red error bar), along with comparable GFAS and GFEDv4.1s/GFEDv4.0 data (2012-2015).

For the autumn burning season of Eastern China, the peak in the GFAS and GFED inventories is much less obvious than that of the summer burning season (Fig. 5.19). Dry Matter Burned (DMB) in October ranges from 0.57 - 1.74 Tg for GFED, significantly higher than the 0.31 - 0.61 Tg reported by GFAS, but

much lower than the 1.62 - 3.05 Tg reported using the VIIRS-IM inventory developed here. The VIIRS-IM derived dry matter burned estimates for Eastern China are therefore 1 to 2 times higher than GFED and 3 to 4 × higher than those of GFAS, and these represent larger differences between VIIRS-IM and the other two inventories than exist for the earlier summer burning season. This indicates that fires burning during the autumn burning season might be on average smaller and/or more isolated from other fires than in the summer burning season, and thus are more likely to be missed by MODIS' active fire (Giglio *et al.,* 2016) or GFED burned area (Giglio *et al.,* 2013) detection algorithms (compared to those in the summer).

Though the figures from GFED lie closer to those of VIIR-IM than those of GFAS, this is likely to be significantly contributed to by the 'small fire' adjustment present in GFEDv4.1s, based on the methodology of Randerson *et al.,* (2012). This will be further discussed in the following Section. This small fire addition used in GFEDv4.1s was not present in the version of GFED used previously to calibrate GFAS (Kaiser *et al.,* 2012), and so is very likely the reason that the GFEDv4.1s and GFAS DMB values diverge quite considerably over Eastern China. In the previous GFED version (e.g. GFEDv4.0) the DMB estimates of Eastern China from GFED were generally lower, rather than current version which is higher than GFAS (Fig 5.19).

Since GFED uses 0.25° grid cells compared to the 0.1° of the VIIRS-IM and GFEAS inventories, a common re-gridding to 0.5° cells was conducted in order to ease product intercomparison. This balanced consideration of keeping spatial resolutions as high as possible, whilst avoiding uncertainty introduced by subdividing the original cells. The metric is also altered slightly from DMB (kg) to DMB per unit area of the grid cell ($g.m^{-2}$), which is the DMB in grams divided by the grid cell area (adjusted for any water or cloud cover). This metric cannot be directly compared to the fuel consumption per unit area in a fire (which typically ranges from perhaps around some 10's to some 1000's $g.m^{-2}$ in diverse types and intensities of landscape fire) because in general only a small fraction of the grid cell will have been burned. In agricultural residue burning types of fire, fuel consumption per unit area burned may range from less than 100 $g.m^{-2}$ in stubble burning of wheat residue (see pictures shown as Fig. 3a in Section 4.2) to perhaps more than a few $kg.m^{-2}$ in piled 'bonfires' (Fig. 3b in Section 4.2 and Li *et al.,* 2007). However, if a grid cell is only 5% burned in fires that consume a mean of 1 $kg.m^{-2}$ of fuel across the burned areas, then the DMB per unit area of the cell would be reported as 50 $g.m^{-2}$.

Fig. 5.20 shows the spatial distribution of the 12 months of dry matter burned areal density data for 2013 for all three datasets, re-gridded to this common 0.5° grid cell size. Though only one year data is shown

here in Fig. 5.20 as an example, the spatial distribution of each dataset was quite similar of a particular month in different years. For the summer burning season (that occurred only in June in 2013), all three datasets show an area of extensive burning extending from 31° N to 35° N, and 113° E to 120° E. However, the values of DMB areal density are far lower towards the outermost edges of this area for GFAS and GFED than they are for VIIRS-IM. Given the extensive examination of the raw VIIRS data of the area and the careful false alarm masking of the resulting VIIRS-IM data product (Chapter 3), it is assumed that the VIIRS-IM active fire record is composed of reliable detections for the area. However, in comparison to VIIRS-IM whose DMB areal density estimates for a cell extend up to 70 $g.m^{-2}$ for the autumn burning season (September to October in 2013), GFAS barely observed any grid cell having a DMB higher than 10 $g.m^{-2}$. It also failed to capture the southwestern area of intensive rice residue burning close to 30° N, 113° E. By contrast, GFED proves apparently better at quantifying the fires of this autumn season, showing relatively strong fire signals in the southwestern area. However, GFED shows a very wide time span of burning in the summer months, starting in May and ending in August. An especially strong area of burning reported by GFED near 30° N, 120° E shows a strong fire signal during July and August, which is suspicious since it is outside of the normal burning season. Furthermore, the agricultural area ratio (see Fig.7 of Section 3.2) is quite low in this area, and comparisons to Google Earth showed that this location includes a high density urban area close to Shanghai, along with a few other cities of over a million people. It thus seems very unlikely that strong agricultural burning happened at this location, and the high DMB areal density estimates reported by GFED seem suspicious.

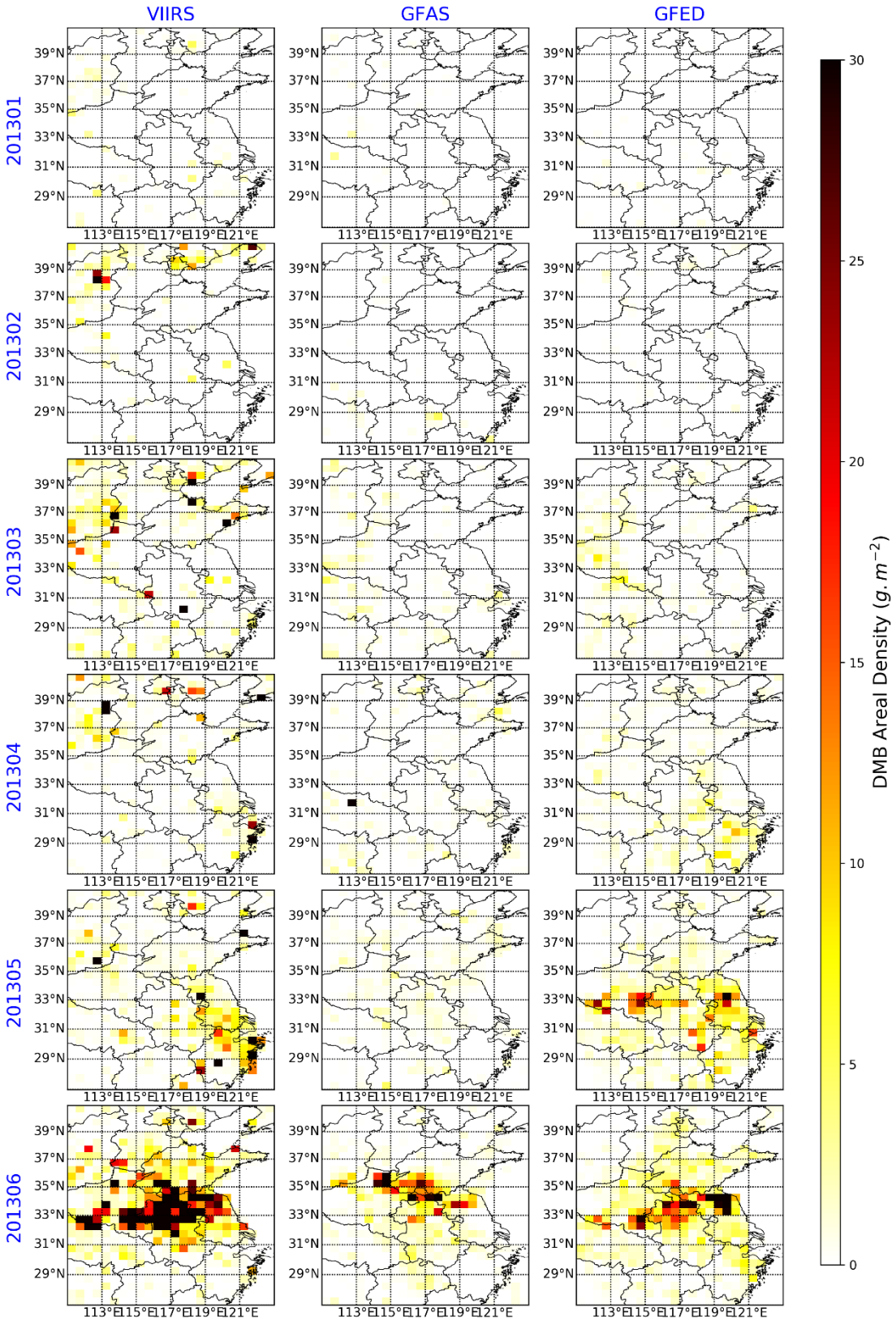
VIIRS
GFAS
GFED
201301
201302
201303
201304
201305
201306
39°N
37°N
35°N
33°N
31°N
29°N
113°E
15°E
17°E
19°E
21°E
DMB Areal Density ($g.m^{-2}$)
30
25
20
15
10
5
0

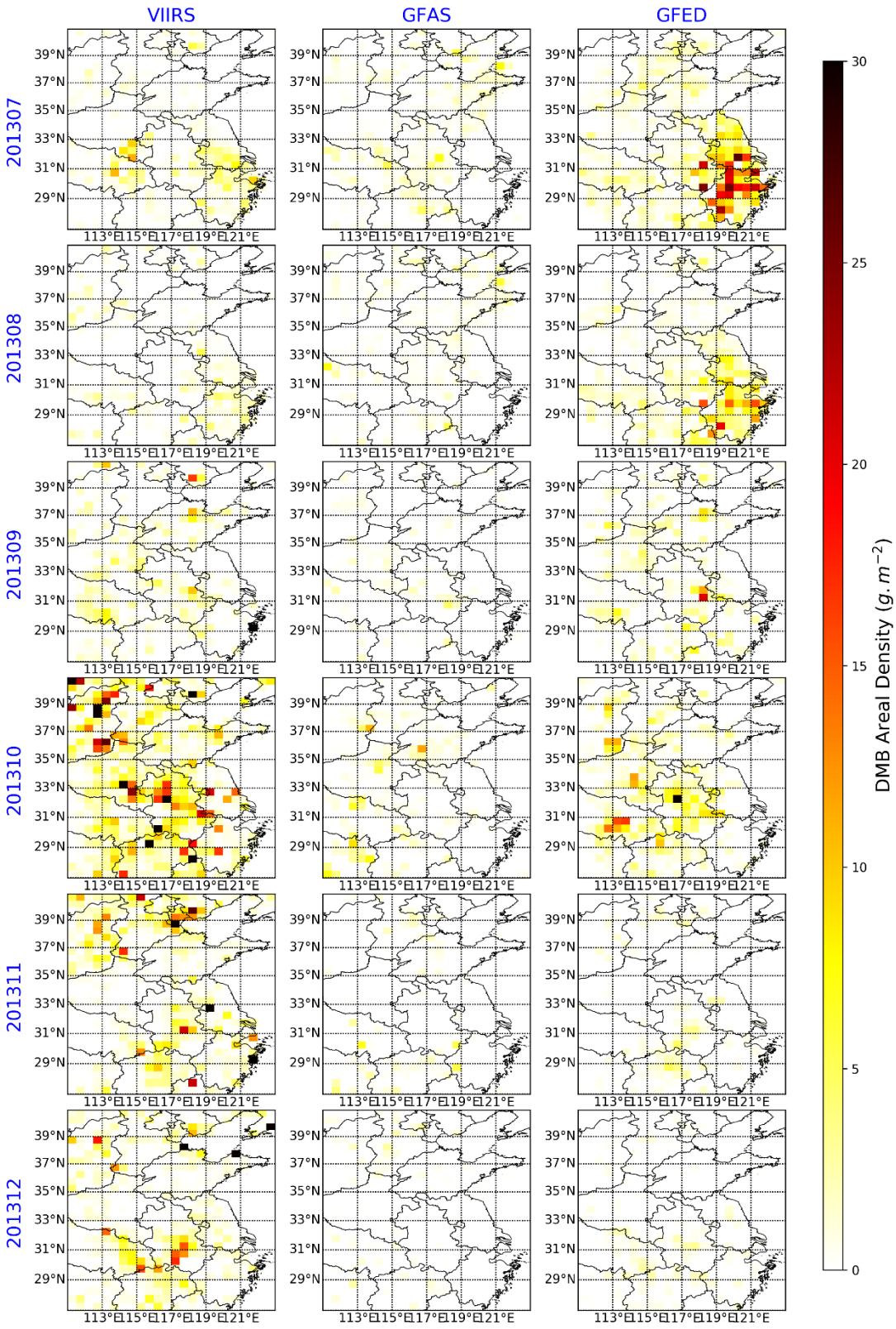

Figure 5.20: Spatial distribution of monthly total grid-cell dry matter burned areal density of agricultural fires occurring in Eastern China in 2013 retrieved from VIIRS, GFAS, and GFED4.1s.

5.3.3 Evaluation of the Impact of Small Fire Boosting on GFEDv4.1s

The purpose of the GFEDv4.1s 'small fire' adjustment is to bias correct the GFED inventory for the impact of 'small' undetected fires that are missed by the GFED burned area product described in Giglo *et al*. (2013). This burned area product is based on 500 m MODIS pixel measurements, and since many agricultural residue burns have areas far smaller than this (indeed very much smaller typically; as detailed in Section 3.2) a series of such fires would typically need to be present in a MODIS 500 m pixel for it to be detected as burned by the MODIS GFED burned area algorithm. The 'small fire boost' present is GFEDv4.1s is aimed at correcting for this deficit, based on the method of Randerson *et al.* (2012) that uses MODIS active fire, burned area and optical band vegetation index data to identify a relation between these, and then applies this to MODIS active fire detections in areas where no burned area was detected in order to provide the bias correction for the impact of undetected smaller burned areas (using the fact that the MODIS active fire product might quite often still be able to see their active fire signature; Eqn 2.3 of Section 2.6.4; Randerson *et al.*, 2012). In Section 5.3.2, the apparent improvement in the fire emission estimates brought about by 'small fire boost' for the autumn burning season has been made apparent, but the unusually long summer burning season lasting from May till July appears contradictory to other data (Fig. 5.17). This Section further explores the reason for these two phenomena and evaluates the efficacy of the 'small fire boosting' applied within GFEDv4.1s.

GFEDv4.0, the closest GFED product available that has no 'small fire boosting' applied, is used here, along with GFEDv4.1s from which the small fire boosting can be subtracted if desired. Fig. 5.21 shows the spatial distribution of burned area reported in GFEDv4.0 and GFEDv4.1s, along with the small fire fraction reported in GFEDv4.1s during June, August and October 2015. These three months represent the summer burning season, the non-burning season and the autumn burning season of the study area. Comparison of burned areas from GFEDv4.0 and GFEDv4.1s show that the small fire boosting has greatly increased the burned area in Eastern China, contributing both to a growing area of fire existing in fire affected grid cells in GFEDv4.0 and expanding the spatial extent of the fire affected grid cells. This can be confirmed by the distribution of the small fire fraction metric. For example, the total observed burned area in GFEDv4.0 is 710 km^2 during June 2015, but increased to 3586 km^2 in GFEDv4.1s, with 2389 km^2 of this in cells with existing fire in GFEDv4.0 and 1197 km^2 from cells that had no fire in GFEDv4.0.

However, a suspiciously large area of burning is also found in GFEDv4.1s around 29-33º N, 119-122º E GFEDv4during June and August, but not October (Fig. 5.21). As mentioned in Section 5.3.2, this is a high density urban area with limited agricultural land. Section 3.2 described that large numbers of VIIRS active fire detections made in industrial areas or close to manmade structures of particular types are false alarms caused by highly reflective and/or warm rooftops (Fig. 6, Section 3.2). The temporal and landcover based filters described in Section 3.2 were developed to mask such false alarms from the final VIIRS-IM active fire product. The MODIS active fire product does not use such false alarm filtering, leaving suspicion that similar false alarms as affect VIIRS prior to the filter application also may affect MODIS (but are not filtered out). This could potentially be the cause of the suspicious burning areas in GFEDv4.1s, because from the MODIS AF product the 'small fire boost' to burned area is generated (Randerson *et al.*, 2012).

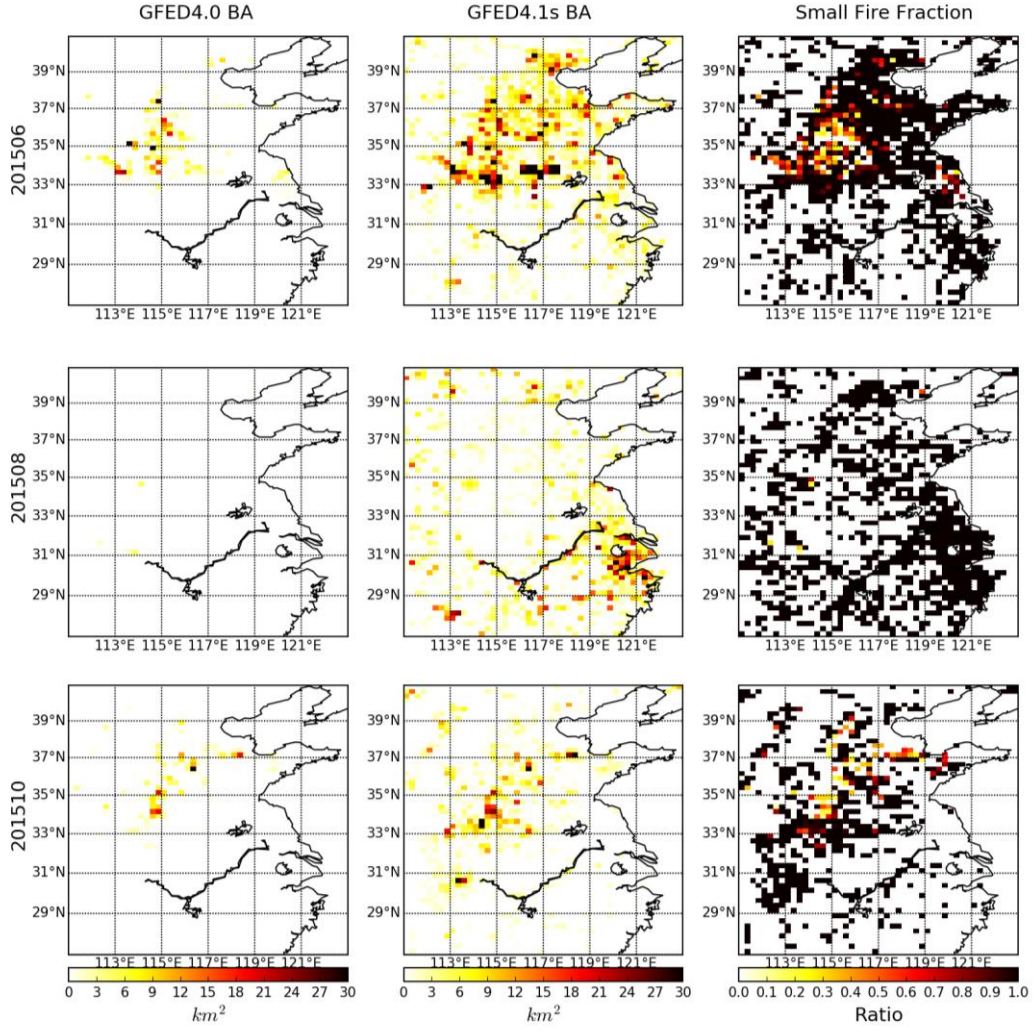

Figure 5.21: Spatial distribution (0.25 × 0.25º grid) of burned area from GFEDv4.0 (left column), GFEDv4.1s (middle column) and small fire fraction used in GFEDv4.1s during June (upper row), August (middle row) and October 2015 (lower row). Small fire fraction is a metric used in GFEDv4.1s to correct the impact of 'small' undetected fires that are missed by the GFED burned area product.

The landcover mask used in the VIIRS active fire false alarm screening process developed herein (Fig. 7, Section 3.2; also seen in Section 3.5) was applied to the MODIS active fire product, and used to classify all MODIS-detected active fire pixels into "suspected true active fires" and "suspected false alarms". Each pixel was then gridded to a 0.25 ^{o} grid, the same spatial resolution as GFED (Fig. 5.22), and the number of each type of active fire examined. High numbers of suspected true active fires were found in June and October 2015 (Fig. 5.22), which are the expected fire seasons. In June (top row) detected fires appear to be occurring in areas that are realistic and where the landcover mask shows the land is agricultural in nature, but there are also substantial numbers of fires present in areas that the landcover mask suggests maybe false alarms related to industrial or urban features. In October (bottom row) detected fires appear to be occurring in areas that are realistic, and where the landcover mask shows the land is agricultural in nature, and there are fewer fires that the landcover mask suggests maybe false alarms. However, in August 2015 there are very large numbers of false alarms located in the area 29-33^{o} N, 119-122^{o} E, which has been identified as a suspicious area of GFED-reported burned area earlier, which could be caused by stronger sunglint during summer.

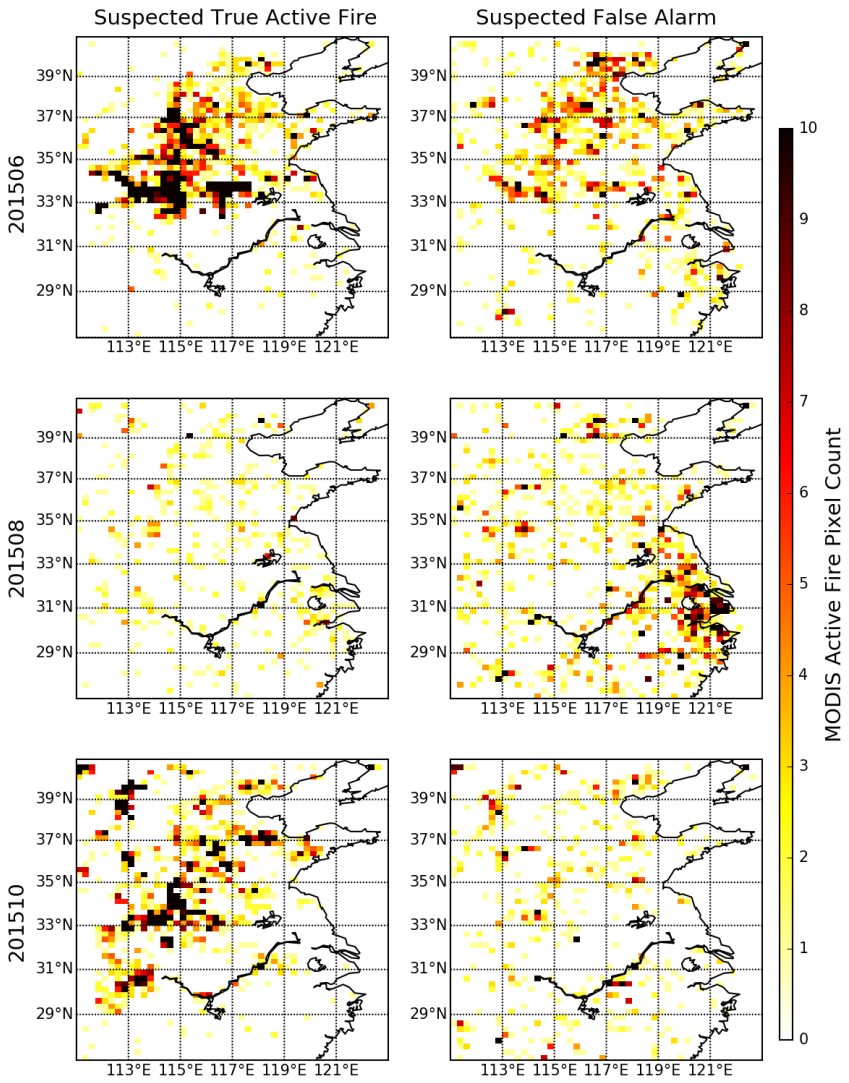

Figure 5.22: Spatial distribution of MODIS active fire pixel counts (for 0.25 × 0.25° grid), classifying as suspected true active fire (left column), and suspected false alarm (right column) using landcover filter from Section 3.2 (Fig.7a, details seen in Section 3.5.3) observed during June (upper row), August (middle row) and October 2015 (lower row).

The classified MODIS active fire pixel counts were then used to evaluate the contribution from suspected true active fires and false alarms in GFEDv4.1s' estimate of DMB. For a 0.25 ° grid cell, if the suspected count of true active fire pixels is larger than the count of false alarms, the burned area from this whole cell was considered to be contributed by active fires that are true active fire detections. If the count of false active fires was larger than the count of true active fires, then the burned area from this whole cell was considered to be contributed by active fires that are false alarms. Fig. 5.23a shows the comparison of DMB from GFEDv4.0 and from the small fire boost only in GFEDv4.1s, and Fig. 5.23b shows the breakdown of contributions from suspected true active fires and false alarms. Apart from June, most months are dominated by DMB that comes from 'small fire boosted burned area' that comes from grid

cells suspected of being dominated by false alarms rather than correct active fire detections. For example, in 2015, total DMB from GFEDv4.0 is 1.28 Tg and the suspected true active fire boost adds a further 2.37 Tg (an additional 185%). However, the total DMB from grid cells dominated by suspected false alarms is 5.03 Tg, more than twice as much that coming from grid cells dominated by suspected true active fire detections.

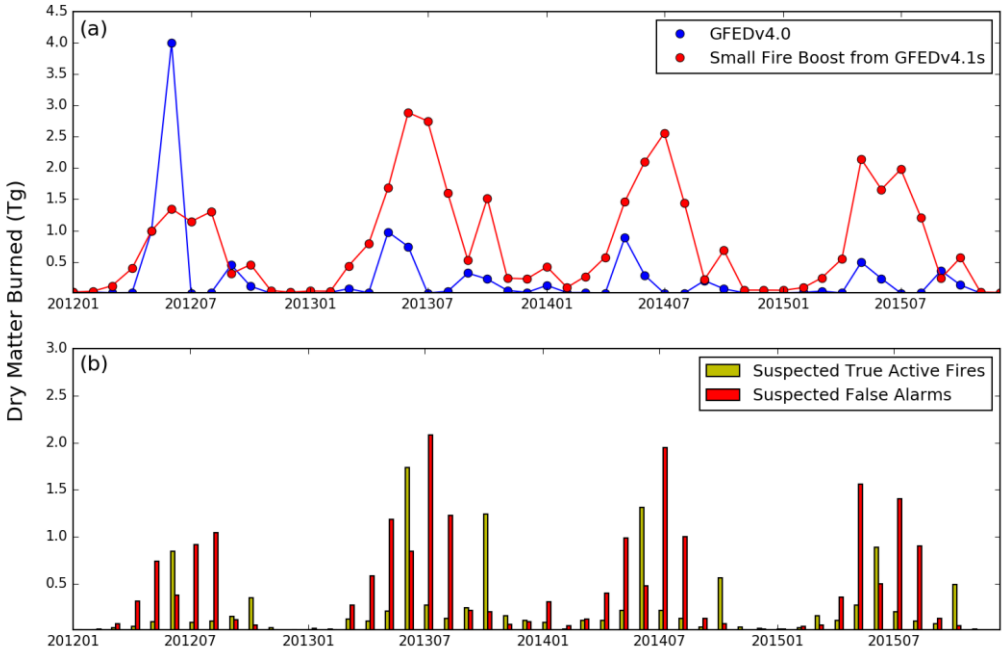

Figure 5.23: Monthly time-series of total dry matter burned from GFED, 2012-2015. (a) comparison of GFEDv4.0 results and small fire boost only results from GFEDv4.1s (already exclude GFEDv4.0), and (b) break down of small fire boost results by suspected true active fires and suspected false alarms using the MODIS active fire counts map shown in Fig. 5.20.

5.3.4 Agricultural Fire Emissions intercomparison

Fig. 5.20 has demonstrated the much higher dry matter burned estimate (expressed per m^2 of agricultural land in a grid cell) from VIIRS-IM compared to GFAS or GFED. Taking the year 2013 as an example, the total yearly DMB from VIIRS-IM, GFAS and GFED is 19.0, 6.2 and 15.2 Tg respectively. Previous research tends to suggest that satellite based methods of fuel consumption estimation will lead to very large underestimations in agricultural burning regions, due to the presence of numerous small fires that are difficult to detect from EO satellites (Yan *et al.*, 2006). However, our results show DMB totals far higher than those for the existing GFED and GFAS databases, and whilst GFEDv4.1s is closer to our total, the previous Section has placed considerable doubt on the efficacy of the "small fire boosting" approach used to increase the DMB totals beyond the far lower values found in GFEDv4.0 (which is 2.44 Tg from

this region; much closer to the value of GFAS). The differing performance of the VIIRS-IM inventory is a direct result of the method combine the small fire detection sensitivity of VIIRS and the diurnal cycle information generated from Himawari-8 - which together deliver a fire radiative energy (FRE) estimate that takes into account small fires and which can be converted into an estimate of DMB using the conversion factor of Wooster *et al*. (2005). This synergy of VIIRS and geostationary data appears to offer a substantial development in relation to EO-based quantifying agricultural burning.

To compare with other reported agricultural fires emissions inventories for China, the DMB estimates were converted to fire emissions estimates using the emissions factors and methods described in Section 5.3.5 and 5.3.6. Results are shown in Fig. 5.24. The total emissions of CO_2 during 2012 - 2014 period cover a narrow range of 27,069 - 31,107 Gg (Table 5.2), but decrease to 16,932 Gg during 2015, mainly due to the fact that CO_2 emission of wheat residue fires of that year is only 11,198 Gg, 48%, 55% and 53% of that in 2012, 2013 and 2014 respectively. This is because less fires occurred in the wheat growing region during the time of the landcover crop map shown in Fig. 5.12. Similar patterns are found for CO, $PM_{2.5}$ and BC (see Fig. 5.24).

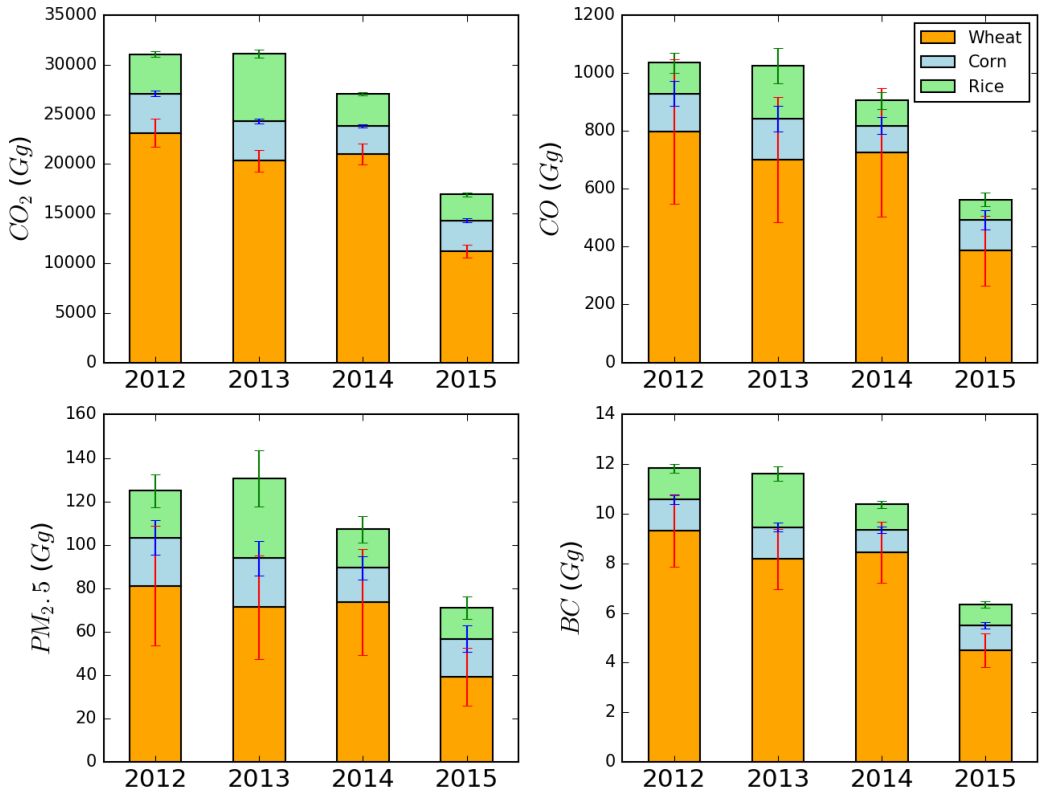

Figure 5.24: Total CO_2, CO, $PM_{2.5}$ and BC emissions (with standard deviation shown as coloured error bar) from three main crop residues burning types (wheat, corn, rice) during 2012-2015.

The primary contributor to the fire emissions of Eastern China is found to be wheat residue burns, which in general accounts for over 50% of the emissions of any particular species from year to year. The contributions of wheat residue burns are 66-77% (CO_2), 69-80%(CO), 55-69% ($PM_{2.5}$) and 71-81% (BC). However, the wheat crop yield is 10% lower than rice yield, and only 20% higher than corn yield according to the yearly National Bureau of Statistics of China (NBSC, 2012). The dry matter production-to-residue ratio of wheat is not higher than any other crop (Wang and Zhang, 2008; also see Table 6.2 in Chapter 6). A higher burning ratio for wheat residue is the only explanation for its dominant contribution to the fire emissions, which might be linked with local management practices and stakeholders' decisions and will be further discussion in Chapter 6.

The emissions estimates derived in this work have been compared with those from previous research conducted in China using satellite-based method or crop yield based approaches (CYBA, Table 5.2), originally reviewed in Section 2.6. Note that a few CYBA methods have more recently tried to use satellite-derived active fire detections to allocate total estimated crop residue burning and create high spatial resolution fire emissions datasets (Huang *et al.,* 2012, Li *et al.,* 2016). However, these are fundamentally still estimates based on the CYBA approach, as shown in Table 5.2. Considering the size of different regions, the results from this study are comparable with those found by Huang *et al.* (2012) who used CYBA methodology, but are around 1-2 times lower than those derived from other CYBA based methodologies. However, this is not because there is a clear underestimate of the fire emissions using the VIIRS-IM and Himawari-8 based satellite method developed herein. On the contrary, it is possible that the CYBA based studies may have overestimated the emissions from corn and rice residue burning by applying very high burning ratios (i.e. the amount of residue burned compared to the total amount generated by farming) in their studies. This will be further discussed in Chapter 6.

Another satellite-based research conducted by Liu *et al.,* (2015) used the FRP product from MODIS, with a modified Gaussian function to simulate a diurnal cycle, to generate daily FRE and then convert it into emissions. Results from Liu *et al.* (2015) for 2012-2014 are more comparable to, but not for all emissions, than those generated by the VIIRS-IM and Himawari-8 products used in this study. The fact they are lower than from VIIRS-IM can be explained by the tendency of MODIS to miss small active fires in comparison to VIIRS, as demonstrated in Chapter 3. Liu *et al.* (2015) also estimated a higher CO_2 emission total for 2012 (26,000 Gg) compared to 2013 (9800 Gg) and 2014 (13,000 Gg). However, the

study did not provide any adjustment for the impact of the MODIS scan geometry 'bow-tie' effect (Chapter 3), which leads to duplicated active fire detections towards the edge of the MODIS swath, which was highlighted as a serious problem by Freeborn *et al.* (2008) and also by the current study (Chapter 3). This problem has been addressed to some extent in GFAS using a weighing factor for the MODIS FRP data related to the view zenith angle (Kaiser *et al.*, 2012), and for GFAS CO_2 emissions from 2012 are only 24% and 10% higher than that from 2013 and 2014, a much lower increase compared to in Liu *et al.* (2015) (also see similar change of DMB in Fig. 5.19).

Table 5.2: Comparison of the agricultural emissions calculated in this study with those of previous studies.

Region	Year	Method	Emissions ($Gg.yr^{-1}$)				Reference
			CO_2	CO	$PM_{2.5}$	BC/EC	
Eastern China	2012	Satellite	31066±1960	1035±327	124±43	11±1.8	This study
	2013		31107±1748	1025±320	130±44	11±1.7	
	2014		27069±1421	904±279	107±36	10±1.5	
	2015		16932±1044	562±177	70±24	6±0.95	
NCP[1]	2012	Satellite	26000	1700	102	13	Liu *et al.*, 2015
	2013		9800	630	39	5	
	2014		13000	820	50	6	
Eastern China	2013	CYBA[2]	72071	2549	445	42	Qiu *et al.*, 2016
NCP	2012	CYBA	68675	5983	452	23	Li *et al.*, 2016
China	2006	CYBA	68000	4000	270	30	Huang *et al.*, 2012
China	2000	CYBA	160000	10000	-	70	Street *et al.*, 2003
China	2000	CYBA	184000	11000	470	80	Yan *et al.*, 2006

[1] NCP refers to the North China Plain, which has a geographic extent similar to that of this study (32-41°N, 113-121°E).

[2] CYBA refers to Crop Yield Based Approaches, see Section 2.6.1

Compare the emissions calculated from this study with other emission sources in Eastern China (Li et al., 2015), the contribution was not significant. All the four species (CO_2, CO, PM2.5, BC) contribute between 0.56%-2.0%, much lower than the main pollution contributed by industry and residential emissions. However, when limited the study time and area to summer burning season in intensive burning area (32-36° N, 112-122° E) only, contribution from above four species can go up to 8.1%, 18%, 22% and 20%. This comparison confirmed the likely strong seasonal impact of agricultural fire emissions on air quality and global change (see Section 2.4).

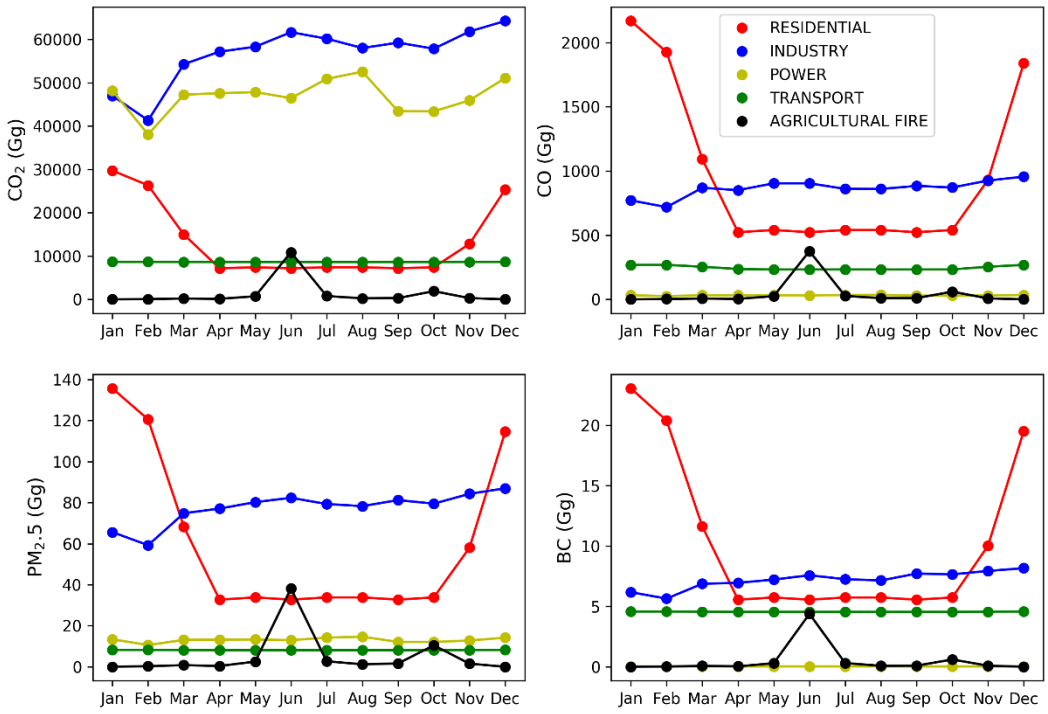

Figure 5.25: Comparison of CO_2, CO, $PM_{2.5}$ and BC from agricultural fire emissions (using 2013 as example) with those from other emission sources (residential, industry, power, transport, data source: Li et al., 2015) in intensive burning area (32-36º N, 112-122º E) of Eastern China.

5.4 SUMMARY

This chapter has combined the newly developed VIIRS-IM FRP product described in Chapter 3, a newly derived agricultural fire diurnal cycle from the geostationary Himawari-8 satellite, and the smoke emission factors measured *in situ* in Eastern China from Chapter 4. The output from this process is a high spatio-temporal resolution agricultural burning emissions product for Eastern China that take into account the type of small agricultural residue fire which dominates the region. A cultivation rotation map has been used to help identify the fuel type of the fires being burned, which is necessary when allocating the emission factors in the most accurate manner for emission estimation (since the EF's from the different fuel types differ somewhat; Section 5.2.7).

The output from this processing has been compared with two state-of-the-art global fire emissions inventories, GFAS and GFEDv4.1s. Dry matter emissions from this study are 1 to 4 times higher than GFAS/GFED 4.1s during two burning seasons, which indicates the very substantial contribution that "small" fires, unable to be detected by the MODIS active fire product or by the MODIS burned area product, make to emissions of the region. An additional comparison to GFEDv4.0 as well as GFEDv4.1

shows that the "small fire boosting" methodology developed by Randerson *et al.,* (2012) and applied in GFEDv4.1s may well have increased the DMB totals to amounts more in line with those from the VIIRS-IM-based inventory, but that very significant amounts of these additional emissions are located in places that appear unlikely to host biomass fires, and overall the additional emissions are mostly based on suspected false alarm active fires than true active fire detections. The efficacy of the 'small fire boost' methodology is therefore called into question, at least in this agricultural burning region.

Using the new fire emissions data based on the VIIRS and Himawari-8 datasets, wheat residue has been found to be the main contributor to agricultural burning emissions in Eastern China for all the species we estimated in this study (representing 55 to 81%), which could be explained by the higher burning ratio of wheat residue compared to other residues. Historical data using the CYBA methodology might have overestimated the burning ratio of corn and rice, leading to overestimation by a factor of 1-2 of the final emission totals. This will be further discussed in the next Chapter.

CHAPTER 6: EO-BASED EXAMINATION OF SOCIETAL BEHAVIOUR WITH RESPECT TO BURNING

6.1 INTRODUCTION

Based on the analysis from Chapter 5, the agricultural burning smoke emissions from fires in Eastern China are further discussed in this Chapter, focusing on their relationship to local and national management practices.

6.2 DISCOVERY OF A WINTER BURNING SEASON

As detailed in Chapter 5, small peaks in the dry matter burned (DMB) time-series are apparent in November-December of each year studied with the VIIRS data (Fig. 5.13). A magnification of these parts of the time-series from 2013 are shown below in Fig. 6.1.

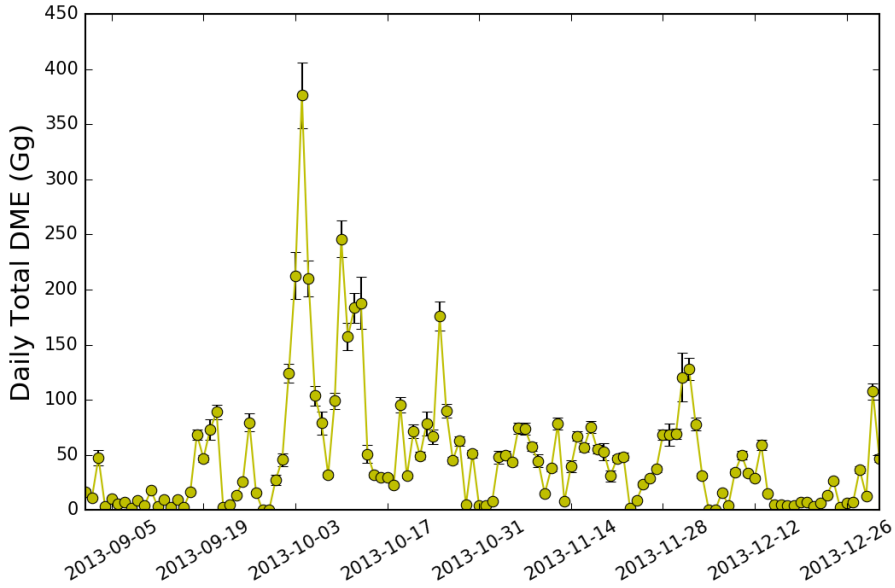

Figure 6.1: Time series of daily total DME (dry matter burned) in Eastern China from September 1st to December 31st, 2013, with standard deviation shown as black error bar.

These were initially considered to be false alarms that had failed to be excluded by the landcover or persistent detection filters detailed in Chapter 3 (e.g. white circle outlined area in Figure 7c of Section 3.2), because mention of a winter burning season was not found in any of the literature reviewed in Chapter 2 (e.g. Chen *et al.,* 2016; Huang *et al.,* 2012; Zhang *et al.,* 2008), and only burning around summer and autumn seasons have been reported. Furthermore, according to the mapped time of harvesting derived from the MIRCA2000 data (Fig. 5.12), there is no obvious harvesting of any of the three studied crop types (wheat, corn, rice) in this winter period. However, close examination of the original VIIRS data and the VIIRS-IM FRP product generated from it shows that most of the active fires detected in Nov and Dec are in fact located in or close to agricultural land (Fig. 6.2), and are in general not located close to industrial areas of the type known to cause false alarms that need to be screened out (Section 3.2; Fig. 6), and nor do they appear multiple times in the same month at the same location as would be expected to be the case if they were false alarms generated by land-based features. Therefore, it seems highly probable that these active fire detections in fact represent identifications of true sites of agricultural burning.

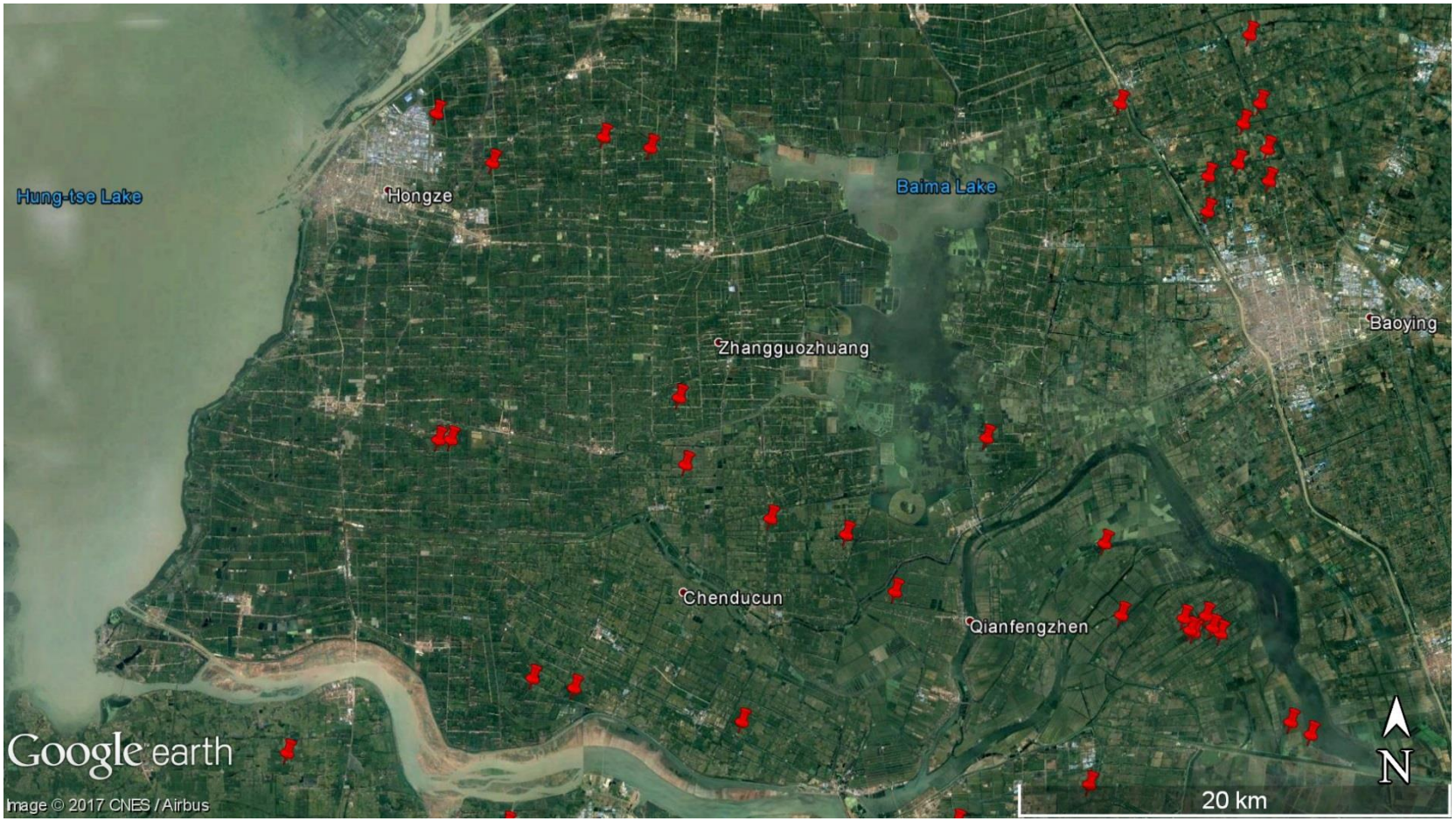

Figure 6.2: Google Earth imagery (centred at 33.210°N, 119.043°E) shows the VIIRS active fire pixels (red pin, fire detection algorithm details seen in Section 3.2) from Nov. 20th to Dec. 10th, 2013.

If the Nov-Dec active fire detections are real, as is believed to be the case, the most reasonable explanation appears to be that the crop residues being burned come from the most recent Sept-Oct harvest season, but that these were not burned at the end of the harvest but rather were left for a few months and burned further into the winter period. Local newspapers, online media and other information sources were checked to find evidence to support or refute this explanation.

After some investigation, sources were found that supported residue burning episodes happening during the winter period in Eastern China. For example, on 5 December 2013 Jiangsu Province TV station reported a huge crop residue burning episode in Hongze, Jiangsu Province, nearby the location shown in Fig. 6.2. Fig. 6.3 shows screenshots from one of the news reports made at the time, where flames and thick smoke can be seen resulting from the crop residue burning (also described in Chinese subtitles). The visibility decrease was such that the TV presenter almost disappears in the smoke by the end of the news report. Similar reports were found in different websites/newspapers from across much of Eastern China area (e.g. Wang and Zhang, 2016; Za, 2015; Zuo, 2015).

Figure 6.3: Evidence for agricultural burning in the winter season (2013). During a live TV news report related to intensive burning of agricultural residues in Hongze, Jiangsu Province (33.2942° N, 118.8731° E) on 5th December 2013, the reporter disappears into the thick smoke (http://www.weibo.com/1301904252/AlVcm8jZ2?type=comment#_rnd1499031542147).

Subsequent to the confirmation that a late winter burning season did indeed occur – at least in 2013 (Fig, 6.1) - and that the Nov-Dec small peak seen in the timeseries of Fig. 5.15 and Fig. 6.1 indeed represent a real event in 2013 (and most likely in the other years as well), an explanation as to why this activity may have occurred outside of the normal burning season was sought. According to Yun Xia, a local Govenor of the Environmental Department in Hefei (interview conducted by Anhui News; Zuo, 2015), fire prohibition in the local area started at beginning of September up until the 20th November. At this time, the local government more strongly enforced its polices that aim to restrict agricultural residue burning, and established almost continuous patrols to identify areas likely to host fires in order to prevent them from occurring. However, without an alternative, cost-effective way to dispose of their crop residues, it seems likely that local farmers simply stored the residue material and burned them soon after the prohibition period and intensive patrols had ceased. The end of the prohibition period therefore coincides with this new winter burning season.

To identify the likely crop residue type being burned in Nov-Dec required a slight alteration of the previous methodology detailed in Section 5.2.8. Because the fires observed with VIIRS during November and December are related to 'left over' material from the autumn harvest season, instead of using the harvest map derived from the MIRCA2000 data in those two months (Fig. 5.11), the October data was instead used. The results have, in fact, already been shown in Fig. 5.13b, where the daily FRE areal density time-series is shown by crop residue type. The winter season accounts for between 19 and 36% of the sum of the autumn and winter FRE from 2012-2015. During the "artificially induced" winter burning season, only corn and rice residues appear to have been burned, and their relative contributions to the total are 49% and 51% respectively. Despite the spatial distribution of fires varying from winter to autumn, this pattern is in fact rather similar to that of the autumn burning season, where corn and rice residues accounted for 54% and 46% of the total FRE released respectively. The reason for the spatial shift of winter fires will be discussed in Section 6.4.

6.3 BURNING RATIOS

The ratio of crop residue burning in the field used to be considered as a key parameter when producing agricultural burning emission estimates via the crop yield based approaches (CYBA, see Section 2.6.1). This metric represents the total annual percentage of crop residue burned in the field compared to total

crop residue amount produced after harvesting (Fig. 6.4; Chen *et al.*, 2016; Gao *et al.*, 2002; Huang *et al.*, 2012; Li *et al.*, 2016).

Compared to a constant ratio (17%) based on 1970s data used in Streets *et al.*, (2003)'s research, more detailed regional values have been used in many more recent studies. Generally, three datasets have been used in CYBA research in China over the last decade:

i) That from Wang and Zhang (2008), who divided all provinces in China into six zones according to their geographical distribution. A questionnaire based survey among farmers within these regions was used to elucidate burning activity, and using the responses it was determined that burning ratios for the different categories ranged from 11% to 33%. This research output has subsequently been cited and applied in a series of fire emission studies (He *et al.*, 2011, Qin and Xie 2011, Zhang *et al.*, 2016).

ii) A set of province-dependent burning ratio datasets adopted from a large-scale investigation of the use of crop residues made across different Chinese provinces (Gao *et al.*, 2002). This work has been used and cited by Huang *et al*. (2012), Yan *et al*. (2006), Zhang *et al*. (2008), as shown in Fig. 6.4.

iii) A derived value based on farmers' income levels, based on the fact that Cao *et al.*, (2006) found a linear correlation between the income of farmers and burning ratio (r = 0.81). This result has been applied within several fire emission studies (Zhao *et al.*, 2015; Sun *et al.*, 2016; Zhang *et al.*, 2017) and will be examined in Section 6.4.

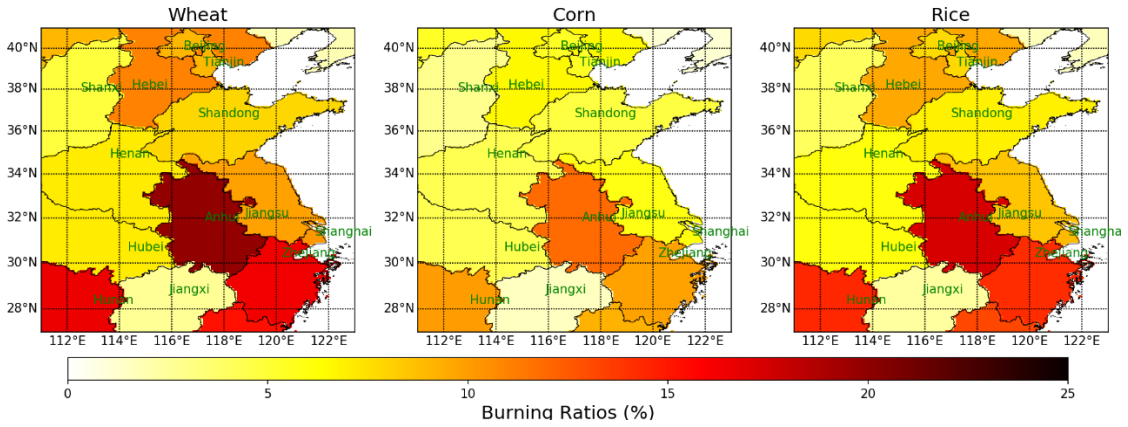

Figure 6.4: Spatial distribution of province-specific burning ratios in Eastern China from results of Gao *et al*. (2002). This metric represents the percentage of crop residue burned in the fields compare to the total amount of crop residue amount produced after harvesting per year.

Using the data in this study, it is straight forward to reverse the CYBA methodology and calculate the burning ratio from the crop-dependent DMB data (as shown in Fig. 5.19, Section 5.3). This procedure can help check whether the outputs derived herein are comparable with those of the existing literature, as well as enabling the advantages offered by the time series data available from satellite remote sensing to be fully exploited. The burning ratios are calculated from:

$$F_{ij} = \frac{M_{ij}}{P_{ij} R_i C} \quad (6.1)$$

Where i stands for crop type and j stands for the province; M_i is dry matter from VIIRS (kg); P_{ij} is the crop yield (kg); R_i is the proportion of dry matter production-to-residue ratios and C is crop combustion completeness.

The province level crop yield P_{ij} is derived from annually published statistical reports, which can be seen in Table 6.1. R_i and C are from literature, and are shown in Table 6.2.

Table 6.1: Province-specific crop yield of three main grains in Eastern China ($\times 10^1$ Gg, National Bureau of Statistics of China, 2012-2015)

Province	2012			2013			2014			2015		
	Wheat	Corn	Rice	Wheat	Corn	Rice	Wheat	Corn	Rice	Wheat	Corn	Rice
Shanghai	24	3	89	23	3	89	18	3	87	19	3	84
Beijing	28	90	0	27	84	0	19	75	0	12	50	0
Tianjin	54	94	11	56	93	11	57	102	13	59	101	12
Anhui	1216	363	1387	1294	428	1394	1332	426	1362	1394	466	1395
Shandong	2104	1979	104	2180	1995	103	2219	1967	104	2264	1988	101
Shanxi	240	855	1	259	904	1	231	956	1	259	938	1
Jiangsu	1023	226	1864	1049	230	1900	1101	216	1922	1160	239	1912
Jiangxi	2	11	1950	2	13	1976	3	12	2004	3	12	2025
Hebei	1276	1640	60	1338	1650	50	1387	1704	59	1430	1671	54
Henan	3123	1697	475	3177	1748	493	3226	1797	486	3329	1732	529
Zhejiang	27	15	649	27	29	608	28	27	580	31	30	590
Hubei	345	276	1617	371	283	1651	417	271	1677	422	294	1730
Hunan	10	189	2575	9	197	2632	11	185	2562	10	189	2634

Table 6.2: Proportion of dry matter production-to-residue ratios (Ri) and crop combustion completeness (*C*, de Zarate *et al.,* 2010; Huang *et al.,* 2012; Turn *et al.*,1997; Wang and Zhang, 2008) from burning of wheat, corn and rice residues. Combustion completeness is high for fine fuels such as these.

	Production-to-residue Ratio	Combustion Completeness
Wheat	1.0	0.86
Corn	2.0	0.92
Rice	1.0	0.89

The crop and province dependent residue burning ratios calculated in this study are shown in Fig. 6.5. The yearly mean wheat burning ratios are generally highest (7.8-12%), followed by corn (1.7 - 2.3%), and rice (0.9 - 2.0%). Comparing these figures to the data from Gao *et al*. (2002, see in Fig. 6.4), in which the mean burning ratios of wheat, corn and rice are 9.8%, 5.9%, 8.5% respectively we see that the wheat burning ratios are of similar levels of past work, whilst the rice and corn burning ratios are much lower. Though previous research tends to indicate that satellite based methods underestimate agricultural fire emissions (Yan *et al.,* 2006), this study has confirmed that during the summer burning season wheat residue fires dominate, and that the estimates of the burning ratio derived from satellite remote sensing with VIIRS and Himawari-8 are similar levels to those of ground-based measures of Gao *et al*. (2002). The smaller ratios we see from rice and corn imply potential error of prior studies on agricultural fire emissions in Eastern China based on the CYBA, because of overestimated burning ratios.

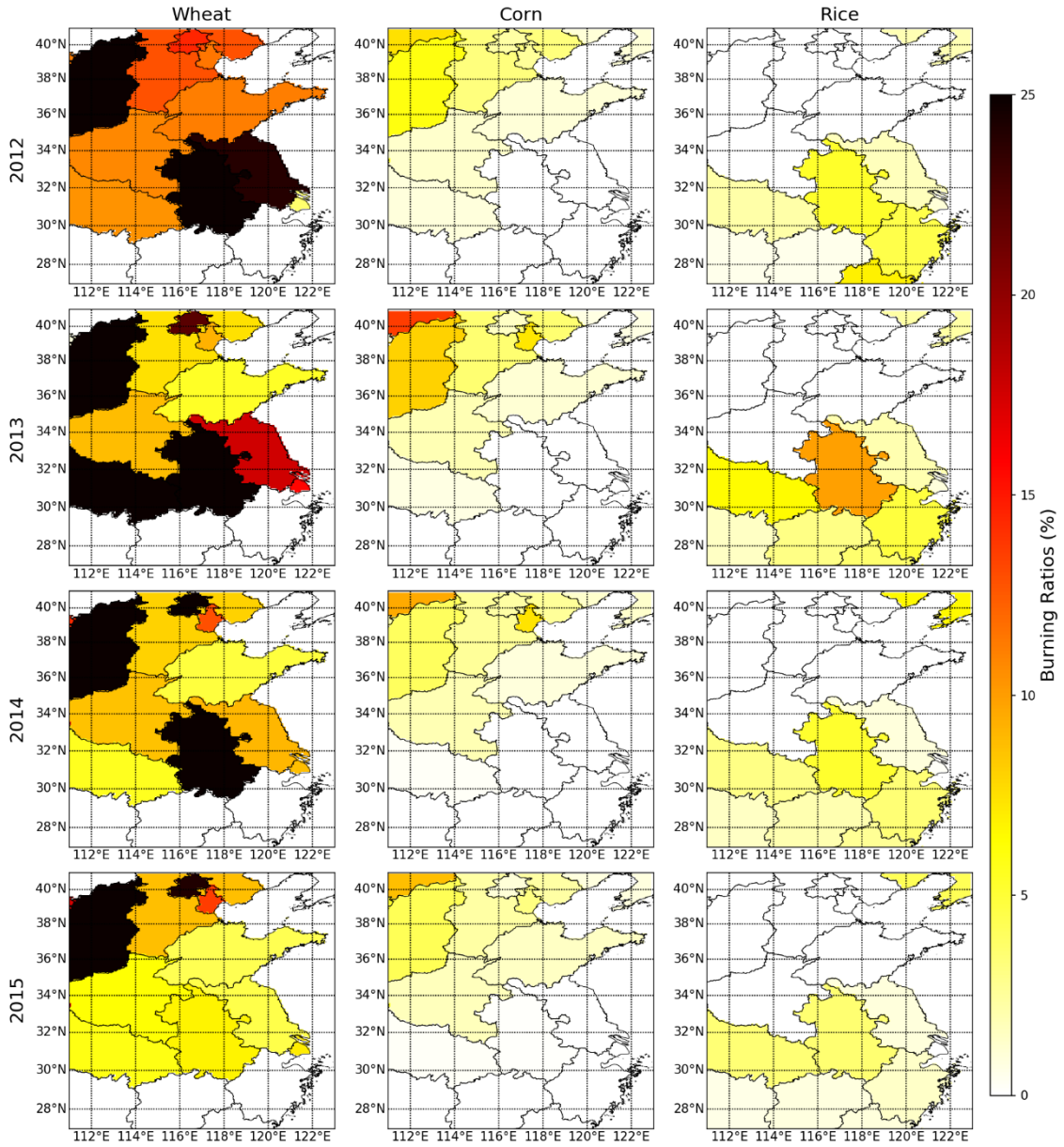

Figure 6.5: Spatial distribution of province-specific percentages of crop residues burned in the fields (burning ratio metrics) of Eastern China using VIIRS results from 2012-2015.

Fig. 6.5 also indicates that burning ratios are not only influenced by crop type or province, but also vary from year to year. For example, the wheat burning ratios of key provinces in 2012, including Anhui (30%), Shandong (11%), Jiangsu (24%) and Henan (11%) are closest to those (20%, 8%, 10%, 7% respectively) from Gao *et al.*, (2002). However, during 2015 values in this study dropped to 6% (Anhui), 4% (Shandong), 4% (Jiangsu) and 6% (Henan) calculated via Eqn. 6.1. This interannual variation might be linked with changing farming activity and local prohibition policies as explained in Section 6.2 (Yang *et al.*, 2008, Li *et al.*, 2016).

6.4 IMPLIED SOCIAL EFFECTS

Rates of agricultural residue burning in the fields have been proposed to vary with the local farmers income level (Cao *et al.*, 2006; Qin and Xie, 2011), with the assumption that higher income areas have better access to electricity or other energy sources and thus have less need to utilise crop residues for heating and cooking – leading to higher ratios of open burning. However, this is not what is observed in the current study.

As shown in Fig. 6.6, the provinces with the highest total DMB estimates (Anhui and Henan; 53 and 38 $kg.m^{-2}.yr^{-1}$ respectively; Fig. 6.4a) have lower GDP values per capita (5580 and 5335 US$ per capita, Fig. 6.4d), while lower provinces showing lower amounts of DMB, Shandong and Jiangsu (28 and 27 $kg.m^{-2}.yr^{-1}$ respectively) show higher GDP per capita (9882 and 13311 USD$ respectively). Across the whole Eastern China, DMB is in fact inversely correlated with GDP per capita ($y = -204x+15700$, $r^2 = 0.72$; at a level significant at the 95% confidence interval; Fig. 6.7).

Furthermore, DMB appears also to be correlated with agricultural area ($y = 1950x + 8240$, $r^2 = 0.49$) and population ($y = 1.23x + 19$, $r^2 = 0.47$; *Fig. 6.7*). Huang *et al.*, (2012) suggested that the lower crop residue burning amounts seen in 2006 compared to 2000 (deduced on the basis of CYBA methodology) might be contributed to the policy of encouraging farmers to use the residues as fertiliser. This policy appears to be perhaps a more reasonable explanation of the spatial and temporal trends we observe in this study, compared to the assumption of Cao *et al*. (2006) that the amount of crop residue burning is proportional to farmers' income level.

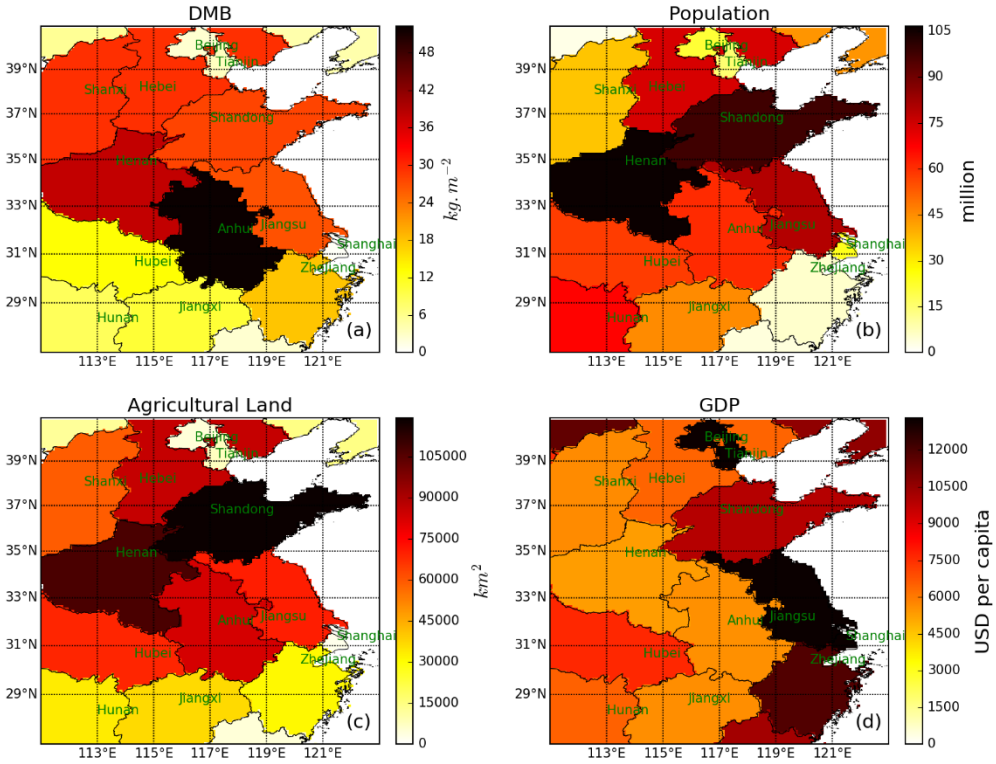

Figure 6.6: Spatial distribution of province-specific: (a) mean yearly dry matter burned retrieved from this study, (b) population (Data source: Fu *et al.*, 2014a), (c) agricultural land area (Data source: GlobeLand30, http://www.globallandcover.com/, see details in Section 3.4) and (d) mean GDP per capita (Data source: Fu *et al.*, 2014b).

The reason that the DMB in a Province is inversely correlated to its DMB might be explained by the variation in action to prohibit burning. This can be explained in two parts:

1. The direct cost of promoting agricultural machinery. For example, the local government of Jiangsu Province released a regulation in 2009 stating that by the end of 2012, over 35% of crop residues should been incorporated into the soil after mechanised harvesting. The regulation also indicated that the local government should include a budget for improving the efficiency of agricultural machinery and subsidise farmers who follow this regulation.
2. The allocation of a budgetary allowance for utilisation of crop residues, which is unfortunately very expensive. For example, research on residue burning power generation shows the government needs to pay at least 20% of the total cost of the operation to keep the plants running, partly because of high cost of residue collection and transportation from the fields (Li and Hu, 2009).

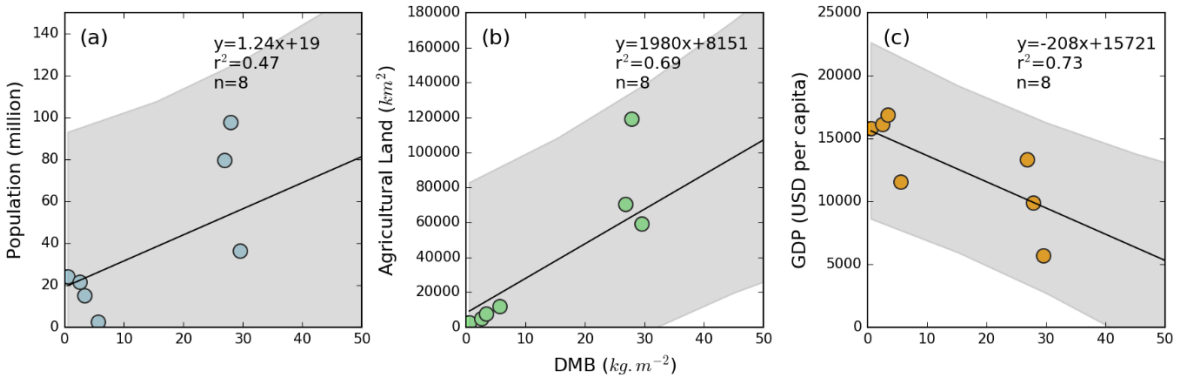

Figure 6.7: Direct comparisons of province-specific mean yearly DMB (dry matter burned) retrieved from this study with (a) population, (b) agricultural land area and (c) mean GDP per capita. The best fit linear relationships are shown, along with its equation, and the grey shaded area represents the 95% confidence limit on the relationship.

The impact of these societal effects on crop burning ratios is seen both at the inter-province level, and at more granular levels such as the 0.1° grid cells. The work presented in Section 6.2 suggests that the winter burning season (Nov-Dec) is caused by delayed burning of residues left over from the autumn harvest season, because of prohibition policies related to burning being more robustly enforced earlier in the season. Fig. 5.14 (show here again as Fig. 6.8) also showed that the spatial distribution of FRE areal density during winter is different from the normal autumn burning season that occurs in Sep-Oct. Generally, the areas of strongest burning are further from the Capital Cities (green stars) during autumn. For example, fires in Anhui Province are mainly distributed in the north during autumn, whilst locations change to south (closer to the Capital Hefei city) during the delayed winter burns. A similar example can also be seen in Hubei Province, where fires are shifting from west to east during the delayed winter burns in Nov-Dec.

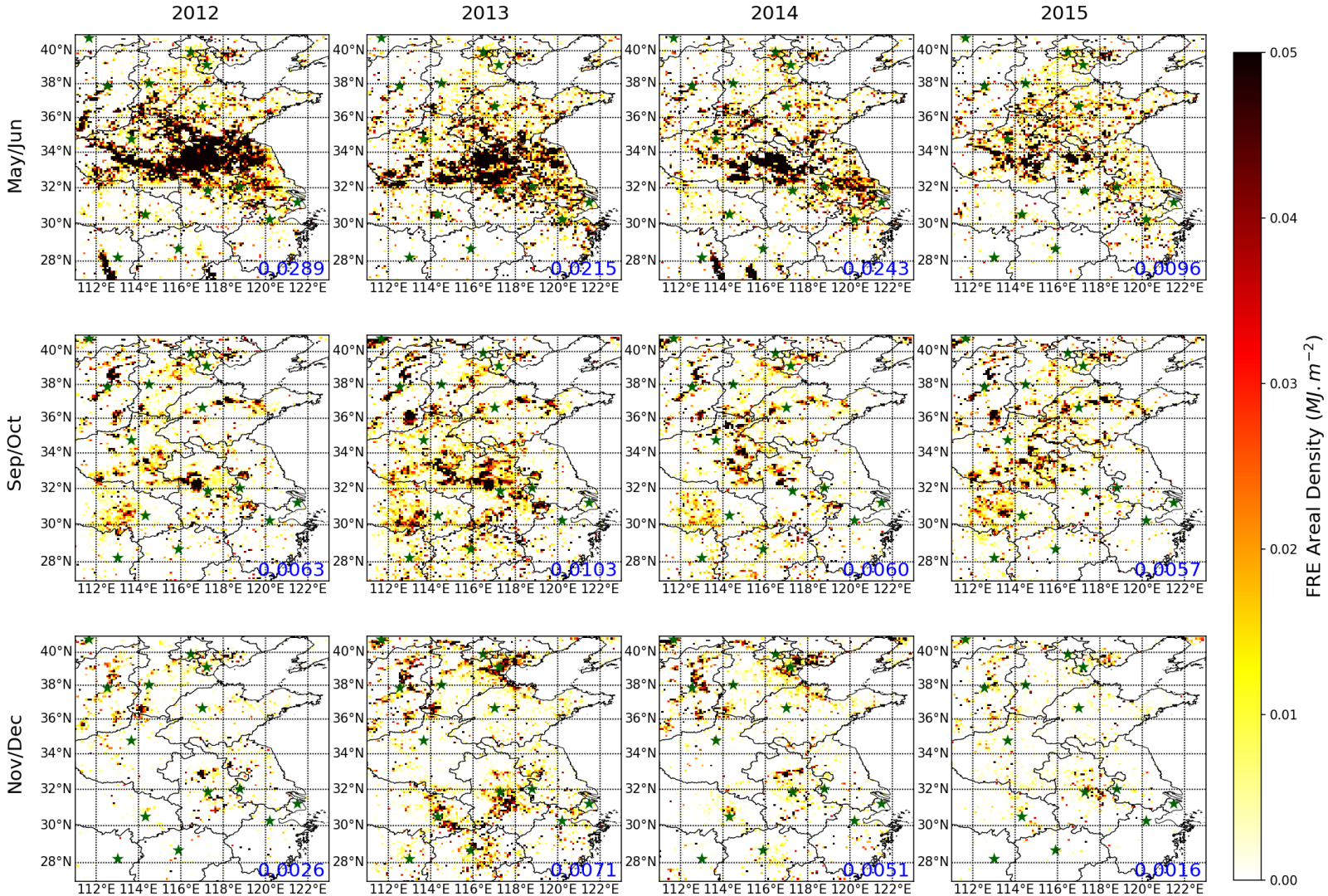

Figure 6.8: Same as Fig. 5.16. Spatial distribution of total grid-cell FRE per m^2 (0.1 deg grid cells) for agricultural fires in Eastern China from 2012 to 2015 (top to bottom rows) split by fire season: summer (May-June, left column), autumn (Sep-Oct, middle column) and winter (Nov-Dec, right column). Mean regional FRE for each season is indicated in blue text, and the capital city location of each province is shown as a green star.

The distance of each 0.1º grid cell centre in Fig. 6.8 to their province capitals was calculated for further examination. Fig. 6.9 shows the normalised frequency distribution of the distance from the highest FRE grid cells (top 10% in each Province) across the three burning seasons. The first and third quartiles of distance values during autumn season are 109 km and 214 km respectively. However, during the delayed winter burning season, the distribution shifts to far shorter distances, with the first and third quartiles 70 km and 153 km respectively. The mean distance to capitals of the high FRE grid cells also deceased to 124 km (winter) from 165 km (autumn). A Kolmogorov–Smirnov (K-S) was performed to evaluate the difference between the distributions of the distances seen in the autumn and winter season. A high K-S statistic value (0.30) and low p-value (5.9×10^{-24}) is generated from this test indicates that the distribution of distances during the winter months is substantially different to those seen during summer and autumn. This geographical shift might also be linked with the prohibition policy. The capital cities may get better access to resource for enforcing the prohibition, while these resources are likely to decrease when expanding into areas more distant from the Capital.

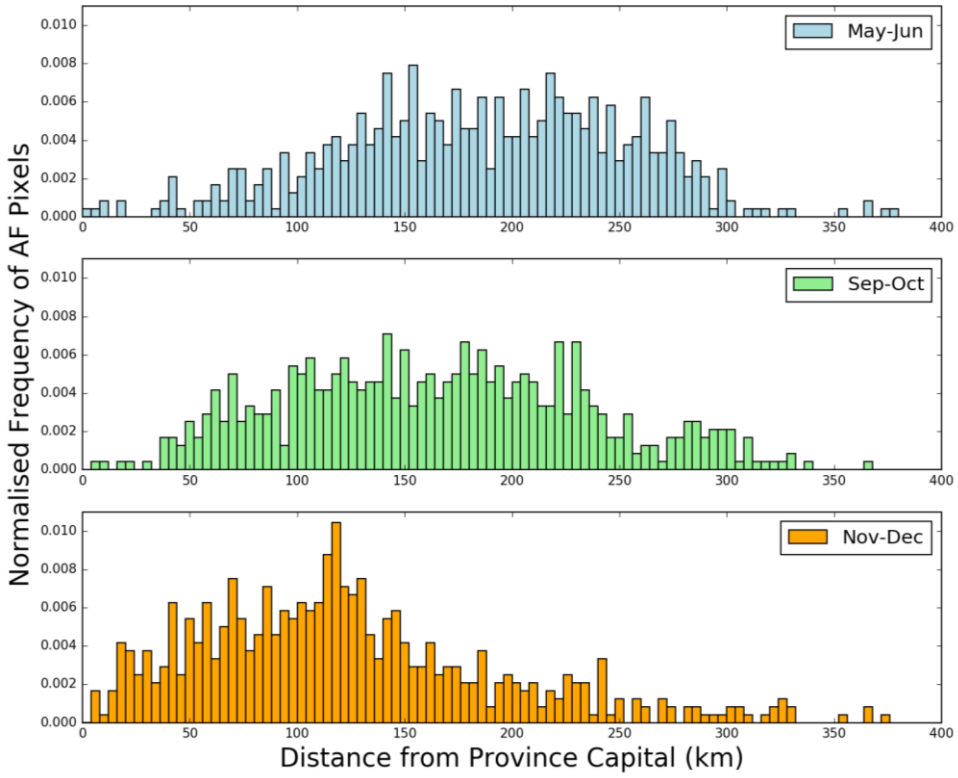

Figure 6.9: Normalised frequency distribution of distance from province capital of the top 10% of high FRE fire pixels during the three burning seasons: Summer - May to June (top, blue), Autumn – September to October (middle, green), and Winter - November to December (bottom, orange). A clear shift towards of the origin can be observed in Nov-Dec compared with Sep-Oct.

6.5 SUMMARY AND CONCLUSIONS

This chapter has used the results from Chapter 5 to analyse aspects of societal behaviour in relation to agricultural burning in Eastern China. The burning ratios, which are metrics representing the percentage of crop residue burned in the field compared to total residue yield, are calculated using total DMB from VIIRS results and crop residue yields from national statistics. The burning ratios are key parameters required when producing agricultural burning emission estimates via the CYBA (crop yield based approach). The comparable values of wheat burning ratios obtained here in comparison with past work based on field data (Yan *et al.,* 2006) demonstrates the potential maturing of satellite based methods in recent years. This is in a large part due to the VIIRS sensor's far improved sensitivity to small fires compared to earlier sensors such as MODIS. The lower values of corn and rice burning ratios from this study indicated that past inventory may have overestimated the emissions from these two crop types by using too high a burning ratio.

This study has confirmed that the newly identified winter burning season (Nov-Dec) is likely caused by the delayed burning of parts of autumn harvest due to local fire prohibition policies. The DMB of winter season accounts for 19 - 36% of the total DMB in autumn and winter, indicating the temporal transfer of this amount of agricultural burning to a later than normal date. A spatial transfer has also been found by comparing the location of fires in the winter to autumn burning seasons, and this might be driven by the lower enforcement of prohibition policies away from political centre of each province.

The close link between the agricultural fire emissions and societal behaviours indicate that, despite some past research suggesting that aggressive emission controls (driven by governmental policy implementation and enforcement) could lead to a 50% fall in premature deaths due to improved air quality by 2030 (Saikawa *et al.,* 2009), more thoughtful management practices than simply prohibiting fires for a set period after harvest time may be needed if the magnitude of burning is really to be reduced rather than just delayed.

CHAPTER 7: DISCUSSION AND CONCLUSION

7.1 INTRODUCTION

This Chapter reviews the findings of this Thesis in relation to the Objectives detailed in Section 2.7. Based on these, a set of conclusions and implications have been summarised in Section 7.4, and suggestions for future work made in the final section.

7.2 REVIEW OF FINDINGS IN RELATION TO THESIS OBJECTIVES

7.2.1 OBJECTIVE (I): QUANTIFY THE SPATIO-TEMPORAL DISTRIBUTION OF AGRICULTURAL RESIDUE BURNING USING ACTIVE FIRE SATELLITE EARTH OBSERVATION APPROACHES THAT TAKE INTO ACCOUNT "SMALL FIRES" MORE EFFECTIVELY THAN CURRENTLY DONE.

The work to accomplish this objective is contained primarily in Chapter 3. An improved quantification of agricultural residue burning in Eastern China was derived, based on the use of data from the new VIIRS (Visible Infrared Imaging Radiometer Suite) sensor carried on the Suomi-NPP satellite, launched in October, 2011. The I-Band of VIIRS provides global observations twice daily at a spatial resolution of 375m (at nadir). A new regional optimised active fire (AF) detection algorithm was developed to use the VIIRS I-Band data, based on a combination of past algorithms including the MODIS active fire detection algorithm (Giglio *et al.,* 2016), the global VIIRS I-Band AF detection algorithm (Schroeder et al. 2014), the BIRD-HSRS active fire and FRP algorithm (Wooster *et al.*, 2003; Zhukov & Oertel, 2001; Zhukov *et al.*, 2006), and the Meteosat SEVIRI Fire and Thermal Anomaly algorithm (Roberts and Wooster, 2008; Wooster *et al.,* 2015). A few of the AF pixels detected using this algorithm have been validated in the Northern China Plain using pre- and post-fire high spatial resolution imagery (taken from Google Earth and a UAV deployment). This validation confirmed the existence of burned areas appearing around the time of the AF detection (Section 3.2).

The regionally specialised AF detection algorithm developed in this study enables detection of an increased proportion of 'small fires' compared to the results from VIIRS global algorithm that also uses

the VIIRS I-Band to attempt their detection (Schroeder et al. 2014). However, the regional algorithm developed here includes use of more liberal detection thresholds which comes at the risk of introducing a higher false alarm rate (Section 3.5). The identified false alarms were often associated with large industrial buildings, having highly reflective and/or warm rooftops and being surrounded by more rural landscapes (Section 3.3). Such occurrences were removed with the help of a spatial and temporal mask, deriving from combination of 30 m spatial resolution GlobeLand30 global landcover mapping, OpenStreetMap with abundant urban area information, and a temporal filter that identified repeated fire detection signatures at the same location that is thought largely incompatible with real active fire behaviour.

The results from the VIIRS-IM AF detection algorithm developed here were also compared with the long-standing MODIS AF detection data. The comparison shows the VIIRS regional algorithm delivers typically 5 to 10 × more AF pixels than does simultaneously-collected MODIS AF data (notwithstanding differences in spatial resolution), and importantly with an AF detection sensitivity that remains much more constant across the swath due to VIIRS pixel aggregation scheme.

7.2.2 OBJECTIVE (II): ESTIMATION OF BIOMASS CONSUMPTION IN AGRICULTURAL RESIDUE BURNING.

This objective was again addressed with the work reported in Chapter 3 (with the construction of a 'synergy' FRP retrieval scheme), and Chapter 5 (building of daily FRE and fire emissions methodology).

The 'synergy' FRP retrieval scheme was built based on the regionally optimised AF detection algorithm derived to meet Obj. (I). Though VIIRS I-Band data is clearly extremely useful for detecting small fires, the higher FRP fires often saturate the I4-Band, leading to an underestimation in FRP retrieval. Therefore the VIIRS-IM 'synergy' FRP product blends the advantages offered by the VIIRS I-Band detection sensitivity to small fires with M-Band FRP retrieval over higher FRP fires, and includes appropriate consideration of the waveband and atmospheric transmittance differences between the VIIRS I4 and M13 bands. The 'synergy' product captured on average 400% more total FRP than near simultaneous MODIS data, even without downward adjustment of the MODIS results for the MODIS 'bow-tie' effect that duplicates MODIS AF pixels towards the swath edge (Freeborn *et al.*, 2011).

The output from VIIRS-IM 'synergy' FRP product was aggregated to 0.1 × 0.1° grid cells and adjusted for partly cloud-covered pixels. A fire diurnal cycle was then needed to convert the FRP data to estimates of daily fire radiative energy (FRE). This was achieved using FRP data derived from Himawari-8, a Japanese geostationary meteorological satellite launched on October, 2014. The FRP data from Himawari-8 was gridded to 0.1 × 0.1° grid cells, then converted to normalised FRP values to minimise the impact of day-to-day variations in the amount of fire activity, and then approximated using an optimally fitted Gaussian function to generate the diurnal cycle (Andela et al. 2015). The FRE results calculated from a combination of the VIIRS FRP retrievals and the Himawari-8 diurnal cycle were converted to daily dry matter burned (DMB) using the conversion factor from Wooster et al. (2005).

7.2.3 OBJECTIVE (III): CONFIRMATION OF THE EMISSIONS FACTORS OF CHINESE CROP RESIDUE FIRES.

This objective was met by the successful construction and deployment of a new portable smoke sampling system for the simultaneous close range measurement of trace gases (CO and CO_2) and aerosols (PM2.5 mass and BC). This system was used to study trace gas and particle emissions from field burns in China conducted during agricultural burning periods (Section 4.2-4.3).

Most prior research on smoke from these types of fuels have either been based on laboratory measurements, and/or have relied on filter-based sampling that provides only the total sampled mass from whole combustion rather than higher temporal resolution information. The system developed and deployed herein offers the advantage of allowing continuous *in situ* measurements of smoke generated by agricultural fires burning naturally in the field, which is important as field burns may well behave quite differently to burns conducted under laboratory conditions (Delmas *et al.,* 1995, also see Section 4.4).

The sampling system has been deployed in Eastern China in June 2014 for collecting the measurements necessary to derive gas and particle emission ratios and EFs for a series of crop residue fires (Section 4.2). Different relationships between fine particle mass (PM2.5) and black carbon mass (BC) were found for smoke produced in the smouldering phase (mass ratio = 80.7) compared to the flaming phase (mass ratio = 2.0), which inspired the generation of a linear mixing model to quantify the contribution of each combustion phase to the smoke being measured at a particular time. Using time series of trace gas

concentrations from different fire cases, instead of a single "fire averaged" EF, 'fire integrated' trace gas EFs were calculated by weighting each instantaneous EF by the corresponding CO_2 and CO excess abundances, (Wooster *et al.,* 2011). The 'fire integrated' EFs were calculated for wheat and rice residue burns as 1739 ± 19 g kg^{-1},1761 ± 30 g kg^{-1}, respectively for CO_2, and 60 ± 12 g kg^{-1}, 47 ± 19 g kg^{-1} respectively for CO. The output from this smoke sampling system agreed well with the results derived via a simultaneously-deployed open path Fourier transform infrared (OP-FTIR) spectrometer. Particulate EFs have also been generated using the gas EFs and the linear best fit relationships between particulate mass and gaseous measurements.

Enhancement of the smoke sampling system was conducted after the first field deployment in June 2014 in China, with the purpose of improving certain performance metrics (Section 4.4). The updated system was briefly deployed once more in China, but also in UK tests, and the confirmed EFs for fires in the fuel types used in Eastern China were later used in the Chinese agricultural fire emissions estimation (Section 5.2).

7.2.4 Objective (IV): Estimate daily agricultural residue burning emissions for Eastern China fire seasons throughout 2013-2015.

This objective was addressed in Chapters 5 and 6, with the final result a new high spatial-temporal resolution agricultural fire emissions inventory for Eastern China, along with the analysis and results below.

This agricultural fire emission inventory was generated based on daily biomass consumption from agricultural residue burning recorded at a 0.1 × 0.1° grid spatial resolution (Obj. ii), emission factors deducted for Chinese residue burning (Obj. iii), and a cultivation rotation map derived from the MIRCA2000 global crop area dataset to identify the fuel type at the grid level (Section 5.2). The yearly total emissions of CO_2, CO, $PM_{2.5}$, BC during 2012-2015 calculated from this inventory were 12716-22611, 343-619, 45-80, 4-7 Gg, respectively (Section 5.3). The output has been compared with two state-of-the-art global fire databases, GFAS and GFED4.1s (introduced in Section 2.6). Dry matter emissions from this study were 1-5 times higher than GFAS/GFED 4.1s during summer season, and 2-7 times higher during autumn season, due to the improved small fire sensitivity of VIIRS compare to MODIS (Section 5.3).

In Eastern China, the wheat residue was found to be the main contributor (49-80%) to total agricultural burning emissions. Historical data (e.g. Huang *et al.,* 2012; Qiu *et al.,* 2016; Yan *et al.,* 2006) calculated from crop yield based approach (CYBA, see Section 2.6) was compared with results from this study. The comparison found an overestimation of a factor of 2 in total emissions from CYBA research, mainly due to the likely overestimated corn and rice burning ratios used in those studies (Section 6.3). This study also discovered winter burning months (Nov-Dec) in Eastern China, which appear likely to be caused by the delayed burning of parts of the autumn harvest materials due to a strongly enforced fire prohibition policy in the earlier months.

The fire prohibition policy led to 19 to 36% (depending on the year) of the material of the autumn harvest being burned later on in the winter, after the policy enforcement had been relaxed, and thus gaseous/particulate emissions were also moved from the autumn to this new winter burning season (Section 6.2). A spatial transfer was also noted, which might be driven by weaker enforcement of prohibition policies at locations further away from the political centre of each province (Section 6.4).

Compare to other emission sources in Eastern China (Li et al., 2015), the contribution of agricultural fire emissions was not significant across the whole year. All the four species (CO_2, CO, PM2.5, BC) contribute between 0.56%-2.0%. However, contribution from above four species can go up to 8.1%, 18%, 22% and 20% when limiting the study time and area to summer burning season in intensive burning area. This comparison confirmed the likely strong seasonal impact of agricultural fire emissions on air quality and global change.

7.3 CONCLUSIONS AND IMPLICATIONS

As described in the beginning of Chapter 1, this PhD project aimed at improving the understanding and quantification of agricultural residue burning in Eastern China, in particular focusing on the emissions to the atmosphere that result. To achieve this, a high spatial-temporal resolution smoke emission inventory covering CO_2, CO, $PM_{2.5}$ and BC has been constructed, with the help of a regionally optimised small active fire detection algorithm based on data from the VIIRS satellite instrument (Chapter 3). A new smoke sampling system has been built and deployed to provide smoke emission factors based on *in situ* data from field burning (Chapter 4). The problems of VIIRS I-Band saturation over larger fires, and the conversion of instantaneous measurements of FRP to time-integrated measurements of FRE, have both

been carefully dealt with using a 'synergy' FRP retrieval scheme based on the VIIRS I- and M-Band data and a Gaussian diurnal cycle generated from data on a geostationary satellite, Himawari-8 (as described in Chapters 3 and 5). The results and comparisons to other fire inventories presented in Chapters 5 - 6 have shown the advantage of this new inventory compared to existing datasets.

The large uncertainties in the magnitude of the agricultural burning activity, as well as its exact timing and specific geographic spread, have limited the understanding of the related emissions and their dispersion (Street *et al.,* 2003; Yan *et al.,* 2006; Huang *et al.,* 2012). By constructing a new agricultural fire emission inventory for Eastern China, which more accurately accounts for the type of 'small fire' that dominates agricultural landscapes, provides a strong potential for improving the assessment of the degree to which such burning contributes to air quality in Eastern China, and more widely to regional atmospheric pollution. The methodology could also potentially be applied near real-time and linked to regional air quality model to improve the forecasting of smoke dispersion from the agricultural fires.

Comparing the results from this study to those from two state-of-the-art MODIS-based global fire emission databases (GFAS and GFED), highlights the advantage of the small fire detection capability of VIIRS. This comparison also proved the importance of such small fires in agricultural burning regions such as Eastern China. The methodology developed here could be applied to other agricultural burning areas such as in India, and to different biomes dominated by smaller or lower FRP fires, for example underground peatland burning in SE Asia (Parker *et al.,* 2016). The methodology could potentially be integrated into existed global fire emission databases such as GFAS, which would enable significant improvements in global fire emission estimation in these 'small fire' dominated regions.

7.4 SOME SUGGESTIONS OF FUTURE WORK

The active fire detections generated from VIIRS and shown in the results of Chapter 3 are those that have passed the spatial and temporal filters introduced to screen out false alarms. The full AF detection omission and commission statistics of this final dataset are not, however, yet available – since there is little independent data to gauge what proportion of the final AF detection set are in fact correct detections, nor what fires are still missed by the methodology. Such assessments should be based on independent validation data, and that requires large scale ground-based fieldwork, or even higher spatial resolution satellite or airborne datasets collected at the same time as VIIRS. These kind of data at the moment are

lacking, not only for our VIIRS regionally optimised active fire detection algorithm but also the global algorithm of Schroeder et al. (2014). Even the long-standing MODIS active fire product has only had the Terra version (not the Aqua version) properly accuracy assessed in terms of errors of omission and commission, because only Terra-MODIS is collected simultaneously with data from a high resolution imaging instrument (ASTER; mounted on the same platform). Validating active fire detections is very difficult because of such limitations, but this will ideally form part of the future work envisaged for this region and for the VIIRS and MODIS AF datasets that cover it.

Another aspect of future work that needs to be examined are the smoke emission factors of corn, which are lacking at this moment from the results of Section 4.2. Due to the restricted local fire prohibition policies, it was very difficult to conduct *in situ* spreading fire measurements after the first fieldwork in June 2014. Though extra experiments were performed using the crop residues collected in China, different burning conditions (i.e. bonfires rather than spreading fires) led to different emission factors resulting, based on using wheat residue as reference (Section 4.4). For now, published EFs for corn are used in the emission estimation procedures reported here (Section 5.2), further fieldwork to estimate the corn residue burning emissions factors should be conducted. A related issue is that the ability to provide a $PM_{2.5}$ calibration for the DustTrak PM2.5 measurements was limited by the short burning time of the agricultural fires and the low flow of the smoke sampling system (Chapter 4). This limited the amount of $PM_{2.5}$ that could be collected on the calibration filter, leading to a large uncertainty in the deposited $PM_{2.5}$ mass. In the experiments using collected Chinese crop residues as fuel, an extra $PM_{2.5}$ filter batch sampler has been deployed to collect simultaneous $PM_{2.5}$ samples with the Dusttrak at much higher flow rates (10× that of the Dusttrak), and this was designed to fix the problem. However, the burning conditions in these fires appeared rather different to those seen in true *in situ* burning conducted in Eastern China, thus the calibration function generated from this experiments wasn't used in this study. It is recommended that experiments are performed *in situ* in Eastern China in the future to provide a trustable calibration.

The methodologies developed and applied in this study are expected to be highly applicable to other agricultural residue burning areas. For example, intensive burning seasons are seen in India every year (Vadrevu *et al.,* 2013), and the State-wise inventory shows ~ 16% of a total of 620 Tg of residue is burnt on farms (Jain *et al.,* 2014). This is reported to be 40% rice straw, 22% wheat straw and 20% sugarcane leaves and bagasse. These figures are of the same magnitude as those detailed by Venkataraman et al.

(2006), which suggests that annual biomass burning totals could be as high as 138 – 350 Tg in India, with a large contribution from agricultural fires. The impact of such burning is unlikely to be limited to regional air pollution and short-term climate adjustment (due e.g. to black carbon radiative forcing), but may extend to impacts on crop growth and final yield through e.g. tropospheric ozone effects (a 36% reduction could result according to Burney and Ramanathan, 2014). However, current estimates in India are often calculated using crop yield based approach [CYBA] (Jain *et al.*, 2014),whereas the satellite based methodology developed in this PhD should be able to provide higher spatio-temporal information based on direct observations of the fires themselves.

REFERENCES

Akagi, S., Yokelson, R., Wiedinmyer, C., Alvarado, M., Reid, J., Karl, T., Crounse, J. & Wennberg, P. 2011. Emission factors for open and domestic biomass burning for use in atmospheric models. Atmospheric Chemistry and Physics, 11(9), pp 4039-4072.

Andela, N., Kaiser, J.W., Van der Werf, G.R. and Wooster, M.J., 2015. New fire diurnal cycle characterizations to improve fire radiative energy assessments made from MODIS observations. Atmospheric Chemistry and Physics, 15(15), pp.8831-8846.

Andreae, M. O. & Merlet, P. 2001. Emission of trace gases and aerosols from biomass burning. Global biogeochemical cycles, 15(4), pp 955-966.

Arraes, C. L., Camacho-Tamayo, J., Pissarra, T. T., Bueno, C. P. & Campos, S. 2010. Temporal analysis of the reduction in gas emission in areas of mechanically-harvested sugarcane using satellite imagery. Ciencia e Investigación Agraria, 37(1), pp 113-121.

Berglee, R., 2012. World Regional Geography: People, Places and Globalization (No. 2012). The Saylor Foundation.

Bi, Y., Gao, C., Wang, Y. and Li, B., 2009. Estimation of straw resources in China. Transactions of the Chinese Society of Agricultural Engineering, 25(12), pp.211-217.

Bond, T. C., Doherty, S. J., Fahey, D., Forster, P., Berntsen, T., DeAngelo, B., Flanner, M., Ghan, S., Kärcher, B. & Koch, D. 2013. Bounding the role of black carbon in the climate system: A scientific assessment. Journal of Geophysical Research: Atmospheres, 118(11), pp 5380-5552.

Cao, G., Zhang, X. & Zheng, F. 2006. Inventory of black carbon and organic carbon emissions from China. Atmospheric Environment, 40(34), pp 6516-6527.

Cao, G., Zhang, X., Wang, Y. and Zheng, F., 2008. Estimation of emissions from field burning of crop straw in China. Chinese Science Bulletin, 53(5), pp.784-790.

Chameides, W. L., Yu, H., Liu, S. C., Bergin, M., Zhou, X., Mearns, L., Wang, G., Kiang, C. S., Saylor, R. D., Luo, C., Huang, Y., Steiner, A. & Giorgi, F. 1999. Case study of the effects of atmospheric aerosols and regional haze on agriculture: An opportunity to enhance crop yields in China through emission controls? Proceedings of the National Academy of Sciences, 96(24), pp 13626-13633.

Chan, C. K. & Yao, X. 2008. Air pollution in mega cities in China. Atmospheric Environment, 42(1), pp 1-42.

Chandler, C., Cheney, P., Thomas, P., Trabaud, L. & Williams, D. 1983. Fire in forestry. Volume 1. Forest fire behavior and effects. Volume 2. Forest fire management and organization: John Wiley & Sons, Inc.

Chen, S.J., Hovde, D.C., Peterson, K.A. and Marshall, A.W., 2007. Fire detection using smoke and gas sensors. Fire Safety Journal, 42(8), pp.507-515.

Chen, J., Chen, J., Liao, A., Cao, X., Chen, L., Chen, X., He, C., Han, G., Peng, S., Lu, M. and Zhang, W., 2015. Global land cover mapping at 30m resolution: A POK-based operational approach. ISPRS Journal of Photogrammetry and Remote Sensing, 103, pp.7-27.

Chen, J., Li, C., Ristovski, Z., Milic, A., Gu, Y., Islam, M.S., Wang, S., Hao, J., Zhang, H., He, C. and Guo, H., 2016. A review of biomass burning: Emissions and impacts on air quality, health and climate in China. Science of the Total Environment.

Cheng, Y., Engling, G., He, K. B., Duan, F. K., Ma, Y. L., Du, Z. Y., Liu, J. M., Zheng, M. & Weber, R. J. 2013. Biomass burning contribution to Beijing aerosol. Atmos. Chem. Phys., 13(15), pp 7765-7781.

Cheng, Z., Wang, S., Fu, X., Watson, J. G., Jiang, J., Fu, Q., Chen, C., Xu, B., Yu, J., Chow, J. C. & Hao, J. 2014. Impact of biomass burning on haze pollution in the Yangtze River delta, China: a case study in summer 2011. Atmos. Chem. Phys., 14(9), pp 4573-4585.

Cofer, W. R., Winstead, E. L., Stocks, B. J., Goldammer, J. G. & Cahoon, D. R. 1998. Crown fire emissions of CO2, CO, H2, CH4, and TNMHC from a dense Jack pine boreal forest fire. Geophysical Research Letters, 25(21), pp 3919-3922.

da Rocha, G. O., Allen, A. G. & Cardoso, A. A. 2005. Influence of agricultural biomass burning on aerosol size distribution and dry deposition in Southeastern Brazil. Environmental science & technology, 39(14), pp 5293-5301.

de Zarate, I.O., Ezzacurra, A., Lacaux, J.P., Dinh, P.V., 2000. Emission factor estimates of cereal waste burning in Spain. Atmospheric Environment 34, 3183–3193

Delmas, R., Lacaux, J.P. and Brocard, D., 1995. Determination of biomass burning emission factors: Methods and results. Environmental Monitoring and Assessment, 38(2-3), pp.181-204.

Desyaterik, Y., Sun, Y., Shen, X., Lee, T., Wang, X., Wang, T. & Collett, J. L. 2013. Speciation of "brown" carbon in cloud water impacted by agricultural biomass burning in Eastern China. Journal of Geophysical Research: Atmospheres, 118(13), pp 7389-7399.

Ding, A. J., Fu, C. B., Yang, X. Q., Sun, J. N., Petäjä, T., Kerminen, V. M., Wang, T., Xie, Y., Herrmann, E., Zheng, L. F., Nie, W., Liu, Q., Wei, X. L. & Kulmala, M. 2013. Intense atmospheric pollution modifies weather: a case of mixed biomass burning with fossil fuel combustion pollution in Eastern China. Atmos. Chem. Phys., 13(20), pp 10545-10554.

Du, H., Kong, L., Cheng, T., Chen, J., Du, J., Li, L., Xia, X., Leng, C. & Huang, G. 2011. Insights into summertime haze pollution events over Shanghai based on online water-soluble ionic composition of aerosols. Atmospheric Environment, 45(29), pp 5131-5137.

Duan, F., Liu, X., Yu, T. & Cachier, H. 2004. Identification and estimate of biomass burning contribution to the urban aerosol organic carbon concentrations in Beijing. Atmospheric Environment, 38(9), pp 1275-1282.

Dusek, U., Frank, G., Hildebrandt, L., Curtius, J., Schneider, J., Walter, S., Chand, D., Drewnick, F., Hings, S. & Jung, D. 2006. Size matters more than chemistry for cloud-nucleating ability of aerosol particles. Science, 312(5778), pp 1375-1378.

Ellicott, E., Vermote, E., Giglio, L. & Roberts, G. 2009. Estimating biomass consumed from fire using MODIS FRE. GEOPHYSICAL RESEARCH LETTERS, 36(L13401.

Freeborn, P. H., Wooster, M. J., Hao, W. M., Ryan, C. A., Nordgren, B. L., Baker, S. P. & Ichoku, C. 2008. Relationships between energy release, fuel mass loss, and trace gas and aerosol emissions during laboratory biomass fires. Journal of Geophysical Research: Atmospheres, 113(D1), pp D01301.

Freeborn, P.H., Wooster, M.J., Roberts, G., Malamud, B.D. and Xu, W., 2009. Development of a virtual active fire product for Africa through a synthesis of geostationary and polar orbiting satellite data. Remote Sensing of Environment, 113(8), pp.1700-1711.

Freeborn, P. H., Wooster, M. J. & Roberts, G. 2011. Addressing the spatiotemporal sampling design of MODIS to provide estimates of the fire radiative energy emitted from Africa. Remote Sensing of Environment, 115(2), pp 475-489.

Fu, J. Y., Jiang, D., Huang, Y. H., 2014a. 1-km grid population dataset of China, Global Change Research Data Publishing & Repository, DOI:10.3974/geodb.2014.01.06.V1

Fu, J. Y., Jiang, D., Huang, Y. H., 2014b. 1-km grid GDP dataset of China, Global Change Research Data Publishing & Repository, DOI:10.3974/geodb.2014.01.07.V1

Fuller, D.O., 2000. Satellite remote sensing of biomass burning with optical and thermal sensors. Progress in Physical Geography, 24(4), pp.543-561.

Gao, X., Ma, W., Ma, C., Zhang, F., Wang, Y., 2002. Analysis of the current status of utilization of crop straw in China. Journal of Huazhong Agricultural University 21, 242–247 (in Chinese).

Giglio, L., Descloitres, J., Justice, C. O. & Kaufman, Y. J. 2003. An enhanced contextual fire detection algorithm for MODIS. Remote sensing of environment, 87(2), pp 273-282.

Giglio, L., Csiszar, I. & Justice, C. 2006. Global distribution and seasonality of active fires as observed with the Terra and Aqua Moderate Resolution Imaging Spectroradiometer (MODIS) sensors. J. Geophys. Res, 111(G02016.

Giglio, L., Loboda, T., Roy, D. P., Quayle, B. & Justice, C. O. 2009. An active-fire based burned area mapping algorithm for the MODIS sensor. Remote Sensing of Environment, 113(2), pp 408-420.

Giglio, L., Randerson, J. T., van der Werf, G. R., Kasibhatla, P. S., Collatz, G. J., Morton, D. C. & DeFries, R. S. 2010. Assessing variability and long-term trends in burned area by merging multiple satellite fire products. Biogeosciences, 7(3), pp 1171-1186.

Giglio, L., Randerson, J.T. and Werf, G.R., 2013. Analysis of daily, monthly, and annual burned area using the fourth‐generation global fire emissions database (GFED4). Journal of Geophysical Research: Biogeosciences, 118(1), pp.317-328.

Giglio, L., Csiszar, I. & Justice, C. 2006. Global distribution and seasonality of active fires as observed with the Terra and Aqua Moderate Resolution Imaging Spectroradiometer (MODIS) sensors. J. Geophys. Res, 111(G02016.

Hagler, G. S., Yelverton, T. L., Vedantham, R., Hansen, A. D. & Turner, J. R. 2011. Post-processing method to reduce noise while preserving high time resolution in aethalometer real-time black carbon data. Aerosol and Air Quality Resarch, 11(5), pp 539-546.

Hays, M. D., Fine, P. M., Geron, C. D., Kleeman, M. J. & Gullett, B. K. 2005. Open burning of agricultural biomass: Physical and chemical properties of particle-phase emissions. Atmospheric Environment, 39(36), pp 6747-6764.

He, M., Zheng, J., Yin, S. & Zhang, Y. 2011. Trends, temporal and spatial characteristics, and uncertainties in biomass burning emissions in the Pearl River Delta, China. Atmospheric Environment, 45(24), pp 4051-4059.

Hosseini, S., Urbanski, S.P., Dixit, P., Qi, L., Burling, I.R., Yokelson, R.J., Johnson, T.J., Shrivastava, M., Jung, H.S., Weise, D.R. and Miller, J.W., 2013. Laboratory characterization of PM emissions from combustion of wildland biomass fuels. Journal of Geophysical Research: Atmospheres, 118(17), pp.9914-9929.

Huang, C., Kalluri, S.N., Townshend, J.R. and Yang, K., 1998, July. Assessing and deconvolving the impacts of the point spread function on satellite remote sensing. In Geoscience and Remote Sensing Symposium Proceedings, 1998. IGARSS'98. 1998 IEEE International (Vol. 4, pp. 2035-2037). IEEE.

Huang, C., Townshend, J.R., Liang, S., Kalluri, S.N. and DeFries, R.S., 2002. Impact of sensor's point spread function on land cover characterization: assessment and deconvolution. Remote Sensing of Environment, 80(2), pp.203-212.

Huang, X., Li, M., Friedli, H. R., Song, Y., Chang, D. & Zhu, L. 2011. Mercury Emissions from Biomass Burning in China. Environmental Science & Technology, 45(21), pp 9442-9448.

Huang, X., Li, M., Li, J. & Song, Y. 2012. A high-resolution emission inventory of crop burning in fields in China based on MODIS Thermal Anomalies/Fire products. Atmospheric Environment, 50(0), pp 9-15.

Ichoku, C. & Kaufman, Y. J. 2005. A method to derive smoke emission rates from MODIS fire radiative energy measurements. Geoscience and Remote Sensing, IEEE Transactions on, 43(11), pp 2636-2649.

Ichoku, C., Giglio, L., Wooster, M. J. & Remer, L. A. 2008. Global characterization of biomass-burning patterns using satellite measurements of fire radiative energy. Remote Sensing of Environment, 112(6), pp 2950-2962.

Jenkins, B. M., Jones, A. D., Turn, S. Q. & Williams, R. B. 1996. Emission factors for polycyclic aromatic hydrocarbons from biomass burning. Environmental Science & Technology, 30(8), pp 2462-2469.

Jiang, D., Zhuang, D., Fu, J., Huang, Y. & Wen, K. 2012. Bioenergy potential from crop residues in China: Availability and distribution. Renewable and Sustainable Energy Reviews, 16(3), pp 1377-1382.

Kaiser, J. W., Heil, A., Andreae, M. O., Benedetti, A., Chubarova, N., Jones, L., Morcrette, J. J., Razinger, M., Schultz, M. G., Suttie, M. & van der Werf, G. R. 2012. Biomass burning emissions estimated with a global fire assimilation system based on observed fire radiative power. Biogeosciences, 9(1), pp 527-554.

Khalil, M. & Rasmussen, R. 2003. Tracers of wood smoke. Atmospheric Environment, 37(9), pp 1211-1222.

Koppmann, R., von Czapiewski, K. & Reid, J. S. 2005. A review of biomass burning emissions, part I: gaseous emissions of carbon monoxide, methane, volatile organic compounds, and nitrogen containing compounds. Atmos. Chem. Phys. Discuss., 5(5), pp 10455-10516.

Korontzi, S., McCarty, J., Loboda, T., Kumar, S. & Justice, C. 2006. Global distribution of agricultural fires in croplands from 3 years of Moderate Resolution Imaging Spectroradiometer (MODIS) data. Global Biogeochemical Cycles, 20(2), pp GB2021.

Kurihara, Y., Murakami, H. and Kachi, M., 2016. Sea surface temperature from the new Japanese geostationary meteorological Himawari‐8 satellite. Geophysical Research Letters, 43(3), pp.1234-1240.

Li, J.F. and Hu, Y.S., 2009. Analysis on investment and operation of straw-fired power plants in Jiangsu province. Electric power technologic economics, 5, p.005 (in Chinese).

Li, Z., Nadon, S., Cihlar, J. and Stocks, B., 2000. Satellite-based mapping of Canadian boreal forest fires: evaluation and comparison of algorithms. International Journal of Remote Sensing, 21(16), pp.3071-3082.

Li, X., Wang, S., Duan, L., Hao, J., Li, C., Chen, Y. & Yang, L. 2007. Particulate and Trace Gas Emissions from Open Burning of Wheat Straw and Corn Stover in China. Environmental Science & Technology, 41(17), pp 6052-6058.

Li, X., Wang, S., Duan, L., Hao, J. & Nie, Y. 2009. Carbonaceous Aerosol Emissions from Household Biofuel Combustion in China. Environmental Science & Technology, 43(15), pp 6076-6081.

Li, W., Shao, L. & Buseck, P. 2010. Haze types in Beijing and the influence of agricultural biomass burning. Atmospheric Chemistry and Physics, 10(17), pp 8119-8130.

Li, M., Zhang, Q., Kurokawa, J., Woo, J.H., He, K.B., Lu, Z., Ohara, T., Song, Y., Streets, D.G., Carmichael, G.R. and Cheng, Y.F., 2015. MIX: a mosaic Asian anthropogenic emission inventory for the MICS-Asia and the HTAP projects. Atmos. Chem. Phys. Discuss, 15(23), pp.34-813.

Li, J., Li, Y., Bo, Y. and Xie, S., 2016. High-resolution historical emission inventories of crop residue burning in fields in China for the period 1990–2013. Atmospheric Environment, 138, pp.152-161.

Lin, G., Wolfe, R.E. and Nishihama, M., 2011. NPP VIIRS geometric performance status.

Liu, H., Jiang, G. M., Zhuang, H. Y. & Wang, K. J. 2008. Distribution, utilization structure and potential of biomass resources in rural China: With special references of crop residues. Renewable and Sustainable Energy Reviews, 12(5), pp 1402-1418.

Mellouki, A., Wallington, T.J. and Chen, J., 2015. Atmospheric chemistry of oxygenated volatile organic compounds: Impacts on air quality and climate. Chemical reviews, 115(10), pp.3984-4014.

Mieville, A., Granier, C., Liousse, C., Guillaume, B., Mouillot, F., Lamarque, J.F., Grégoire, J.M. and Pétron, G., 2010. Emissions of gases and particles from biomass burning during the 20th century using satellite data and an historical reconstruction. Atmospheric Environment, 44(11), pp.1469-1477.

Nakajima, T., Yoon, S.C., Ramanathan, V., Shi, G.Y., Takemura, T., Higurashi, A., Takamura, T., Aoki, K., Sohn, B.J., Kim, S.W. and Tsuruta, H., 2007. Overview of the Atmospheric Brown Cloud East Asian Regional Experiment 2005 and a study of the aerosol direct radiative forcing in east Asia. Journal of Geophysical Research: Atmospheres, 112(D24).

NBSC (National Bureau of Statistic of China) China Statistical Yearbook, 480 2003–2015, China Statistics Press, Beijing (2004–2016) (in Chinese).

Pachauri, R.K., Allen, M.R., Barros, V.R., Broome, J., Cramer, W., Christ, R., Church, J.A., Clarke, L., Dahe, Q., Dasgupta, P. and Dubash, N.K., 2014. Climate change 2014: synthesis report. Contribution of Working Groups I, II and III to the fifth assessment report of the Intergovernmental Panel on Climate Change (p. 151). IPCC.

Pan, X. L., Kanaya, Y., Wang, Z. F., Komazaki, Y., Taketani, F., Akimoto, H. & Pochanart, P. 2013. Variations of carbonaceous aerosols from open crop residue burning with transport and its implication to estimate their lifetimes. Atmospheric Environment, 74(0), pp 301-310.

Portmann, F. T., Siebert, S. & Döll, P. 2010. MIRCA2000—Global monthly irrigated and rainfed crop areas around the year 2000: A new high-resolution data set for agricultural and hydrological modeling. Global Biogeochemical Cycles, 24(1), pp n/a-n/a.

Preble, C. V., Hadley, O. L., Gadgil, A. J. & Kirchstetter, T. W. 2014. Emissions and Climate-Relevant Optical Properties of Pollutants Emitted from a Three-Stone Fire and the Berkeley-Darfur Stove Tested under Laboratory Conditions. Environmental science & technology.

Qin, Y. & Xie, S. D. 2011. Historical estimation of carbonaceous aerosol emissions from biomass open burning in China for the period 1990–2005. Environmental Pollution, 159(12), pp 3316-3323.

Randerson, J., Chen, Y., Werf, G., Rogers, B. & Morton, D. 2012. Global burned area and biomass burning emissions from small fires. Journal of Geophysical Research: Biogeosciences (2005–2012), 117(G4), pp.

Reid, J., Koppmann, R., Eck, T. & Eleuterio, D. 2005. A review of biomass burning emissions part II: intensive physical properties of biomass burning particles. Atmospheric Chemistry and Physics, 5(3), pp 799-825.

Roberts, G., Wooster, M. J., Perry, G. L. W., Drake, N., Rebelo, L. M. & Dipotso, F. 2005. Retrieval of biomass combustion rates and totals from fire radiative power observations: Application to southern Africa using geostationary SEVIRI imagery. Journal of Geophysical Research: Atmospheres, 110(D21), pp D21111.

Roberts, G., Wooster, M. J. & Lagoudakis, E. 2009. Annual and diurnal african biomass burning temporal dynamics. Biogeosciences, 6(5), pp 849-866.

Roberts, T. J., Braban, C. F., Oppenheimer, C., Martin, R. S., Freshwater, R. A., Dawson, D. H., Griffiths, P. T., Cox, R. A., Saffell, J. R. & Jones, R. L. 2012. Electrochemical sensing of volcanic gases. Chemical Geology, 332(74-91.

Roberts, T.J., Saffell, J.R., Oppenheimer, C. and Lurton, T., 2014. Electrochemical sensors applied to pollution monitoring: Measurement error and gas ratio bias—A volcano plume case study. Journal of Volcanology and Geothermal Research, 281, pp.85-96.

Roberts, G., Wooster, M.J., Xu, W., Freeborn, P.H., Morcrette, J.J., Jones, L., Benedetti, A., Jiangping, H., Fisher, D. and Kaiser, J.W., 2015. LSA SAF Meteosat FRP products–Part 2: Evaluation and demonstration for use in the Copernicus Atmosphere Monitoring Service (CAMS). Atmos. Chem. Phys, 15, pp.13241-13267.

Roy, D., Lewis, P. & Justice, C. 2002. Burned area mapping using multi-temporal moderate spatial resolution data—A bi-directional reflectance model-based expectation approach. Remote Sensing of Environment, 83(1), pp 263-286.

Roy, D. P., Frost, P. G. H., Justice, C. O., Landmann, T., Le Roux, J. L., Gumbo, K., Makungwa, S., Dunham, K., Du Toit, R., Mhwandagara, K., Zacarias, A., Tacheba, B., Dube, O. P., Pereira, J. M. C., Mushove, P., Morisette, J. T., Santhana Vannan, S. K. & Davies, D. 2005. The Southern Africa Fire Network (SAFNet) regional burned - area product - validation protocol. International Journal of Remote Sensing, 26(19), pp 4265-4292.

Roy, D. P., Boschetti, L., Justice, C. O. & Ju, J. 2008. The collection 5 MODIS burned area product—Global evaluation by comparison with the MODIS active fire product. Remote Sensing of Environment, 112(9), pp 3690-3707.

Heinemann, E., Prato, B. and Shepherd, A., 2011. Rural Poverty Report 2011. International Fund for Agricultural Development (IFAD), Rome.

Saikawa, E., Naik, V., Horowitz, L.W., Liu, J. and Mauzerall, D.L., 2009. Present and potential future contributions of sulfate, black and organic carbon aerosols from China to global air quality, premature mortality and radiative forcing. Atmospheric Environment, 43(17), pp.2814-2822.

Schroeder, W., Oliva, P., Giglio, L. & Csiszar, I. A. 2014. The New VIIRS 375 m active fire detection data product: Algorithm description and initial assessment. Remote Sensing of Environment, 143(0), pp 85-96.

Seinfeld, J. H. & Pandis, S. N. 2012. Atmospheric chemistry and physics: from air pollution to climate change: John Wiley & Sons.

Smith, P., Martino, D., Cai, Z., Gwary, D., Janzen, H., Kumar, P., McCarl, B., Ogle, S., O'Mara, F., Rice, C., Scholes, B., Sirotenko, O., Howden, M., McAllister, T., Pan, G., Romanenkov, V., Schneider, U. & Towprayoon, S. 2007. Policy and technological constraints to implementation of greenhouse gas mitigation options in agriculture. Agriculture, Ecosystems & Environment, 118(1–4), pp 6-28.

Smith, P., Martino, D., Cai, Z., Gwary, D., Janzen, H., Kumar, P., McCarl, B., Ogle, S., O'Mara, F. & Rice, C. 2008. Greenhouse gas mitigation in agriculture. Philosophical Transactions of the Royal Society B: Biological Sciences, 363(1492), pp 789-813.

Streets, D.G., Yarber, K.F., Woo, J.H. and Carmichael, G.R., 2003. Biomass burning in Asia: Annual and seasonal estimates and atmospheric emissions. Global Biogeochemical Cycles, 17(4).

Stroppiana, D., Bordogna, G., Carrara, P., Boschetti, M., Boschetti, L. and Brivio, P.A., 2012. A method for extracting burned areas from Landsat TM/ETM+ images by soft aggregation of multiple Spectral Indices and a region growing algorithm. ISPRS Journal of Photogrammetry and Remote Sensing, 69, pp.88-102.

Sun, J., Peng, H., Chen, J., Wang, X., Wei, M., Li, W., Yang, L., Zhang, Q., Wang, W. & Mellouki, A. 2016. An estimation of CO2 emission via agricultural crop residue open field burning in China from 1996 to 2013. Journal of Cleaner Production, 112, Part 4(2625-2631.

Townshend, J., Huang, C., Kalluri, S., Defries, R., Liang, S. & Yang, K. 2000. Beware of per-pixel characterization of land cover. International Journal of remote sensing, 21(4), pp 839-843.

Turn, S., Jenkins, B., Chow, J., Pritchett, L., Campbell, D., Cahill, T. & Whalen, S. 1997. Elemental characterization of particulate matter emitted from biomass burning: Wind tunnel derived source profiles for herbaceous and wood fuels. Journal of Geophysical Research: Atmospheres (1984–2012), 102(D3), pp 3683-3699.

van der Werf, G. R., Randerson, J. T., Giglio, L., Collatz, G. J., Mu, M., Kasibhatla, P. S., Morton, D. C., DeFries, R. S., Jin, Y. & van Leeuwen, T. T. 2010. Global fire emissions and the contribution of deforestation, savanna, forest, agricultural, and peat fires (1997–2009). Atmos. Chem. Phys., 10(23), pp 11707-11735.

van der Werf, G. R., Randerson, J. T., Giglio, L., van Leeuwen, T. T., Chen, Y., Rogers, B. M., Mu, M., van Marle, M. J. E., Morton, D. C., Collatz, G. J., Yokelson, R. J., and Kasibhatla, P. S.: Global fire emissions estimates during 1997–2016, Earth Syst. Sci. Data, 9, 697-720, https://doi.org/10.5194/essd-9-697-2017, 2017.

van Wilgen, B. W. and Scholes, R. J.: The vegetation and fire regimes of southern hemisphere Africa, in: Fire in Southern African Savannas: Ecological and Atmospheric Perspectives, edited by: van Wilgen, B. W., Andreae, M. O., Goldammer, J. G., Lindesay, J., *et al.*, 27–46, Witswatersrand Univ. Press, Johannesburg, South Africa, 1997.

Wang & Zhang, 2016, http://news.chengdu.cn/2016/1106/1829718.shtml,Chengdu Business Daily

Wang, S. & Zhang, C. 2008. Spatial and temporal distribution of air pollutant emissions from open burning of crop residues in China. Sciencepaper online, 3(5), pp 329-333.

Wang, X., Yang, L., Steinberger, Y., Liu, Z., Liao, S. & Xie, G. 2013. Field crop residue estimate and availability for biofuel production in China. Renewable and Sustainable Energy Reviews, 27(0), pp 864-875.

Ward, D. E. & Radke, L. F. 1993. Emissions measurements from vegetation fires: A comparative evaluation of methods and results. Fire in the Environment: The Ecological, Atmospheric and Climatic Importance of Vegetation Fires, 13(53-76.

Wolfe, R.E., Lin, G., Nishihama, M., Tewari, K.P., Tilton, J.C. and Isaacman, A.R., 2013. Suomi NPP VIIRS prelaunch and on‐orbit geometric calibration and characterization. Journal of Geophysical Research: Atmospheres, 118(20).

Wooster, M. J., Zhukov, B. & Oertel, D. 2003. Fire radiative energy for quantitative study of biomass burning: derivation from the BIRD experimental satellite and comparison to MODIS fire products. Remote Sensing of Environment, 86(1), pp 83-107.

Wooster, M. J., Roberts, G., Perry, G. L. W. & Kaufman, Y. J. 2005. Retrieval of biomass combustion rates and totals from fire radiative power observations: FRP derivation and calibration relationships between biomass consumption and fire radiative energy release. Journal of Geophysical Research: Atmospheres, 110(D24), pp D24311.

Wooster, M. J., Freeborn, P. H., Archibald, S., Oppenheimer, C., Roberts, G. J., Smith, T. E. L., Govender, N., Burton, M. & Palumbo, I. 2011. Field determination of biomass burning emission ratios and factors via open-path FTIR spectroscopy and fire radiative power assessment: headfire, backfire and residual smouldering combustion in African savannahs. Atmos. Chem. Phys., 11(22), pp 11591-11615.

Wooster, M.J., Roberts, G., Smith, A.M., Johnston, J., Freeborn, P., Amici, S. and Hudak, A.T., 2013. Thermal remote sensing of active vegetation fires and biomass burning events. In Thermal Infrared Remote Sensing (pp. 347-390). Springer Netherlands.

Wooster, M. J., Roberts, G., Freeborn, P. H., Xu, W., Govaerts, Y., Beeby, R., He, J., Lattanzio, A., Fisher, D. & Mullen, R. 2015. LSA SAF Meteosat FRP products – Part 1: Algorithms, product contents, and analysis. Atmos. Chem. Phys., 15(22), pp 13217-13239.

Xu, W., Wooster, M.J., Kaneko, T., He, J., Zhang, T. and Fisher, D., 2017. Major advances in geostationary fire radiative power (FRP) retrieval over Asia and Australia stemming from use of Himarawi-8 AHI. Remote Sensing of Environment, 193, pp.138-149.

Xue, Y., Xu, H., Guang, J., Mei, L., Guo, J., Li, C., Mikusauskas, R. & He, X. 2014. Observation of an agricultural biomass burning in central and east China using merged aerosol optical depth data from multiple satellite missions. International Journal of Remote Sensing, 1-13.

Yamaji, K., Li, J., Uno, I., Kanaya, Y., Irie, H., Takigawa, M., Komazaki, Y., Pochanart, P., Liu, Y., Tanimoto, H., Ohara, T., Yan, X., Wang, Z. & Akimoto, H. 2010. Impact of open crop residual burning on air quality over Central Eastern China during the Mount Tai Experiment 2006 (MTX2006). Atmos. Chem. Phys., 10(15), pp 7353-7368.

Yan, X., Ohara, T. & Akimoto, H. 2006. Bottom-up estimate of biomass burning in mainland China. Atmospheric Environment, 40(27), pp 5262-5273.

Yang, S., He, H., Lu, S., Chen, D. & Zhu, J. 2008. Quantification of crop residue burning in the field and its influence on ambient air quality in Suqian, China. Atmospheric Environment, 42(9), pp 1961-1969.

Yokelson, R. J., Goode, J. G., Ward, D. E., Susott, R. A., Babbitt, R. E., Wade, D. D., Bertschi, I., Griffith, D. W. T. & Hao, W. M. 1999. Emissions of formaldehyde, acetic acid, methanol, and other trace gases from biomass fires in North Carolina measured by airborne Fourier transform infrared spectroscopy. Journal of Geophysical Research: Atmospheres (1984–2012), 104(D23), pp 30109-30125.

Yokelson, R. J., Burling, I. R., Gilman, J. B., Warneke, C., Stockwell, C. E., de Gouw, J., Akagi, S. K., Urbanski, S. P., Veres, P., Roberts, J. M., Kuster, W. C., Reardon, J., Griffith, D. W. T., Johnson, T. J., Hosseini, S., Miller, J. W., Cocker Iii, D. R., Jung, H. & Weise, D. R. 2013. Coupling field and laboratory measurements to estimate the emission factors of identified and unidentified trace gases for prescribed fires. Atmos. Chem. Phys., 13(1), pp 89-116.

Yusiharni, E. & Gilkes, R. 2012. Minerals in the ash of Australian native plants. Geoderma, 189–190(0), pp 369-380.

Za, 2015, http://www.chinanews.com/sh/2015/11-04/7606112.shtml, Legislative Evening Newspaper

Zhang, H., Ye, X., Cheng, T., Chen, J., Yang, X., Wang, L. & Zhang, R. 2008. A laboratory study of agricultural crop residue combustion in China: Emission factors and emission inventory. Atmospheric Environment, 42(36), pp 8432-8441.

Zhang, H., Hu, D., Chen, J., Ye, X., Wang, S. X., Hao, J. M., Wang, L., Zhang, R. & An, Z. 2011. Particle size distribution and polycyclic aromatic hydrocarbons emissions from agricultural crop residue burning. Environmental science & technology, 45(13), pp 5477-5482.

Zhang, T. R., Shi, J. H., Gao, H. W., Zhang, J. & Yao, X. H. 2013. Impact of source and atmospheric processing on Fe solubility in aerosols over the Yellow Sea, China. Atmospheric Environment, 75(0), pp 249-256.

Zhang, L., Liu, Y. and Hao, L., 2016. Contributions of open crop straw burning emissions to PM2. 5 concentrations in China. Environmental Research Letters, 11(1), p.014014.

Zhang, H., Hu, J., Qi, Y., Li, C., Chen, J., Wang, X., He, J., Wang, S., Hao, J., Zhang, L., Zhang, L., Zhang, Y., Li, R., Wang, S. & Chai, F. 2017. Emission characterization, environmental impact, and control measure of PM2.5 emitted from agricultural crop residue burning in China. Journal of Cleaner Production, 149(629-635.

Zhao, J., Zhang, G. & Yang, D. 2011. Estimation of Carbon Emission from Burning of Grain Crop Residues in China. Journal of Agro-Environment Science, 30(4), pp 812-816.

Zhao, Y., Nielsen, C.P. and McElroy, M.B., 2012. China's CO 2 emissions estimated from the bottom up: recent trends, spatial distributions, and quantification of uncertainties. Atmospheric environment, 59, pp.214-223.

Zhao, H., Tong, D. Q., Gao, C. & Wang, G. 2015. Effect of dramatic land use change on gaseous pollutant emissions from biomass burning in NorthEastern China. Atmospheric Research, 153(429-436).

Zuo 2015, http://www.chinanews.com/gn/2015/12-11/7666514.shtml, Anhui News

Appendix A

This section includes a published paper, which the thesis author was a co-author, describing the active fire detection and FRP algorithm using Himawari-8, a Japanese geostationary meteorological satellite. The output of this paper has been used to generate diurnal cycle in this study (Chapter 5).

Remote Sensing of Environment 193 (2017) 138–149

Contents lists available at ScienceDirect

Remote Sensing of Environment

journal homepage: www.elsevier.com/locate/rse

Major advances in geostationary fire radiative power (FRP) retrieval over Asia and Australia stemming from use of Himarawi-8 AHI

Weidong Xu [a,b], Martin J. Wooster [a,b,*], Takayuki Kaneko [c], Jiangping He [a], Tianran Zhang [a,b], Daniel Fisher [a,b]

[a] King's College London, Department of Geography, Strand, London WC2R 2LS, UK
[b] NERC National Centre for Earth Observation (NCEO), UK
[c] Earthquake Research Institute, University of Tokyo, 1-1-1 Yayoi, Bunkyo-ku, Tokyo 113-0032, Japan

ARTICLE INFO

Article history:
Received 30 May 2016
Received in revised form 20 February 2017
Accepted 28 February 2017
Available online 9 March 2017

Keywords:
Biomass burning
Fire radiative power
Himawari-8
Geostationary

ABSTRACT

Characterising the highly variable temporal dynamics of landscape-scale fire activity is best achieved using geostationary satellites, and the Himawari-8 Advanced Himawari Imager (AHI) now provides views of Asian and Australian fires at an unprecedented 10 min temporal resolution and 2 km nadir thermal channel spatial resolution. We here develop the first processing system to identify active fires and retrieve their fire radiative power (FRP) from AHI data, based on the geostationary Fire Thermal Anomaly (FTA) algorithm and FRP retrieval method originally developed for use with Meteosat SEVIRI over Africa and Europe. This scheme detects active fires covering as little as 10^{-3} to 10^{-4} of an AHI pixel, and we compare performance to the same scheme applied to data from the forerunner geostationary MTSAT imager and the FengYun-2 (FY-2) Stretched Visible and Infrared Spin Scan Radiometer (S-VISSR), and also to 1 km (at nadir) polar-orbiting MODIS active fire data. We find major benefits of Himawari-8 AHI over both MTSAT and FY-2, being able to detect a substantially greater proportion of fire activity and with little impact from sensor saturation. AHI-derived FRP retrievals of detected fires show a very strong agreement and a low (3 MW) bias with respect to near-simultaneous MODIS retrievals, though fires having FRP ≤ 40 MW are undercounted by AHI due to its 4× larger pixel area (at nadir) than MODIS. Large parts of Asia are characterised by smaller/lower FRP fires associated with e.g. agricultural residue burning, meaning many are at or below this AHI minimum FRP detection limit, and during June 2015 AHI fails to detect around 66% of the hotspots that MODIS detects when both sensors view the same area simultaneously. However, AHI provides 144 observation opportunities per day compared to 4 typical observations from MODIS, and shows a low (8%) active fire detection error of commission. We demonstrate the unique value of the geostationary FRP retrievals made from AHI data for full fire diurnal cycle assessment and for Fire Radiative Energy (FRE) calculations. We conclude that these FRP data demonstrate major benefits for studies of active fires over Asia and Australia, and expect them to become an important component of the global geostationary active fire observation system.

1. Introduction

Landscape fires are frequent across much of Asia and Australia, and EO satellites are vital to assessing their terrestrial and atmospheric impacts in this globally important biomass burning region (e.g. Williams et al., 1998; Wooster et al., 2012; Li et al., 2016). Many fires in Asia are associated with agricultural residue burning and/or tropical forest degradation and deforestation, and are often individually small and so quite difficult to detect via moderate spatial resolution burned area mapping approaches. Active fire products offer improved sensitivity to such 'small' fires (Roy et al., 2008), though the typically short-lived nature of agriculgtural residue burning fires still poses a challenge, and such observations can be accompanied by retrievals of a fires radiative power (FRP) output that relates directly to its fuel consumption and smoke emission (e.g. Wooster et al., 2005). Here we develop for the first time a new very high temporal resolution capability for active fire detection and FRP characterisation over Asia and Australia, using the first of a new generation of geostationary Earth imaging satellites - Himawari-8 (Bessho et al., 2016; Kurihara et al., 2016; JMA, 2014), which will be followed by the Geostationary Operational Environmental Satellite-R Series (GOES-R) over the America's and by Meteosat Third Generation (MTG) over Africa and Europe. We demonstrate the significant advantages of this new technology for active fire characterisation and FRP assessment, evaluating performances against near-simultaneously acquired MODIS active fire data available a few times per day over the same regions.

Geostationary active fire detection has previously been provided over Asia and Australia using the Japanese Multifunctional Transport

* Corresponding author at: King's College London, Department of Geography, Strand, London WC2R 2LS, UK.
E-mail address: martin.wooster@kcl.ac.uk (M.J. Wooster).

http://dx.doi.org/10.1016/j.rse.2017.02.024

Satellite (MTSAT) imager and the Korean Communication, Ocean and Meteorological Satellite (COMS) (Zhang et al., 2012), though FRP assessment has typically not been available. Himawari-8 offers potential for much improved performance due to its enhanced sensor characteristics, and we use an adaptation of the geostationary Fire Thermal Anomaly (FTA) algorithm of Wooster et al. (2015) to provide this capability, applying the same FTA algorithm to data from MTSAT and the Chinese FengYun-2 (FY-2) geostationary satellite for comparison. We compare results from each system to those from MODIS, and briefly explore the landscape fire characteristics of a variety of key biomes in Asia and Australia using these new active fire data, pointing the way to what the forthcoming GOES-R system in particular should deliver over the Americas from 2017.

2. Asian and Australian fire activities and the potential of geostationary data

Fires in Asia and Australia appear responsible for around a quarter to a third of annual global burned area (Giglio et al., 2006; Van der Werf et al., 2010), resulting from e.g. annual savannah and forest fires in Australia (Stephenson et al., 2013), the burning of agricultural residues across much of Asia (e.g. Zhang et al., 2012; Zhang et al., 2015 and Li et al., 2016), and fires in drained peatlands and often already degraded forests in SE Asia that show particular activity peaks during El Niño-related droughts (Van der Werf et al., 2004; Van der Werf et al., 2010; Huijnen et al., 2016). This fire activity affects landcover and terrestrial ecosystem functioning, contributes significantly to modification of the regional atmosphere, and can impact concentrations of atmospheric greenhouse gases in globally significant ways (Bowman, 2000; Johnston et al., 2011; Reid et al., 2013; Huijnen et al., 2016).

Landscape fires are highly dynamic, often changing their nature in a matter of minutes and typically showing very strong diurnal cycles (Giglio, 2007; Roberts et al., 2009a). Such details can only be directly revealed from geostationary satellites, which provide multiple observations every hour that enable identification of even short-lived fires provided they are not too small to be detected, full fire radiative energy (FRE) characterisation over the diurnal cycle, and better recognition of fires burning in cloudy areas since cloud gaps can be fully exploited (e.g. Roberts et al., 2005; Roberts and Wooster, 2008). Using Meteosat data of Africa and Europe, the value of geostationary FRP information for fire emissions and smoke plume transport modelling has been demonstrated by Wooster et al. (2005), Roberts et al. (2005); Baldassarre et al. (2015) and Roberts et al. (2015), and for fire diurnal cycle assessment and characterisation by e.g. Roberts et al. (2009a). However, even when using detection algorithms capable of identifying fires covering as little as 10^{-4} of a pixel (Roberts et al., 2005; Wooster et al., 2015), a limitation of geostationary active fire remote sensing has been its inability to detect the lowest FRP fires due to the typically large pixel areas involved (Roberts and Wooster, 2008; Hyer et al., 2013). However, new generations of geostationary satellites offer increasing spatial fidelity, reducing the importance of this issue over time and offering the best opportunity to detect fires at an early stage via their high imaging frequency (Roberts et al., 2015).

3. Geostationary satellites operating over Asia and Australia

3.1. MTSAT and Himawari-8

MTSAT carrying the MTSAT Imager was operated from 2008 to 2015 by the Japan Meteorological Agency (JMA) over the equator at 140° East. Himawari-8 is the first of the third generation of geostationary weather satellites, launched on 7th October 2014 carrying the new AHI instrument to replace MTSATs capability. We used Himawari-8 AHI data from June 2015, the month when agricultural fire activity in eastern China typically peaks and fire activity in South Asia and Australia starts to intensify (Zhang et al., 2012; Li et al., 2016; Chand et al., 2007; Williams et al., 1998).

Prior to Himawari-8 AHI, the MTSAT imager provided 10-bit, full disk imagery at half past every hour in five spectral bands at a spatial sampling distance of 1 km (visible channel) and 4 km (Infrared channels) at the sub-satellite point (SSP) (Table 1), along with a half disk (northern hemisphere) image every hour. Himawari-8 AHI significantly improves on this, providing full disk 10-bit, radiometrically and geometrically calibrated data in 16 spectral channels every 10 min, with the potential updates every minute over sub-regions (Bessho et al., 2016). Fig. 1 shows an example AHI full disk colour composite image, along with detail over fires in northern Australia. We were not able to access MTSAT data of June 2016, so we instead used Feb. 2009 to coincide with the Australian 'Black Saturday bushfires' and the date of the FengYun-2 satellite data discussed next.

3.2. FengYun-2

FengYun-2 (FY-2) is the first generation of Chinese geostationary spin stabilized meteorological satellite (Guo et al., 2009), and carries the five channel Stretched Visible and Infrared Spin Scan Radiometer (S-VISSR) operating at an SSP spatial sampling distance of 1.25 km for the visible band and 5 km for the thermal infrared channels (Table 1). S-VISSR provides a single full disk, 8-bit image every hour, and Fig. 2 shows a rendition of near simultaneous FY-2 and MTSAT imagery.

4. FTA algorithm application to Asian geostationary satellites

To detect active fire pixels we use the geostationary Fire Thermal Anomaly (FTA) algorithm (Roberts and Wooster, 2008) and the MIR radiance FRP retrieval method (Wooster et al., 2003), originally designed for use with Meteosat SEVIRI (Wooster et al., 2005; Roberts et al., 2005), and now used to generate the real-time Meteosat FRP-PIXEL products within the EUMETSAT Land Surface Analysis Satellite Application Facility (LSA SAF; Wooster et al., 2015). The active fire detection and FRP characterization process occurs over three stages: Firstly, identification of pixels having signals suggestive of actively burning fires; secondly a more detailed contextual set of multi-spectral tests used to confirm whether or not these 'potential fire pixels' do indeed contain fires; and thirdly derivation of atmospherically corrected FRP estimates and associated uncertainties for each confirmed active fire pixel. Full algorithm details are provided in Roberts and Wooster (2008) and Wooster et al. (2015). Since AHI has a higher spatial resolution than SEVIRI, and slightly different waveband coverage, certain of the FTA algorithm thresholds required optimization use with Himawari-8. The initial thresholds were checked for suitability via visual inspection of the output and comparison to MODIS active fire detections. Thresholds were adjusted to maximize detection of true fires while minimizing false alarms, as per Roberts and Wooster (2008) and Wooster et al. (2015). Application of the FTA algorithm to MTSAT and FY-2 proceeded similarly, and all adaptations were found relatively straightforward, as was previously the case when using the FTA with GOES-E and -W data (Xu et al., 2010). Unlike Meteosat, neither Himawari-8, MTSAT nor FY-2 data come with a dedicated cloud mask, so we adapted the image based cloud masking procedure described in Xu et al. (2010). Finally, the power law scaling coefficient a ($mW \cdot m^{-2} \cdot sr^{-1} \cdot (cm^{-1})^{-1} \cdot K^{-4}$) used in the FRP retrieval algorithm for each sensor (Eq. 1) was calculated according to Wooster et al. (2005), and the MWIR band atmospheric transmission (τ_{MIR}) calculated according to Wooster et al. (2015).

$$FRP_{MIR} = \frac{A_{samp}\sigma\varepsilon}{a\varepsilon_{MIR}}\left(\frac{L_{MIR}}{\tau_{MIR}}\right) \quad (1)$$

where A_{samp} is the pixel sampling area (m^2), σ is Stefan-Boltzman constant (5.67E-8 $Js^{-1} \cdot m^{-2} \cdot K^{-4}$), ε is the fire emissivity and ε_{MIR} the spectral emissivity in the MIR (and fires are assumed to be grey bodies so

Table 1
Basic characteristics of the imagers carried by Himawari-8, MTSAT and FY-2. Notice only the channels used herein are listed, alongside their use in the active fire detection and characterization algorithm.

Satellite & imager	Spectral channel	Wavelength range (μm)	Spatial sampling distance at SSP (km)	Primary use in active fire detection & FRP derivation scheme
Himawari-8 AHI	3	0.63–0.66	0.5	Cloud masking
	7	3.74–3.96	2	Active fire detection & FRP derivation (MWIR band saturates at high BT of 400 K)
	14	11.1–11.3	2	Active fire detection
MTSAT Imager	1	0.55–0.80	1	Cloud masking
	2	10.3–11.3	4	Active fire detection
	5	3.5–4.0	4	Active fire detection & FRP derivation (though MWIR band saturates at relatively low BT of 320 K, leading to extensive saturation over even warm backgrounds).
FY-2 S-VISSR	1	0.55–0.75	1.25	Cloud masking
	2	10.3–11.3	5	Active fire detection
	4	3.5–4.0	5	Active fire detection & FRP derivation (MWIR band saturates at moderate temperature of 340 K).

that $\varepsilon = \varepsilon_{MIR}$), and L_{MIR} is the contribution of the fire to the total MWIR band spectral radiance of the active fire pixel ($mW \cdot m^{-2} \cdot sr^{-1} \cdot (cm^{-1})^{-1}$).

5. Asian geostationary FTA algorithm evaluation

5.1. Methodology

Our performance evaluation of the resulting geostationary active fire datasets was based on comparison to MODIS Collection 5 MOD14 and MYD14 active fire products from the Terra and Aqua satellites (Giglio et al., 2003). With a nadir spatial resolution of 1 km, MODIS is capable of detecting sub-pixel sized fires having an FRP significantly lower than the minimum detectable from geostationary imagers (Roberts et al., 2015). We followed the intercomparison procedure recently used between MODIS and the LSA SAF Meteosat SEVIRI FRP-PIXEL product (Roberts et al., 2015), making comparisons only when data were collected within ±6 min of one other and within a MODIS scan angle of ±30° to limit MODIS' pixel area growth to a factor of ~1.7 compared to nadir (Freeborn et al., 2011, 2014).

5.1.1. Active fire detection evaluation methodology

Following Roberts et al. (2015), MODIS imagery and active fire data were first spatially remapped to the relevant geostationary imaging grids to deal with the varying pixel sizes (Wolf and Just, 1999), and if two or more MODIS active fire pixels fell within one grid cell their FRP values were summed. The original MODIS imagery aided interpretation, and the remapped MODIS active fire data (termed here MODIS-R) were quantitatively compared to the geostationary data, with active fire detection errors of omission occurring when a MODIS-R grid cell containing at least one active fire pixel was matched to a location imaged within ±6 min by the geostationary sensor but which showed no actual geostationary fire detection within a 5×5 pixel window (Freeborn et al., 2014). Geostationary errors of commission occurred when an actually detected geostationary active fire pixel had no matching MODIS-R active pixel within the corresponding 5×5 pixel window.

Fig. 3 indicates the methodology applied to a single matched AHI and MODIS subscene of China. Comparison of Fig. 3d and e demonstrates that certain active fires detected in the MODIS data fail to be detected by the lower spatial resolution AHI data, but that many other fires are successfully identified in both. Overall, in this example, MODIS detects 1246 active fire pixels, equivalent to 859 MODIS-R pixels after remapping to the AHI grid. Among these 859 remapped fire pixels, 602 (~70%) had no corresponding AHI detection in the matching 5×5 window, an error of omission very similar to the 73% reported recently for the Meteosat SEVIRI FRP-PIXEL product that uses the same FTA detection algorithm (Roberts et al., 2015). This is reasonable performance given that the fire affected region of Fig. 3 is quite far from the AHI subsatellite point and thus has a ground pixel area around 4× to 8× larger than MODIS, depending on MODIS scan angle. At the same time, AHI detected 162 individual active fire pixels, with 152 (~94%) having a corresponding MODIS active fire pixel, demonstrating a low (6%) false alarm/error of commission rate. Results akin to those from this single matchup scene were accumulated across one month of data from each geostationary sensor (June 2015 for Himawari, Feb.2009 for MTSAT and FY-2).

For Himawari-8 AHI, the June 2015 full disk imagery included fires mainly located in China, Thailand, Indonesia and Australia. For the MTSAT and FY-2 evaluation, the full disk Feb. 2009 data saw fires across

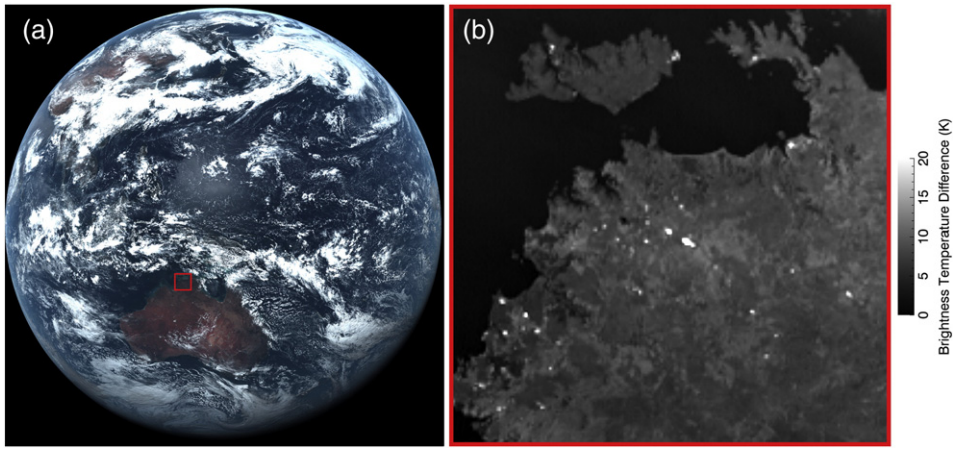

Fig. 1. Example data from the Himawari-8 Advanced Himawari Imager (AHI), collected at 03:00 UTC on 7th June 2015. (a) Colour composite full disk image (RGB = AHI Channels 3, 2, 1), and (b) subset of northern Australia highlighted in (a) and shown as the difference between the recorded MWIR and LWIR brightness temperatures (Channels 7 and 14; Table 1) so that pixels containing sub-pixel active fires are highlighted as high values, as explained in Xu et al. (2010) and Wooster et al. (2013, 2015). Areal coverage of actively burning fires down to sizes of 10^{-3} to 10^{-4} of a pixel typically increase this BT difference metric to 5–10 K or greater, which is generally sufficient to enable active fire detection to occur (Wooster et al., 2005).

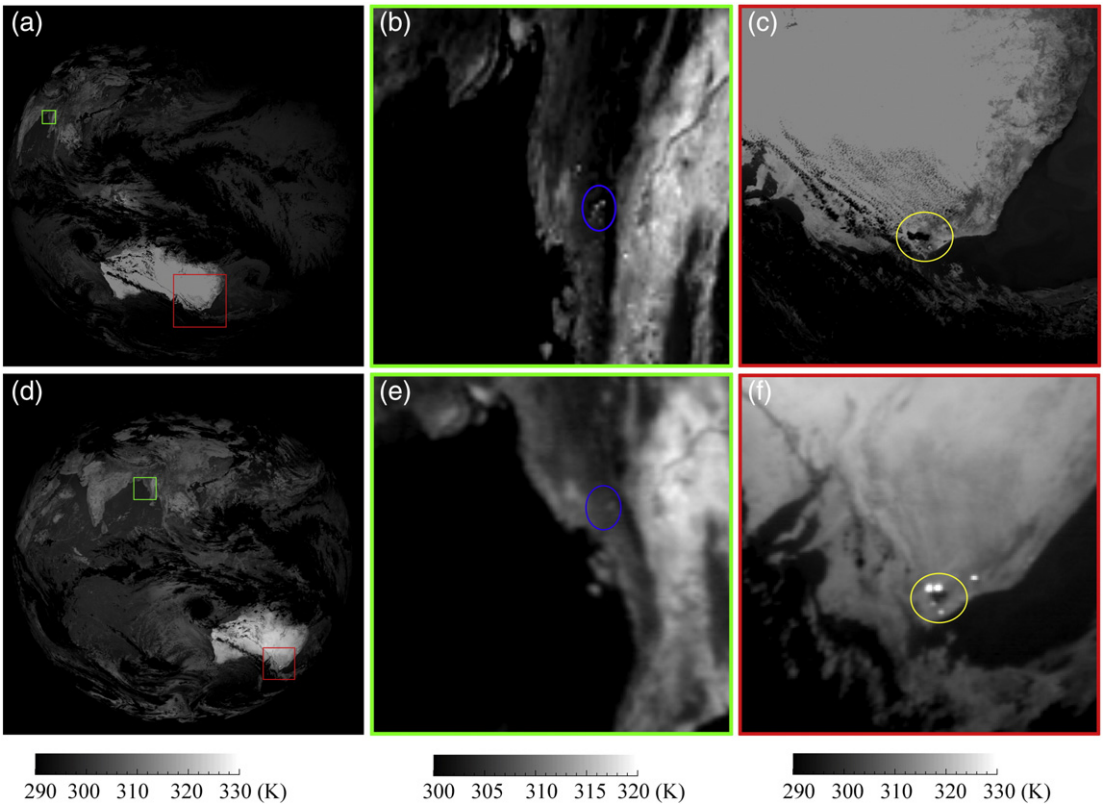

Fig. 2. Near simultaneous MWIR brightness temperature imagery from the MTSAT imager (top row) and FY-2 S-VISSR imager (bottom row), collected on 7th February 2009. (a) Full disk MTSAT image (5:30 UTC) with areas in Australia and Myanmar highlighted in red and green respectively; (b) MTSAT sub-image over Myanmar outlined in (a) where a few fires are circled in blue are visible but which are not apparent in the almost simultaneous FY-2 VISSR imagery shown in (e); (c) MTSAT sub-image covering parts of New South Wales and Victoria (Australia) during the 'Black Saturday bushfires' (circled in yellow) – of which only a small part can be discerned due to MWIR channel saturation affecting large areas; (d) full disk FY-2 S-VISSR scene collected at 5:00 UTC; (e) S-VISSR sub-image outlined by the green rectangle in (d) and matching the MTSAT sub-image in (c); (f) S-VISSR sub-image covering parts of New South Wales and Victoria of Australia matching the MTSAT sub-image shown in (c) and where the 'Black Saturday bushfires' do appear as a group of high MWIR BT pixels circled in yellow.

parts of Australia and Thailand. It was not possible to directly intercompare MTSAT and FY-2 active fire detection outputs on a point-by-point basis, because of the different imaging times of each system – further supporting use of the MODIS active fire detection data as the standard against which the geostationary sensors are assessed. The number of MOD14/MYD14 products matching within ±6 min of each Asian geostationary satellite dataset, and which of these had active fires present within them, are listed in Table 2. Of course, since landscape burning is highly dynamic, active fire detection performances typically vary somewhat across locations, times of day and season (e.g. Roberts and Wooster, 2008; Freeborn et al., 2014). The differences we report here between the errors of omission and commission of the three geostationary sensors are likely to be somewhat influenced by this, but our broad findings regarding the general performance are considered representative.

5.1.2. FRP evaluation methodology

Following the type of active fire pixel clustering procedure used in Zhukov et al. (2006), Roberts and Wooster (2008), Xu et al. (2010), we first compared the FRP recorded by Himawari-8 AHI to that recorded by MODIS on a 'per fire' basis, defined as a contiguous or near-contiguous group of active fire pixels detected near-simultaneously. MODIS retrievals were made using the same Wooster et al. (2003, 2005) MIR radiance approach as with the geostationary datasets (Eq. 1), which is now also used to generate MODIS' Collection 6 FRP data (Giglio et al., 2016). MODIS FRP was atmospherically corrected using the same procedure as with AHI (described in Wooster et al. (2015)).

Whilst per-fire comparisons between geostationary and MODIS FRP retrievals have previously reported low bias (e.g. Roberts and Wooster, 2008; Xu et al., 2010; Roberts et al., 2015), there typically remains significant regional-scale FRP underestimation because of the inability of geostationary data to detect the lowest FRP fires (e.g. Roberts and Wooster, 2008; Xu et al., 2010; Roberts et al., 2015). To assess this, the Himawari-8 and MTSAT active fire data were subset to cover the same geographic area as each MODIS scene (within a ±30° MODIS scan angle) and each datasets total FRP compared to assess the importance of fires missed by the geostationary sensors but detected by MODIS.

5.2. Results

5.2.1. FY-2 evaluation

Taking FY-2 first, MODIS-R data contemporaneous with FY-2 showed 2035 active fire grid cells, but only 9 were matched by active fire pixels detected by FY-2, indicating a near total failure by FY-2 to detect them (Table 3). Such a high omission error rate results from a combination of the S-VISSR sensors lower spatial resolution and decreased radiometric sensitivity compared to the MTSAT imager and Himawari-8 AHI (as well as compared to MODIS), and the apparently relatively poor quality of the S-VISSR MWIR spectral band measurements (see Fig. 2).

FY-2 S-VISSR does have a better vantage point for observing certain Asian-Pacific areas compared to MTSAT, due to its orbital position (e.g. the region of Myanmar highlighted in green, where FY-2 has pixel spatial sampling distance of ~5.4 km and MTSAT ~6 km, Fig. 2). Nevertheless, MTSAT often appears to better identify actively burning fires than FY-2 even in such areas (e.g. compare Fig. 2b showing MTSAT with the near simultaneous FY-2 S-VISSR imagery of Fig. 2e). However, where large fires and high ambient background temperatures lead to

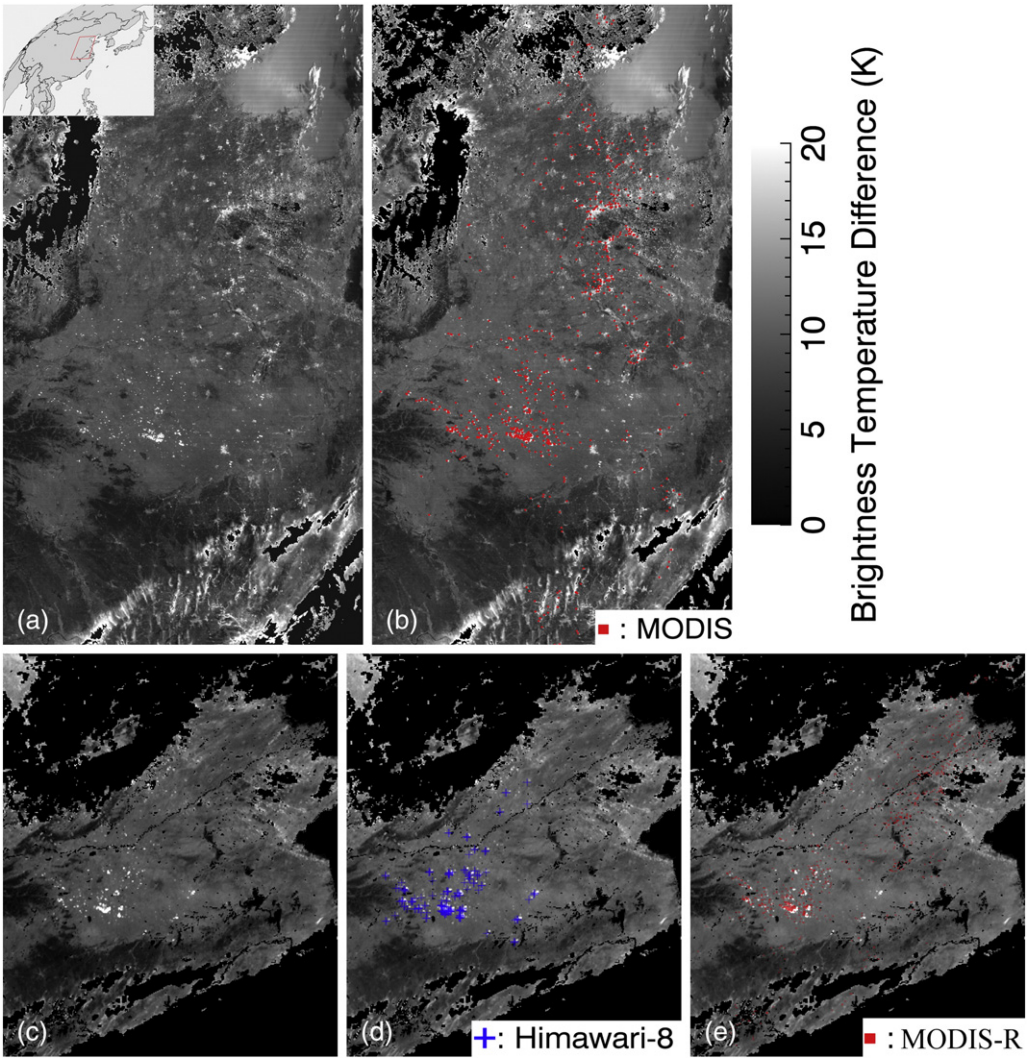

Fig. 3. Example methodology used for geostationary active fire detection performance evaluation. Here, Himawari-8 AHI data and matching MODIS data are shown over China (03:10 UTC on 11th June 2015; for location see top left inset). (a) MODIS MWIR-LWIR Band Brightness temperature (BT) difference image, and (b) matching active fire detections (red) superimposed with a one pixel offset for clarity. Areas of cloud and standing water are masked out in these MODIS subscenes. (c) and (d) show from Himawari-8 the same MWIR-LWIR BT difference metric (now calculated using the AHI imagery), along with the corresponding AHI-detected active fire detections (blue). (e) MODIS active fire detections made within a ±30° MODIS scan angle (red), mapped to the AHI image projection.

saturation of the MTSAT MWIR spectral band FY-2 can still show some advantage. An example is during the extreme 'Black Saturday bushfires' that burned intensely across the Australian state of Victoria on 7th February 2009 (Engel et al., 2013). Clearly seen in FY-2 data, albeit appearing somewhat 'blurred' (Fig. 2f), in MTSAT they appear far less clearly (circled yellow in Fig. 2c). This results from the comparatively low 320 K saturation temperature of the MTSAT MWIR band (Channel 5; Table 1). Due to the high environmental temperatures seen at this time, MTSAT Channel 5 saturation is occurring over many of the background pixels as well as almost all the fire pixels, severely hampering discrimination of the latter. This is not the case with FY-2 S-VISSR, and Fig. 4 shows a comparison between the FRP timeseries from MODIS, FY-2 and MTSAT, where the latter shows a particular inability to detect these large fires during much of the day (as in Fig. 2c). However, though FY-2 can detect the fires after ~11:00 h local solar time, their FRP retrieval closest to the ~14:00 h daytime MODIS overpass is only around one third of that of MODIS, again partly due to MWIR band saturation - but in the case of S-VISSR only over the fires themselves (Fig. 4).

Table 2
Number of Collection 5 MOD14 and MYD14 active fire products used in comparisons to our Himawari-8 AHI, MTSAT and FY-2 active fire data.

	Himawari-8	MTSAT	FY-2
MODIS products coincident with the geostationary data (±6 min)	4243	672	664
MODIS products coincident with the geostationary data (±6 min) and in which the MODIS products showed the presence of active fires	204	58	34

Table 3
Active fire detection errors of omission and commission for the FTA algorithm applied to Himawari-8 AHI, MTSAT imager and FY-2 S-VISSR data, calculated via comparison to near-simultaneous MODIS active fire pixels detected (MOD14 and MYD14).

Asian geostationary satellite	Himawari-8	MTSAT	FY-2
No. of fire pixels present at times coincident with a MODIS overpasses	1974	140	8
Fire pixels detected by MODIS at these times	1825	124	6
Geostationary active fire detection error of commission	8%	11%	25%
No. of MODIS fire pixels	12,229	3279	3468
No. of MODIS fire pixels after remapped to geostationary projection	8575	1830	2035
No. of MODIS fire pixels after remap detected by geostationary satellite	2895	259	9
Geostationary active fire detection error of omission	66%	86%	99%

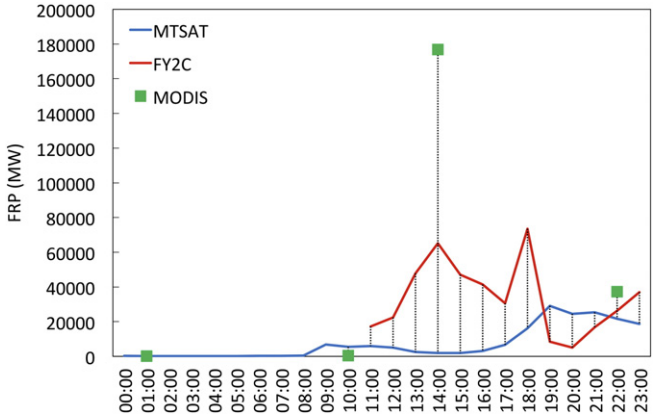

Fig. 4. FRP time series data of the Australian 'Black Saturday bushfires' for 7th Feb 2009. MTSAT and FY-2 show very significant FRP underestimation compared to the simultaneous MODIS observations, though with FY-2 performing in this case apparently better than MTSAT due to the latter's extreme levels of MWIR band saturation during the early afternoon diurnal fire peak (see main text). X-axis shows local solar time.

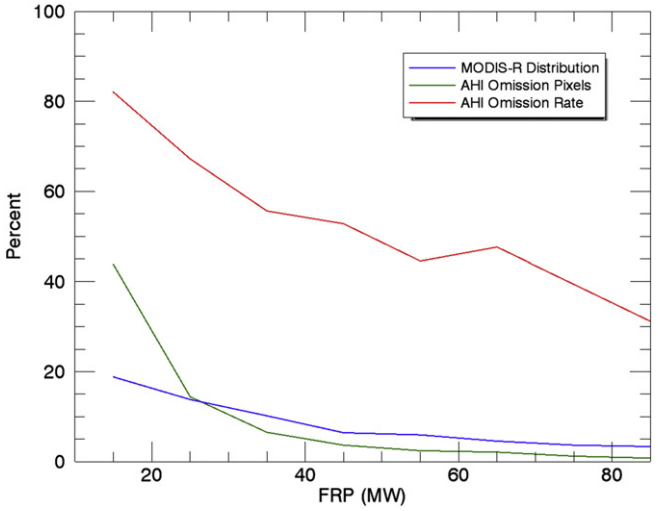

Fig. 5. Details of AHI active fire pixel omissions with respect to MODIS, binned into 10 MW intervals. Blue line shows the relative frequency (expressed as a percentage) of remapped MODIS (i.e. MODIS-R) pixels at each FRP level. Red line shows the percentage of MODIS-R pixels at each FRP level that remained undetected by AHI (i.e. the omission rate at that FRP value). Green line shows the relative importance of the undetected fire pixels at each FRP level, expressed as a percentage of the FRP of the total undetected fire pixel set. See main text for a full explanation of MODIS-R data.

After around 18:00 h, background brightness temperatures typically fall below 320 K in MTSAT's MWIR band, and MTSAT once again becomes preferable to use (Fig. 4). We conclude therefore that whilst FY-2 S-VISSR does offer some limited benefit for detection of very large fires burning in high ambient temperature conditions, in general they appear to be poorly suited to the active fire application and their use was not pursued further herein.

5.2.2. AHI and MTSAT active fire detection evaluation

Table 3 reports results of the active fire detection evaluation for both Himawari-8 AHI and the MTSAT imager. For the AHI, 66% of MODIS-R fire pixels made within the AHI full disk had no corresponding AHI-detected active fire pixel, an omission error higher than the 53–59% found when the FTA algorithm prototype was applied to limited amounts of Meteosat SEVIRI data (Roberts and Wooster, 2008), but lower than the 73% reported with the operational FTA algorithm (Roberts et al., 2015). Errors of omission rates differ over time for SEVIRI, due in part to different seasons (and thus fire affected areas and locations) being included in the comparisons. Those for AHI lie in between, though since the AHI ground pixel area at same view zenith angle is smaller than that of SEVIRI, the omission error for AHI might be expected to be lower. However, the domination of small (low FRP) agricultural residue burning fires across much of Asia provides a set of targets likely to be in general more difficult to detect than the larger grassland fires dominating much of Africa (Giglio et al., 2016; Li et al., 2016). Therefore, though the geostationary data do offer the advantage of capturing almost continuous imagery for better detection of short-lived agricultural residue fires, their typically low FRP can make them a challenge to detect if only a few are burning simultaneously in a particular AHI pixel. This is exacerbated here, because in June 2015 most of the fire-affected areas within the AHI disk are actually quite far from the sub-satellite point, resulting in increased AHI pixel areas and a higher minimum FRP detection limit compared to closer to nadir (see Fig. 10). Simultaneous AHI and MODIS data make it clear that AHI misses some fire pixels that MODIS can successfully detect, though Fig. 5 indicates that the AHI active fire detection omission rate decreases sharply with increasing FRP, being around 80% for MODIS-R active fire pixels of ~15 MW, around 50% at ~40 MW, and below 40% in excess of 80 MW. Performance beyond an FRP of 90 MW is not considered due to the limited number of high FRP MODIS-R fire pixels available.

Fig. 5 also shows the number of MODIS-R fire pixels coincident with an AHI image at each FRP level (expressed as a percentage of the entire MODIS-R coincident fire pixel set), along with the proportion AHI fails to detect (expressed as a percentage of the total number of omissions). MODIS-R fire pixels having an FRP of ~15 MW or less are those most commonly missed by AHI, comprising ~20% of the total MODIS-R fire pixel set, and as their aforementioned 80% omission rate attests to they represent a large proportion (45%) of the MODIS-R fire pixels that AHI fails to detect. As FRPs increase, those fire pixels omitted by AHI become a smaller fraction of the overall AHI omitted pixel set. These data confirm that the majority of active fire pixels that AHI misses but MODIS detects are 'small' low FRP fires, as would be expected from the formers larger (nadir) pixel area. Of course, other effects also impact the rate of omission, such as the quality and sensitivity of the cloud masks applied to each data type (Freeborn et al., 2014).

Fig. 6 displays the spatial distribution of AHI's errors of omission compared to MODIS-R using 0.5° grid cells. Because lower FRP fires dominate those missed (Fig. 5), the percentage of grid-cell MODIS-R fire counts that are missed by AHI (Fig. 6a) is typically higher than the percentage of the MODIS-R grid-cell FRP that these non-detections represent (Fig. 6b). AHI tends to miss higher proportions of MODIS-detected active fire pixels in areas where fires are less common and/or are more dominated by smaller/lower FRP events (e.g. in June 2015 in China, Indonesia and Thailand) and lower proportions in areas like Northern Australia where individual fires are larger and often burn more intensely.

In terms of active fire errors of commission, 8% of the AHI-detected active fire pixels had no matching MODIS detection, a similar commission error to the 6–8% reported using the FTA algorithm with Meteosat over Africa (Roberts and Wooster, 2008) and the 8% found with GOES across South America (Xu et al., 2010).

In terms of MTSAT, its active fire data show higher errors of omission (86%) and commission (11%) than Himawari-8 AHI, most likely reflecting the formers larger pixel area and thus lower sensitivity to active fires, and also the impact of MTAT's MWIR band saturation problem over warmer backgrounds (as discussed in Section 3.2 and shown in Fig. 2).

5.2.3. AHI and MTSAT FRP characterisation

5.2.3.1. Per-fire FRP intercomparison. Fig. 7 presents results of the per-fire AHI to MODIS FRP intercomparison, showing high correlation (r^2 = 0.98) and a slope of 0.99 for the linear-best fit. AHI shows a low bias of 3 MW compared to MODIS, a standard deviation of 156 MW (32%),

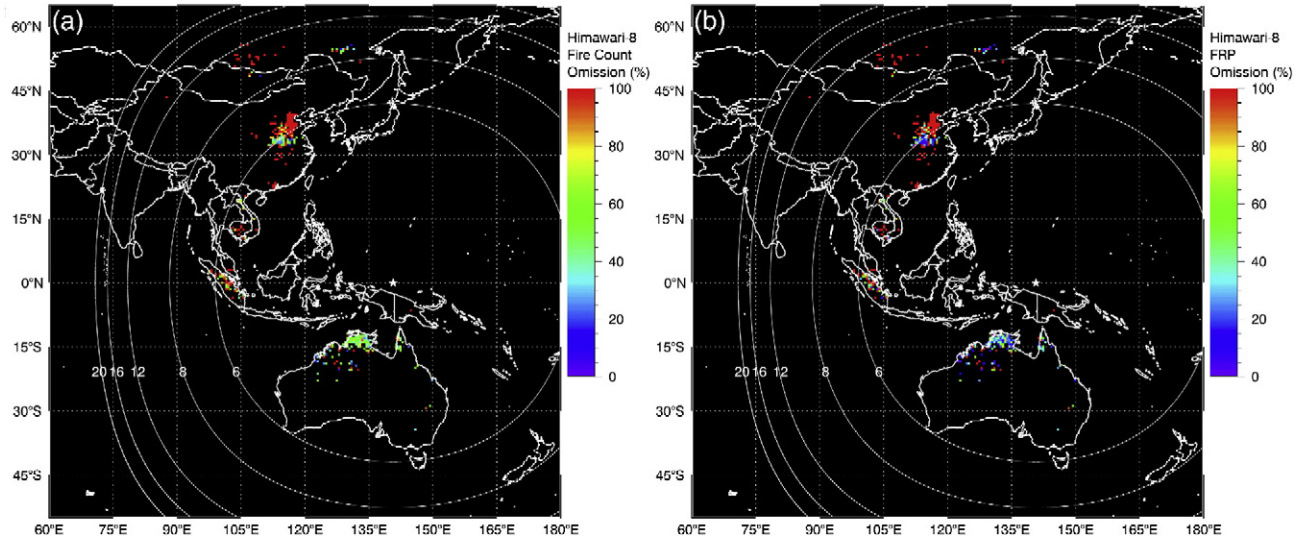

Fig. 6. Regional distribution (0.5° resolution) of Himawari-8 AHI active fire omissions relative to near simultaneous MODIS-R data. (a) Percentage of MODIS active fire pixels missed by AHI in each grid-cell, and (b) percentage of grid cell total FRP as measured by the MODIS-R data that is represented by fire pixels remaining undetected by AHI. AHI sub-satellite point is indicated by the white star above Papua New Guinea/West Papua, whilst white circles indicate contours of AHI pixel area (labels are area in km^2).

and 79% of the FRP retrievals have a difference <50%, with 39% <20%. Considering that almost exactly simultaneous MODIS FRP measures of the same fire pixel indicate an FRP uncertainty of 27% (1σ) for MODIS alone (Freeborn et al., 2014), the degree of AHI to MODIS FRP agreement seems very reasonable and comparable to that between MODIS and the LSA SAF Meteosat SEVIRI FRP product (Roberts et al., 2015).

MTSAT and MODIS matchups from Feb. 2009 are also shown on Fig. 7. Due to relatively fewer fires being present at this time compared to June 2015, to the reduced temporal resolution of MTSAT compared to AHI, and to the aforementioned problem MTSAT has detecting fires against warm backgrounds, there were far fewer MTSAT-to-MODIS matchups than there were AHI-to-MODIS. Furthermore, MTSAT fire clusters were only used when all constituent fire pixels were unsaturated (BT_{MWIR} < 320 K). Despite the limited number of matchups, the FRP data of MTSAT and MODIS still show a reasonable correlation (r^2 = 0.74) and slope of the linear best fit (0.89), with a bias slightly higher than AHI to MODIS (14 MW; 6%), though a smaller standard deviation (86 MW, 33%). All matchups have an FRP difference <50%, with 46% <20%. Overall MTSAT shows a strong degree of agreement with MODIS provided its data are unsaturated, but the performance in terms of active fire detection is far worse than that of AHI.

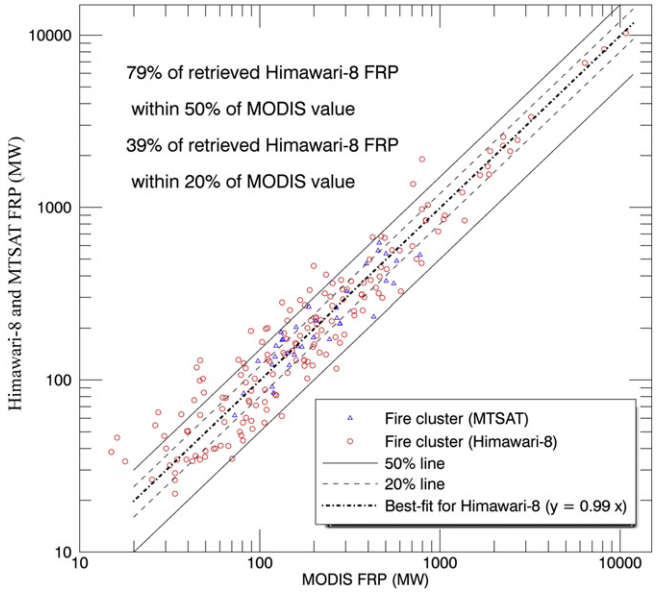

Fig. 7. Per-fire FRP intercomparison made using FRP retrievals from the MTSAT imager, Himawari-8 AHI and MODIS. Matching MODIS and AHI data are from June 2015, and those from MTSAT and MODIS from Feb 2009. Each symbol represents data from a single active fire cluster, representing a spatially contiguous or near-continuous group of active fire pixels detected near simultaneously by both sensors. In total, 168 AHI fire clusters and 35 MTSAT fire clusters are used, with the latter particularly low in part because the much higher active fire omission error and MWIR channel saturation of that sensor (Table 3) makes it more challenging to identify suitable matchups (see main text).

5.2.3.2. Per-area FRP intercomparison. When AHI and MODIS simultaneously detect the same active fire, AHI provides a reliable FRP measure (Fig. 7), but AHI does miss 66% of the MODIS-R fire pixels (Section 5.2.2) – primarily those at or below the nominal AHI FRP detection limit (Fig. 5). Many of these undetected low FRP fires are likely to be due to agricultural residue burning, which represents a very substantial fraction of fire activity in Asia (Zhang et al., 2012; Zhang et al., 2015; Li et al., 2016), and this 'small fire' detection bias demonstrably leads to significant regional-scale FRP underestimation when using AHI (Fig. 8) as well as other geostationary sensors (e.g. Freeborn et al., 2009; Roberts et al., 2015; Wooster et al., 2015; Xu et al., 2010). Of course, MODIS only observes an area a few times per day, whereas AHI provides almost continuous observations opportunities, and Wooster et al. (2015) show that in the case of the LSA SAF Meteosat SEVIRI active fire data, most fires missed by the geostationary observation made at the time of the MODIS overpass are detected by the geostationary data at other points during the fires lifetime.

Freeborn et al. (2014) used the ratio between the total cumulative FRP ($\sum$FRP) measured simultaneously in the same geographic region by Meteosat SEVIRI and by MODIS to quantify the impact of the (primarily low-FRP) fires not detected by the former. We found the ratio of $\sum FRP_{AHI}$ to $\sum FRP_{MODIS}$ as 0.54, and $\sum FRP_{MTSAT}$ to $\sum FRP_{MODIS}$ as 0.31, with the former higher because of AHI's lower active fire detection omission error compared to MTSAT (Section 5.2.2) and because of the MWIR band saturation problems of MTSAT that result in FRP underestimation for stronger fires (Fig. 2). Hyer et al. (2013) already report that MTSAT data processed with the WF_ABBA active fire detection algorithm developed show a rather lower overall active fire detection efficiency, particularly around local noon due to MWIR channel saturation. Our work confirms MTSAT's tendency to miss very many fires that MODIS can detect, even if they are burning rather strongly, but we see significant improvement in this situation using AHI.

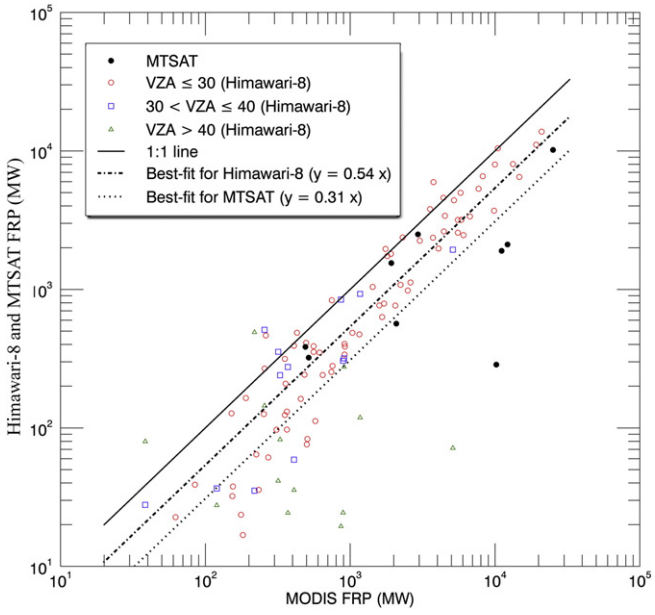

Fig. 8. Comparison of total FRP measured in spatially matched regions imaged contemporaneously by Himawari-8 AHI and MODIS throughout June 2015 at a MODIS scan angle of less than ±30°. The least squares linear best-fit passing through the origin is shown (dot dash line), and AHI tends to generally underestimate total FRP primarily due to the non-detection of most fires burning below its minimum FRP detection limit.

5.2.4. FRP frequency magnitude analysis

Following the kind of analysis shown in Freeborn et al. (2011) for Meteosat SEVIRI, Fig. 9 shows the frequency of all active fire pixels of different FRPs recorded by AHI and by MODIS over the AHI full disk region in June 2015, along with those detected by both sensors almost simultaneously. The Collection 5 MOD14/MYD14 MODIS active fire products have a minimum FRP detection limit of ~8–10 MW, and in most fire affected regions there are typically many more fire pixels approaching this limit than there are than higher FRP fire pixels. AHI can detect some fire pixels approaching the FRP detection limit of MODIS, but frequency of detection peaks at ~30 MW. Below this, AHI fails to detect many fire pixels that MODIS can detect, due to the larger pixel areas. Above 40 MW, the frequency distributions of the near simultaneous AHI and MODIS data are very similar, confirming that the majority of AHI active fire pixel omissions are low FRP (Fig. 5). Also demonstrated is the fact that AHI does not show an upper FRP breakpoint, such as the one exhibited by SEVIRI (Roberts and Wooster, 2008; Freeborn et al., 2011), largely because MTSAT's 400 K MWIR band maximum measurable signal (c.f. 335 K for SEVIRI) largely prevents saturation. In data of June 2015, only 0.06% (173 pixels) of the AHI-detected active fire pixels are saturated.

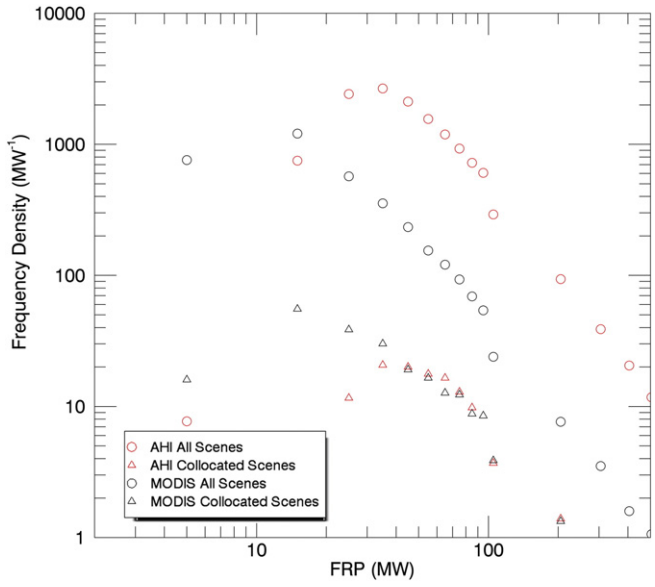

Fig. 9. Frequency density vs. FRP magnitude distributions of active fire pixels detected by MODIS and Himawari-8 AHI, constructed from (i) the number of active fire pixels detected by all scenes collected in June 2015, and (ii) the number of those in only collocated scenes taken within ±6 min of one another. Fire pixels with an FRP > 500 MW are not shown due to their rarity.

6. Asian and Australian fire activity records

Section 5's performance assessment indicates that Himawari-8 AHI offers major advantages over FY-2 and MTSAT for geostationary active fire detection and FRP characterisation, and we now turn our attention to briefly demonstrating the utility of the AHI fire radiative power retrievals. Future work will exploit longer datasets to build upon the limited analyses presented herein.

6.1. Large scale spatial patterns

Fig. 10 summarises MODIS' active fire data of June 2015 at 0.5° resolution, and compares it side-by-side to that of AHI. Substantial burning across parts of Asia is common at this time (Li et al., 2016), with similar patterns seen from the two sensors. Grid cells showing high total FRP result from either large numbers of active fire pixels, individual fires of particularly high FRP, or persistent or re-occurring fires in the same grid over the month. Areas showing concentrations of high FRP grid cells include eastern China, resulting from numerous agricultural residue fires (Randerson et al., 2012; Zhang et al., 2015; Li et al., 2016), southeast Asia which hosts a mixture of agricultural burning, forest clearance and peatland fires (Gaveau et al., 2013), and northern Australia that sees savannah burns (Williams et al., 1998).

Some clear differences between the AHI- and MODIS-derived FRP records can also be seen, for example in northern India where Chand et al. (2007) reported heavy burning in Uttaranchal State, and in Russia (Western from 120°E) and Kazakhstan, where MODIS typically shows increased fire signatures compared to AHI – probably related to the large view zenith angle of AHI at these higher latitudes (with AHI pixel areas >4× larger than at the SSP).

6.2. Diurnal cycles

The most unique aspect of geostationary imaging satellites is their ability to provide almost continuous observations (cloud cover permitting), and thus highly detailed temporal information on the daily cycle of fire activity (Roberts et al., 2009a, 2009b). Fig. 11 shows the hourly mean FRP recorded in June 2015 across the AHI full disk in the three main regional land cover types (based on the IGBP 1 km resolution land cover map; Loveland and Belward, 1997). Savannah fires are generally responsible for the highest total FRP, whilst agriculture typically shows the least - apart from on 11th June 2015 when an anomalously large group of crop residue fires are observed in eastern China (Fig. 11c), discussed further below. Fig. 11 also demonstrates that forest burning apparently showed a significant increase in the second half of June, mostly related to fires in Indonesia and Australia.

In Fig. 11, the middle and right columns show the monthly mean and standard deviation of FRP and normalised diurnal cycle (DC), calculated using the approach of Roberts et al. (2009a, 2009b). Smooth cycles are seen for each landcover, with a nighttime minimum, a daytime peak occurring around 13:00 h local solar time (though the mean DC of agriculture peaks slightly earlier), and generally weakening afternoon fire

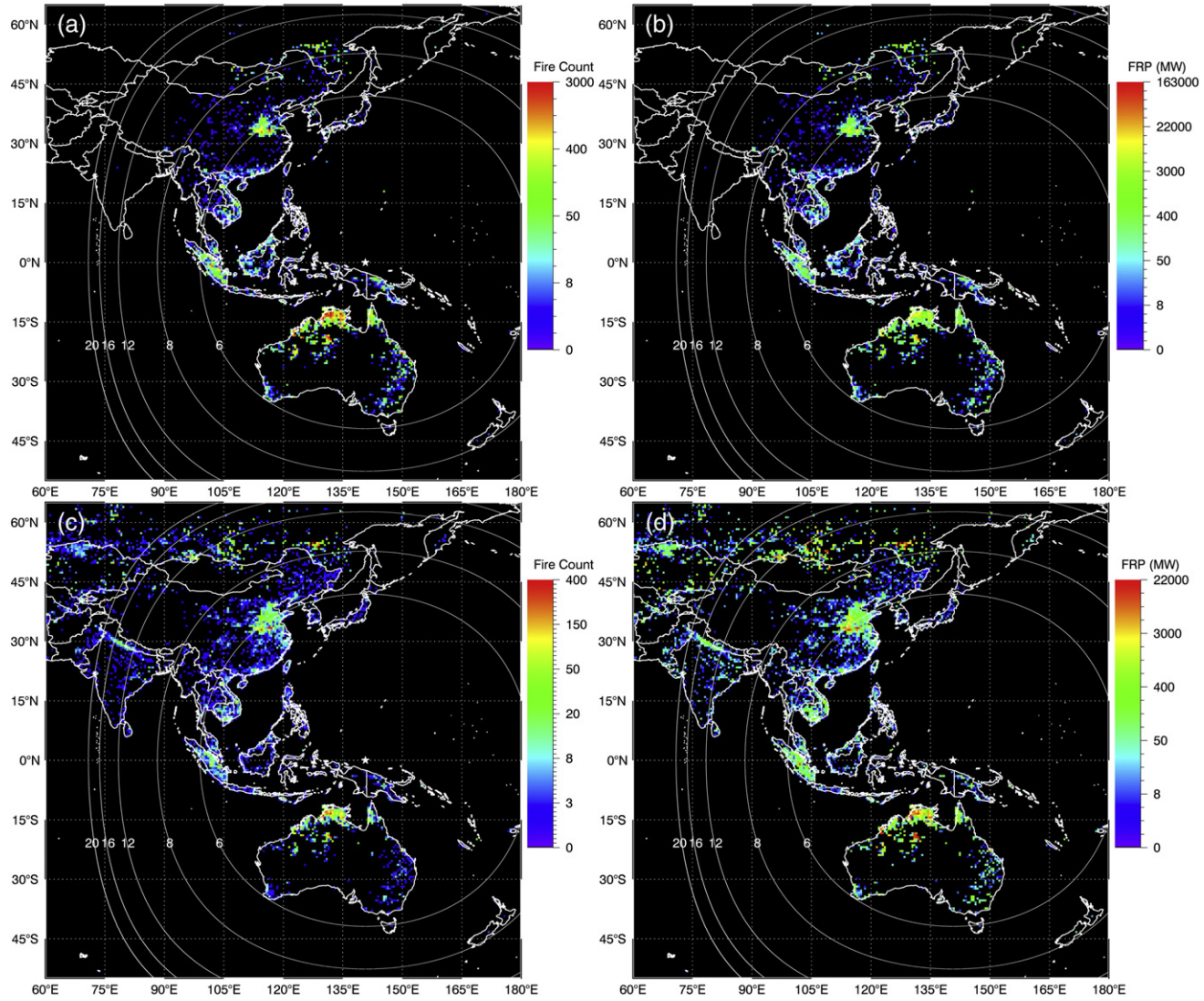

Fig. 10. Total fire count and total FRP of actively burning fires detected within 0.5° grid cells in June 2015 using all observation opportunities from AHI and MODIS. (a) Fire count from Himawari-8 AHI; (b) FRP from AHI; (c) Fire count from MODIS; (d) FRP from MODIS. AHI sub-satellite point is indicated by the white star above Papua New Guinea/West Papua, whilst the white circles indicate the pixel area variations (labels are area in km^2).

activity. Whilst savannah shows a continuously decreasing trend into the night, forest and agriculture show small local FRP peaks around 20:00–21:00 h local solar time, possibly due to timings of anthropogenic burning practices in areas where the authorities formally outlaw burning and thus some fires are purposely conducted after nightfall. Also, the standard deviation shown in the diurnal cycle (DC) plots is significantly smaller and more consistent across the day than is the standard deviation of FRP. Agriculture shows the largest variability and savannah the smallest, perhaps due to agricultural fires bring solely anthropically-driven.

Overall, the diurnal cycles in Fig. 11 for Asia and Australia appear broadly similar to those reported by Roberts et al. (2009a, 2009b) over Africa for the same landcovers. The peaks around 13:00 h local solar time seem a little earlier than the 13:00 h (Kalimantan) to 15:00 h (Northern Australia) peaks reported by Giglio (2007), though we have used only a single month of AHI data compared to the seven years of MODIS and TRMM VIRS data in Giglio (2007), and have focused over the full AHI disk rather than regionally as did Giglio (2007). As the AHI active fire data record lengthens, we will perform more nuanced analyses to determine whether the near continuous observations provided from geostationary orbit do indeed alter conclusions so-far made largely from polar orbiters.

Fig. 12 provides more detail on the diurnal variation in FRP for 11th June 2015 in Henan province (North China Plain), which Fig. 11c shows demonstrates an unusually large FRP peak. AHI and MODIS both indicate its existence, but the former shows much more temporal detail and captures the FRP maximum just before 14:00 h local solar time, whereas the sparser MODIS record provides an artificial peak time of at 11:10 h (as shown in Fig. 3a, where multiple fires are clearly seen) due to the early afternoon Aqua MODIS overpass recording the area at a very large view zenith angle and thus coarse pixel area (6.4 km^2; larger than the AHI pixels) whilst resulted in many fire pixels remaining undetected by MODIS. MODIS' difficulties in detecting fires at larger view angles are detailed in e.g. Freeborn et al. (2011). Clearly, when using polar obiter data alone (e.g. Vermote et al., 2009) care must be taken not to allow far-off nadir observations to introduced unwanted impacts (as identified by Freeborn et al., 2011), not only regarding FRP magnitude but also the timing of diurnal peaks. This clearly demonstrates

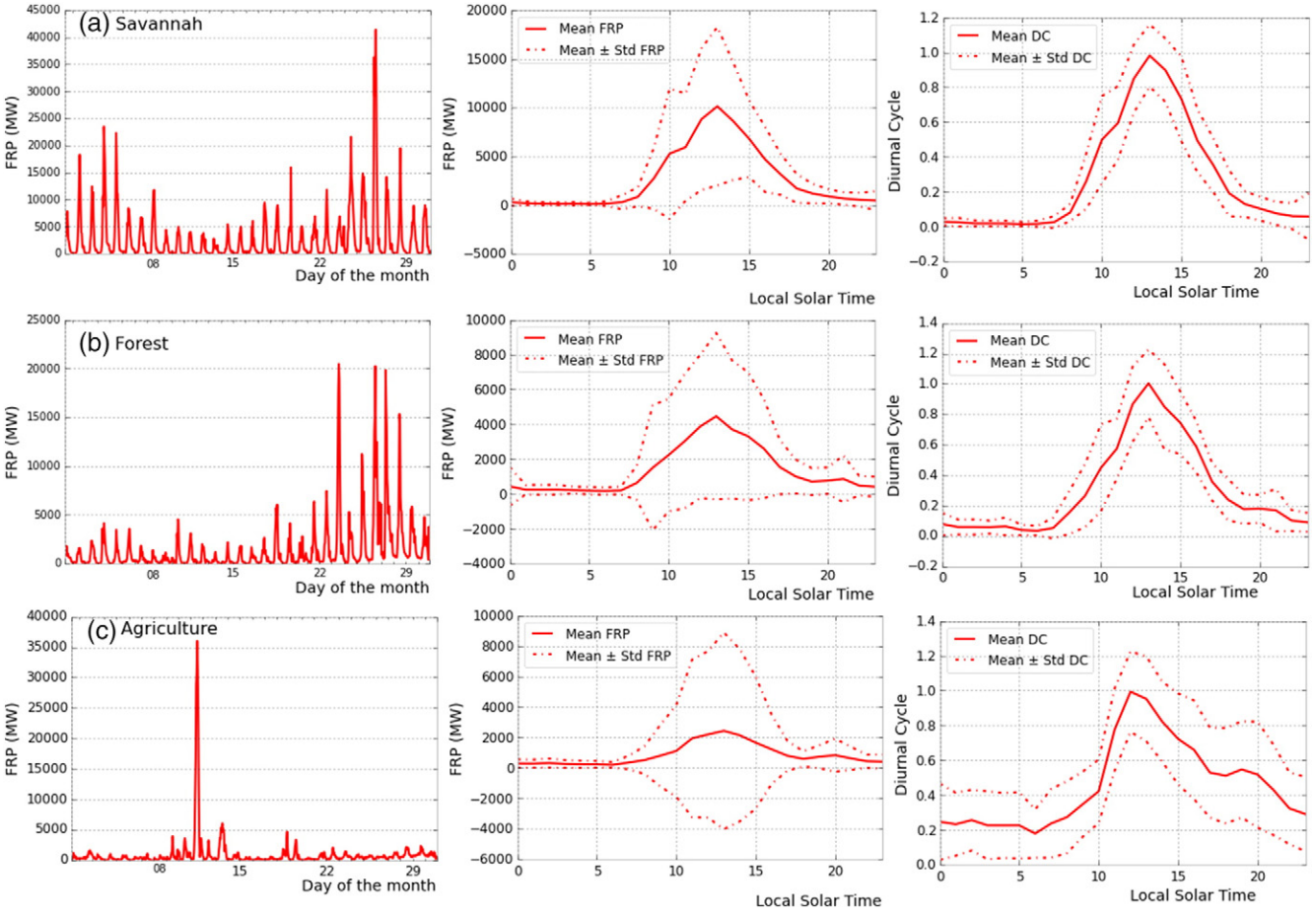

Fig. 11. Active fire information derived across the Himawari-8 AHI full disk in June 2015 for the three key IGBP land cover types; (a) Savannah, (b) Forest, and (c) Agriculture. Shown are (left column) hourly mean FRP, (middle) monthly mean ($\pm 1\sigma$) of FRP, and (right) normalised diurnal cycle. Local solar time is shown rather than UTC. Fires typically peak in the early afternoon, and activity is generally low at night.

the value of geostationary observations, and also very likely additional benefits can be gained by combining them with polar orbiting data to better understand the fire diurnal cycle (e.g. Freeborn et al., 2009; Freeborn et al., 2011; Roberts et al., 2011; Andela et al., 2015). Such diurnal cycle information remains important when linking fire emissions estimates to atmospheric transport models (e.g. Wang et al., 2006) and in converting 'snapshot' FRP measures from sensors such as MODIS into estimates of temporally integrated FRE (e.g. Vermote et al., 2009; Andela et al., 2015).

7. Summary and conclusions

We have developed algorithms for active fire detection and fire radiative power (FRP) retrieval across Asia and Australia, based on data

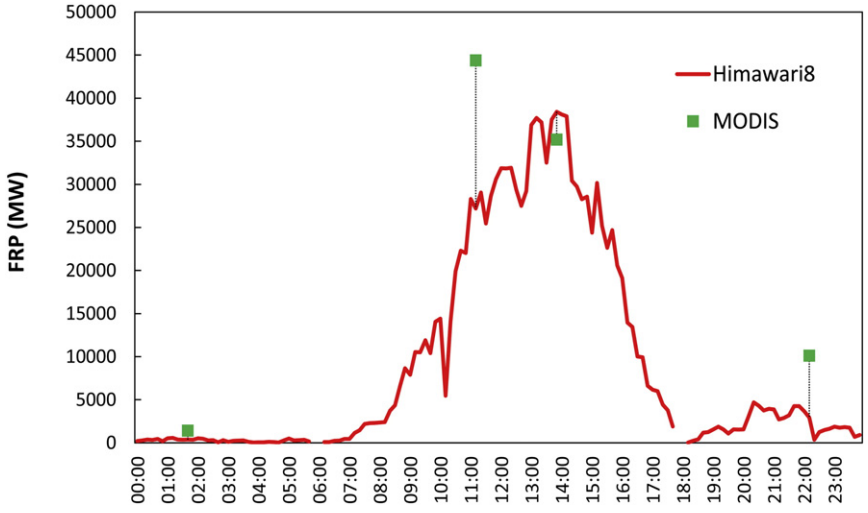

Fig. 12. Diurnal cycle of agricultural residue burning fires in Eastern China on 11th June 2015, whose signatures were recorded by Himawari-8 AHI and MODIS. Note this study area is the same as the map inserted on the top left of the Fig. 3 as indicated by the red rectangle.

from the FY-2 S-VISSR, MTSAT imager and Himawari-8 AHI, the geostationary Fire Thermal Anomaly (FTA) active fire detection algorithm of Roberts and Wooster (2008) and Wooster et al. (2015), the cloud masking procedures of Xu et al. (2010), and the MIR radiance method of FRP retrieval (Wooster et al., 2003, 2005, 2013). For the first time we have intercompared active fire data generated from each of these geostationary data sources, and compared each to simultaneous active fire data from MODIS. FY-2 misses almost all active fires, mainly due to poor MWIR channel image quality and a low spatial resolution (5 km at the SSP). MTSAT (SSP spatial resolution of 4 km) shows a reasonable ability to detect active fires and retrieve their FRP, as long as ambient background temperatures are low enough and the fire not too large so that MWIR channel saturation is avoided. Himawari-8 offers much better capability than the other two sensors, with an ~8% active fire detection error of commission and ~66% of error of omission compared to MODIS, a performance similar to the FTA algorithm applied to data from Meteosat SEVIRI and the GOES imager (Roberts and Wooster, 2008; Roberts et al., 2015; Xu et al., 2010). When AHI and MODIS detect the same fire at the same time we see a very low 3 MW bias between their FRP retrievals, though regionally AHI underestimates FRP by around 50% compared to the simultaneous MODIS view because it cannot easily detect the (rather common) fires whose FRP lies below ~40 MW.

We have used AHI to provide the first genuine diurnal cycle derivation for Asian and Australian fires available from a geostationary satellite. Diurnal patterns are similar to those of the same landcovers found in Africa (e.g. Roberts et al., 2009a, 2009b), with early afternoon peaks fairly comparable but not identical to those reported by Giglio (2007) using data from polar orbiters (MODIS and TRMM). Despite limitations imposed by their relatively coarse spatial resolution, the high temporal resolution offered by geostationary satellites is a key advantage for active fire applications, and highly valuable when driving smoke emissions estimates for use in atmospheric transport models (Reid et al., 2009; Baldassarre et al., 2015; Roberts et al., 2015). We find that the Himawari AHI system offers major advantages over the prior geostationary systems operating over Asia, and we expect that the scheme detailed herein will enable real-time processing of AHI data to join that of GOES (Xu et al., 2010) and Meteosat SEVIRI (Wooster et al., 2015) and becoming an important component of a consistent global geostationary FRP characterisation system. Furthermore, since the Advanced Baseline Imager (ABI) sensor onboard the forthcoming GOES-R spacecraft is extremely similar to AHI (Schmit et al., 2005), the optimised FTA algorithm evaluated here should be easily applicable to the GOES-R mission.

Acknowledgements

We wish to thank to Dr. Takeshi Murata of the National Research and Development Institute of Information and Communications Technology Integrated Data System Research Development Office, and for use of the National Institute of Information and Communications Technology (NICT) Science Cloud who enabled access to Himawari-8 data. FY-2 data was kindly provided by Professor Liu Cheng of the Chinese Meteorological Administration (CMA), and MTSAT data from Professor Wei Fan in the East China Sea Fisheries Research Institute. MODIS data are courtesy of NASA, and we wish to also acknowledge all the National Space Agencies and related organisations whose work made the collection and use of these datasets possible. The parts of this work dealing with MTSAT and FY2 were supported by funding from Innovation China UK (KCL09), with development of the Himawari (H8) algorithm by the UK National Center for Earth Observation (NCEO-King's), and with the validation of the H8 outputs with funding from the European Union. That material is being communicated/published in the name of the Commission, and the Commission is not responsible for any use that may be made of the information. We thank the four reviewers for their constructive comments and suggestions.

References

Andela, N., Kaiser, J.W., Van der Werf, G.R., Wooster, M.J., 2015. New fire diurnal cycle characterizations to improve fire radiative energy assessments made from MODIS observations. Atmos. Chem. Phys. 15, 8831–8846.

Baldassarre, G., Pozzoli, L., Schmidt, C.C., Unal, A., Kindap, T., Menzel, W.P., Whitburn, S., Coheur, P.F., Kavgaci, A., Kaiser, J.W., 2015. Using SEVIRI fire observations to drive smoke plumes in the CMAQ air quality model: a case study over Antalya in 2008. Atmos. Chem. Phys. 15 (14), 8539–8558.

Bessho, K., Date, K., Hayashi, M., Ikeda, A., Imai, T., Inoue, H., Kumagai, Y., Miyakawa, T., Murata, H., Ohno, T., 2016. An introduction to Himawari-8/9—Japan's new-generation geostationary meteorological satellites. J. Meteorol. Soc. Japan 94, 151–183.

Bowman, D.M.J.S., 2000. Australian Rainforests: Islands of Green in a Land of Fire. Cambridge University Press.

Chand, T.K., Badarinath, K.V.S., Murthy, M.S.R., Rajshekhar, G., Elvidge, C.D., Tuttle, B.T., 2007. Active forest fire monitoring in Uttaranchal State, India using multi-temporal DMSP-OLS and MODIS data. Int. J. Remote Sens. 28 (10), 2123–2132.

Engel, C.B., Lane, T.P., Reeder, M.J., Rezny, M., 2013. The meteorology of Black Saturday. Q. J. R. Meteorol. Soc. 139, 585–599.

Freeborn, P.H., Wooster, M.J., Roberts, G., 2011. Addressing the spatiotemporal sampling design of MODIS to provide estimates of the fire radiative energy emitted from Africa. Remote Sens. Environ. 115, 475–489.

Freeborn, P.H., Wooster, M.J., Roberts, G., Xu, W., 2014. Evaluating the SEVIRI fire thermal anomaly detection algorithm across the Central African Republic using the MODIS active fire product. Remote Sens. 6, 1890–1917.

Freeborn, P.H., Wooster, M.J., Roberts, G., Malamud, B.D., Xu, W.D., 2009. Development of a virtual active fire product for Africa through a synthesis of geostationary and polar orbiting satellite data. Remote Sens. Environ. 113, 1700–1711.

Gaveau, D.L., Kshatriya, M., Sheil, D., Sloan, S., Molidena, E., Wijaya, A., Wich, S., Ancrenaz, M., Hansen, M., Broich, M., Guariguata, M.R., 2013. Reconciling forest conservation and logging in Indonesian Borneo. PloS One 8 (8), p.e69887.

Giglio, L., Descloitres, J., Justice, C.O., Kaufman, Y.J., 2003. An enhanced contextual fire detection algorithm for MODIS. Remote Sens. Environ. 87 (2), 273–282.

Giglio, L., 2007. Characterization of the tropical diurnal fire cycle using VIRS and MODIS observations. Remote Sens. Environ. 108, 407–421.

Giglio, L., Schroeder, W., Justice, C.O., 2016. The collection 6 MODIS active fire detection algorithm and fire products. Remote Sens. Environ. 178, 31–41.

Giglio, L., Van der Werf, G.R., Randerson, J.T., Collatz, G.J., Kasibhatla, P., 2006. Global estimation of burned area using MODIS active fire observations. Atmos. Chem. Phys. 6, 957–974.

Guo, Q., Li, X.Y., Chen, G.L., 2009. On-orbit Mtf evaluation for thermal infrared band of Fy-2 satellite and its application in image quality improvements. J. Infrared and Millimeter Waves 28, 335–341.

Huijnen, V., Wooster, M.J., Kaiser, J.W., Gaveau, D.L.A., Flemming, J., Parrington, M., Inness, A., Murdiyarso, D., Main, B., van Weele, M., 2016. Fire carbon emissions over maritime Southeast Asia in 2015 largest since 1997. Sci. Report. 6, 26886.

Hyer, E.J., Reid, J.S., Prins, E.M., Hoffman, J.P., Schmidt, C.C., Miettinen, J.I., Giglio, L., 2013. Patterns of fire activity over Indonesia and Malaysia from polar and geostationary satellite observations. Atmos. Res. 122, 504–519.

JMA, 2014. JMA/MSC: Himawari-8/9. Japan Meteorological Agency (Retrieved 7 October 2015).

Johnston, F., Hanigan, I., Henderson, S., Morgan, G., Bowman, D., 2011. Extreme air pollution events from bushfires and dust storms and their association with mortality in Sydney, Australia 1994–2007. Environ. Res. 111, 811–816.

Kurihara, Y., Murakami, H., Kachi, M., 2016. Sea surface temperature from the new Japanese geostationary meteorological Himawari-8 satellite. Geophys. Res. Lett. 43, 1234–1240.

Li, J., Bo, Y., Xie, S., 2016. Estimating emissions from crop residue open burning in China based on statistics and MODIS fire products. J. Environ. Sci. 44, 158–170.

Loveland, T., Belward, A., 1997. The IGBP-DIS global 1km land cover data set, DISCover: first results. Int. J. Remote Sens. 18, 3289–3295.

Randerson, J.T., Chen, Y., Werf, G.R., Rogers, B.M., Morton, D.C., 2012. Global burned area and biomass burning emissions from small fires. J. Geophys. Res. Biogeosci. 117 (G4).

Reid, J.S., Hyer, E.J., Johnson, R.S., Holben, B.N., Yokelson, R.J., Zhang, J., Campbell, J.R., Christopher, S.A., Di Girolamo, L., Giglio, L., Holz, R.E., Kearney, C., Miettinen, J., Reid, E.A., Turk, F.J., Wang, J., Xian, P., Zhao, G., Balasubramanian, R., Chew, B.N., Janjai, S., Lagrosas, N., Lestari, P., Lin, N.-H., Mahmud, M., Nguyen, A.X., Norris, B., Oanh, N.T.K., Oo, M., Salinas, S.V., Welton, E.J., Liew, S.C., 2013. Observing and understanding the Southeast Asian aerosol system by remote sensing: An initial review and analysis for the Seven Southeast Asian Studies (7SEAS) program. Atmos. Res. 122, 403–468.

Reid, J.S., Hyer, E.J., Prins, E.M., Westphal, D.L., Zhang, J.L., Wang, J., Christopher, S.A., Curtis, C.A., Schmidt, C.C., Eleuterio, D.P., Richardson, K.A., Hoffman, J.P., 2009. Global monitoring and forecasting of biomass-burning smoke: description of and lessons from the fire locating and modeling of burning emissions (FLAMBE) program. Ieee Journal of Selected Topics in Applied Earth Observations and Remote Sensing. 2, pp. 144–162.

Roberts, G., Wooster, M., Freeborn, P.H., Xu, W., 2011. Integration of geostationary FRP and polar-orbiter burned area datasets for an enhanced biomass burning inventory. Remote Sens. Environ. 115, 2047–2061.

Roberts, G., Wooster, M.J., Lagoudakis, E., 2009a. Annual and diurnal African biomass burning temporal dynamics. Biogeosciences 6, 849–866.

Roberts, G., Wooster, M.J., Lagoudakis, E., Freeborn, P., Xu, W., 2009b. Continental Africa biomass burning temporal dynamics derived from MSG SEVIRI. 2009 Ieee International Geoscience and Remote Sensing Symposium. 1–5, pp. 1458–1461.

Roberts, G., Wooster, M.J., Perry, G.L.W., Drake, N., Rebelo, L.M., Dipotso, F., 2005. Retrieval of biomass combustion rates and totals from fire radiative power observations: